ARO 34451.1-EL-CF

CEEDINGS OF THE THIRD INTERNATIONAL SYMPOSIUM ON

LONG WAVELENGTH INFRARED DETECTORS AND ARRAYS: PHYSICS AND APPLICATIONS III

Edited by

S.S. Li
University of Florida
Gainesville, Florida

M.Z.Tidrow
Army Research Laboratory
Fort Monmouth, New Jersey

H.C. Liu
ional Research Council
tawa, Ontario, Canada

W.A. Beck
Martin Marietta Laboratory
Baltimore, Maryland

A. Singh
Kirtland Air Force Base, New Mexico

DISTRIBUTION STATEMENT A
Approved for public release;
Distribution Unlimited

DIELECTRIC SCIENCE AND TECHNOLOGY, ELECTRONICS,
AND LUMINESCENCE AND DISPLAY MATERIALS DIVISIONS

Proceedings Volume 95-28

ECTROCHEMICAL SOCIETY, INC., 10 South Main St., Pennington, NJ 08534-2896

SF 298 MASTER COPY KEEP THIS COPY FOR REPRODUCTION PURPOSES

REPORT DOCUMENTATION PAGE

Form Approved
OMB NO. 0704-0188

1. AGENCY USE ONLY *(Leave blank)*

2. REPORT DATE

3. REPORT TYPE AND DATES COVERED
Final 1 May 95 - 30 Apr 96

4. TITLE AND SUBTITLE
Proceedings of the Third International Symposium on Long Wavelength Infrared Detectors and Arrays: Physics and Applications III

5. FUNDING NUMBERS
DAAH04-95-1-0332

6. AUTHOR(S)
Roque J. Calvo (principal investigator)

7. PERFORMING ORGANIZATION NAMES(S) AND ADDRESS(ES)
Electrochemical Society Inc
Pennington NJ 08534-2896

8. PERFORMING ORGANIZATION REPORT NUMBER

9. SPONSORING / MONITORING AGENCY NAME(S) AND ADDRESS(ES)
U.S. Army Research Office
P.O. Box 12211
Research Triangle Park, NC 27709-2211

10. SPONSORING / MONITORING AGENCY REPORT NUMBER
ARO 34451.1-EL-CF

11. SUPPLEMENTARY NOTES
The views, opinions and/or findings contained in this report are those of the author(s) and should not be construed as an official Department of the Army position, policy or decision, unless so designated by other documentation.

12a. DISTRIBUTION / AVAILABILITY STATEMENT
Approved for public release; distribution unlimited.

12 b. DISTRIBUTION CODE

13. ABSTRACT *(Maximum 200 words)*

The third symposium on Long Wavelength Infrared Detectors and Arrays: Physics and Applications was held at the Fall Meeting of the Electrochemical Society October 8-13 1995 in Chicago. A collection of papers were published in the proceedings of the Third International Symposium.

14. SUBJECT TERMS

15. NUMBER IF PAGES

16. PRICE CODE

17. SECURITY CLASSIFICATION OR REPORT
UNCLASSIFIED

18. SECURITY CLASSIFICATION OF THIS PAGE
UNCLASSIFIED

19. SECURITY CLASSIFICATION OF ABSTRACT
UNCLASSIFIED

20. LIMITATION OF ABSTRACT
UL

NSN 7540-01-280-5500

Standard Form 298 (Rev. 2-89)
Prescribed by ANSI Std. 239-18
298-102

PROCEEDINGS OF THE THIRD INTERNATIONAL SYMPOSIUM ON

LONG WAVELENGTH INFRARED DETECTORS AND ARRAYS: PHYSICS AND APPLICATIONS III

Edited by

S.S. Li
University of Florida
Gainesville, Florida

H.C. Liu
National Research Council
Ottawa, Ontario, Canada

M.Z.Tidrow
Army Research Laboratory
Fort Monmouth, New Jersey

W.A. Beck
Martin Marietta Laboratory
Baltimore, Maryland

A. Singh
Kirtland Air Force Base, New Mexico

DIELECTRIC SCIENCE AND TECHNOLOGY, ELECTRONICS, AND LUMINESCENCE AND DISPLAY MATERIALS DIVISIONS

Proceedings Volume 95-28

THE ELECTROCHEMICAL SOCIETY, INC., 10 South Main St., Pennington, NJ 08534-2896

Published by:

The Electrochemical Society, Inc.
10 South Main Street
Pennington, NJ 08534-2896
Telephone: (609) 737-1902
Fax: (609) 737-2743

Library of Congress Catalog Number: 95-61601

ISBN 1-56677-124-2

Printed in the United States of America

PREFACE

The Third International Symposuim on Long Wavelength Infrared Detectors and Arrays: Physics and Applications was held at the Fall Meeting of the Electrochemical Society, October 8 -13, 1995 in Chicago, Illinois. The purpose of this symposuim was to present a forum for the presentation of recent results and state-of-the-art capabilities for a wide variety of topics in the infrared detector field. The presentations covered the areas of intersubband transition physics, material growth and characterization, device processing and operation, fabrication and performance of focal plane arrays (PLAs) and the readout electronics. The symposuim was sponsored jointly by the Electronics and the Dielectric Science and Technology Divisions of the Society and the U.S. Army Research Office.

The program consisted of five half-day sessions and included twelve invited papers and sixteen contributed papers on a wide range of theoretical and experimental topics such as intersubband spectroscopy, multiquantum well infrared photodetectors (QWIPs), p-type strained-layer QWIPs, multicolor QWIPs, 256x256 focal plane arrays (FPAs) using GaAs/AlGaAs QWIPs for 8-12 μm IR imagery, low noise 1024x1024 HgCdTe/Al_2O_3 FPAs for 3.2 μm thermal imaging, MBE technology for HgCdTe FPAs, modeling and characterization of noises in QWIPs, device physics, fabrication, and characterization of GaInSb/InAs and InAsSb/GaSb type-II superlattices for LWIR detection as well as physical study of type-II superlattices.

I would like to thank all the authors and attendees of the symposuim for their interesting and stimulating presentations and discussion. Special thanks are due to our invited speakers J. Zavada, W. A. Beck, K. K. Choi, J. Van Anda, O. K. Wu, A. Singh, H. C. Liu, C. A. Hoffman, A. Perera, M. Z. Tidrow, R. H. Miles, J. Wagner, and M. O. Manasreh. Their contribution and participation in this symposuim are especially important in setting a high standard for this symposuim.

I am grateful to my symposuim co-organizers Drs. M. Z. Tidrow, H. C. Liu, A. Singh, and W. A. Beck for their assistance and contributions in all aspects of this symposuim. I would also like to thank the session chairpersons for their willingness to chair the session and to review the papers for the conference proceedings. The assistances of Brian Rounsavill and John Stanley of The Electrochemical Society in various symposuim matters are gratefully acknowledged. My special thanks are due to Dr. John Zavada of the U. S. Army Research Office for his financial support and interest in this symposuim. Finally, for those who have a chance to read this volume of the proceedings, I would like to invite you to participate in the next IR symposuim: *The Fourth International Symposuim on Long Wavelength Infrared Detectors and Arrays: Physics and Applications,* to be held in Paris, France, August 31 - September 5, 1997, for the Fall Meeting of The Electrochemical Society.

Sheng S. Li
University of Florida

December, 1995

TABLE OF CONTENTS

FACTS ABOUT THE ELECTROCHEMICAL SOCIETY, INC.

The Electrochemical Society, Inc., is an international, nonprofit, scientific, educational organization founded for the advancement of the theory and practice of electrochemistry, electrothermics, electronics, and allied subjects. The Society was founded in Philadelphia in 1902 and incorporated in 1930. There are currently over 6000 scientists and engineers from more than 60 countries who hold individual membership; the Society is also supported by more than 100 corporations through Patron and Sustaining Memberships.

The Technical activities of the Society are carried on by the Division sand Groups. Local Section of the Society have been organized in a number of cities and regions.

Major international Meetings of the Society are held in the Spring and Fall of each year. At these Meetings, the Divisions and Groups hold general sessions and sponsor symposia on specialized subjects.

The Society has an active publications program which includes the following:

JOURNAL OF THE ELECTROCHEMICAL SOCIETY - The Journal is a monthly publication containing technical papers covering basic research and technology of interest in the areas of concern to the Society. Papers submitted for publication are subjected to careful evaluation and review by authorities in the field before acceptance, and high standards are maintained for the technical content of the Journal.

THE ELECTROCHEMICAL SOCIETY INTERFACE - Interface is a quarterly publication containing news, reviews, advertisements, and articles of technical matters of interest to Society Members in a lively, casual format. Also featured in each issue are special pages dedicated to serving the interests of the Society and allowing better communication between Divisions, Groups, and Local Sections.

EXTENDED ABSTRACTS - Extended Abstracts of the technical papers presented at the Spring and Fall Meetings of the Society are published in serialized softbound volumes.

PROCEEDINGS VOLUMES - Papers presented in symposia at Society and Topical Meetings are published from time to time as serialized Proceedings Volumes. These provide up-to-date views of specialized topics and frequently offer comprehensive treatment of rapidly developing areas.

MONOGRAPH VOLUMES - The Society has, for a number of years, sponsored the publication of hardbound Monograph Volumes, which provide authoritative accounts of specific topics in electrochemistry, solid state science, and related disciplines.

THE ARMY'S RESEARCH PROGRAM IN INFRARED SENSORS

J. M. Zavada
US Army Research Office, PO Box 12211
Research Triangle Park, NC 27709

The Army has had a major involvement in the development of materials and devices for infrared imagers and infrared detectors for DoD applications. Presently, the HgCdTe semiconductor material system forms the basis for the Army's focal plane arrays (FPAs) operating at wavelengths between 3-5 and 8-12 microns. While these FPAs demonstrate very high performance, there are limitations caused by material quality, power usage, and the need for low-temperature operation. Over the past few years there have been a number of exciting advances concerning quantum well infrared photodetectors and uncooled bolometric sensors that may alleviate some of these limitations. This paper presents an overview of the role that the Army Research Office (ARO) plays in sponsoring the basic research in infrared sensors. The Army's requirements for infrared sensors are described as well as research projects that have made significant recent contributions to this field.

ARMY RESEARCH OFFICE

The Army Research Office (ARO) is a separate reporting activity of the Army Materiel Command (AMC). As an executive agent for AMC, ARO links the Army to the world-wide research community through contracts and grants to educational institutions, research institutes, industrial and government laboratories.

The ARO investment strategy is driven by the operational capabilities and requirements as specified in documents such as the Army Technology Base Master Plan, Army 21[1] and AirLand Operation. Research thrusts are focused to enhance current capabilities, and to develop new, key emerging technologies to impact future Army systems. The ARO program is also strongly influenced by new scientific and technological opportunities.

ARO manages approximately one half of the total AMC basic research funds, about $58 million per year. The other half is managed by the Army Research Laboratory (ARL). In addition, ARO leverages about $60 million per year in funding from the Advanced Research Projects Agency (ARPA) and the Ballistic Missile Defense Organization (BMDO) for Army programs. The total funding is invested in contracts and grants, principally with universities. The program includes over 800 single investigators in research institutions and 14 interdisciplinary university centers, as well as a number of special programs.

The mission of the ARO is to seed scientifically sound, and technologically important, efforts which will enhance Army capabilities. Results of prior research sponsored by ARO have led to major changes in Army operations. The development of the laser provided a completely new capability to precisely measure the range to the target, and to designate targets. The Army's capability to fight at night was a direct result of scientific studies dealing with semiconductor materials and photoelectric phenomena for image intensification and infrared detection.

ARO's research program represents the long range view that the Army has for changes in its technology. High-performance electronic/optoelectronic systems are essential for the Army to meet its future information-processing requirements. Functions, such as very intelligent surveillance and target acquisition; command, control, and communications; and, electronic warfare must be accomplished typically under adverse conditions and in real-time. To support the Army's thrust to realize the Digital Battlefield, these systems will need to operate at much higher speeds, have greatly increased functionality, and have much higher levels of integration than present day technology provides. Fundamental research on solid state devices & components is an essential requirement in the development of these future systems.

Major breakthroughs in electronic systems usually occur at the device level. These breakthroughs are due to higher quality materials, improved device processing, new device structures, or greater device integration. Advances in device performance propagate quickly through existing subsystems and systems, enabling greater functionality to be realized. Gains at device and component level lead the way to systems with higher-performance. Examples of device research that have produced revolutionary improvements in systems include: high capacity semiconductor RAM chips for computer memories; low power transistors for wireless communications; and, high performance infrared sensors. All of these advances have had a major impact on both military and commercial systems. At the same time, improvements at the device level represent input to the system designers and profoundly affect the types of architectures and system structures that are possible.

With the Army's emphasis on the Digital Battlefield, research in the areas of optoelectronic devices and circuits is critical. However, novel optoelectronic devices and circuits need to be directed toward specific Army applications to impact this major focus. Advanced optoelectronic device concepts are crucial for providing a revolutionary increase in the overall performance for communications, target recognition, and information processing in the Digital Battlefield. To achieve this goal, high risk research, with high potential payoff, is necessary to stimulate the development of new device concepts for these applications. Requirements of the Digitial Battlefield include: high speed, high volume communications; optical interconnects for high speed, high data rate signal processing; and, high volume, rapid access information storage. Advances in optoelectronic devices are needed in order to transmit, manipulate, and process the enormous amounts of signal, voice and video data present in the battlefield. While there are corresponding requirements in the commercial sector, military operations place extraordinary demands on the integrity and performance of the optoelectronic devices.

Additionally, optoelectronic circuits with higher functionality are required to address specific needs of the Army, such as the optical control of microwave antennas and infrared target recognition. In all these applications, the efficiency, reliability, potential manufacturability and integrability of the optoelectronic devices and circuits must be emphasized.

INFRARED SENSOR RESEARCH

High resolution, high sensitivity, "multicolor" infrared focal plane arrays (IRFPA) are required for target acquisition, recognition, and identification in the Digital Battlefield. Future Army systems will be based on the fusion of data from infrared sensor suites operating at several different wavelengths. Such systems will provide autonomous target acquisition for surveillance, fire control, and identification of friend or foe. The next generation infrared imaging systems will use staring focal plane arrays with considerable front-end processing to provide simultaneous multi-wavelength spatial and temporal detection. This will allow imaging of low observable targets in a clutter environment. Research opportunities include topics leading to the development of low-cost, large area arrays based on II-VI, III-V quantum well, or group IV semiconductor devices operating in the 3-5 and 8-12 micrometer regions. To expand the possibility of dual use, research is needed to improve the quality of II-VI intrinsic detector materials in order to raise the temperature of operation into a region attainable by new thermoelectric coolers. Future image processing will involve operations on a million pixels at rates up to a thousand frames/second and at resolutions of twelve bits and above. This will require advances in parallel processing capability consistent with the determined algorithms. The development of the necessary architectures and the choice of electronic or optical processing will provide significant challenges for the device designer. "Smart" sensors that combine detection with processing are also being investigated. In the area of uncooled imaging, focal plane arrays with moderate performance have been successfully demonstrated with detection limits approaching a tenth of a degree. Further research in thin film ferroelectric and bolometric materials is underway to improve the uniformity, sensitivity, and producibility of future uncooled imagers.

In recent years there have been many scientific contributions that have enhanced the capability of infrared sensing. ARO has been instrumental in providing support that has led to these advances. Several of these contributions are described below.

Electronic Doping of HgCdTe

At Hughes Research Laboratories, Dr. O. Wu, has made significant advances in controlling the electronic doping of HgCdTe semiconductor materials grown by molecular beam epitaxy (MBE). Through a series of careful experiments, he has succeeded in producing both n-type and p-type thin films. Based on these results he has grown multilayer HgCdTe structures designed for long wavelength infrared detection. Using these thin films Hughes Research Laboratories have demonstrated performance of the first IRFPAs fabricated through MBE technology. This research research has a large potential impact on the design and the development of the next generation of Army night vision systems that rely on two color detection.

Electronic Transport in HgCdTe Semiconductors

Research by Professor M. Shur, at the University of Virginia, has led to an improved understanding of electronic transport properties in HgCdTe semiconductor materials. Using Monte Carlo simulation methods, he has shown that the classical theory of impact ionization in these materials needs to include the non-parabolic electronic band structure of these semiconductors. His calculations have yielded excellent agreement with experimental data for electron mobility and electrical breakdown. This research has an influence on the design and performance of infrared focal plane arrays.

Normal Incidence Quantum Well Infrared Photodetectors

Professor K. Wang, at the University of California at Los Angeles (UCLA), has used novel MBE growth techniques to fabricate silicon-germanium (SiGe) multilayer structures to perform normal incidence infrared detection. These structures, known as quantum well infrared photodetectors (QWIPs), consist of SiGe/Si quantum wells grwon on Si substrates. The UCLA team has demonstrated normal incidence detection of infrared radiation at 10 microns through intersubband transitions of the quantum wells. Operation at normal incidence is an important step in utilization of QWIP components in futrue night vision systems.

Novel Energy Filters for Quantum Well Infrared Photodetectors

At Princeton University, Professor D. Tsui has made an important breakthrough in the development of low noise QWIPs. A major problem associated with these devices has been the large dark current which has prevented their use at temperatures above 60 K. A new device concept that involves a multilayer electron barrier structure that effectively suppresses the dark current under applied bias voltages has been developed. Such barrier structures have reduced the dark current in QWIP devices by nearly four orders of magnitude and background limited performance at 77 K has been demonstrated. This research was performed in close collaboration with personnel at ARL.

FUTURE DIRECTIONS

The Army's plan for mobile systems for the Digital Battlefield calls for the development of optoelectronic systems based on minimum power/energy consumption. Advances in materials, devices, and system architectures are needed to achieve this goal. For infrared sensors, lower power and lighter weight components are needed. It is simply impractical to burden the soldier with a heavy load of batteries to power the night viewing systems used on the battlefield. Along with this requirement comes the need to have the infrared sensors operate at higher temperatures. This would lead to size and cost reductions for these components. System costs are presently a major issue in the Army and will probably remain so. No longer will it be possible to optimize system performance without regard for additional cost factors. ARPA has already initiated a program for low cost manufacturing of optoelectronic components. Once the system costs are reduced, there will be greater use of infrared sensors by the military. A related issue is the reliability of the components. It is not sufficient to simply reduce the manufacturing costs of components. The life cycle costs also need to be considered and to be kept as low as possible.

The QWIP devices show high potential for use in future IRFPAs. They are based on a semiconductor technology that has already shown excellent control of material properties and high reproducibility. The QWIP structures can be easily integrated into the large IRFPAs that are in demand for future systems. However, the low operating temperature requirements for the QWIPs impose a severe limitation on their use in current military systems. Further improvements must be made to extend the operational performance to temperatures above 77 K. Once this happens, the QWIP IRFPAs are expected to find widespread military and commercial applications.

Uncooled bolometric detectors, based on Si or ferroelectric materials, are making considerable advances in room temperature infrared detection. Their low cost will also give further incentive for using these sensors on the individual soldier platform. Commercial applications such as law enforcement and vehicle avoidance systems are already being tested. These applications illustrate that there is a continuing need to infrared sensors and that these devices will impact both the military and commercial sectors.

ACKNOWLEDGMENTS

The author gratefully acknowledges the assistance of J. Malamas and F. Semendy from the Army Research Laboratory in preparing this paper.

REFERENCES

1. STAR 21, Strategic Technologies for the Army of the Twenty-first Century (National Academy Press, Washington, D.C.) 1992.

256x256 FOCAL PLANE ARRAYS USING MINIBAND TRANSPORT MULTIPLE QUANTUM WELL INFRARED PHOTODETECTORS

W.A. Beck[†], T.S. Faska, J.W. Little[†], and A.C. Goldberg[†]
Lockheed Martin Laboratories
1450 South Rolling Road
Baltimore, MD 21227

J. Albritton and M. Sensiper
Lockheed Martin Electronics & Missiles
P.O. Box 555837
Orlando, FL 32855

The performance of 256x256 miniband-transport multiple quantum well focal plane arrays (FPAs) is presented. The total noise equivalent temperature difference using f/1.7 optics was about 21 mK, with approximately equal contributions from temporal and spatial components. Measured minimum resolvable temperature (MRT) was 7 mK at low spatial frequencies and 35 mK at Nyquist frequency. Corrected nonuniformity is presented as a function of operability.

INTRODUCTION

Focal plane arrays (FPAs) formed from quantum well infrared photodetectors (QWIPs) have demonstrated excellent imaging and sensitivity(1-4). Several MQW configurations have been reported based on transitions from bound-to-extended (BE) states(5), bound-to-miniband states(6), and between miniband states(7). This paper presents recent progress in the development of long wavelength infrared (LWIR) miniband transport (MBT) MQW detectors and FPAs.

As a class QWIP FPAs have several advantages. Large wafers (up to 6 inches in diameter) are available. Reproducible and precise growth using molecular beam epitaxy (MBE) and a simple fabrication process have produced high yields in both detectors and FPAs. The large wafers and uniformity that can be achieved with MBE offer a unique capability for low-cost production of large, high-sensitivity staring FPAs. Figure 1 shows FPA formats that have been demonstrated at Lockheed Martin (the 640x480 format will be demonstrated in early 1996), and Figure 2 shows the rapid increase in FPA size and improvement in noise-equivalent temperature difference (NETD) that have occurred over the last few years. In addition, measurements made on Lockheed

---

[†] Present address: U.S. Army Research Laboratory, 2800 Powder Mill Rd, Adelphi, MD 20783-1145.

Martin devices have shown that MQW detectors have very high tolerances to both nuclear (8) and laser (9) radiation.

The MBT detector (Figure 3), which is functionally equivalent to the bound-to-miniband design (6), uses doped QWs containing two bound states separated by short-period superlattice barrier layers. The use of two bound states in the QW removes the requirement imposed by the BE design for a unique solution for the well width and barrier height for a given operating wavelength (i.e., it is possible to obtain the same operating wavelength with a continuous range of well widths and barrier heights). Since the excited state of the well is designed to be in resonance with the miniband, the absorption of a photon leaves the electron in a conducting channel (as in the BE designs) through which it can flow and generate photocurrent.

The detector arrays reported here were grown by molecular beam epitaxy (MBE). The active region of the detectors consisted of 40 Si-doped GaAs QWs separated by superlattice barriers consisting of alternating layers of undoped $Al_xGa_{1-x}As$ and GaAs. A highly doped GaAs layer was grown at each end of the active region to provide ohmic contacts. Two-dimensional (square) diffraction gratings were formed by reactive ion etching (RIE) into the top contact layer followed by metallization. The active detector areas were square mesas defined by RIE down to the lower doped contact.

Imaging FPAs were formed by indium bump-bonding the 256x256 MBT detector arrays to Lockheed Martin-designed multiplexers (MUXs), followed by thinning of the GaAs detector substrates to a thickness of less than 6 μm. The thinning traps diffracted light within the pixel, which dramatically reduces optical crosstalk and increases responsivity for focused sources. Thinning also permits the GaAs detector array to follow the thermal expansion and contraction of the Si MUX, thereby allowing very large FPAs. The MUXs used a 1.2-μm p-well silicon complimentary metal-oxide-semiconductor (CMOS) process with 63×10^6 carrier charge well capacity. The detectors were operated at a bias of −2V (applied to the indium bump) for all measurements.

RESULTS

The spectral response of one of the detectors is shown in Figure 4. The peak responsivity was 0.36 A/W, as directly measured using unpolarized light and not corrected for the 30% reflection at the air/GaAs substrate interface.

A 256x256 FPA was mounted in a camera with f/1.7 optics, and the camera was aimed at an extended blackbody source. The FPA temperature was maintained at 60K with an integration time of 5.4 ms. A buffered video board was used to collect sets of 16 sequential digital frames of data at blackbody temperatures of 25, 27, 29, 31, 33, and 35°C. The data in each frame were then converted to apparent temperature, T, by computing gain and offset coefficients from the mean response at 25°C and 35°C.

The Night Vision Laboratories (NVL) 3D noise analysis technique (10) was used to separate the temporal and spatial noise components of the FPA. The results for the center 128x128 section of the FPA are shown in Figure 5. Note that the temporal (tvh) and spatial (vh, v, and h) components were all below 20 mK. The results for the full 256x256 FPA were similar except that a gradual decrease in apparent temperature toward the corners of the FPA (caused by the cold shield) increased the vh component to a maximum of 60 mK.

Figure 6 shows measured minimum resolvable temperature (MRT) vs. spatial frequency (of standard 4-bar targets) for the FPA in the f/1.7 camera. The low-frequency MRT of 7 mK and Nyquist-frequency MRT of 35 mK are both excellent results for a LWIR FPA.

An example of the excellent uniformity of QW FPAs is provided in Figure 7 which shows the corrected response nonuniformity (CNU) as a function of operability for the center 64x64 section of a 256x256 FPA. (The center section was used to permit collection of a large number of consecutive frames in available memory, and was typical of the rest of the FPA.) Note that the CNU is less than 0.04% with only 10 pixels excluded. The result was obtained by using the setup and conditions described for the 3D noise measurements and collecting 248 consecutive frames at blackbody temperatures of 20, 30, and 40°C. The data in each frame were converted to apparent temperature by computing gain and offset coefficients from the mean response at 20°C and 40°C, and finally the mean apparent temperature at each pixel was calculated by averaging over the frames. (The averaging over many frames reduces the contribution of temporal noise to negligible levels.) Finally, the spatial fluctuation in mean apparent temperatures in the 30°C data set was converted to CNU using the known blackbody photon flux contrast at the center wavelength of the detectors. For example, the contrast of a 40°C-blackbody at 9.1 µm is 1.62%/K so a temperature deviation of 1 K implies a corrected response deviation of 1.62%. The indicated dependence on operability was generated by first calculating the CNU over all pixels, then excluding the "worst" pixel from the calculation, then the next worst, and so on.

Video has been collected from a variety of military and non-military objects, including people, tanks, ships, and submarines. Figure 8 shows a single frame of a tank collected from an S-VHS videotape using the same conditions as described for the 3D noise analysis. Note the exhaust plume and the driver, whose head protrudes from the front deck.

CONCLUSION

The results presented demonstrate that MBT MQW FPAs are capable of excellent sensitivity. The temporal and spatial noise components of less than 20 mK at f/1.7 are very competitive with other LWIR technologies as is the demonstrated MRT.

ACKNOWLEDGMENTS

The valuable contributions of others to this work is gratefully acknowledged. In particular, the MBT detectors were built by Mike Taylor, Toby Olver, Kim Olver, and Kerri Wright. The detectors were formed on MBE structures grown by Fred Towner and Dave Gill. Single-pixel tests were performed by Chris Cooke.

REFERENCES

1. B. F. Levine, J. Appl. Phys. **74,** R1 (1993).

2. W. A. Beck, J. W. Little, A. C. Goldberg, and T. S. Faska, in Proc. First International Symposium on Long Wavelength Infrared Detectors, Electrochemical Society, New Orleans, (1993) .

3. W. A. Beck, T. S. Faska, J. W. Little, J. Albritton, and M. Sensiper, in Proc. Infrared Detectors and Focal Plane Arrays III, Orlando, FL, (SPIE), p. 130 (1994) .

4. W. A. Beck, T. S. Faska, J. W. Little, J. Albritton, and M. Sensiper, in Proc. Second International Symposium on Long Wavelength Infrared Detectors, 186th Meeting of the Electrochemical Society, Miami, FL, p. 1 (1994) .

5. B. F. Levine, A. Zussman, S. D. Gunapala, M. T. Asom, J. M. Kuo, and W. S. Hobson, J. Appl. Phys. **72,** 4429 (1992).

6. L. S. Yu and S. S. Li, Appl. Phys. Lett. **59,** 1332 (1991).

7. B. O, J.-W. Choe, M. H. Francombe, K. M. S. V. Bandara, D. D. Coon, Y. F. Lin, and W. J. Takei, Appl. Phys. Lett. **57,** 503 (1990).

8. W. A. Beck, A. C. Goldberg, J. W. Little, and T. S. Faska, "Investigation of the feasibility of developing hardened superlattice detectors," Final report on contract F29601-88-C-0025 to United States Air Force, Air Force Weapons Laboratory, (1993).

9. C. A. Hoffman, J. R. Meyer, F. J. Bartoli, J. R. Lindle, and E. R. Youngdale, in Proc. IRIS Detector Specialty Group, (ERIM), p. 11 (1991) .

10. L. B. Scott and J. A. D'Agostino, in Proc. Infrared Imaging Systems: Design, Analysis, Modeling, and Testing III, Orlando, FL, (SPIE), (1992) .

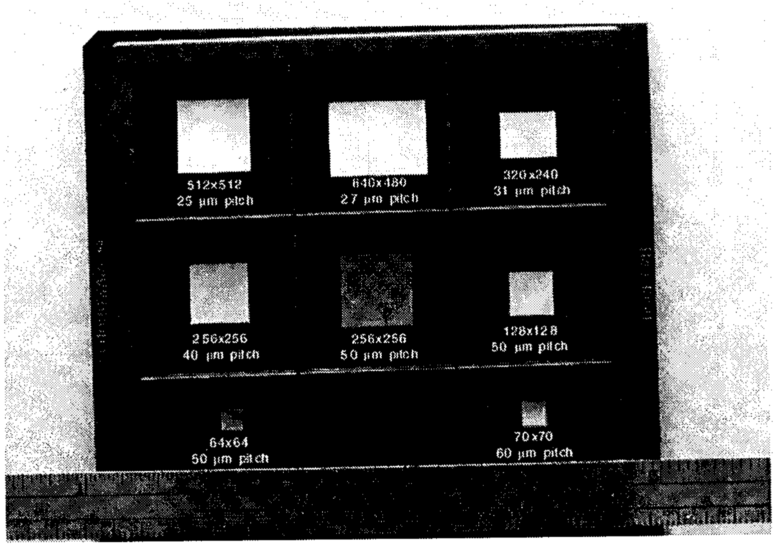

Figure 1: Demonstrated FPA formats (and 640x480 to be demonstrated in early 1996).

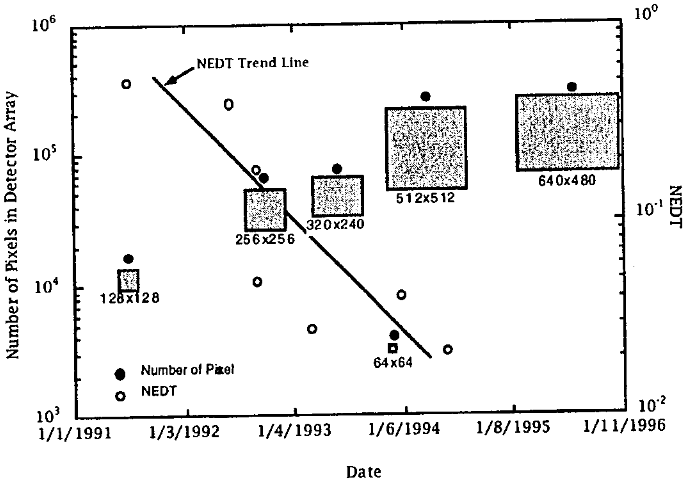

Figure 2: Evolution of QWIP FPA size and temporal NETD vs time.

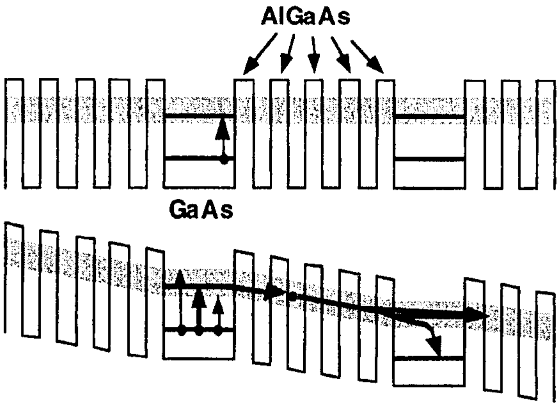

Figure 3: Schematic band diagram of the MBT detector structure.

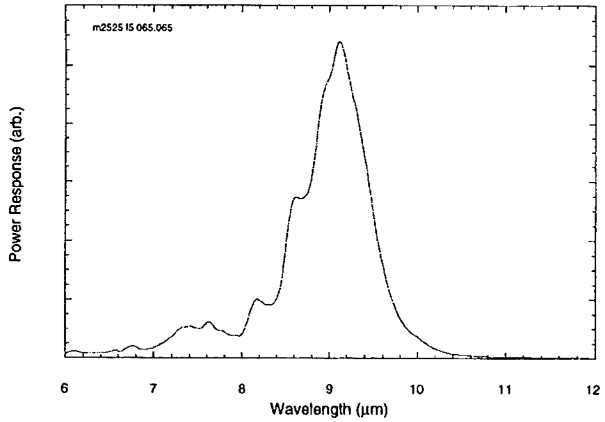

Figure 4: Spectral response of a pixel from the same wafer as used for the FPA results.

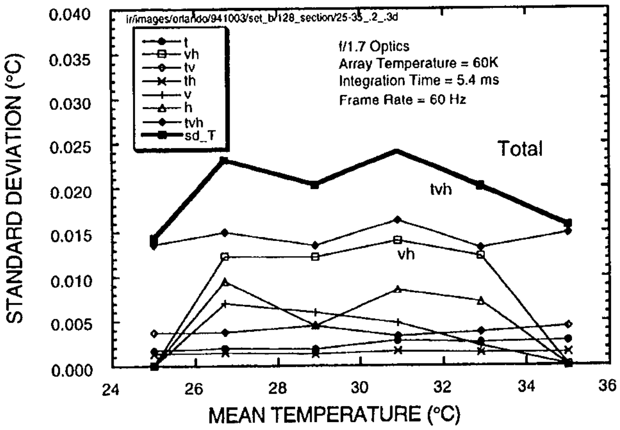

Figure 5: 3D noise analysis of center 128x128 section of a 256x256 MBT FPA (f/1.7 optics). The "tvh" component is uncorrelated temporal noise. The "vh" component is fixed pattern noise.

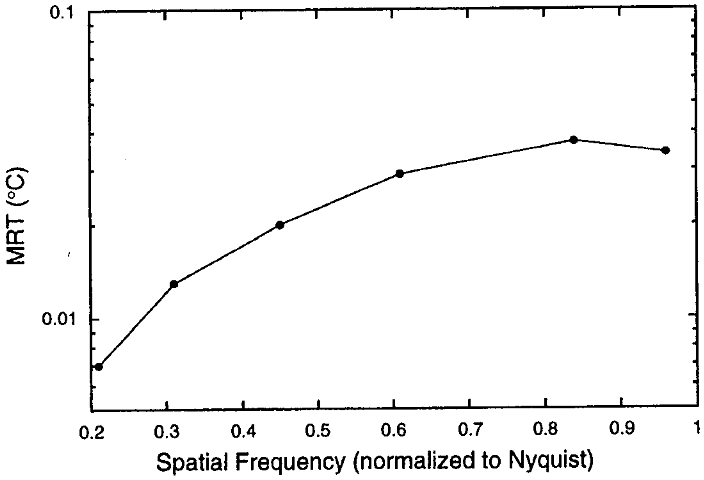

Figure 6: Minimum resolvable temperature for a 256x256 MQW FPA in a f/1.7 camera.

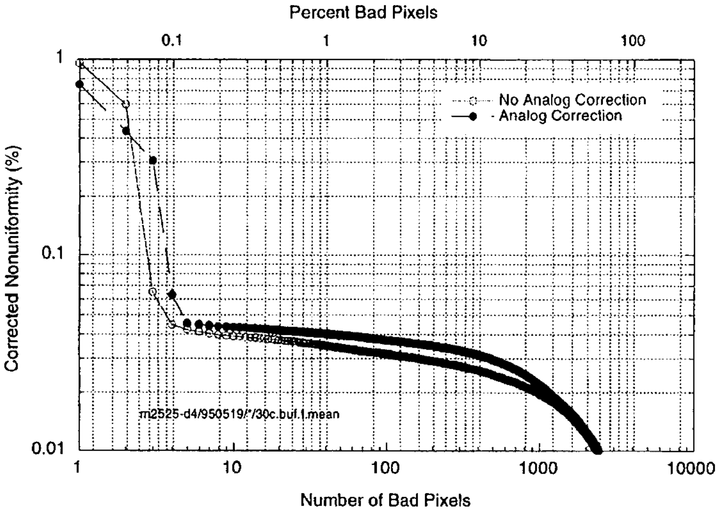

Figure 7: Corrected response nonuniformity vs operability of center 64x64 section of a 256x256 MBT FPA (f/1.7 optics). Calibration is at scene temperatures of 20 and 40°C. Nonuniformity is shown at the midpoint of the calibration interval (30°C).

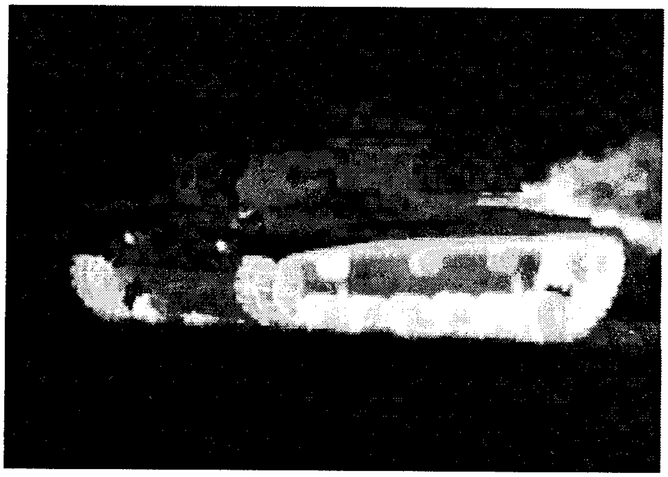

Figure 8: Night image of a tank and driver from a video tape made with a 256x256 MQW FPA at 60K.

INFRARED HOT-ELECTRON TRANSISTORS FOR SYSTEM APPLICATIONS

K. K. Choi, C. J. Chen*, M. Z. Tidrow, A. J. DeAnni, and W. H. Chang

U. S. Army Research Laboratory
Fort Monmouth, NJ 07724-5601

*Permanent address: Dept. of Electrical Engineering, Princeton University, Princeton NJ 08540.

Recently, quantum well infrared photodetector (QWIP) technology has been shown to be capable of producing high quality infrared image in the long wavelength range. In this paper, we propose several approaches to further improve its sensitivity and operating temperature for specific system applications. These approaches include optimization of a basic QWIP, adding an energy filter to form an infrared hot-electron transistor (IHET), and adopting a new scheme for normal incidence light coupling.

I. OPTIMIZATION OF BASIC QWIP STRUCTURES

Since the optoelectronic properties of a QWIP can be designed by varying its structural parameters, one can select optimum device characteristics that fit a specific application. For example, a QWIP detector array may be used for thermal imaging of terrestrial objects at a normal TV frame rate, which is 30 frames/sec. If the detector is sensitive in the 8 to 10 μm band, the number of photons received by a 50 × 50 μm^2 detector using a *f*/2 optics is 3.44×10^{11} ph/s, assuming a blackbody target of 300 K and no transmission or system optical loss. For a charge handling capacity of 5×10^7 e^- per pixel, even a small detector quantum efficiency of 0.44 % is able to generate sufficient optical signal to fill up its integrating capacitor and produce a small $NE\Delta T$ of 11 mK. (In this estimation, we have assumed the photoconductive gain of 1.) Since the average quantum efficiency η of a QWIP in this 2-μm spectral bandwidth based on a typical light coupling scheme is about 10 %, it is 20 times more than sufficient to produce a good thermal image. At this level of η, the extra photoelectrons have to be drained or the duty cycle has to be reduced in order not to saturate the readout circuit.

For high temperature operation, in addition to background photocurrent J_p, the presence of detector dark current J_d will further reduce the photoelectron integration capacity. System performance can be improved if J_p can be made much larger than J_d, which can be achieved either by increasing J_p or by reducing J_d. However, according to the above discussion, it is preferable for this particular application to choose the latter approach. Therefore, in the detector design, it is less important to obtain a broad band detector with a high quantum efficiency, which tends to increase J_p, but rather it is more important to reduce the dark current even though the absorption band may be narrower. At high temperatures, J_d consists mostly thermionic emission current J_{th}, which is exponentially dependent on the quantum well barrier height H. J_{th} can be minimized by having H approximately equal to the second subband E_2, for a fixed peak absorption wavelength λ_p. In such case, the ratio R of the background photocurrent J_p to detector total current $(J_{th}+J_p)$ can be maximized. It can be shown that $NE\Delta T$ is inversely proportional to R while the $\%BLIP$ is directly proportional to $R^{1/2}$. Therefore, R is the system parameter to be optimized. This optimization scheme is different from optimizing the blackbody detectivity $D_{bb}{}^*$ since $D_{bb}{}^*$ is directly proportional to $J_p/(J_{th}+J_p)^{1/2}$ and thus prefers a large quantum efficiency. $D_{bb}{}^*$ should be optimized if there is no limit of charge integration imposed by the readout circuit. To maximize R, bound-to-quasi-bound state (BQ) detectors will be more favorable than the bound-to-extended state (BE) detectors even though $D_{bb}{}^*$ of BQ detector may be lower than that of the BE detector. The lower $D_{bb}{}^*$ is due to the narrower spectral width and a smaller escape probability of a photoelectron in a BQ detector.

It turns out that there is an one-to-one correspondence between λ_p and a BQ detector structure, *ie.* there is a unique BQ structure for every given λ_p. In this structure, the second subband is in resonance with the barrier height H, the quantization condition is

$$\frac{\sqrt{2m^*E_2}\,W}{\hbar} = \pi\ , \tag{1}$$

where $E_2 = H = 748x$ meV, x is the Al molar ratio of the barriers and W is the well width. Eq. (1) determines the relationship between x and W. When x and W are fixed, the first subband energy E_1 is also fixed and can be obtained either by Kronig-Penney model or by transfer-matrix method (TMM). With the known subband energies, $\lambda_p = hc/(E_2-E_1)$ can be obtained, where h is the Planck constant and c is the speed of light. Fig. 1 shows E_1, E_2 and λ_p as a function of W. For example, if λ_p is designed to be at 9 μm, the lower figure shows W to be 52 Å. With this value of W, the upper figure shows E_2 to be 210 meV. The value of x having $H = 210$ meV is 0.28. Therefore, the structure of a 9 μm BQ detector is completely fixed at $x = 0.28$ and $W = 52$ Å. Similarly, for a 15 μm detector, x and W will be 0.17 and 66 Å respectively.

In the above discussion, we have based on a single-band, single-particle theory. Other physical processes that may affect the absorption energy have been ignored. It turns out that they are usually small and tend to cancel each other. For example, considering a typical x of 0.25, starting from the energy separation between E_1 and E_2 calculated using TMM with an energy independent m^*, the corrections include band nonparabolicity (-3 meV), residue direct Coulomb interaction due to dopant migration into the barrier (+1 meV for a dopant diffusion length of 50 Å), exchange and correlation interaction of the

2-dimensional electron gas (+6 meV), electron-phonon interaction (+0.5 meV), and resonant screening in the presence of infrared radiation (-1 meV). Consequently, there is a net increase in the subband separation by 3.5 meV. This result however does not include (1) a possible reduction of 1 meV from the effective mass mismatch between the well and the barrier, and (2) a small reduction in the presence of a finite static electric field during detector operation. It is remarkable that the final correction accounts for only 2.8 % increase in the absorption energy when the detector is design for 10 μm operation, where the subband separation E_{12} = 124 meV. This correction is in fact within the uncertainty introduced by the lack of precise determination of the barrier height H. If H is assumed to be $0.85\Delta E_g$ instead of $0.60\Delta E_g$ presently assumed, E_{12} would have been increased by about 18 meV. Therefore, the correction can be partially accounted for by assuming a slightly different H in the TMM calculation. Experimentally, it turns out that if one assumes $H = 0.60\Delta E_g$, TMM calculation is consistent with the absorption data without taking a correction.

It should be mentioned that all of the above corrections, except the residual direct Coulomb (RDC) interaction, are intrinsic and will not cause experimental fluctuations in the absorption energy when W and x are exactly reproduced. For RDC interaction, due to different extent of dopant migration during the material growth, the actual doping profile depends on the growth condition and can be different from wafer to wafer. When the dopants are confined within a well as that in a delta doped sample, the RDC correction for the first subband is smaller than the second subband because of the more confined first subband wavefunction. Since the RDC correction raises the energy of a subband, the level separation thus increases in this case. However, when the dopant diffusion is substantial, the RDC correction for the first subband can be larger than the second subband, leading to a reduction in the subband separation.

Although the BQ detectors are nearly optimized, they have one serious practical problem. Because the unique relationship between x and W, the structure places a stringent requirement on the growth condition. A more practical approach is to design E_2 to be $\Gamma/2$ above the barrier height where Γ is the full absorption width at half maximum. This approach ensures substantial fraction of photoelectrons to be able to escape from the original well in case the growth parameters are slightly off. In order to fully optimize a QWIP structure in terms of quantum well width, barrier height and doping density etc, we have carried out an experimental as well as theoretical investigation on the relevant optical and transport properties of a basic QWIP structure.[1] Based on a simple semi-empirical theory, it is able to predict the opto-electronic properties and the potential performance for a given set of structural parameters. An example is shown in Fig. 2 for the predicted and the measured background limited temperature T_b of a set of relatively well optimized detectors using the standard 45° light coupling scheme. T_b is the detector operating temperature at which J_d is equal to J_p. In Fig. 2, the field of view is 36°, which corresponds to *f*/1.5 optics. In this study, we found that for a cutoff wavelength λ_c = 9.8 μm, T_b is increased from 65 K to 73 K by increasing the well width from 40 Å (a BE detector) to 50 Å (a BQ detector), in agreement with the above discussion.

Notice that in Fig. 2, when λ_c is below 10 µm, T_b of a QWIP is sensitively dependent on λ_c. T_b can be substantially increased by slightly reducing λ_c in this range of wavelengths. In choosing the detection wavelength in the 8-12 µm band, let us compare two detectors; detector #1 has aluminum molar ratio x of 0.25, and that of detector #2 is 0.27. The absorption band of detector #1 is calculated to be from 8.8 µm to 10.1 µm, and detector #2 is from 7.9 µm to 9.2 µm. By reducing the cutoff from 10.1 µm to 9.2 µm, the dark current is reduced by a factor of 8.7 at 80 K, while the number of photons received by the two detectors differs only by 13 %. As a result, T_b of detector #2 (80 K) is calculated to be 7 K higher than that of detector #1 (73 K). Furthermore, since $(SNR)_p$ of a pixel can be expressed as $(D^*I_o)^2A/B$, where I_o is the source radiance, A is the pixel area and B is the noise bandwidth, $(SNR)_p$ of detector #2 will be a factor of 6.7 larger than detector #1 array at 80 K for the same A and B. This analysis shows that within the 8 to 12 µm band, the detector with x = 0.27 is a better choice than the detector with x = 0.25. Therefore, by choosing a proper cutoff and an optimized QWIP design, one should be able to operate a QWIP array at liquid nitrogen temperature.

II. INFRARED HOT-ELECTRON TRANSISTOR (IHET)

Due to the high current level, even an optimized QWIP is necessarily operated at a reduced duty cycle at 77 K. Its performance can be further improved by adding an energy filter next to a QWIP, forming an infrared hot-electron transistor (IHET). Fig. 2 also shows the experimental T_b for the IHETs, which is consistently higher than that of a QWIP with the same λ_c. This improvement comes from the elimination of several current components, such as the thermally assisted tunneling current in the presence of electron scattering, the thermally assisted impurity tunneling current through the dopant states in the barriers, and part of the thermionic emission current with energy different from the photoelectrons.

One of the important functions of an IHET is to reduce the total current level of a QWIP, including both J_d and J_p, with J_d more than J_p. As discussed in section I, the background photocurrent from a QWIP alone will saturate a readout for the normal TV frame rate. The typical optimized QWIP characteristics for a 9.8 µm cutoff are shown in Fig. 3, showing J_p a factor of 20 too large.[2] With an IHET structure, the total current level can be greatly reduced to within the limit of the readout. As a result, the $NE\Delta T$ is improved by 3.2 times after current reduction. A larger resultant detector impedance also reduces the readout noise.

The current reduction depends on the filter design, it can be tailored to a specific level. For high speed thermal imaging, the frame rate can be as high as 1000 frames/sec. In this case, only a small current reduction is required for detector improvement. Fig. 4

shows an example of the emitter characteristics of an IHET with λ_c = 10.8 μm. The QWIP is BLIP at 65 K. In order to operate the QWIP at 70 K without saturating the readout, the detector needs to be operated below 0.3 V, where the detector is far from background limited. On the other hand, Fig. 5 shows that the collector is BLIP at 70 K at -0.75 V without saturating the readout. For this IHET, the current reduction is less than the previous IHET, being 10 times for the dark current and 4 times for the photocurrent at T = 70 K and V_e = -0.75 V. As a result, the *NEΔT* of an IHET array operated at 1000 Hz is improved by a factor of 2.5.

An IHET improves system performance even if D_{bb}^* is the only relevant figure of merit. Fig. 6 shows the performance of an IHET against a specification for thermal imaging. In this specification, $D_{bb}^* = 6 \times 10^9$ cm√Hz/W needs to be fulfilled. Assuming a quantum efficiency of 25%, an optimized QWIP without nonideal current has a D_{bb}^* of 5.8×10^9 cm√Hz/W at 90 K when λ_c = 9.2 μm, barely satisfying the specification. On the other hand, the figure also shows three IHETs with different combinations of photocurrent and dark current transfer ratios measured at the BLIP temperature. We emphasize that these IHETs are designed at different λ_c, therefore, the combination of transfer ratios at this particular cutoff has yet to be confirmed by experiment. Assuming that this is the case, a D_{bb}^* as high as 9×10^9 cm√Hz/W at 90 K can be obtained, satisfying the specification.

For high temperature operations, an IHET not only is able to filter out the lower energy dark current but also the high energy dark current.[3] Notice that in Fig. 1, there are several detectors with T_b substantially higher than that predicted for high pass filters. They are made of narrow bandpass filters, which accept only a very small range of electron energy. Since there is a large energy spread of thermal current at high temperatures, the ability of a bandpass filter to discriminate the dark current of high and low energies greatly improves the operating temperature. For example, for a cutoff at 14 μm using 45° light coupling, the QWIP detector is BLIP at 52 K. On the other hand, after filtering, the detector is BLIP at 62 K, and can be operated up to 77 K with 45 %BLIP without saturating the readout circuit The estimated *NEΔT* of this IHET array operated at 77 K is 38 mK at 60 Hz with *f*/1.5 optics.

III. OPTIMIZATION OF LIGHT COUPLING

In Fig. 6, η is assumed to be 25 %, which may be achievable by conventional 2d gratings[4] or random gratings[5] in large detector pixels. However, these approaches rely on either grating diffraction effect or multiple reflections between the top contact and the substrate, and hence both are pixel size dependent. When the pixel size becomes small as in high resolution detector arrays, these approaches are less effective. A size independent coupling scheme is much needed. In this section, we propose a new detector structure for normal incident light coupling, which will be referred as the corrugated quantum well infrared photodetector (C-QWIP).[6] A C-QWIP consists of an array of QWIP wires with slanted sidewalls. They are created by etching a number of grooves through the detector active region down to the bottom contact. The cross-section of the detector is shown in Fig. 7. It is known that for certain chemical solutions, the etching rate is different for different crystallographic planes. As a result, triangular wires are created with sidewalls inclined at 54° with the (100) surface along the $[01\bar{1}]$ direction. The new detector utilizes the total internal reflection (TIR) at the AlGaAs-air interface, rather than diffraction, to direct incident light from the normal direction to a nearly parallel direction for infrared absorption.

The C-QWIP structure has a number of advantages over the existing approaches. (1) Since TIR does not depend on the number of wires in a single pixel, in contrast to the grating effect which diminishes with the number of grating periods, the C-QWIP geometry is more effective when the pixel size is smaller than $50 \times 50\ \mu m^2$. (2) TIR directs all the light into a single preferred direction, whereas diffraction generally channels light into several diffraction orders traveling at different angles. TIR is expected to be more efficient. (3) In a C-QWIP structure, the light travels nearly parallel to the layers only in the active region and in a much steeper angle in the substrate region. The light reflected from the substrate is more likely remaining in the same pixel as shown in Fig. 7. For the AlGaAs-air interface, the critical angle is 17.6°, which is smaller than all of the incident angles inside the material under normal incidence. As a result, the light beam undergoes five total internal reflections before it emerges perpendicularly from the substrate. Up to four passes in the detector active region can then be achieved in thinned substrates without causing a cross-talk. A more advanced 2-dimensional groove pattern will further improve the efficiency. For the grating coupling devices, the directions of light in both regions are the same, only one pass can be achieved if it is nearly parallel to the layers. (4) A C-QWIP depends on the reflection at the GaAlAs-air sidewalls, it is more robust than the reflection at the GaAs-metal grating interface since the latter depends on the morphology of the alloyed contact. (5) Since TIR is wavelength independent, there is no spectral bandwidth narrowing effect. A C-QWIP can be used for broad band detection or multi-color detection. (6) Since half of the detector active region is removed, the dark current is substantially reduced. (7) Device processing of C-QWIP is simpler. Since it does not consist of a grating, there are no stringent grating parameters to follow. A thick grating layer also becomes unnecessary. Plasma etching of gratings, which often leads to material damage, can also be avoided.

We have applied the new coupling scheme to a two-color C-QWIP. It consists of a mid-wave (MW) stack and a long-wave (LW) stack of MQWs. Fig. 8 shows the ac spectral response measured using three different light coupling schemes. Curve A is the responsivity of a C-QWIP with 1-dimensional grooves and without substrate thinning. Curve B is the responsivity of a device without a grating but under normal light incidence. Curve C is the responsivity using the standard 45° edge coupling. In calculating the responsivity, the substrate reflection of the incident light, the optical area correction for the 45° coupling device and the partially polarized nature of the light from the monochromator were not taken into account. At low biases ($V < 5$ V), most of the potential is dropped across the MW stack due to its larger resistance, and only a single detection peak at $\lambda_p = 4.7$ μm is observed. When the bias increases to 6 V, the voltage drop across the LW stack becomes appreciable and a second detection peak at $\lambda_p = 9.4$ μm begins to appear. As the bias is increased beyond 7 V, the peak at $\lambda_p = 9.4$ μm becomes dominant. From Fig. 8, curve A is 1.2 times larger than that of curve C in both wavelength ranges without spectral narrowing effect as commonly observed in the grating coupled detectors. This result shows that C-QWIP is capable of multi-color detection. In addition to the responsivity enhancement, a factor of two reduction of J_d at 9 V is observed, which further increases the detectivity of the C-QWIP. The experimental responsivity of the C-QWIP is consistent with the numerical simulation of the optical electric field distribution inside the detector by Roberts and West.[7]

IV. SUMMARY

In summary, we have proposed several approaches to improve the performance of a QWIP. The proper approach depends on specific applications. In general, bound-to-quasi-bound state detector is more favorable than bound-to-extended state detector in terms of system performance. Within the 8 to 12 μm window, a smaller $NE\Delta T$ can be achieved by choosing a shorter wavelength cutoff. An IHET structure further increases the operating temperature, relaxes the material quality requirement and improves the compatibility of the detector and the readout circuit. For high speed applications, high resolution imaging, broad band detection and multi-color detection, we propose the corrugated QWIP structure for light coupling. The initial detector structures with 1-dimensional wires and unthinned substrates show responsivity enhancement compared with both 45° coupling detectors and unthinned 2-dimensional grating coupled detectors,[8] with a concomitant reduction of dark current. In order to fully explore the potential performance of a C-QWIP, more numerical simulations are needed for different 2-dimensional C-QWIP patterns and cross-sections in order to determine an optimized structure. New fabrication procedures may also be needed to produce these new structures. Since the corrugated structure can also be applied to an IHET, the two approaches can be combined to form a CI-HET for further detector improvement.

V. REFERENCE

1. K. K. Choi, C. Y. Lee, M. Z. Tidrow, W. H. Chang, and S. D. Gunapala, Appl. Phys. Lett., **65** 1703 (1994).
2. K. K. Choi, M. Z. Tidrow, M. Taysing-Lara, W. H. Chang, C. H. Kuan, C. W. Farley, and F. Chang, Appl. Phys. Lett. **63**, 908 (1993).
3. C. Y. Lee, K. K. Choi, R. P. Leavitt, and L. F. Eastman, Appl. Phys. Lett., **66**, 90 (1995).

4. J. Y. Anderson, and L. Lundqvist, J. Appl. Phys. **71**, 3600 (1992).
5. G. Sarusi, B. F. Levine, S. J. Pearton, S. V. Bandara, and R. E. Liebenguth, Appl. Phys. Lett. **64**, 950 (1994).
6. C. J. Chen, D. C. Tsui, K. K. Choi and M. Z. Tidrow, unpublished.
7. C. W. Roberts and L. C. West, private communication.
8. M. Z. Tidrow, K. K. Choi, A. J. DeAnni, W. H. Chang, and S. P. Svensson, to be published in Appl. Phys. Lett.

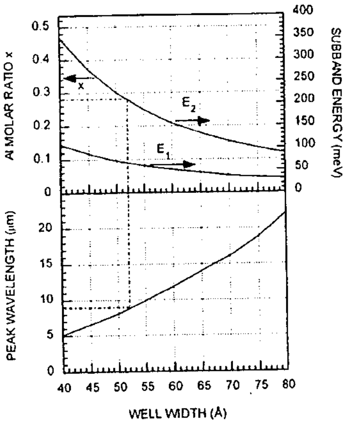

Fig. 1 The figure shows the Al molar ratio and the peak wavelength of a QWIP having E_2 aligned with H as a function of well width.

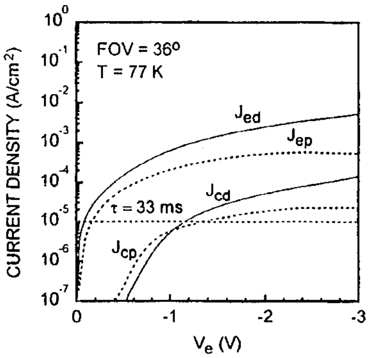

Fig. 3 The dark current and background photocurrent characteristics of an IHET having λ_c = 9.8 µm and 45° light coupling.

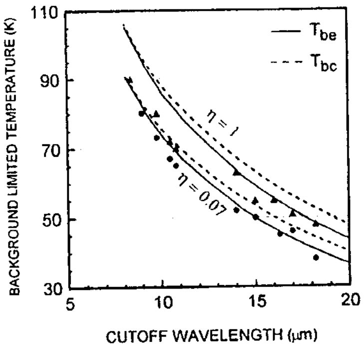

Fig. 2 The calculated (curves) and the measured (symbols) background limited temperature of QWIPs and IHETs as a function of λ_c. The external η using 45° coupling is estimated to be 7%.

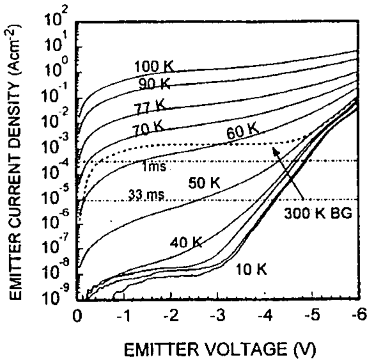

Fig. 4 The dark current and background photocurrent characteristics of a QWIP having λ_c = 10.8 µm and 45° light coupling.

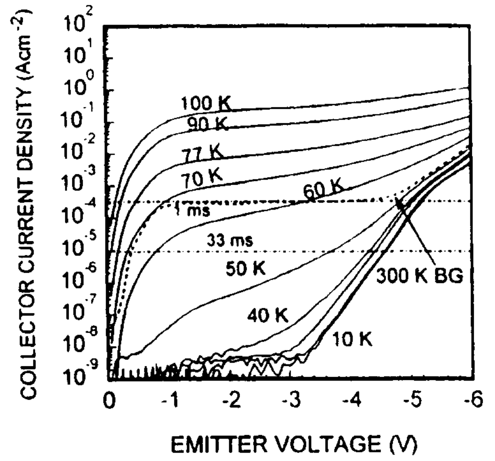

Fig 5 The dark current and background photocurrent characteristics of an IHET having λ_c = 10.8 μm and 45° light coupling.

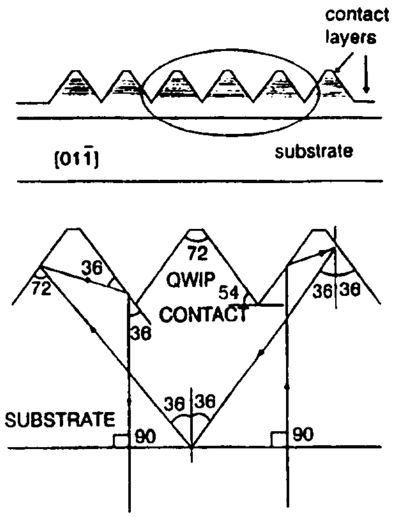

Fig. 7 The cross-section of a C-QWIP. Up to four passes can be achieved using this device geometry.

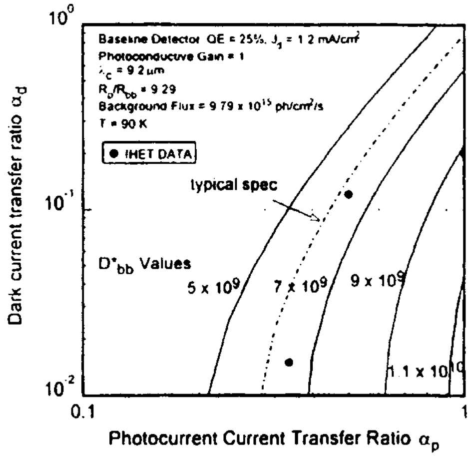

Fig 6 The figure shows the D_{bb}* of an IHET with different combinations of dark current and photocurrent transfer ratios. It is based on extrapolated detector dark current characteristics at 90 K, a spectral width of 1.3 μm and f/2 optics. The ratio of peak responsivity R_p to blackbody responsivity R_{bb} is 9.29.

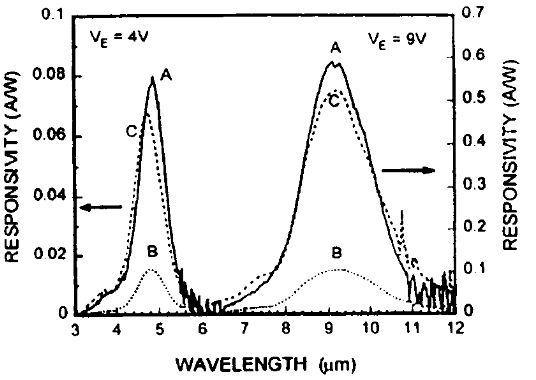

Fig 8 The spectral response of a C-QWIP (A), a QWIP (B) and a QWIP with 45° light coupling (C).

READOUT ELECTRONICS AND CRYOSYSTEM DESIGN FOR A QWIP FPA.

James B. Van Anda
Digital Imaging Inc.
1428 E. Semoran Blvd., Suite 114
Apopka, FL. 32703

ABSTRACT

Quantum Well Infrared Photodetector (QWIP) performance has intensified industry activity toward moving these devices from experimental single element devices, into imaging staring focal plane arrays. Two critical technologies are needed to prepare the staring focal plane array for integration into an imager: (1) a readout multiplexer in a vacuum dewar, and (2) a method of holding the FPA at a constant cryogenic temperature. This paper discusses advantages and drawbacks of various approaches to accomplishing these tasks.

INTRODUCTION

Performance results from prototype Quantum Well Infrared Photodetectors (QWIPs) has intensified industry activity toward moving these devices from experimental single element devices, into thermal imaging staring focal plane array systems.

As these low cost QWIP devices continue to mature both in producibility and performance, parallel developments in low cost readout circuitry and low cost, hi-rel cryogenic cooling devices will be linked to QWIPs to enable hi performance staring FPA QWIP systems that can meet the demanding requirements of military and commercial thermal imaging systems.

READOUT TECHNOLOGY

Historical Perspective

Contemporary IR imagers use linear arrays of IR detectors. Typically, a row of Mercury-Cadmium-Telluride (MCT) detectors horizontally scanned across the field of view to produce a two dimensional thermal image is the approach taken (Figure 1A). These detectors had an acceptable low number of detectors (usually less than 240 elements) to allow direct connection output to the processing electronics via individual wires through a vacuum dewar housing. Each detector was amplified by a separate amplifier and then processed for display. As the marketplace demanded higher performance, a larger number of detectors was required to provide this higher performance. Soon the number of detectors exceeded the ability to output them via wire bonding and wires through the dewar. Alternate solutions were investigated and silicon readout multiplexers were developed that could operate at the cryogenic temperatures required by the MCT detectors.

The first configurations (Figure 1B) considered for silicon readout multiplexers were MCT array densities of 120 elements by 4 elements in a two dimensional array. Four of these MCT chips were configured to produce a 480 element by 4 element detector array. This detector was scanned by a scanner assembly and improved performance was achieved through time displacement and addition of the 4 elements in the scanned direction. The combined number of detectors in this approach is almost 2000 individual detectors.

Photoconductive MCT, the detector process in use at the time, was not acceptable for the newer detector configurations because the high bias power needed for photo conduction became excessive when the number of detectors increased. Photovoltaic MCT became the new accepted process. In the photovoltaic process the photo response mechanism changes the MCT diode operating point and therefore does not require a large bias current.

High impedance from the sensor became a driving design characteristic because the development of the readout circuit was built around a high impedance source. Readout technology most used by industry was an integrating stage where the charge on a capacitor is controlled by the photo diode current. This stage, along with silicon switched or CCD stages, formed the early readout technology. By proper processing, the charge on a single capacitor was accumulated from the 4 detectors in the scan direction. This technique is called time displacement and integration (TDI), and TDI was the first technique to use cryogenic readout electronics.

The problem of detector-to-readout interconnection could not be solved by wire bonding due to the close spacing of the detectors in the TDI configuration. A new technology - that of indium bump bonding - was developed (Figure 2). This process involves an array of small balls of indium that are placed between the detector diodes and the input pads of the silicone readout circuits. Compression force is applied to the detector/indium bump/silicon sandwich to make a permanent connection between the detector and the readout. The indium 'bumps' also provide the needed mechanical interface between the MCT detector and the silicon readout to allow for the differences in the expansion coefficients between the silicon readout and the MCT detector as mechanical movement is induced by cycling between room temperature and cryogenic temperatures.

Once the problems of interconnection, thermal expansion, and cryogenic operation of silicon MOS drivers were solved, larger staring configuration began to appear. The first non-scanning, 2- dimensional staring arrays, shown in Figure 1C, were 32x32 and

64x64 configurations. This led to the development of longer integration times and the integration of other IR detector technologies such as Indium Antimonide (InSb) and multiple Quantum Well GaAs. Availability of these arrays has spurred the development of large staring arrays operating in the midwave and longwave IR wavelengths.

CIRCUIT TECHNOLOGIES

Readout circuit technologies have developed around two factors: detector impedance, and polarity. The emergence of midwave detectors has introduced higher detector impedance (lower detector currents) and the development of multiple quantum well detectors has introduced high impedance, low current photoconductivity to the market.

The majority of the multiplexer techniques used in the readout are switched MOS transistors. However, some multiplexers still use CCD technology. The major difference between existing readouts and newer readouts is in the area of the input detector interface unit cell.

Unit cell designs take several different approaches. The main challenges are to design a circuit that has both low noise, wide range, good linearity, and also occupies very little space. Each detector in the array must be connected to one unit cell so the unit cells must fit in the area of one detector spacing. As FPA density increases, the detector spacing decreases, which limits the unit cell area. Some unit cells must be as small as 20 μm x 20 μm, or even smaller.

The first unit cell design was the direct injection (DI) stage. This design was borrowed from visible CCD designs and is shown in Figure 3. The gate voltage of the buffer stage operates to bias the detector and the drain current, which is the same as the detector current, is used to charge the integration capacitor. A reset FET is used to discharge the storage at the end of the integration time. This is the simplest unit cell and uses the least area (dependent upon capacitor size). The injection FET will remain biased sufficiently to maintain high gain at medium to high irradiance levels. However, at low irradiance levels, larger variations in gain will cause large nonuniformity in the image. To reduce noise, the photodiodes need to be operated at very low bias levels (near 50 mv). In this mode, gate threshold variations on the input channels cause a significant variation in detector noise and in offset uniformity. This gate threshold variation is not as noticeable when biasing QW detectors because of the relatively high bias used (1 - 3 volts) or more, and the photoconductive nature of the QW device usually provides sufficient bias for good gain even at low impedance levels.

An improvement in the performance of the DI stage was the buffered direct injection stage (BDI) (see Figure 4). This design adds a feedback operational amplifier to the gate circuit of a DI stage. This reduces the gate threshold variations and improves transfer efficiency and bandwidth by lowering the input impedance. The CMOS amplifiers, with higher gains, allow the minimum operating irradiance levels to be lowered by several orders of magnitude. The BDI design requires a larger unit cell and is operated with higher power than the BDI. This configuration is most popular with fairly low density staring arrays and scanning TDI arrays. When used with Quantum Well arrays, this design will improve injection efficiency, dynamic range, and operation at low irradiance levels.

Another popular design is the current mirror design (Figure 5). This design is popular in detectors to be used in very high backgrounds and large dark currents. When used with photodiode detectors it exhibits poor uniformity and does not have a stable uniform detector bias needed for low 1/f noise. When used with a QW detector that exhibits a relatively high dark current and has high bias voltages, this circuit may have better performance than with photodiodes. This circuit has fairly good linearity and requires a small unit cell area.

The final unit cell design is the capacitor feedback transimpedance amplifier (CTIA) shown in Figure 6. This circuit is a reset integrator with the capacitor as the feedback element. The advantages of this circuit are very low input impedance and a very stable uniform detector bias voltage. Its gain is set by a very predictable feedback capacitor. This circuit exhibits a kTC noise and may need special auto zeroing circuits. It is a complicated circuit that needs the same unit cell area as the BDI circuit.

These four circuits are all applicable to QW implementation. However, for high density arrays, the two circuits (DI and CM) may be the most useful in Quantum Well arrays.

Future in Readouts

These readout unit cells and their multiplexers continue to grow and become more useful as technology allows. The multiplexers are becoming more self clocking to minimize the number of clocks needed to operate the mux. This reduces the number of vacuum dewar penetrations.

Improvements in signal performance are also being developed. Several parts, where course correction coefficients can be loaded, will improve linearity, uniformity, and dynamic range by providing an offset correction at the unit cell.

Multiple A-D conversions on chip and digital multiplexing are being studied along with modulation schemes that allow fiber optic and capacitive or inductive, feed-through schemes to be used without vacuum dewar penetration. Other on-focal plane processing developments include; image subframing, where a controlled area of the focal plane can be muxed out at higher frame rates; image processing for defective pixel; edge enhancement;

and compression algorithms. Future readout technologies will include alternate substrates to silicon such as GaAs where monolithic Quantum Well multiplexers can be fabricated.

COOLER TECHNOLOGIES

Almost all high performance IR sensors need active cooling to reduce the operating temperature to a level where thermal noise in detectors is not the dominate noise. Earlier in the development of IR sensors, closed cycle cooling engines were not available so powerful dewars and high pressure cryostat systems were used for cooling. In the early 1960's, the closed cycle sterling engine coolers were developed by US Army Night Vision Laboratory.

Detailed descriptions of the Stirling thermodynamic cycle are found in a number of articles and books such as the one by Walker (1). A brief description of the cycle follows. The Stirling cycle produces refrigeration by the isentropic expansion of gaseous helium. In a closed cycle, the helium is alternately compressed in a compression space at ambient temperature and expanded to the required low temperature in an expansion space. The gas reciprocates between the compression and expansion spaces through a regenerator, which serves as a heat exchanger and heat sink for the incoming and returning gas flow. The Stirling cycle can be ideally described in terms of two constant temperature volume processes as shown in Figure 7.

The compression piston (Fig. 7), regenerator, and expansion piston are represented schematically and the contribution to the cycle pressure and volume curve is shown for each of the four processes. The four cycles are described below:

1. With the expansion volume at its minimum and the compression space at its maximum (Fig. 7, 1 to 2), the compression piston moves to the left, compressing the gas in the compression space. As the gas is compressed, heat is removed from the cylinder walls so that the process is isothermal.

2. Both the compression and expansion pistons move to the left, keeping the volume constant and transferring the gas through the regenerator (Fig. 7, 2 to 3). During the transfer, the gas is cooled by the regenerator mass that stores the heat contained in the gas, thus allowing it to enter the expansion space at the approximate temperature of that space.

3. The expansion piston moves to the left (Fig. 7, 3 to 4), expanding the gas in the expansion space. As the gas is expanded, heat is absorbed from the thermal load (the detector elements) so that the process is isothermal.

4. Both compression and expansion pistons move to the right (Fig. 7, 4 to 1), keeping the volume constant, and transferring the gas through the regenerator from the expansion space back to the compression space.

During the transfer, the gas is warmed by the stored heat in the generator, thus allowing the gas to enter the compression space at the approximate temperature of that space.

In the actual operation of a cooler, a significant departure from this idealized process arises as a result of the continuous motion of the pistons. The four steps of the ideal cycle are not sharply defined, and this results in a pressure-volume curve which is a smooth, continuous envelope such as is shown in Figure 8.

The first widely used miniature refrigerator employing the Stirling cycle achieved the necessary compression and expansion of the helium working fluid by a compression piston and a displacer that are 90 degrees out of phase and are driven by a single eccentric shaft. This configuration required that the entire unit be located in the immediate vicinity of the detector, which presents a problem for systems where weight, vibration, EMI, and/or packaging space in the detector area is restricted to a minimum. A commonly used configuration that overcomes these disadvantages is the split cycle Stirling cooler. This type of cooler is basically a valveless device consisting of a mechanical compressor and a pneumatically driven displacer (Figure 9). Oscillatory motion of the displacer results from combined forces of the compressor periodic pressure wave and a restoring force caused by pneumatic "spring" volume pressure acting on the displacer. The compressor and displacer are connected by small-diameter, high pressure tubing that offers the packaging flexibility of locating the compressor in a position removed from the immediate vicinity of the detector.

The split configuration has seen significant improvements in efficiency and in reliability. The latest configuration uses a linear resonant drive system in the compressor instead of the rotary compressor to achieve low vibration forces and very low noise. These units can achieve cooling to wells below 60°K and have versions from 1/10 W to 1 Watt of cooling capability. Other schemes for developing compression necessary are under development. One very promising scheme uses piezo-electric expansion to create the necessary pressure wave to operate the sterling cycle refrigerator. The advantage of this scheme is that the complete compressor can be manufactured as a sealed unit without rotating parts. The piezo expansion occurs in solid ceramic material. This scheme produces no magnetic fields and has low vibration. These properties make it a candidate for a small integral dewar built around the ceramic actuators.

The high reliability that the coolers exhibit make them candidates for integral detector dewar assemblies (IDA). Typically detectors are mounted in glass or metal vacuum dewars and the cooler assemblies were mechanically mated through a thermal interface assembly. These assemblies are not in the vacuum dewar and therefore, are the source of many thermal mismatch issues.

In a slip-on dewar, it is virtually impossible to achieve a constant uniform temperature profile across a large detector. The solution to this problem is to mount the detector on the end of the cold finger and then place the cold finger inside the vacuum dewar; i.e. make the cold finger part of, or integral, to the dewar. The (IDA) is much more efficient in its ability to deliver cooling uniformly to the detector, thereby allowing smaller cooling engines to be used in IR systems. Even more efficiency can be achieved by eliminating the transfer line and returning to the integral cooler compressor. Newer designs with their low noise, low vibration, and small size, allow the return to the integral design without the problems that lead to the split design. Only the problem of EMI (with large magnetic fields near the detector) still exists. This problem is eliminated by the piezo drive design approach due to the elimination of magnetics. At lower cooling power, the magnetic systems are commonly used in IDA configuration.

CONCLUSION

This paper has discussed the advances in multiplexer and dewar-cooler technologies. The combination of these technologies will lead to a small integral detector assembly that will contain staring FPA detectors, multiplexer, dewar, cooler, and interface, in a compact assembly useful in many staring focal plane array thermal imaging systems.

REFERENCES

Books

1. G. Walker, Stirling Cycle Machines, Clarendon Press, Oxford (1972)

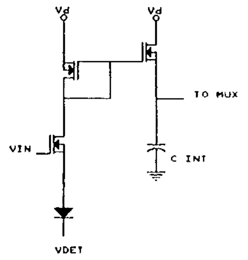

Figure 5. Current Mirror

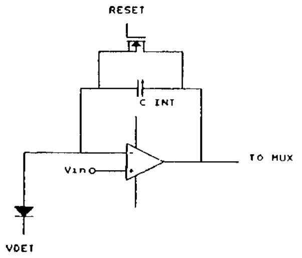

Figure 6. Capacitor Feedback
Transimpedance Amplifier

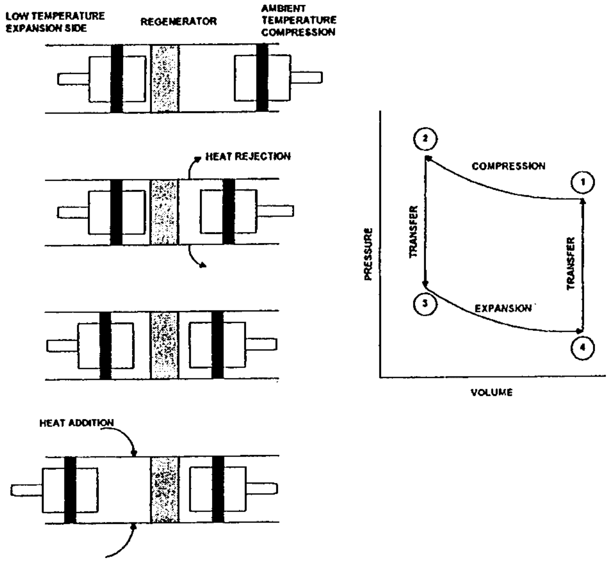

Figure 7. Stirling Cycle

Recent Advances In HgCdTe MBE Technology

O. K. Wu, R. D. Rajavel, T. J. DeLyon and J. E. Jensen
Hughes Research Laboratories
3011 Malibu Canyon Road, Malibu, CA 90265
and
C. A. Cockrum, S. M. Johnson, G. M. Venzor,
G. R. Chapman and W. A. Radford
Santa Barbara Research Center, 75 Coromar Drive,
Goleta, CA 93117

Abstract

Major advances in controlling the structural and electrical properties of HgCdTe alloys have been made in MBE technology during last couple of years. Device quality materials with desired characteristics have been grown with the alloy compositions required for short-wavelength infrared (SWIR, 1-3 micron) to very long-wavelength infrared (VLWIR, 16-20 micron) applications. The breakthroughs to achieve In (n-type) and As (p-type) doping in situ at HRL have provided greater flexibilities for fabricating advanced double-layer heterojunction devices. High performance IR focal plane arrays (128x128) with R_0A of 220 Ω-cm^2 and D* of 2.2×10^{11} cm$\sqrt{\text{Hz}}$/W at a temperature of 80K for a 9.92 μm detection have been fabricated; and IR images obtained from these MBE-grown arrays are shown. In addition, heteroepitaxy growth of HgCdTe on silicon will be discussed.

Introduction

Current and future demands in the IR industry require low-volume, fast cycle time and flexible manufacturing of high performance focal plane arrays (FPAs) with stringent noise and uniformity requirements. While the current LPE technology has several limitions on the control of composition and doping profiles for the advanced device structures needed for smart FPA applications, HgCdTe MBE technology offers low temperature growth under an ultra-high vacuum environment, in situ n-type and p-type doping, and control of composition, doping and interfacial profiles. All these advantages are essential for the growth of advanced double-layer, multi-layer structures and superlattices for optimal smart FPA devices. Significant progress has been made in HgCdTe MBE technology over the last two years [1&2].

In this paper, we will briefly review (1) the flexibility of HgCdTe MBE growth for SWIR, MWIR, LWIR and VLWIR FPA applications, (2) the material characteristics which can be achieved today, (3) the fabrication of high performance FPAs (128x128) based on MBE in-situ grown double-layer heterojunction structures and lastly, (4) heteroepitaxy growth of HgCdTe on silicon substrates.

The Flexibility of HgCdTe MBE Growth

About fifteen laboratories worldwide are pursuing the MBE growth of Hg-based alloys and superlattices since Faurie et al. demonstrated the growth of HgCdTe by MBE in 1982 [3]. The growth of device quality $Hg_{1-x}Cd_xTe$ alloys with desired structural and electrical properties has been demonstrated at Hughes Research Laboratories routinely over the range of interest for SWIR-VLWIR infrared detector applications. The composition of HgCdTe alloys can be varied readily by choosing appropriate beam flux ratios. We have shown that over the range from x=0.22 to x=0.50, excellent control of composition can be achieved by varying the CdTe source flux with a constant flux of Hg at 3×10^{-4} mbar and Te at 8×10^{-7} mbar during the MBE growth. For x-values outside this range, an additional adjustment of Hg and Te fluxes is required.

The flexibility and reproducibility of HgCdTe MBE growth technology are illustrated in fig.1. This figure shows the reproducibility of cutoff wavelength of HgCdTe base layers grown in a series of experiments that first targeted for the SWIR band (1.3 μm at room temperature) followed by another series of experiments targeted for LWIR band (10.5 μm at 77K), and finishing with the same SWIR as the first targeted to demonstrate the flexibility of the HgCdTe MBE growth technology. These data indicate that HgCdTe MBE technology is mature for the growth of advanced multi-layer device structures for infrared detectors for both military and commercial applications.

Material Characteristics

Today, the majority of the HgCdTe MBE efforts are centered on the (211) orientation of CdZnTe substrates with a 4% concentration of zinc for lattice matching with $Hg_{0.78}Cd_{0.22}Te$. Device quality MBE-grown HgCdTe epilayers have been grown in a few laboratories [4,5&6]. For instance, we have shown at Hughes that excellent crystallinity of HgCdTe alloys (FWHM<30 arc-sec) can be grown routinely as demonstrated by the four-crystal rocking curve measurement shown in fig 2. Fig.2 shows the x-ray rocking curve data for two sets of 30 samples. The results indicate that the average x-ray full width at half maximum is 27 arc-sec. We anticipated that this average value will be reduced as the quality of CdZnTe substrates improves.

Most of the early HgCdTe MBE research [3] was focused on the growth of HgCdTe on the CdTe(111) orientation due to the least amount of Hg flux required for the growth process[3]. Later on, some efforts were devoted to the growth of HgCdTe on the CdTe(100) orientation [4]. However, problems of twinning and hillocks were found in the materials that were grown on the (111) and (100) orientations, respectively. Thus, most of the advances in recent years are in the (211) orientation.

N-type doping control in the growth of II-VI semiconductor materials is relatively easy as compared to that of the p-type doping control. At Hughes, we have demonstrated that the In (n-type) concentration can be varied from 1×10^{15}-$5\times10^{18}/cm^3$. [5&6] Fig.3 shows the Hall data for a typical HgCdTe alloy with a 22% Cd concentration and a doping of $2\times10^{15}/cm^3$ for LWIR 10 μm detection, the Hall mobility was greater than 1×10^5 cm^2/V-sec at 77K and greater than $2\times10^5 cm^2/V$-sec at 40K. A comparison of SIMS and Hall effect data shows the In is nearly 100% active.

For p-type doping, we employed cadmium arsenide compound [6] and achieved acceptor carrier concentrations from 10^{16} to $10^{18}/cm^3$. Fig.4 showed the temperature dependent Hall effect data which indicate that acceptor mobilities are about 100 cm^2/V-sec at 77K with an activation of 7 meV, and a combination of SIMS, Hall and C-V measurements indicates an activation efficiency of at least 60%.

In addition, minority carrier lifetimes greater than 1 μsec and etch pit density (EPD) values less than $2\times10^5/cm^2$ were observed in the In-doped HgCdTe epilayers. These values compare well with the-state-of-the-art LPE grown materials for current FPA production. Table 1 summarizes the properties of current status of MBE-grown HgCdTe epilayers.

IRFPAs Fabricated with MBE-Grown HgCdTe DLHJ

Recently, we demonstrated high performance HgCdTe 64x64 and 128x128 focal plane arrays (FPAs) for medium (MWIR) and long(LWIR) wavelength infrared detection, using HgCdTe double layer heterojunction structures (DLHJ) grown by MBE [1]. These DLHJs were based on a p-on-n structure and had cutoff wavelengths for detection of 5-10 μm at 77K. The structure consisted of an 8 μm base layer of $HgCd_{1-x}Te_x$ (x=0.22 for LWIR and x=0.3 for MWIR) doped with In at 1-$2\times10^{15}/cm^3$ and a 2 μm cap layer of $HgCd_{1-x}Te_x$ (x=0.30 for LWIR and x=0.35 for MWIR) doped with As at 0.5-$1\times10^{18}/cm^3$ as shown in fig.5 for an LWIR DLHJ detector structure.

The performance of detectors fabricated from MWIR and LWIR layers compared very well to the SBRC LPE-based production process. For example, figures 6 A & B showed the spectral response and quantum efficiency of an MBE-grown LWIR 128x128 FPA. Fig.6A showed that this LWIR FPA has a mean cutoff at 9.92 μm with a standard

deviation of 0.035 μm and fig.6B showed that this FPA has an average quantum efficiency greater than 60% without antireflection coating at 78K.
In addition, this LWIR FPA has an average R_0A greater than 220 ohm-cm^2 at 78K and a detectivity (D*) of 2.2×10^{11} cmHz$^{1/2}$W^{-1} at 85K. All these data indicate that HgCdTe MBE technology is capable of producing high performance IRFPAs.

This 128x128 array was hybridized to a Si readout circuit to form a sensor chip assembly and a high performance LWIR camera was constructed for the first time using the in-situ MBE-grown DLHJ technology. The actual operation of this LWIR camera has been demonstrated and high resolution IR images are obtained as shown in fig.7 The structure of the airplane was quite visible using this high performance 128x128 IRFPA.

Heteroepitaxy of HgCdTe(211) Infrared Detector Structures on Si(211) Substrates

As the size of the hybrid infrared focal-plane array increses, achieving long-term thermal cycle reliability of the array hybrid becomes more difficult because of the thermal expansion mismatch between the Si readout electronics chip and the bulk CdZnTe substrate on which the HgCdTe array is fabricated.[8] One approach to solving this problem is to fabricate the HgCdTe detector array on Si substrate, rather than CdZnTe, so that the array's thermal expansion is constrained to match that of the Si readout chip.

We have made a significant advance towards the goal of producing reliable, large-area FPA's on Si substrates by demonstrating the first all-MBE-grown HgCdTe IR detector structures deposited directly on Si substrates.[9] This achievement has been enabled by the development of the technology for MBE deposition of high quality films of CdTe(211) [10] and HgCdTe(211) directly on Si(211) substrates without GaAs initiation layers. These CdTe and HgCdTe films are twin-free down to the detection limits of x-ray diffraction and exhibit x-ray rocking curve FWHM as low as 72 arc-sec and 86 arc-sec, respectively, and EPD of 2×10^6cm^{-2} and $3\text{-}22\times10^6$cm^{-2}, respectively.[9]

The performance of detectors fabricated on these Si-based substrates is comparable to that obtained on bulk CdZnTe at operating temperatures above approximately 125K. The temperature dependence of the diode R_0A product has been measured and a typical result is plotted in fig.8. An array-average RoA of 4.3×10^3 ohm-cm^2 has been measured at 78K with a cutoff wavelength of 7.8 μm. The data show that the diode performance is diffusion-limited down to approximately 125K. At lower temperatures, the R_0A product exhibits little temperature dependence, which is characteristic of performance limited by tunneling. It is likely that this tunneling current is associated with the 10^7 cm^{-2} threading dislocation density present in the HgCdTe detector structure. This suggests that further reduction in the HgCdTe defect density will be necessary to improve the detector performance for operation below this temperature. This first demonstration of all-MBE-grown HgCdTe IR detector structures on Si substrates represents a significant advance towards the goal of producing reliable large-area FPA.s directly on Si.

Summary

In summary, major advances have been made in HgCdTe MBE technology during last couple of years. Device quality materials have been grown with the alloy compositions required for short-wavelength infrared (SWIR, 1-3 micron) to very long-wavelength infrared (VLWIR, 16-20 micron) detection with excellent repeatability and flexibility. In addition, the breakthroughs to achieve In (n-type) and As (p-type) doping in situ have provided capabilities for fabricating advanced double-layer heterojunction devices. High performance IR imaging arrays (128x128) have been fabricated for the first time using MBE in-situ grown double layer structures and high resolution IR images obtained. Lastly, the first all-MBE-grown HgCdTe IR detector structures deposited directly on silicon substrates has also been demonsterated.

References

1. O. K. Wu, D. M. Jamba, G. S. Kamath, G. R. Chapman, S. M. Johnson, J. M. Peterson, K. Kosai, and C. A. Cockrum, J. Elec. Mat. Vol. 24, No.5, (1995)

2. J. Bajaj, J. M. Arias, M. Zandian, J. G. Pasko, L. J. Kozlowski, R. E. Dewames, and W. E. Tennant, J. Elec. Mat. Vol. 24, No.9, (1995)

3. J. P. Faurie and A. Million, J. Cryst. Growth 54, 582, (1982)

4. K. A. Harris, T. H. Meyers, R. W. Yanka, and L. M. Mohnkern, R. W. Green and N. Otsuka, J. Vac. Sci. Technol. A8(2), 1013, (1990)

5. O. K. Wu, D. N. Jamba and G. S. Kamath, J. Crystal Growth 127, 365, (1993)

6. O. K. Wu, Mat. Res. Soc. Symb. Proc. Vol. 302, 423 (1993)

7. J. M. Arias, J. G. Pasko, M. Zandian, S. H. Shin, G. M. Williams, L. O. Bubulac, R.Dewames, and W. E. Tennant, Appl. Phys. Lett. 62(9) 976 (1993)

8. S. M.Johnson, T. J. de Lyon, C.A. Cockrum, W.J.Hamilton,T. Tung, F. I. Gesswein, B. A. Baumgratz, L. M. Ruzicka, O. K. Wu, and J. A. Roth, J. Electron. Mater. **24**, 467, (1995)

9. T. J. de Lyon, R. D. Rajavcl, J. E. Jensen, O. K. Wu, S.M. Johnson, C.A. Cockrum and G.M. Venzor, The 1995 U. S. workshop on the physics and chemistry of HgCdTe and other IR materials. Abstract 131, 1995

10. T. J. de Lyon, R. Rajavel, S. M. Johnson, and C. A. Cockrum, Appl. Phys. Lett. 66, 2119 (1995).

Acknowledgement

The authors wish to thank Rudy A. Bondio, Doug M. Jamba, and Leslie D. Warren of Hughes Research Laboratory for their technical assistance and J. M. Peterson, Bonnie A. Baumgratz, Ken Kosai, Jerry A. Wilson and Libby A. Patten of Santa Barbara Research Center for their valuable discussions and technical supports. In addition, we wish to thank G. Sanjiv Kamath and Mary H. Young for their guidance and encouragement.

Table 1

Properties	Characteristics	Measurement Techniques
1. Composition	Cd=0.18-0.80	FTIR
2. Crystal Quality	FWHM<30 arc-sec	X-ray diffraction
3. N-type doping	10^{15}-10^{18}/cm^3	SIMS/Hall
4. N-type mobility	1x10^5 cm^2/V-sec(77K)	Hall
5. P-type doping	10^{16}-10^{18}/cm^3	SIMS/Hall
6. P-type mobility	100 cm^2/V-sec(77K)	Hall
7. Etch pit density	1-2x10^5/cm^2	Chemical Etch
8. Minority carrier lifetime	1-3 µsec	Photoconductive decay

Figure 1 shows the FTIR room temperature cutoff wavelength as a function of run number. The first four growth runs targeted for the SWIR(1.3 μm), followed by a set of seven growth runs targeted for the LWIR(6.72 μm), then the last three growth runs returned back to target for SWIR (1.3 μm). These data indicated that HgCdTe MBE technology offers the flexibility and repeatability for the growth of wide range of HgCdTe alloys for IR applications.

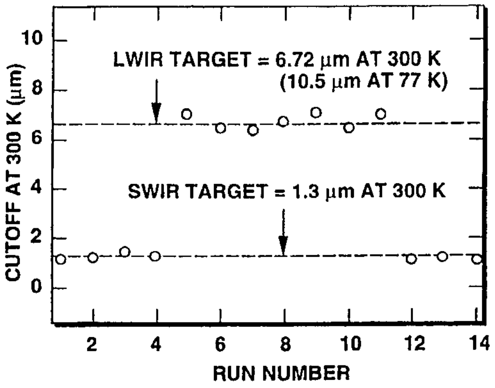

Figure 2 shows the X-ray rocking curve data for 30 samples. The data indicate that the average x-ray full width at half maximum is 27 arc-sec, which is indicative of excellent crystallinity of HgCdTe alloys.

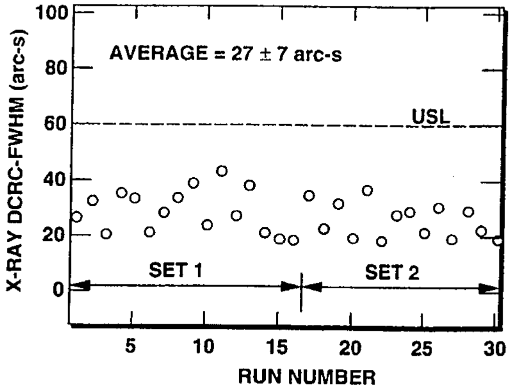

Figure 3 shows the carrier concentration and Hall mobility data as a function of temperature for a typical In-doped (N-type) HgCdTe alloy with a 22% Cd concentration. The data indicated that Hall mobility was greater than 1×10^5 cm^2/V-sec at 77K and greater than $2\times10^5 cm^2/V$-sec at 40K for a donor concentration of $2\times10^{15}/cm^3$.

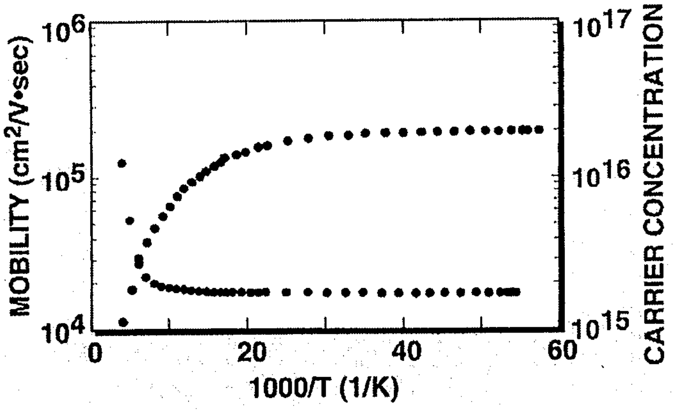

Figure 4 shows the carrier concentration and Hall mobility data as a function of temperature for a typical As-doped (P-type) HgCdTe alloy with a 30% Cd concentration. The data indicated that Hall mobility was about 100 cm^2/V-sec at 77K for an acceptor concentration of $4\times10^{17}/cm^3$.

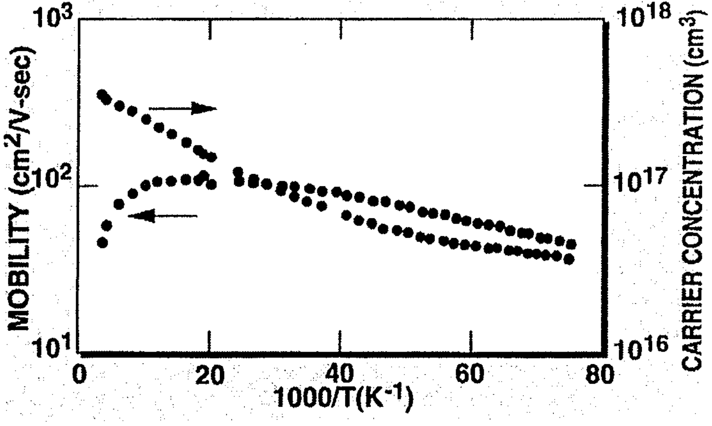

Figure 5 shows a schematic diagram of the MBE grown double-layer structure, consisting of an 8 µm base layer of $HgCd_xTe_{1-x}$ (x=0.22 for LWIR and x=0.3 for MWIR) doped with In at $1\text{-}2x10^{15}/cm^3$ and a 2 µm cap layer of $HgCd_xTe_{1-x}$ (x=0.30 for LWIR and x=0.35 for MWIR) doped with As at $0.5\text{-}1x10^{18}$ /cm^3.

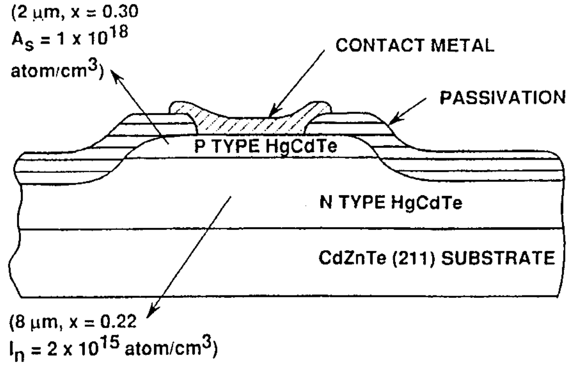

Figure.6 A & B showed the spectral response and quantum efficiency of an MBE-grown LWIR 128x128 FPA. This FPA has a mean cutoff at 9.92 µm with a standard deviation of 0.035 µm and an average quantum efficiency greater than 60% (without antireflection coating) at 78K.

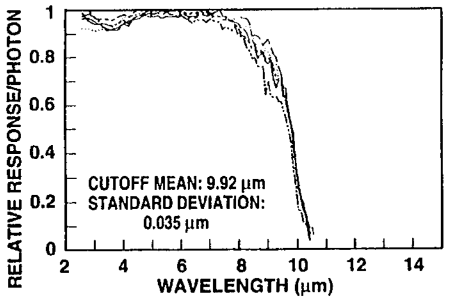

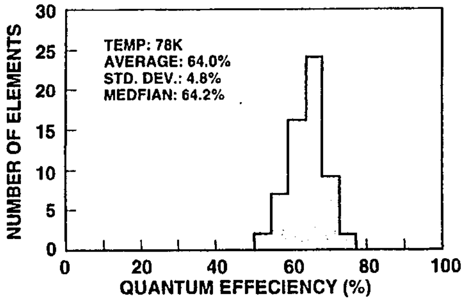

Figure 7 IR image of a commercial airplane obtained from the MBE-grown HgCdTe double layer heterojunction 128x128 FPA. It should be noted that the structure of this airplane is quite visible from this high performance 128x128 LWIR FPA.

Figure 8 Temperature dependence of R0A product measured at 0 FOV for HgCdTe DLHJ detector (7.8 μm cutoff at 78K) grown on Si(112) substrate by MBE.

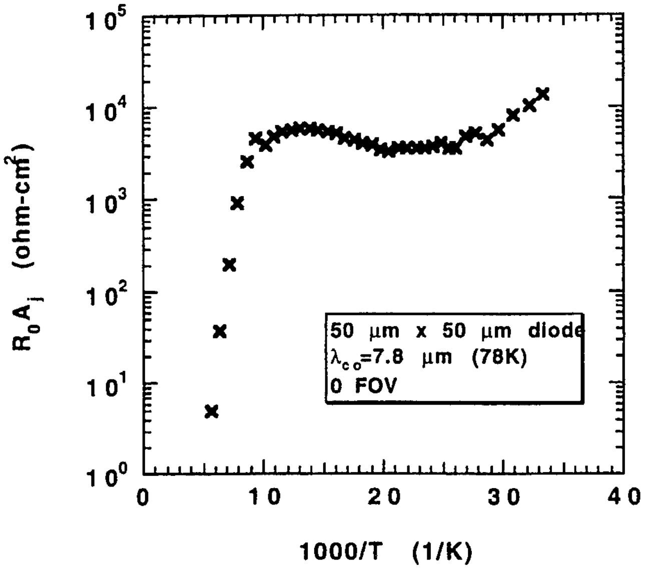

INTEGRATED QUANTUM WELL INTERSUBBAND PHOTODETECTOR AND LIGHT EMITTING DIODE FOR THERMAL IMAGING APPLICATIONS

H. C. Liu, Jianmeng Li, Z. R. Wasilewski, and M. Buchanan
Institute for Microstructural Sciences
National Research Council
Ottawa, Ontario K1A 0R6, Canada

Abstract

This paper presents a new approach to the fabrication of infrared imaging arrays. The approach involves the integration of quantum well infrared photodetectors with light emitting diodes using III-V semiconductor heterosystems. The first demonstration device is made and the performance issues are discussed.

1 Introduction

In a state-of-the-art high performance thermal imaging system the focal plane array (FPA) is usually a HgCdTe or a InSb detector arrays hybrid bonded by In bumps with a Si multiplexer. Photo-signal from each detector pixel is fed into the Si circuit through the In bump. This scheme is shown schematically in Fig. 1. The following factors make such a FPA costly: (1) the use of less mature detector materials in comparison with other mature semiconductor materials such as Si or GaAs, and (2) the use of special Si integrated circuit chips for multiplexing and the use of a hybrid bonding manufacture process. Factor (1) presents an intrinsic problem for the HgCdTe material system. The other issue is the thermal mismatch between the detector array and the multiplexer, which may limit the physical size of the FPA.

The wish then would be for a FPA that uses all standard technologies preferably based on Si or GaAs. If the operation temperature of 77 K is acceptable, the only such detector technology with high performance is the quantum well infrared photodetector (QWIP)[1, 2] based on GaAs. Figure 2 shows schematically the basic structure and operating principle of a QWIP. However, thus far, the conventional approach of hybrid bonding has been employed for the fabrication of QWIP FPAs[3] resulting in a relatively costly final product. In principle, the GaAs QWIP can be integrated monolithically with GaAs circuits either based on bipolar or field effect transistor technologies. This monolithic approach is very attractive and could potentially result in an inexpensive FPA in a mass production mode. We are currently investigating this possibility using a QWIP-HBT (heterojunction bipolar transistor) approach. A monolithically integrated HgCdTe or InSb FPA would be very difficult and require substantial investments to develop HgCdTe or InSb transistors and circuits.

2 The QWIP-LED approach

In this paper, we propose an optoelectronic integration approach which uses standard and existing technologies. We combine the newly developed QWIP technology with the well-established quantum well light emitting diode (LED) technology both based on GaAs and related epitaxially grown alloys, such as AlGaAs and InGaAs. A quantum well LED is schematically shown in Fig. 3. The full device is a vertically integrated QWIP and LED in which the QWIP drives or modulates the LED emission. Structurally, the QWIP and LED are grown in a single stack, and electrically, they are connected in series. The resulting device is simply an mid- or far-infrared (M/FIR) to near-infrared (NIR) converter. The QWIP detects the far- or mid-IR depending on its detection wavelength, and the LED emits in the near-IR. The new approach is well suited for large and high fill-factor two-dimensional array fabrication. The completed array would be a thermal to near infrared image converter. The resulting near infrared emission "picture" is then easily imaged by a conventional Si charge coupled device (CCD). Figure 4 shows this approach, and the advantage of this integrated QWIP-LED is of extreme importance technologically. In this scheme, one can make large format two-dimensional FPAs with a high pixel fill factor *without* the need of making any circuits on the FPA chip and *without* the need of hybrid bonding with a Si multiplexer chip. Additionally, this optical link approach eliminates the electrical noise generated by a closed cycle cooler and coupled to the readout circuitry.

3 A first device demonstration

A demonstration device has been made with the QWIP operating at a peak detection wavelength of 9 μm and the LED emitting at 930 nm. The experimental details are described in Ref. [4]. Figure 5 shows the device structure with a GaAs/AlGaAs n-QWIP with an InGaAs/GaAs quantum well LED. Using a molecular beam expitaxy system and starting with a semi-insulating (100) GaAs substrate, a QWIP structure was grown and then an InGaAs/GaAs quantum well LED. The QWIP consisted of the following layers (in growth sequence): a bottom contact layer of 800 nm n^+-GaAs doped with Si to a density of 1.5×10^{18} cm^{-3}, a 5 nm GaAs spacer, and 50 repeat $Al_{0.25}Ga_{0.75}As$/GaAs quantum wells with 40 nm barrier and 5.9 nm well. The wells were doped with a Si-δ-spike to a density of 5×10^{11} cm^{-2}. These δ-spikes were positioned away from the well center towards the substrate by about 2.5 nm to counter-balance the Si segregation during growth and ensure the symmetry of the QWIP structure.[5] Growth continued with the following LED layers: a 40 nm graded $Al_xGa_{1-x}As$ layer from $x = 0.25$ to 0.12, a 30 nm GaAs, a 7.0 nm $In_{0.2}Ga_{0.8}As$ well, a 30 nm GaAs, a 40 nm graded $Al_xGa_{1-x}As$ layer from $x = 0.12$ to 0.25, a 50 nm p^+-$Al_{0.25}Ga_{0.75}As$ with Be doping graded from 1 to 8×10^{18} cm^{-3}, a 40 nm graded p^{++}-$Al_xGa_{1-x}As$ layer from $x = 0.25$ to 0.12 with its doping increased from 8×10^{18} to 10^{19} cm^{-3}, and finally a 200 nm p^{++}-GaAs top contact layer with 10^{19} cm^{-3} doping. The advantage of using InGaAs as the well material is that the emitted light is not absorbed in any other layers.

Mesa devices with an area of 290×140 μm^2 were made using standard GaAs lithography techniques. The narrow ring shaped top p-type contacts near the mesa edge resulted in an emission window of 200×100 μm^2 for the NIR light from the LED. A 45°-edge facet was polished near the devices to facilitate FIR coupling to the intersubband transition.[6] The device geometry is schematically shown in Fig. 6. The device was mounted in a 77 K cold-finger optical cryostat, and actual device temperature was estimated to be 82 K. A 1000 K blackbody source or a CO_2 laser was used as the FIR source. A grating monochromator or a Fourier transform spectrometer was used for wavelength selection. A Si photodiode was used to measured the NIR emission.

Figure 7 summarizes the experimental results. Since the QWIP and the LED are in series, the bias current is common. Panel (a) shows the LED emitted power at a wavelength of 927 nm versus bias current. The inset shows schematically the device geometry. Panel (b) presents the QWIP responsivity for unpolarized light at a wavelength of 9.2 μm. The insets are the schematic device geometry and the normalized spectral response. Panel (c) gives the measured increase of the LED emission for several FIR power values at a wavelength of 9.2 μm.

For our simple test structure, the observed external efficiency of the LED is only about 0.8% from Fig. 7(a) by comparing the output photon rate (photons/second) with the input current (electrons/second). Assuming a near unity internal efficiency, which is realistic for our high quality InGaAs/GaAs quantum wells, two main factors lead to the low external efficiency. First, the top ring contact metal blocks part of the emission. The ratio of the emitting area and the diode area is about 0.49. Second, the high material refractive index leads to a small escape cone angle, which ideally gives a faction of escaped light of about 2%. Combining these factors, the expected external efficiency is 1.0% in agreement with our experimental result of 0.8%. Our FIR detector performance shown in Fig. 7(b) is typical for a state-of-the-art QWIP. Even with the poor LED external efficiency, we were able to easily observe the increase of its emission for a FIR illumination power of as little as 1.5 μW as shown in Fig. 7(c). This shows the relative ease of detecting NIR light compared with FIR light. NIR detectors normally have much higher detectivity values than those for FIR detectors.

Many techniques exist to improve the LED external efficiency. As an example, an impressive 72% external efficiency[7] was obtained by trapping the emitted light in a thin layer. To demonstrate the improvement by thinning the substrate, we thinned the substrate of a LED chip and compared the LED output power with that from a un-thinned device at room temperature. The results are shown in Fig. 8. An enhancement of nearly a factor of two was obtained with a substrate thickness of about 36 μm. Limited by the mechanical thinning and handling process, we could not thin the substrate further than 36 μm. Another possibility is to grow a high reflector, e.g., a quarter-wave stack, which should provide a larger enhancement since the this would trapping the emitted light to the QWIP-LED layers of a total thickness of about 4 μm.

4 Performance issues

The most basic question is if the QWIP-LED together with a Si diode for NIR detection can perform just as well as the QWIP, used as a M/FIR detector. For 77 K operation, a well-designed QWIP can be very efficient[8, 9] with easily higher than 20% absorption; and the LED technology is well developed.

Specifically, since the cooled LED has nearly 100% internal quantum efficiency, the interband recombination process does not cause any extra noise. The fluctuation of the emitted number of NIR photons therefore corresponds to the fluctuation of the driving current from the QWIP. This implies that the signal-to-noise ratio in the NIR emission is the same as that in the QWIP. A Si detector used subsequently for the NIR detection can easily have a detectivity far higher than that of a QWIP. An optimized QWIP-LED therefore should be very efficient with very little or no loss of performance compared with the QWIP alone used as a M/FIR detector.

Concerning the array performance, the envisioned final FPA uses a Si CCD to image the NIR emission from an array of QWIP-LED. If approximately 10 mK noise equivalent temperature difference (NEΔT) of the FPA performance is required, the dynamic range of the CCD and the analog-to-digital converter (ADC) should be better than $(4 \times NE\Delta T/T_B)^{-1}$, where T_B is the background temperature and the factor of 4 comes from the Stefan law. For $T_B = 300$ K, the required dynamic range is 7500. The CCD pixel should therefore have a maximum electron capacity of large than 10^4 assuming a readout noise of a few electrons, and the ADC should therefore have more than 12 bits. These values can be easily achieved in practice.

5 Conclusions

We have proposed and demonstrated a new optoelectronic integration scheme for making large focal plane thermal imaging arrays. Making use of its photoconductive nature, a conventional quantum well infrared photodetector (QWIP) in series with a light emitting diode (LED) performs as a mid- or far-infrared to near-infrared converter. Using this approach, we are currently fabricating two-dimensional arrays.

Acknowledgments – We thank P. Chow-Chong, P. Marshall, J. Stapledon, and P. H. Wilson for sample preparation. This work was supported in part by DND DREV.

References

[1] B. F. Levine, J. Appl. Phys. **74**, R1 (1993).

[2] H. C. Liu, *The basic physics of photoconductive quantum well infrared detectors*, in **Long Wavelength Infrared Detectors**, Gordon Breach, PA, edited by M. Razeghi (1995, to be published).

[3] B. F. Levine, C. G. Bethea, K. G. Glogovsky, J. W. Stay, and R. E. Leibenguth, Semicond. Sci. Technol. **6**, C114 (1991).

[4] H. C. Liu, J. Li, Z. R. Wasilewski, and M. Buchanan, Electron. Lett. **31**, 832 (1995).

[5] H. C. Liu, Z. R. Wasilewski, M. Buchanan, and H. Chu, Appl. Phys. Lett. **63**, 761 (1993).

[6] B. F. Levine, K. K. Choi, C. G. Bethea, J. Walker, and R. J. Malik, Appl. Phys. Lett. **50**, 1092 (1987).

[7] I. Schnitzer, E. Yablonovitch, C. Caneau, and T. J. Gmitter, Appl. Phys. Lett. **62**, 131 (1993).

[8] J. Y. Andersson and L. Lundqvist, Appl. Phys. Lett. **59**, 857 (1991).

[9] G. Sarusi, B. F. Levine, S. J. Pearton, K. M. S. Bandara, and R. E. Leibenguth, Appl. Phys. Lett. **64**, 960 (1994).

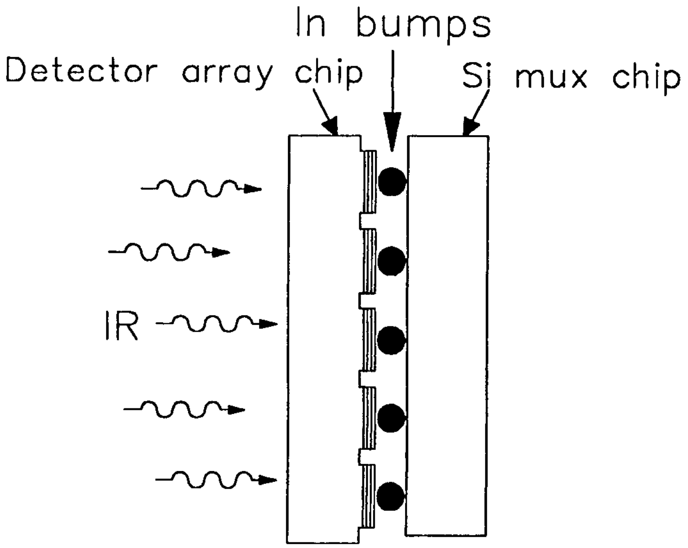

Figure 1: Conventional approach of In bump bonded focal plane array. The detector array chip contains mesa isolated pixels, hybrid bonded to a Si multiplexer. The infrared (IR) signal illuminates the array from the backside.

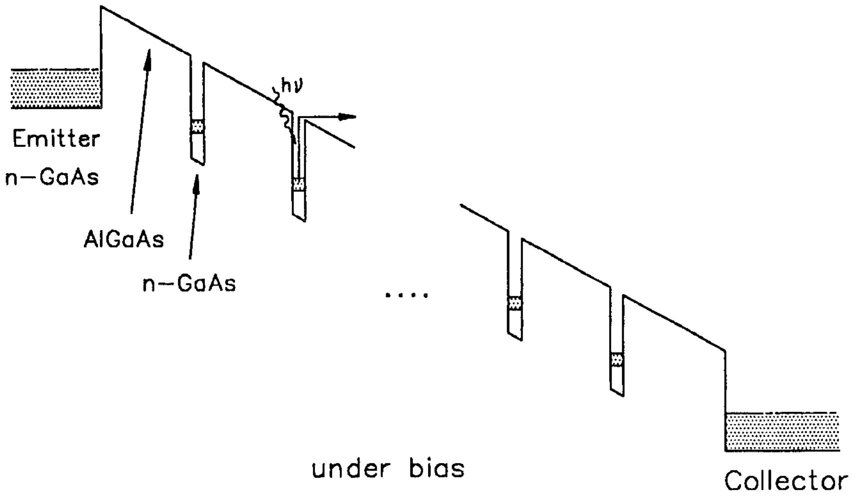

Figure 2: The conduction bandedge profile of an AlGaAs-GaAs quantum well infrared photodetector. Hatched regions show carrier occupation. Under a bias voltage, an electron can be excited from the wells resulting in a photocurrent. The operation is similar to a conventional photoconductor.

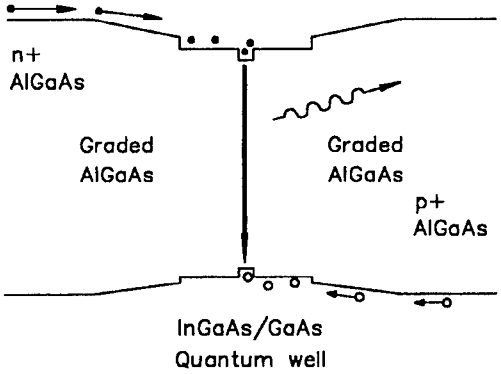

Figure 3: Bandedge profile of a quantum well light emitting diode under operating conditions.

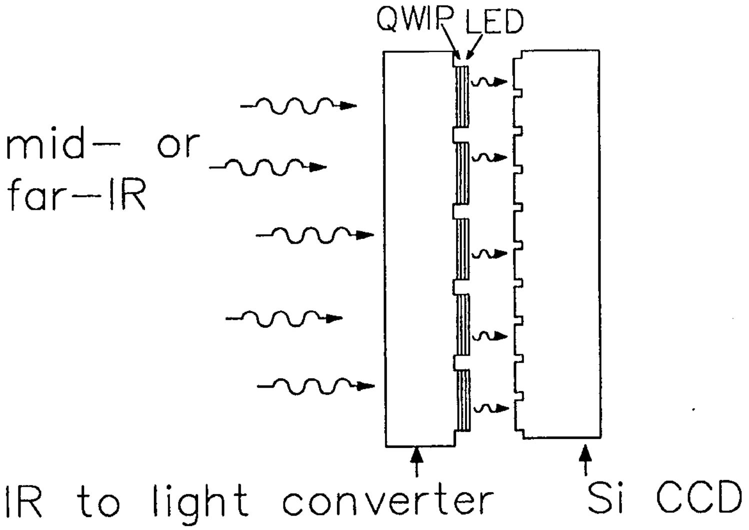

Figure 4: Novel approach of optoelectronically integrated focal plane array using a quantum well infrared photodetector (QWIP) and light emitting diode (LED). The QWIP-LED array acts as a mid- or far-infrared (IR) to near-IR converter. A Si charge coupled device (CCD) detects the converted image. In comparison with Fig. 1, the In bumps which act as wires connecting the detector and the multiplexer are replaced by near-IR light. Here the Si CCD is placed in close proximity with the QWIP-LED array, but in practice, it may be more convenient to map the LED emission image to the focal plane of the CCD by a lens.

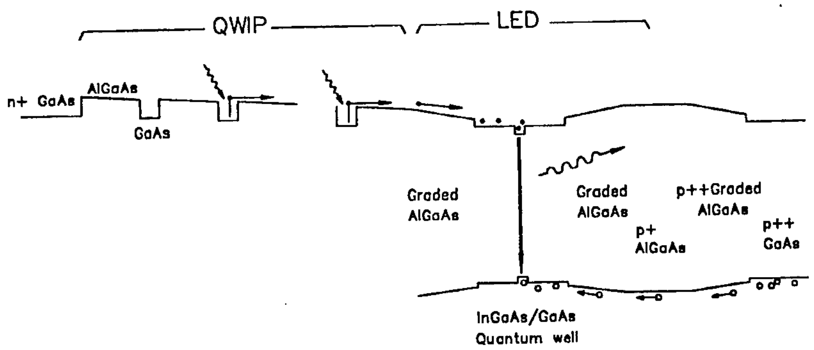

Figure 5: Bandedge profile of the proposed integrated quantum well intersubband photodetector (QWIP) and light emitting diode (LED). For the QWIP part, only the conduction bandedge is shown.

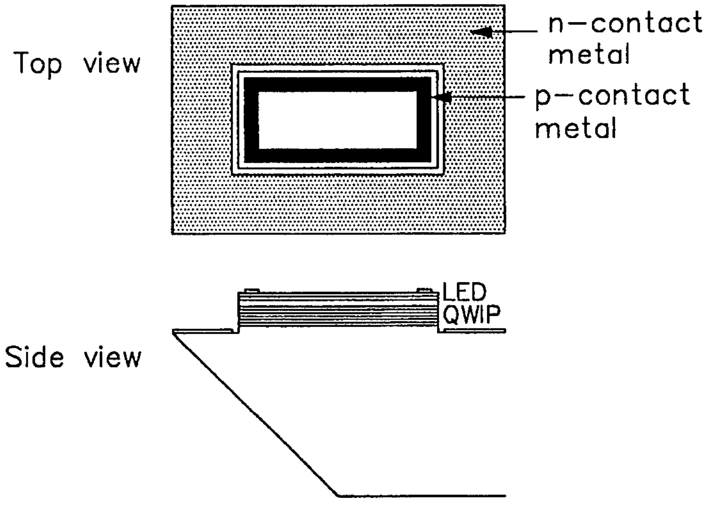

Figure 6: Schematic top and side view of the mesa structure.

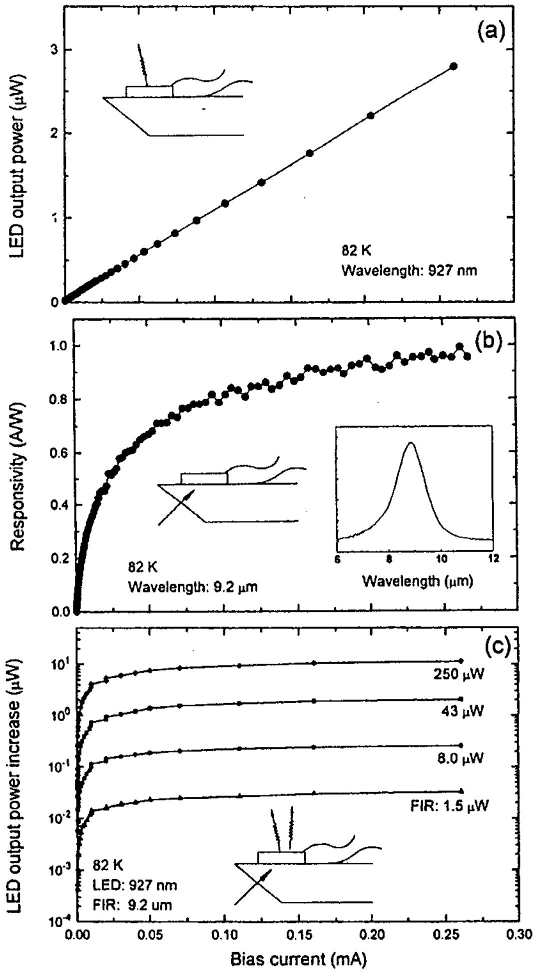

Figure 7: Experimental results: (a) LED output power at 927 nm, (b) QWIP responsivity at 9.2 μm, and (c) increase of LED output power under 9.2 μm far-infrared (FIR) illumination, all versus bias current. Insets show schematically the device geometries and in (b) the normalized spectral response. All data were taken at a device temperature of 82 K.

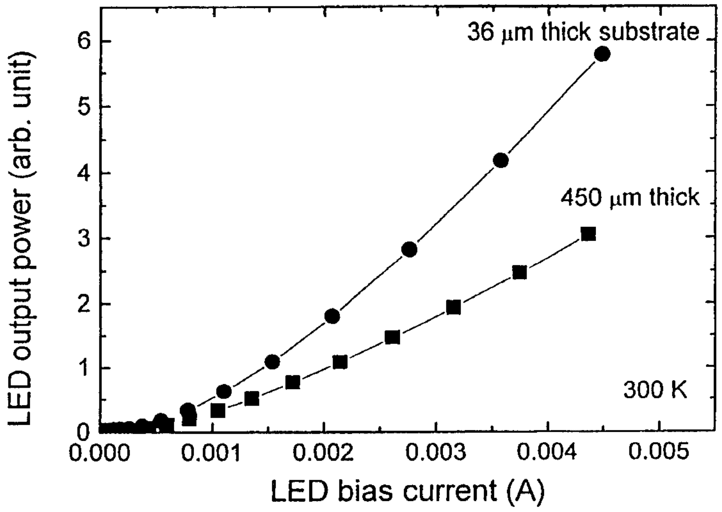

Figure 8: Comparison of light emitting diode (LED) output power for thinned (36 μm) and un-thinned (450 μm) substrates.

9 μm Cutoff 256x256 $GaAs/Al_xGa_{1-x}As$ Quantum Well Infrared Photodetector Focal Plane Array Camera

S. D. Gunapala, J. K. Liu, M. Sundaram, J. S. Park*, C. A. Shott+, T. Hoelter+, T. L. Lin, S. T. Massie++, P. D. Maker, R. E. Muller, and G. Sarusi#**

Center for Space Microelectronics Technology, Jet Propulsion Laboratory California Institute of Technology, Pasadena, CA 91109

In this paper, we discuss the development of very sensitive long wavelength infrared (LWIR) $GaAs/Al_xGa_{1-x}As$ quantum well infrared photodetectors (QWIPs), fabrication of random reflectors for efficient light coupling, and the demonstration of a LWIR 256 x 256 focal plane array imaging camera. Excellent imagery, with a noise equivalent differential temperature (NEΔT) of 25 mK has been achieved.

INTRODUCTION

There are several applications that require long wavelength, large, uniform, reproducible, low cost, low 1/f noise, low power dissipation, and radiation hard infrared (IR) focal plane arrays (FPAs). For example, the absorption lines of many gas molecules, such as ozone, water, carbon monoxide, carbon dioxide, and nitrous oxide occur in the wavelength region from 3 to 18 μm. Thus, IR imaging systems that operate in the long wavelength IR (LWIR) region (6 - 18 μm) are required in many space applications such as monitoring the global atmospheric temperature profiles, relative humidity profiles, cloud characteristics, and the distribution of minor constituents in the atmosphere which are being planned for NASA's Earth Observing System [1]. In addition, 8 - 15 μm FPAs would be very useful in detecting cold objects such as ballistic missiles in midcourse (when a hot rocket engine is not burning most of the emission peaks are in the 8-15 μm IR region) [2]. The GaAs based Quantum Well Infrared Photodetector (QWIP) [3,4,5] is a potential candidate for such spaceborne and ground based applications and it can meet all of the requirements mentioned above for this spectral region.

* Present address: Intel Corporation, Santa Clara, CA 95052
+ Amber, A Raytheon Company, Goleta, CA 93117
** Present address: Siliconix, Santa Clara, CA 95056
++ Quantum Epitaxial Designs, Inc., Bethlehem, PA 18015
# Present address: elop-Electroptics Industries Ltd., Rehovot 76111 Israel

Fig. 1 shows the schematic conduction band diagram of a typical *bound-to-continuum* QWIP [6] which utilizes bound-to-continuum intersubband absorption. By carefully designing the quantum well structure, as well as the light coupling to the detector, it is possible to optimize the material to have an optical response in the desired spectral range and determine the spectral response shape [7]. In QWIPs, the dark current originates from three different mechanisms [8]. As shown in Fig. 1, the dark current arising from the first process is due to quantum mechanical tunneling from well to well through the $Al_xGa_{1-x}As$ barriers (sequential tunneling). This process is independent of temperature. Sequential tunneling dominates the dark current at very low temperatures (<30 K). The second mechanism is thermally assisted tunneling which involves a thermal excitation and tunneling through the tip of the barrier into the continuum energy levels. This process governs the dark current at medium temperatures. The third mechanism is classical thermionic emission and it dominates the dark current at higher temperatures (>55 K for 9 µm cutoff QWIPs). Consequently, for QWIPs operating at higher temperatures the last mechanism is the major source of dark current [8]. Therefore, the LWIR FPA we have discussed here in detail consisted of *bound-to-quasibound* QWIPs [9]. The advantage of the bound-to-quasibound QWIP over the bound-to-continuum QWIP [9] is that in the case of a bound-to-quasibound QWIP the energy barrier for thermionic emission is the same as it is for photoionization as shown in Fig. 2. In the case of the bound-to-continuum QWIP shown in Fig. 2 the energy barrier for the thermionic emission is about 6 meV less than the photoionization energy. Thus, the dark current of bound-to-quasibound QWIPs is reduced by a factor of 3 (i.e., $I_d \propto e^{-\frac{\Delta E}{kT}} \approx e^{-1}$ for T = 70 K) compared with bound-to-continuum QWIPs operating at the same peak wavelength.

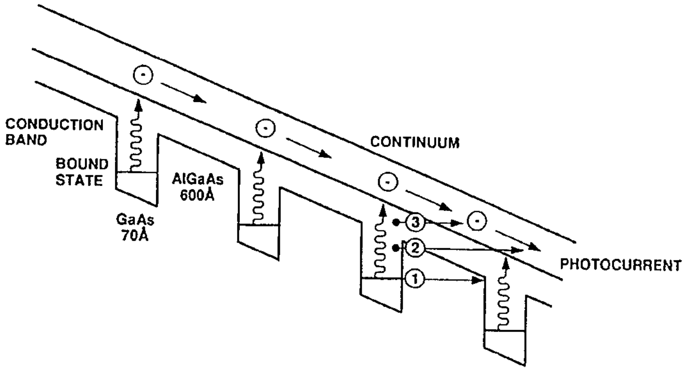

Fig. 1 Schematic diagram of the conduction band in a bound-to-continuum QWIP with an electric field. Absorption of IR photons can photoexcite electrons from the ground state of the quantum well into the continuum, causing a photocurrent. Three dark current mechanisms are also shown: ground state tunneling (1); thermally assisted tunneling (2); and thermionic emission (3).

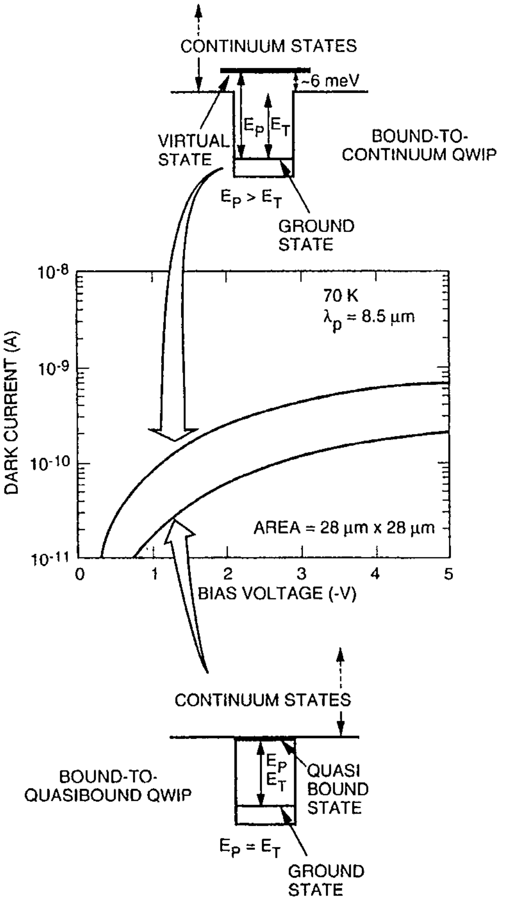

Fig. 2 Comparison of dark currents of bound-to-continuum and bound-to-quasibound LWIR QWIPs as a function of bias voltage at temperature T = 70 K. Data were taken with a 200 μm diam test structure and normalized to 28x28 μm^2 pixel.

TEST STRUCTURE RESULTS

The device structure consists of 50 periods, each period containing a 45 Å well of GaAs (doped n = 4×10^{17} cm^{-3}) and a 500 Å barrier of $Al_{0.3}Ga_{0.7}As$, sandwiched between 0.5 µm GaAs top and bottom contact layers doped n = 5×10^{17} cm^{-3}, grown on a semi-insulating GaAs substrate by molecular beam epitaxy (MBE). Then a 0.7 µm thick GaAs cap layer on top of a 300 Å $Al_{0.3}Ga_{0.7}As$ stop-etch layer was grown *in situ* on top of the device structure to fabricate the light coupling optical cavity. The MBE grown QWIP structure was processed into 200 µm diameter mesa test structures (area = 3.14 x 10^{-4} cm^2) using wet chemical etching, and Au/Ge ohmic contacts were evaporated onto the top and bottom contact layers. The dark current-voltage curves of the QWIP were measured as a function of temperature from T = 30-90 K and the T = 70 K curve is shown in Fig. 2 with the dark current-voltage curve of a 8.5 µm peak bound-to-continuum QWIP. The virtual excited level of this bound-to-continuum QWIP is 6 meV above the $Al_xGa_{1-x}As$ barrier. Theoretically this should give a factor of 3 higher dark current and it closely agrees with the experimental value of a factor of 4 higher dark current at bias V_B = -2V.

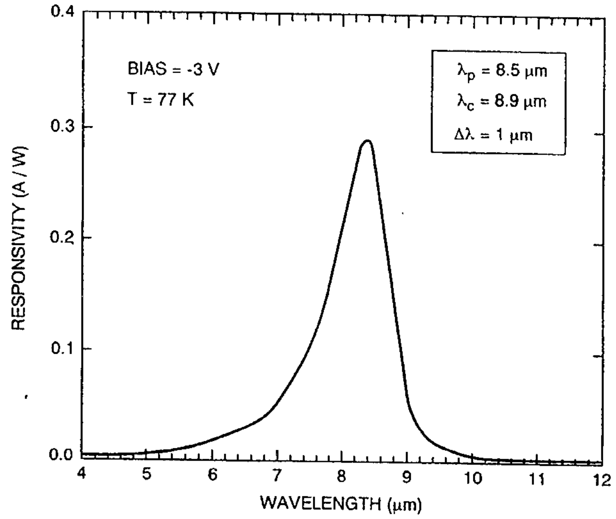

Fig. 3 Responsivity spectrum of a bound-to-quasibound LWIR QWIP test structure at temperature T = 77 K. The spectral response peak is at 8.5 µm and the long wavelength cutoff is at 8.9 µm.

The responsivity spectra of these detectors were measured using a 1000 K blackbody source and a grating monochromator. The absolute peak responsivities (R_p) of the detectors were measured using a calibrated blackbody source. The detectors were back illuminated through a 45° polished facet [7] and a responsivity spectrum is shown in Fig. 3. The responsivity of the detector peaks at 8.5 μm and the peak responsivity (R_p) of the detector is 300 mA/W at bias V_B = -3 V. The spectral width and the cutoff wavelength are $\Delta\lambda / \lambda$ = 10% and λ_c = 8.9 μm respectively. The bias dependent peak responsivity of the detector is shown in Fig. 4. The measured absolute peak responsivity of the detector is small up to about V_B = -0.5 V. Beyond that it increases nearly linearly with bias reaching R_P = 380 mA/W at V_B = -5 V. This type of behavior of responsivity versus bias is typical for a bound-to-quasibound QWIP. The peak quantum efficiency was 7% at bias V_B = -1 V (lower quantum efficiency is due to the lower well doping density) for a 45° double pass.

The current noise i_n was measured using a spectrum analyzer and the photoconductive gain g was experimentally determined using [10] $g = i_n^2 / 4eI_DB + 1/2N$, where B is the measurement band width and N is the number of quantum wells. The photoconductive gain of the detector reached 0.98 at V_B =-5 V. Since the gain of QWIP is inversely proportional to the number of quantum wells N, the better comparison would be the well capture probability p_c, which is directly related to the gain [11] by $g = 1/Np_c$. The calculated well capture probabilities are 25% at

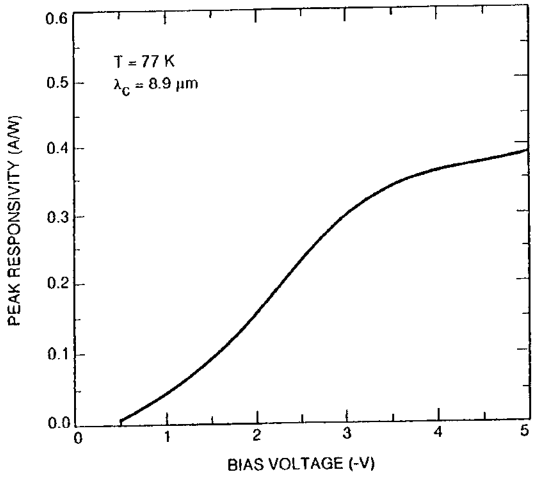

Fig. 4 Peak responsivity as a function of bias voltage at temperature T = 77 K.

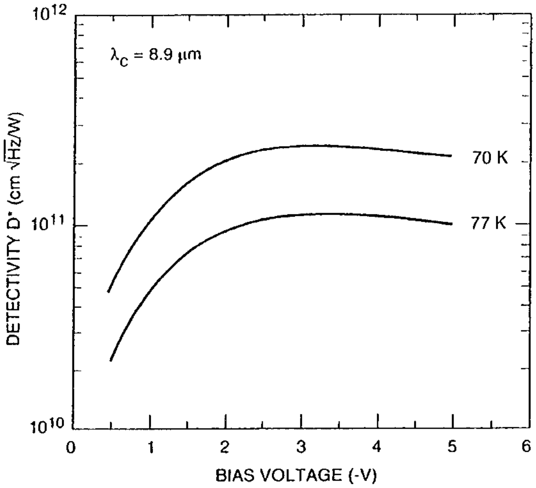

Fig. 5 Detectivity as a function of bias voltage at temperatures T = 70 and 77 K.

low bias (i.e., $V_B = -1$ V) and 2% at high bias (i.e., $V_B = -5$ V) which together indicate the excellent hot-electron transport in this device structure. The peak detectivity is defined as $D_P^* = R_P \sqrt{AB} / i_n$, where R_P is the peak responsivity, A is the area of the detector and $A = 3.14 \times 10^{-4}\ cm^2$. The measured peak detectivity at bias $V_B = -3.2$ V and temperature T = 70 K is 2.3×10^{11} cm√Hz/W.

LIGHT COUPLING

QWIPs do not absorb radiation incident normal to the surface since the light polarization must have an electric field component normal to the superlattice (growth direction) to be absorbed by the confined carriers. As shown in Fig. 6(a) when the incoming light contains no polarization component along the growth direction, the matrix element of the interaction vanishes (i.e., $\vec{\varepsilon}.\vec{p}_z = 0$ where $\vec{\varepsilon}$ is the polarization and $\vec{p}_z$ is the momentum along the z direction). As a consequence, these detectors have to be illuminated through a 45° polished facet [7] as shown in Fig. 6(b). Clearly, this illumination scheme limits the configuration of detectors to linear arrays and single elements. For imaging, it is necessary to be able to couple light uniformly to two dimensional arrays of these detectors.

Many more passes of IR light inside the detector structure can be obtained by incorporating a randomly roughened reflecting surface on top of the detectors which also removes the light coupling limitations and makes two dimensional QWIP imaging

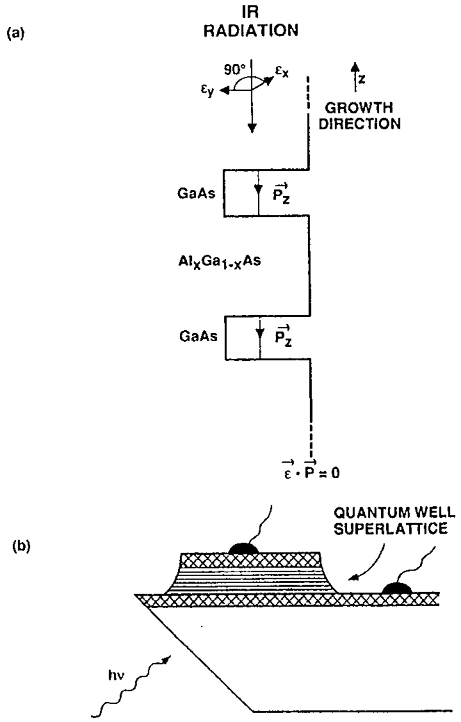

Fig. 6 (a) Intersubband absorption process of QWIPs at normal incidence. (b) 45° polished facet light coupling.

arrays feasible. A factor of eight enhancement in QWIP responsivity compared to 45° illumination geometry has been achieved with a randomly roughened reflecting surface [11]. The random structure on top of the detector prevents the light from being diffracted normally backward after the second bounce as happens in the case of cross-grating. After each bounce, light is scattered at a different random angle and the only chance for light to escape out of the detector is when it is reflected towards the surface within the critical angle of the normal. For the GaAs/air interface this angle is about 17°, defining a very narrow escape cone for the trapped light. The reflector was designed with two levels of scattering surfaces located at quarter wavelength separations, as shown in Fig. 7. The area of the top unetched level is equal to the area of the etched level ($\lambda_{GaAs}/4$ deep). Therefore, the normally reflected light intensities from the top and bottom surfaces of random reflector are equal and 180° out of phase, thus

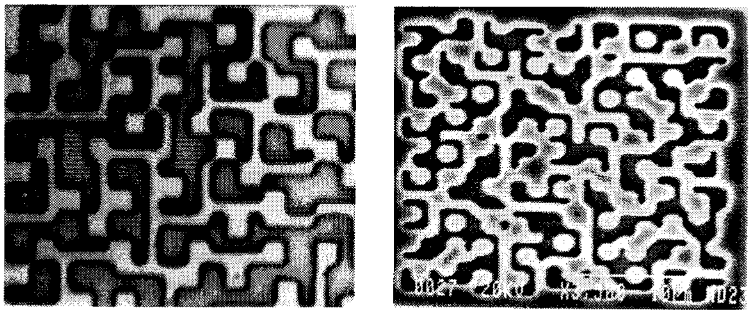

a b

Fig. 7 (a) Two level random reflector on a pixel (38x38 μm^2) of 15 μm cutoff QWIP FPA. The minimum feature size is 1.25 μm. (b) Two level random reflector on a pixel (28x28 μm^2) of 9 μm cutoff QWIP FPA. The minimum feature size is 0.6 μm. This random reflector was less sharp and had fewer scattering centers when compared to Fig. 7(a) due to the difficulties associated with sub-micron photolithography.

maximizing the destructive interference at normal reflection and hence lowering the light leakage through the escape cone. This random structure was fabricated on the detectors by using standard photolithography and CCl_2F_2 selective dry etching. The advantage of the photolithographic process over a completely random process is the ability to accurately control the feature size and preserve the pixel to pixel uniformity which is a prerequisite for high sensitivity imaging FPAs.

IMAGING ARRAYS

Figures 7(a) and 7(b) show random reflectors on a pixel of 15 μm cutoff 128x128 and 9 μm cutoff 256x256 QWIP FPAs respectively. The minimum feature size of the random reflectors of 15 μm cutoff and 9 μm cutoff FPAs were 1.25 and 0.6 μm respectively. As shown in Fig. 7(b) the random reflectors of the 9 μm cutoff FPA were less sharp and had fewer scattering centers compared to Fig. 7(a) and this is due to the difficulties associated with sub-micron photolithography. After the random reflector array was defined by the lithography and dry etching, the photoconductive QWIPs of the 256x256 FPAs were fabricated by wet chemical etching through the photosensitive $GaAs/Al_xGa_{1-x}As$ multi-quantum well layers into the 0.5 μm thick doped GaAs bottom contact layer. The pitch of the FPA is 38 μm and the actual pixel size is 28x28 μm^2. Then the random reflectors on top of the detectors were covered with Au/Ge and Au for Ohmic contact and reflection. Figure 8 shows twenty five processed QWIP FPAs on a 3 inch GaAs wafer. Then indium bumps were evaporated on top of the detectors for Si readout circuit (ROC) hybridization. A single QWIP FPA was chosen and hybridized (via indium bump-bonding process) to a 256x256 Si multiplexer (Amber AE-166) and biased at $V_B = -1.0$ V. The FPA was back-illuminated through the flat thinned substrate membrane (thickness ≈ 1300 Å). This initial array gave excellent images with 99.98%

of the pixels working (number of dead pixels ≈ 10) , demonstrating the high yield of GaAs technology.

We have used the following equation to calculate the noise equivalent temperature difference NEΔT of the FPA.

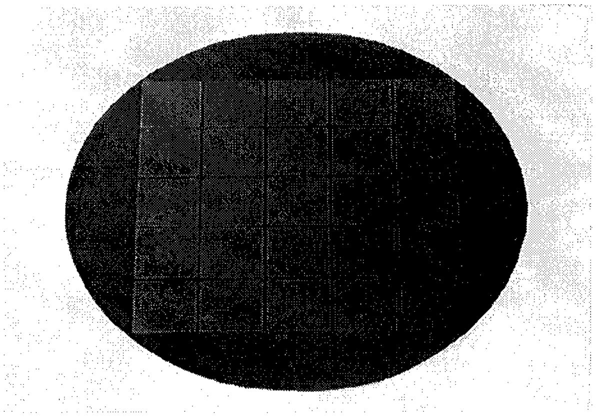

Fig. 8 Twenty five 256x256 QWIP focal plane arrays on a 3 in. GaAs wafer.

$$\mathrm{NE\Delta T} = \frac{\sqrt{AB}}{D_B^*(dP_B/dT)\sin^2(\theta/2)} \qquad (1)$$

where D_B^* is the blackbody detectivity and dP_B/dT is the derivative of the integrated blackbody power with respect to temperature. Figure 9 shows the NEΔT of the FPA estimated from the test structure data as a function of temperature for bias voltages V_B = -1, -2, and -3 V and the frame rate of 30 Hz. The background temperature T_B = 300 K and the area of the pixel A = (28 μm)^2. The measured mean NEΔT of the FPA was 25 mK at an operating temperature of T = 70 K and bias V_B = -1 V for 300 K background. This reasonably agrees with our estimated value of 7 mK based on test structure data. The peak quantum efficiency of the FPA was 9.5% (much lower quantum efficiency than expected can be attributed to the poor grating fill factor) and this corresponds to an average of 3 passes of IR radiation through the photosensitive multi-quantum well region. The uncorrected photocurrent uniformity (pixel-to-pixel) of the 65,536 pixels of the 256x256 FPA is about 7% (= sigma/mean). The uniformity after two point (17° and 27° Celsius) correction was 0.05%. As mentioned earlier this high yield is due to the excellent GaAs growth uniformity and the mature GaAs processing technology.

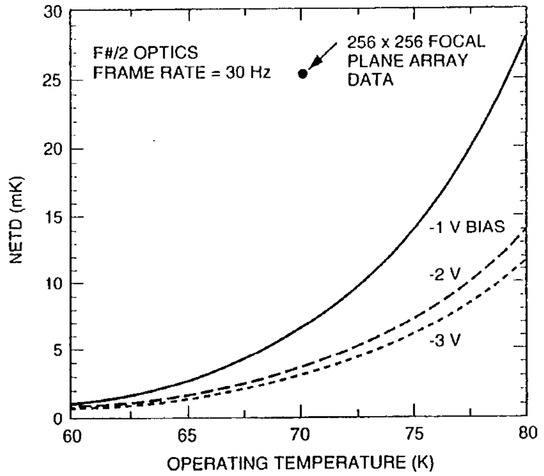

Fig. 9 Noise equivalent temperature difference NEΔT estimated from test structure data as a function of temperature for bias voltages V_B = -1, -2, and -3 V. The background temperature T_B = 300 K and the area of the pixel A = (28 μm)^2. The measured NEΔT of the focal plane array is 25 mK at an operating temperature of 70 K and bias V_B = -1 V.

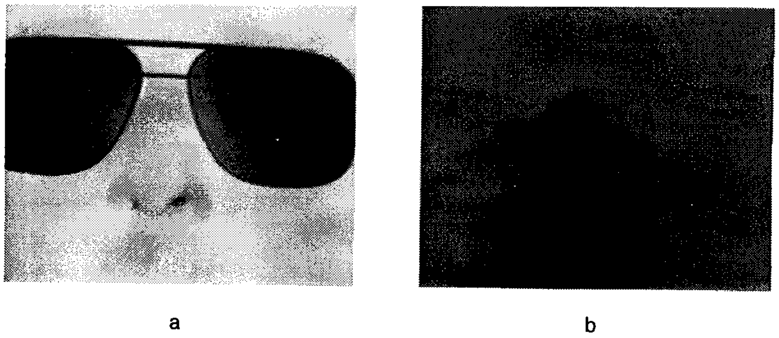

Fig. 10 (a) One frame of video image taken with the 9 μm cutoff 256x256 QWIP camera. The tiny dark squares on each frame of the glasses are the reflections of cold FPA in the camera. (b) An absorption image of acetone fumes (acetone has a strong IR absorption at 8.8 μm) taken with a 9 μm cutoff 256x256 QWIP FPA camera.

Video images were taken at a frame rate of 30 Hz with f/2 anti-reflection coated germanium optics at temperatures as high as T = 70 K, using a ROC capacitor having a charge capacity of 9×10^6 electrons. Figure 10 (a) shows one frame of a video image taken with a 9 μm cutoff 256x256 QWIP camera. The 2 tiny dark squares on the glasses are the reflections of cold FPA of the camera. Figure 10(b) shows an absorption image of acetone fumes (acetone has a strong IR absorption at 8.8 μm) taken with the same camera. These images demonstrate the high sensitivity of the 256x256 QWIP staring array camera.

No band pass filters were used and are unnecessary in QWIP camera systems because of the narrow spectral response of QWIPs. It should be noted that these initial unoptimized FPA results are far from optimum. The gratings were not optimized (as described earlier) for maximum light coupling efficiency; no microlenses were used; no antireflection coatings were used on the backside of the FPA; and finally the multiplexer used was a photovoltaic InSb multiplexer which is certainly not optimized to supply the proper bias and impedance levels required by photoconductive QWIPs. Implementation of these improvements should significantly enhance the QWIP FPA operating temperature (i.e., 77 K for 9 μm).

ACKNOWLEDGMENTS

We are grateful to C. A. Kukkonen, V. Sarohia, S. K. Khanna, K. M. Koliwad, T. N. Krabach, and P. J. Grunthaner of the Jet Propulsion Laboratory, D. Duston and L. Caveny of the Ballistic Missile Defense Organization, and G. Johnston of the National Aeronautics and Space Administration (NASA) Headquarters for encouragement and support of this work. The research described in this paper was performed by the Center for Space Microelectronics Technology, Jet Propulsion Laboratory, California Institute of Technology, and was jointly sponsored by the BMDO/IS&T Office, and the NASA Office of Space Access and Technology.

References

[1] M. T. Chahine, "Sensor requirements for Earth and Planetary Observations," *Proceedings of Innovative Long Wavelength Infrared Detector Workshop*, Pasadena, California, pp. 3-31, April 24-26, 1990.

[2] D. Duston, "BMDO's IS&T faces new hi-tech priorities," *BMD Monitor*, pp. 180-183, May 19, 1995.

[3] C. G. Bethea, B. F. Levine, M. T. Asom, R. E. Leibenguth, J. W. Stayt, K. G. Glogovsky, R. A. Morgan, J. D. Blackwell, and W. J. Parrish, "Long Wavelength Infrared 128 x 128 AlxGa1-xAs/GaAs Quantum Well Infrared Camera and Imaging System," *IEEE Trans. Electron. Devices*, vol. 40, pp. 1957-1963, 1993.

[4] L. J. Kozlowski, G. M. Williams, G. J. Sullivan, C. W. Farley, R. J. Andersson, J. Chen, D. T. Cheung, W. E. Tennant, and R. E. DeWames, "LWIR 128x128

GaAs/AlGaAs Multiple Quantum Well Hybrid Focal Plane Array," *IEEE Trans. Electron. Devices*, vol. ED-38, pp. 1124-1130, 1991.

[5] W. A. Beck, T. S. Faska, J. W. Little, J. Albritton, and M. Sensiper, *Proceedings of the Second International Symposium on 2-20 μm Wavelength Infrared Detectors and Arrays: Physics and Applications*, October 10-12, 1994, Miami Beach, Florida.

[6] B. F. Levine, C. G. Bethea, G. Hasnain, V. O. Shen, E. Pelve, R. R. Abbott, and S. J. Hsieh, "High sensitivity low dark current 10 μm GaAs quantum well infrared photodetectors," *Appl. Phys. Lett.*, vol. 56, pp. 851-853, 1990.

[7] B. F. Levine, "Quantum Well Infrared Photodetectors," *J. Appl. Phys.*, vol. 74, pp. R1-R81, 1993.

[8] Sarath Gunapala, Gabby Sarusi, Jin Park, True-Lon Lin, and Barry Levine, "Infrared Detectors Reach New Lengths," *Physics World*, pp. 35-40, December, 1994.

[9] S. D. Gunapala, J. S. Park, G. Sarusi, T. L. Lin, J. K. Liu, P. D. Maker, R. E. Muller, C. A. Shott, T. Hoelter, and B. F. Levine "128 x 128 GaAs/Al$_x$Ga$_{1-x}$As Quantum Well Infrared Photodetector Focal Plane Array for Imaging at 15 μm," submitted to *IEEE Electron Device Letters*.

[10] W. A. Beck, "Photoconductive gain and generation-recombination noise in multiple-quantum-well infrared detectors," *Appl. Phys. Lett.* , vol. 63, pp. 3589-3591, 1993.

[11] G. Sarusi, B. F. Levine, S. J. Pearton, K. M. S. V. Bandara, and R. E. Leibenguth, "Improved performance of quantum well infrared photodetectors using random scattering optical coupling," *Appl. Phys. Lett.*, vol. 64, pp. 960-962, 1994.

PROCESSING, CHARACTERIZATION AND OPTIMIZATION OF DETECTOR STRUCTURES INTENDED FOR UNCOOLED MICROBOLOMETERS ARRAYS.

P. Eriksson*, J. Y. Andersson**, G. Hansson***, K. Joelsson***, G. Stemme*,
*Dep. of Signals Sensors and Systems, Royal Institute of Technology, Stockholm,
Sweden, Tel: 46 8 7906613, e-mail: pone@instrlab.kth.se
** Industrial Microelectronics Center (IMC), S-164 21 Kista, Sweden
*** Linköping Institute of Technology, S-581 83 Linköping, Sweden

ABSTRACT

Surface micromachining has enabled the fabrication of thermal infrared (IR) detector arrays based on the measurement of IR induced temperature changes of thermally insulated membranes. Two critical parameters of thermal IR detectors are the thermal resistance and the thermal mass which set the limits for the responsivity and speed. The aim of this work is the optimization of these parameters when fabricating a membrane structure constituting the key part of a thermal IR detector. Considering aspects such as thermal conductivity, compatibility with silicon IC processing, step coverage and etching selectivity, we have chosen polyimide as a sacrificial layer, plasma deposited silicon nitride as the membrane material, and platinum for electrical connection to the membrane. The membranes have been characterized by measuring their thermal resistance and thermal mass. Considerations regarding interferometric structures for absorption and silicon and silicon/germanium as possible thermistor materials are given.

INTRODUCTION

An uncooled thermal IR (infrared) detector works according to a two step process where the absorbed IR radiation gives rise to an increase of the detector temperature which in turn is detected as a change of some electrical property. Two important detector parameters are its responsivity, $\Re$, and its thermal time constant, τ_{th}, where the responsivity is defined as the change of output (volt or ampere) per unit incident radiation. These two parameters depend on the detailed design of a thermally insulated membrane, the latter being a key structure of the thermal IR detector. This membrane provides a thermal resistance, R_{th}, between the membrane and the substrate and contributes a part of the thermal mass, C_{th}, of the detector. R_{th} is defined as the change of the average membrane temperature per absorbed unit power, whereas C_{th} is the change of heat content per unit temperature of the detector.

From the relations $\Re \propto R_{th}$, and $\tau_{th} = R_{th}C_{th}$, it is evident that an optimization of a thermal IR detector must maximize R_{th} while simultaneously fulfilling the condition $\tau_{th} \leq \tau_{max}$ where τ_{max} is set by the operating frequency of the detector.

To maximize R_{th}, the membrane material should possess a low heat conductivity and the membrane should be designed with long thin supporting legs. To minimize τ_{th} the membrane should be designed with the lowest possible thermal mass.

Another detector parameter of utmost importance is *NEP* or the noise equivalent power, which depends on the responsivity and noise properties of the detector. *NEP* is defined as the rms incident radiant power which gives rise to an rms signal voltage (or current) equal to the rms noise voltage (or current). *NEP* can be written

$$NEP = \frac{i_N \sqrt{\Delta f}}{\Re}, \qquad (1)$$

where i_N is the noise current ($A/\sqrt{Hz}$) and Δf the noise bandwidth. i_N may be divided into Johnson noise and excess noise (including $1/f$ noise and generation-recombination noise). Excess noise is often the dominant noise source, especially when semiconductor based layers (thermistors) are used as temperature detection.

The technique of surface micromachining described below has enabled the fabrication of high resolution arrays (>256 x 256 pixels) based on uncooled detectors [1].

MEMBRANE PROCESSING

Surface Micromachining

A frequently used method of fabricating these membranes is surface micromachining. This method makes use of a sacrificial layer on which the membrane material is deposited. Later in the process the sacrificial layer is etched away leaving the membrane supported by its legs. This procedure enables the fabrication of detectors on a substrate where complimentary metal-oxide-semiconductor (CMOS) read out electronics is already implemented. The disadvantage of this monolithic fabrication is the temperature limit of the processing which has to be carried out below 400-450°C due to the risque of damage of the CMOS circuits.

Problems that are likely to occur during membrane processing are: i) poor step coverage, ii) deformation of membranes due to stress, and iii) undesired etch of membranes during etch of sacrificial layers.

i) The degree of step coverage depends mainly on two factors, a) the growth rate isotropy when depositing the membrane material, and b) the topographic profile of the walls of the sacrificial layer.

a) The growth rate isotropy has to be high when depositing the membrane material. Parameters that have a positive impact on the isotropy are a short mean free path (MFP) of the atoms/molecules in the deposition process and a high degree of surface migration as the atoms/molecules hit the surface. The MFP is reduced when the pressure of deposition is increased and the surface migration can be improved by increasing the temperature of the substrate. The type of material and the deposition process affect the isotropy.

Sputtering normally provides good step coverage, CVD (Chemical Vapor Deposition) gives different results depending on the deposited material, whereas evaporation normally gives poor step coverage.

b) If the isotropy of the deposition process is poor the final step coverage can still be acceptable if the walls of the sacrificial layer are sloped. The profile of the walls depends on the technique used when patterning the sacrificial layer. If dry etching is used the profile mainly depends on etching parameters such as pressure and bias voltage which give more freedom to control the profile. On the other hand, if wet etching is used sloped walls are often obtained more easily but with limited freedom to control the profile.

ii) The residual stress of the membrane material depends on both the deposition process and the type of material. If the stress is too high the membrane can break or it can be buckled. The membrane together with the substrate can be used as an integral part of an interferometric structure for increasing absorption. Therefore the distance between the membrane and substrate is critical. With too high stress in the membrane this distance is affected and hence also the absorption. It is often necessary to optimize a deposition process with respect to the stress and this optimization can be very complicated since many parameters have an influence.

iii) The extent of membrane removal when etching the sacrificial layer depends on the membrane design and the etching selectivity, i.e. the ratio of the etch rate between the sacrificial layer and the membrane. It can often be necessary to etch a long distance beneath the membrane when etching the sacrificial layer. This results in long etch times which require high etching selectivity. By designing the membrane with extra holes in it the etch times and the requirement of etching selectivity can be reduced. The etching of the sacrificial layer can be performed with both wet etching and dry etching.

Choice of Membrane Material

After considering the aspects given under i), ii) and iii), we have chosen SiN_x (silicon nitride deposited with a Plasma Enhanced CVD technique, henceforth denoted SiN) as the membrane material. An example of a fabricated membrane made of SiN is shown in Fig. 1.

SiN is a dielectric material which is often used as a passivation layer in IC fabrication. The plasma technique makes it possible to deposit SiN at 300 °C with good step coverage. The heat conductivity can vary from one process to another. The literature gives values in the range of 2-18 W/mK. The stress found is fairly low and can be both tensile and compressive with the possibility of reducing it to a negligible value after optimization. A common technique to deposit SiN is to use Plasma Enhanced CVD (PECVD). Our PECVD process takes place at a temperature of 300 °C, a pressure of 600 mtorr, a power of 15 W and a frequency of 13.56 MHz. The process uses SiH_4, He, NH_3, N_2 and Ar with a deposition rate of 63 Å/min. The parameters of the process have a significant impact on properties of the SiN such as stress. This stress is evaluated by measuring the curvature of a Si wafer before and after deposition. The relation between stress and the curvature is given by the Stoney equation,

$$\sigma = \frac{Et_s^2}{(1-\upsilon)t_f}\left(\frac{1}{r_a} - \frac{1}{r_b}\right) \qquad (2)$$

where E is Young's modulus, υ the Poisson ratio, t_s the thickness of the substrate, t_f the thickness of the film, and r_a and r_b are the curvatures of the substrate after and before the deposition, respectively.

The curvature was measured with a Dektak profilometer. According to. Eq. 2 the stress is 65 MPa (tensile). This value has proven to be acceptable for membranes 50x50 μm^2 in size. If the stress is too high there are methods of reducing it after deposition by using ion bombardment [2].

To maximize R_{th}, a small cross sectional area of the supporting legs is necessary which requires a thin film and narrow legs. The thickness of the film is limited by its mechanical strength, whereas the width of the legs is limited by the mechanical strength and the exposure as well as of the etching technique used when patterning the membrane. Since the width of the legs should be narrow the etching has to be carried out with a high anisotropy, implying dry etching.

Choice of Sacrificial layer

After considering the aspects given under i), ii) and iii), we have chosen polyimide as the sacrificial layer. Polyimide is an organic material which can be made photosensitive and patterned in the same way as photoresist. After the patterning a heat treatment at 350-400 °C initiates the imidisation. As an organic material polyimide shows excellent etching selectivity with SiN both with wet as well as dry etching. Different techniques can be used to obtain sloped walls of polyimide.

We have used a polyimide from OCG, HTR 3-100, which was spin coated on four inch wafers at 3000-6000 rpm depending on the desired thickness. The spin deposition is a disadvantage when accurate control of the thickness is required, especially when the substrate has a nonuniform surface which may require a planarisation process. The profiles of the polyimide depend on how the exposure is carried out. One way of obtaining sloped walls is to use a filter to block the i-line from a high pressure mercury light source, using a print gap of 20 μm, and to perform the exposure without nitrogen purge. This is an easy and convenient technique but a simultaneous reduction of the film thickness must be accepted. Such a reduction is due to oxygen interfering with the crosslinking of the polyimide which makes it less resistant to the developer. Another method of obtaining sloped walls of polyimide is to make use of the fact that its etching rate in oxygen plasma is close to the etching rate of photoresist. After the polyimide has been cured the photoresist is lithographically patterned on its surface. When etching these films in an oxygen plasma in a barrel reactor they leave the polyimide with sloped walls. The angle of the slope is set by the ratio of the lateral etching rate of photoresist and the vertical etching rate of polyimide, see Fig. 2. A similar method is to etch photoresist and the polyimide in O_2/CF_4 plasma where the concentration of CF_4 is used to control the angle of the slope [3].

It is important that the sloped surfaces have are smooth since even a small sharp edge is replicated in the membrane and results in a mechanically weak structure.

Choice of Contact material

If the membrane material is electrically insulating, an electrical connection is necessary along the membrane legs, in order to contact the detector material on top of the membrane. If a metal is chosen as the contact material it will have a very high thermal conductivity which can significantly reduce R_{th} if the film is made too thick. If this material is patterned after the membrane the requirement of alignment between these layers may be high, 0.5 μm, depending on the width of the legs. It is therefore desirable to make use of a self aligning process where after patterning the contact material serves as a mask for the legs when patterning the membrane. Due to the high anisotropy required when etching the legs a Reactive Ion Etch (RIE) is often used. Inherently it has a degree of sputter effect. If the contact material is a metal it has to be relatively thin. This can be a problem if it does not withstand the sputter etch well.

In the case of the simple metal bolometer the contact material could also serve as a temperature sensitive resistor. When selecting suitable metals, the temperature coefficient of the resistivity (β) must be taken into account in addition to its properties as a mask, its thermal conductivity and its ease of deposition.

We have designed and fabricated a metal bolometer according to this simple design in order to characterize the thermal properties of the membrane. As a resistor material we have used platinum with a high β relative to other metals. It also withstands the sputter effect of RIE (based on NF_3). During the design it is important to consider that β of a thin metal film is lower than its bulk value. For example, a 250 Å thick Pt film have $\beta \approx 0.20\ \%$, about a factor of two lower than its bulk value.

ABSORBER

An absorber should meet two requirements. It should have a high integrated absorption, A, which is defined as,

$$A = \frac{\int_{8}^{12} A(\lambda)W(\lambda)d\lambda}{\int_{8}^{12} W(\lambda)d\lambda} \qquad (3)$$

where $W(\lambda)$ is the emitted radiation of a blackbody at 290 K and 8-12 µm has been chosen as the wavelength range of interest. An absorber should also have a low thermal mass, C_{th}, in order not to increase the thermal time constant excessively.

Absorption of IR radiation is mainly achieved in three different ways, i) a thin metal film, ii) a porous metal film, and iii) an interferometric structure.

i) By depositing a thin metal film with a sheet resistance, R_s, of 188 Ω/□, 50 % absorption is obtained in a broad wavelength range. This gives a low C_{th} but a relatively low A. It also requires an accurate control of the sheet resistivity.

ii) A porous metal film like black gold can give a high A over a wide wavelength range but it is normally achieved with a relatively high C_{th}. Such an absorber is deposited by evaporating the metal in a nitrogen atmosphere [4]. Its disadvantages are the difficulty of controlling the deposition process and that it normally makes a significant contribution to the total C_{th}.

iii) An interferometric structure (IS) meets the two requirements of high absorption and low thermal mass best [5]. An IS makes use of three separate films according to Fig. 4. Considering IS, the reflector typically consists of a metal film with a low sheet resistance. The thickness of the dielectric film should be $\lambda_{max} / 4n$ where λ_{max} is the wavelength of optimum absorption and n the refractive index of the dielectric material. The top metal film is made with $R_s = 377$ Ω/□. This gives 100 % absorption at λ_{max} and 0 % absorption at $\lambda_{max}/2n$. The major part of C_{th} is the dielectric film whose thickness can be reduced by choosing a material with a higher refractive index, but has the drawback of reducing the optical bandwidth. A high value of A implies a low n. A low C_{th} is achieved by using a dielectric material with a low specific heat and/or a high n. To use of vacuum between the reflector and the resistive film is an excellent solution since it does not add any thermal mass and it gives the highest possible value of A. This solution requires careful control of the distance between the reflector and the resistive film. A problem is that the membrane and the detector material constitute an integral part of this structure which affects the absorption. This can be taken into account when designing the absorber if the complex indices of the two films are known. Such a solution avoids the deposition of an absorber onto the membrane, which is important since the residual stress can buckle the membrane.

CHARACTERIZATION OF MEMBRANES

The membranes were characterized in vacuum ($<2*10^{-4}$ mbar) with regard to thermal resistance, R_{th}, and thermal time constant, τ_{th}. Vacuum operation is desirable in order to eliminate the thermal loss due to heat conduction and convection through the air or gas phase. The relation between the temperature and the resistance of Pt is well described by the equation

$$R = R_o\left(1 + \beta\left(T - T_o\right)\right) \qquad (4)$$

where R_o is the resistance at the temperature T_o and β is the TCR of Pt. Assuming ohmic power dissipation one obtains

$$T - T_o = RI^2 R_{th} \qquad (5)$$

where I is the current, it is found that

$$\frac{1}{R} = \frac{1}{R_o} - \beta\, R_{th} I^2. \qquad (6)$$

By plotting $1/R$ as a function of I^2 the product $\beta\, R_{th}$ can be found from curve fitting. Since the temperature coefficient β is easily measured by other means the thermal resistance R_{th} can be determined. If part of the power is dissipated in the legs it gives a somewhat lower value than can be expected from a bolometer where normally all the power is absorbed on the membrane.

The thermal resistance due to heat conduction through the membrane material, R_{th}^{m}, can be calculated if the thermal resistance through the electrical resistance, R_{th}^{e}, is known. An estimation of R_{th}^{e} can be made by using the Wiedemann-Franz law which relates the electrical conductivity to the thermal conductivity.

The thermal time constant, τ_{th}, can be measured using different techniques. If the membrane is made with a resistor integrated onto its surface but with no absorber, the membrane may be heated by applying a time dependent current through the resistor. The time constant can then be extracted from the resulting time dependent voltage across the resistor. An easier method is to deposit an absorber onto the membrane and heat it with chopped radiation. In this case a thin metal film is a convenient absorber due to its wide wavelength range absorption and its negligible thermal mass. The signal from the bolometer is amplified by a lock-in amplifier and a frequency spectrum is obtained from which the thermal time constant is calculated. The latter method using optical absorption was used in our measurements due to its larger signal to noise ratio.

THERMISTOR MATERIAL

For a bolometer the temperature change of the membrane is detected through a temperature dependent resistance. In order to achieve a sufficiently high sensitivity two properties are important: a high temperature coefficient and a low noise.

For thin metal films $\beta \approx 0.2\,\%$ whereas for thin semiconducting films $\beta \approx -1 - -3\%$. This difference is to some extent decreased when noise properties such as 1/f noise is taken into account.

As thermistor materials, vanadium dioxide has been exploited by Honeywell [1], and both amorphous or polycrystalline silicon or silicon/germanium layers [6] are interesting candidates. Usually radio-frequency sputtering och plasma-enhanced chemical vapor deposition are used. We have investigated both microcrystalline Si (B doped: $3 \cdot 10^{17}$-$4 \cdot 10^{18}$ cm^{-3}) layers, as well as SiGe (B doped: $3 \cdot 10^{18}$ cm^{-3}) thin films deposited by a Balzers UMS 360 Molecular Beam Epitaxy (MBE) system at 400 °C. The SiGe films were grown with a Si content ranging from 70 % - 78 %. The thicknesses range from 1500 - 2000 Å, and the layers were grown onto silicon wafers covered with a silicon nitride layer. Test samples were defined by mesa etching and finally aluminum contacts were evaporated onto the upper surface of the layers. The layers were biased by applying a voltage between two contacts (lateral conduction).

RESULTS AND DISCUSSION

Membranes of size 50x50 μm^2 have been fabricated and characterized in terms of the thermal resistance, R'''_{th}, and thermal time constant τ_{th}. Depending on the type of membrane design, their thicknesses range from 0.2 μm to 0.5 μm, the widths of the legs 2 - 6 μm, while their length varied from 30 to 60 μm.

The thermal resistance of the membranes, R'''_{th}, as found by plotting $1/R$ as a function of I^2 as described above, was in the range $2\text{-}12 \cdot 10^6$ K/W. The thermal time constant τ_{th} was between 2 and 12 ms, as obtained from the optical absorption method, also desribed above. These values were used to calculate the heat conductivity of SiN: λ_{SiN}=2.5–3.5 W/Km and the specific heat, c_{SiN}=1200 J/kgK.

It is a difficult task to provide specified values of the thermal resistance and thermal mass of a membrane intended for application in the field of thermal imaging. This requires that the necessary noise equivalent temperature difference and the frame time are known. But there are other aspects of interest such as the yield of the membrane fabrication. Our results indicate that an array of membranes with a thermal resistance, $R'''_{th} = 10^7\ K/W$, and a time constant, $\tau_{th} = 5\ ms$, should be possible to fabricate with a high yield.

The use of Si as well as SiGe thermistor layers were investigated. An initial attempt to characterize the as-grown silicon layers showed that these were highly resistive which prevented further measurements. Therefore the samples were annealed at 800 ^{0}C for 15 min, despite the fact that such a high temperature treatment is unacceptable since it would destroy CMOS circuitry. X-ray diffraction confirmed that the layers after annealing was microcrystalline. I-V characteristics showed perfect linearity, thus indicating good contacts. Measurements of β gave about 2.0 % for the samples with a doping concentration < $2 \cdot 10^{18}$ cm^{-3}, whereas for higher doping β declined to very low values (<0.1 %). Noise measurements gave evidence for 1/f noise. Assuming a simple model for 1/f noise of bulk origin one has [7]

$$i_n^2 = \frac{K\, I_0^2\, R_0}{f} = \frac{K P_0}{f}, \qquad (8)$$

where K is a constant, I_0 the DC bias current, R_0 the total resistance, and P_0 the power dissipation. A calculation of K gave values $\approx 10^{-18}\ \Omega^{-1}$, nearly independent on f and I_0. The fact that the contacts were linear in combination with that Eq. 8 is followed, indicate that the origin of noise is the bulk layer and not the contacts.

In order to assert that thermistor layers were microcrystalline at the growth temperature of 400 ^{0}C SiGe was used, since alloying with Ge is known to crystallize more easily than Si due to higher atomic mobility. The crystallite size as deduced from TEM (transmission electron microscopy) was 400 Å. The obtained values of β were 2.6 - 3.3 %. Due to the low deposition temperature and the absence of annealing the resistivity ρ was high, ρ=130 Ω cm. Such a high resistivity renders it difficult to make good ohmic contacts, and I-V characteristics showed nonlinear behaviour.

Measurements showed that 1/f noise was the dominating noise source. This noise may have different origin. Either it is generated in the bulk SiGe (including its interface to air), or in the aluminum contacts. If the former applies some techniques of passivation may be effective. Therefore ozone treatment was attempted, known to passivate dangling bonds by surface oxidation. Also hydrogen doping with a similar effect as ozone was tried. Due to the higher diffusivity of hydrogen compared with ozone, the former method is more effective in passivating dangling bonds buried deep in the microcrystalline bulk material. However, the effect of ozone treatment was minor. Hydrogen doping of SiGe films were performed by subjecting to a hydrogen plasma at 200 ^{0}C. However, not even in this case any improvement of 1/f noise performance was obtained. These results indicate that the source of 1/f noise is not in the bulk material but in the contacts.

In order to further confirm this hypothesis dedicated test structures of rectangular shape were processed, having constant contact area and layer width, but varying layer length (and therefore varying bulk layer resistance). A known constant current was forced through these structures. At such conditions the noise contribution from the contacts may be assumed to be constant, whereas Eq. 8 shows that the bulk contribution increases with increasing total resistance. From this it was confirmed that the contact noise dominated the total noise.

Improving the contacts by using either ion implantation or highly doped SiGe contact layers beneath the contact metal are under way.

CONCLUSIONS

When fabricating membranes intended for thermal infrared detectors, it is shown that silicon nitride and polyimide are good choices as the membrane material and the sacrificial layer, respectively. These materials meet the requirements of good step coverage, negligible stress, high etching selectivity and IC compatibility. Fabricated membranes have been characterized in terms of thermal resistance and thermal mass. The results are promising as regards fabrication of membranes with high yield.

Microcrystalline silicon and SiGe grown by MBE have been investigated as thermistor materials. Silicon was not obtained microcrystalline at temperatures around 400 ^{0}C. SiGe, on the other hand was microcrystalline, but possessed high levels of 1/f noise. There are strong indications that the noise originates in the contacts, and means of improving the latter will probably decrease the noise level.

REFERENCES

1 R. A. Wood, Proceeding of SPIE, **2020**, 322 (1993)

2 E. P. Eernisse, J. Appl. Phys., **48**, 3337 (1977)

3 M. Deschler and P. Balk, Microelectronic Eng., **4**, 207 (1986)

4 L. Lang, K. Kühl and H. Sandmaier, Sensors and Actuators, **A34**, 243 (1992)

5 P. Eriksson, J.Y. Andersson and G. Stemme, Physica Scripta, **T54**, 165 (1994)

6 M. H. Unewisse, K. C. Liddiard, B. I. Craig, S. J. Passmore, R. J. Watson, R. E. Clarke, and O. Reinhold, Proceedings of SPIE, **2552, 77** (1995)

7 A. van der Ziel, Noise in Solid State Devices and Circuits, p. 148, Wiley Interscience (1986).

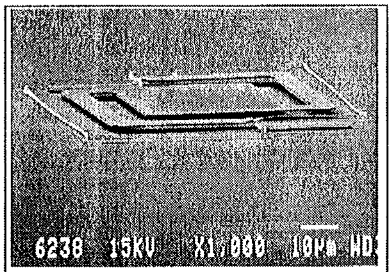

Fig. 1 A free standing membrane of SiN. The "fence" surrounding the membrane is sputter etched SiO.

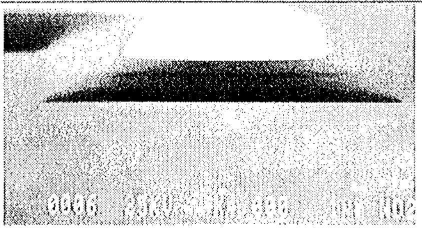

Fig. 2 The profile of polyimide which has been patterned by using photoresist as a mask.

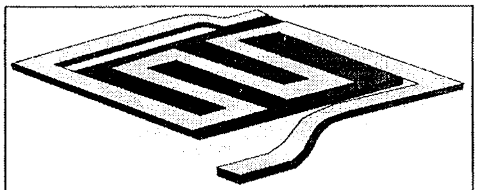

Fig. 3 A bolometer with a metal resistance which has also served as a mask when defining the legs of the membrane.

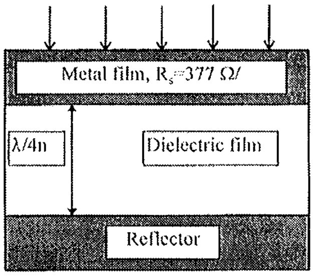

Fig. 4 An interferometric structure whose theoretical absorption is 100% at the wavelength λ.

InAs/GaSb/AlSb QUANTUM WELLS FOR INFRARED ELECTRO-OPTIC APPLICATIONS

C. A. Hoffman, J. R. Meyer, and F. J. Bartoli
Code 5610, Naval Research Laboratory, Washington, DC 20375

L. R. Ram-Mohan
Worcester Polytechnic Institute, Worcester, MA 01609

The InAs/GaSb/AlSb family of quantum heterostructures is found to be especially adaptable to the use of band structure engineering to achieve desired optical and electronic properties. Multi-layer structures combining small and large energy gaps, Γ and L conduction valleys, Type-I and Type-II band alignments, etc., are shown to provide an attractive basis for a wide variety of novel devices including electro-optical modulators, frequency converters, and diode lasers operating in the infrared.

INTRODUCTION

Electro-optical devices incorporating GaAs-based and InP-based quantum wells have been under intensive development for a number of years. As a result, the technology for near-infrared quantum well diode lasers is now relatively mature, and that for near-IR electro-optical modulators employing the excitonic quantum confined Stark effect is advancing rapidly. By contrast, the progress toward analogous semiconductor devices for the mid-wave and long-wave infrared (MWIR and LWIR) spectral regions lags far behind, in part because many of the mechanisms which yield attractive electro-optical properties at shorter wavelengths become ineffective at $\lambda > 2\ \mu$m. This has significantly impeded the development of practical systems addressing such important IR applications as remote chemical sensing, pollution monitoring, laser surgery, and multi-spectral IR sensing. In this paper, we will review several recently-proposed concepts for novel MWIR and LWIR electro-optical (EO), nonlinear optical (NLO), and diode laser devices based on the InAs/GaSb/AlSb family of semiconductors. These materials offer a broad flexibility in material design since a uniquely diverse array of key band structure, electronic, and optical properties can be tailored to suit the needs of a given application. For example, one may specify either narrow-gap or wide-gap, Type-I or Type-II band alignment in real space, Γ or

L point conduction band minimum, large or small interband optical matrix elements, large or small intersubband matrix elements at normal incidence, etc.

In order to quantitatively model the EO, NLO and lasing properties of InAs/GaSb/AlSb devices exploiting this flexibility, we have used a multi-band finite-element method (FEM) $k \cdot P$ formalism[1] to calculate wavefunctions, quantized energy levels, optical matrix elements, gain properties, etc., for complex multi-layer configurations. In the modeling results which follow, Γ-valley properties were derived from the full 8-band FEM calculation, whereas L-valley properties were obtained from a 1-band version using the quantization effective masses.[2] We will discuss the unique advantages of heterostructures fabricated from this group of materials for several types of MWIR and LWIR devices.

ELECTRO-OPTICAL MODULATORS

Fast EO modulators operating at wavelengths beyond 3μm are urgently needed for a number of important applications, particularly multi-spectral IR sensing and optical communications using future ultra-low-loss IR fibers. While intersubband interactions in asymmetric quantum structures have been suggested as a possible basis for IR modulators,[3,4] the development of practical devices currently remains at a relatively primitive stage despite the experimental confirmation of quite large EO coefficients.[5,6,7,8,9,10] This is due in part to the polarization selection rule which yields vanishing interactions between the intersubband system and normal-incidence radiation whenever the electrons populate the isotropic Γ-valley, since coupling to the beam then requires a component of the optical electric field along the quantization axis.[11] However, it has been predicted theoretically[2] and demonstrated experimentally[12,13,14] that when the electrons populate highly-anisotropic L valleys and the symmetry axes of the elliptical constant-energy surfaces are tilted with respect to the confinement axis, the in-plane and growth-direction motions become coupled and strong normal-incidence intersubband interactions result.

Figure 1 illustrates the Γ and L band edge profiles, quantized energy levels, and L-valley wavefunctions for an AlSb/GaSb/$Ga_{1-x}Al_xSb$/$Ga_{1-x}In_xSb$/AlSb asymmetric double quantum well (ADQW). Note that the GaSb well on the left has its conduction-band minimum at the L-point while the $Ga_{1-x}In_xSb$ well on the right has its minimum at the Γ-point (this well may alternatively be composed of InAs). The structure is designed such that the lowest quantized levels in the two wells lie close enough in energy that the net ground state for the ADQW can be modulated by reversing the direction of the applied electric field (F) from positive [Fig. 1(a)] to negative [Fig. 1(b)]. It should also be noted that most of the electrons remain in the L well whenever the two bands are evenly aligned in energy, since the L-valley density of states is nearly 30 times greater due to its 4-fold degeneracy and larger density-of-states mass. For a $Ga_{1-x}Al_xSb$ spacer layer thickness of 100 Å, $N_s = 1 \times 10^{12}$ cm^{-2} electrons per period, and an operating temperature of 77 K, a field of ±50 kV/cm is sufficient to switch from <4% to >94% of the electron population in the L-well, and slightly higher fields produce a nearly complete transfer. This controllable transfer of electrons from L states to Γ states provides an effective mechanism for modulating the IR absorption coefficient and refractive index. Furthermore, the conduction-band offset between GaSb and AlSb is large enough that the same basic scheme may be employed for EO modulators spanning IR wavelengths between 1.5 and 20 μm.

The absorption coefficient due to intersubband transitions is given by[4]

$$\alpha_{12}(\hbar\omega) = \frac{\Gamma^2 \alpha_{12}^0}{(\hbar\omega - E_{12})^2 + \Gamma^2} \quad , \tag{1}$$

where $\hbar\omega$ is the photon energy, Γ is the broadening parameter, $E_{12} \equiv E_{2\ell}^L - E_{1\ell}^L$ is the field-dependent intersubband splitting, and α_{12}^0 is the peak magnitude. Since we can actually *eliminate* the absorption line through variation of the field, the calculated contrast ratio is quite high (over 20:1). A recent experimental investigation of Γ-L ADQW devices at Columbia University has confirmed significant EO modulation of the MWIR transmission at normal incidence.[15]

The Γ-L transfer of electrons also results in a resonant intersubband contribution to the refractive index having the approximate form[4]

$$n_{12}(\hbar\omega) \approx -\frac{c\alpha_{12}^0}{2\omega} \frac{(\hbar\omega - E_{12})\Gamma}{(\hbar\omega - E_{12})^2 + \Gamma^2} \quad , \tag{2}$$

where c is the speed of light. For $N_s = 1 \times 10^{12}$ cm^{-2} and normal incidence, the dashed curve in Fig. 2 represents the modulation of n_{12} corresponding to a field variation ΔF of -100 kV/cm ($+40 \rightarrow -60$ kV/cm).

While the index shift is seen to be strong, a serious limitation of modulators based solely on the intersubband interactions is that the resonant Δn is largest in regions where there is also significant absorption loss. If we define L_π to be the propagation length required to induce a phase shift of π, the figure of merit

$$L_\pi \alpha = \frac{\pi c \alpha}{\omega |\Delta n|} \tag{3}$$

must be kept as small as possible if insertion losses are to be minimized. For a conventional stepped well or ADQW in which the main effect of the applied field is to shift the transition energy by an amount ΔE_{12}, without inducing intervalley transfer, it is apparent from Eqs. (1) and (2) that the ratio $\alpha_{12}/\Delta n_{12}$ will be minimized well away from resonance, where

$$L_\pi^{12} \alpha_{12} \approx \frac{2\pi\Gamma}{\Delta E_{12}} \quad . \tag{4}$$

This implies that for realistic values of Γ (at least ≈ 5 meV) and ΔE_{12} (less than ≈ 40 meV), it becomes nearly impossible to design a modulator with $L_{\pi}^{12}\alpha_{12} \ll 1$. This may be seen from the dashed curve in Fig. 3, which plots the spectral dependence of $L_{\pi}^{12}\alpha_{12}$ for an $In_{0.53}Ga_{0.47}As/In_{0.52}Al_{0.48}As$ ADQW with $\Gamma = 5$ meV and $E_{12} \approx 120$ meV at $F = 0$.

On the other hand, a crucial advantage of the Γ-L ADQW structure is that the interwell transfer modulates not only n_{12}, but also the plasma contribution to the dielectric constant. This has the form

$$\epsilon_p(F) = -\sum_{j}^{\Gamma,L} \frac{4\pi N_s^j(F)e^2}{\omega^2 d m_x^j} \quad , \tag{5}$$

where m_x^j is the in-plane effective mass for valley j and d is the total period of the multiple quantum well. In conventional Γ-Γ asymmetric designs, $\Delta\epsilon_p \approx 0$ because the total density is fixed by the doping level and the field modulation of the energy levels and wavefunctions is not accompanied by any appreciable modification of the in-plane mass. However, in the Γ-L ADQW the plasma contribution to the index shift: $\Delta n_p \approx n\Delta\epsilon_p/2\epsilon_\infty$ can be quite large, since the effect of the field reversal is to transfer the carriers from L states with a heavy in-plane mass ($m_x^L \approx 0.2m_0$) to Γ states with a much lighter mass ($m_x^\Gamma \approx 0.05m_0$). The solid curve in Fig. 2 represents the net index change due to the combined contributions by the resonant intersubband and plasma processes.

Besides increasing the net $|\Delta n|$ at all photon energies below the resonance energy, the plasma mechanism is particularly attractive because it remains large in regions where the resonant intersubband absorption is weak. Thus the Γ-L ADQW can yield $L_\pi\alpha \ll 1$ as long as one moves far away from the intersubband resonances, as may be seen from the solid curve in Fig. 3. If one wishes to extend the low-insertion-loss region to larger $\hbar\omega$, it is necessary only to increase the resonance energy E_{12}^L by employing thinner quantum wells. For example, $E_{12}^L = 180$ meV yields $L_\pi\alpha < 0.3$ for operation at $\hbar\omega = 120$ meV. In addition, since the Γ-L ADQW modulator can operate at normal incidence, it is adaptable to a wide range of device geometries that cannot be used in conjunction with conventional Γ-valley intersubband systems. These include normal-incidence EO-tunable absorption filters for multi-spectral detection as well as any configuration incorporating a Fabry-Perot resonator.

The need for coherent, high-intensity optical sources in the MWIR where few convenient ones currently exist has driven the research into MWIR nonlinear optical materials for second harmonic generation (SHG) and sum and difference frequency mixing.[16,17,18,19,20,21] While an enhancement of the SHG susceptibility by a factor of 1000 with respect to bulk GaAs has been reported for GaAs/AlGaAs asymmetric multi-quantum wells (AMQW),[18,19] the actual output power and SHG efficiency have been quite low. This is largely due to the fact that those studies dealt with electron subband transitions at or near the Γ-point, which is spherically symmetric and requires an optical polarization along the MQW growth axis for non-zero coupling to the SHG susceptibility. Experiments have therefore been limited to having the optical beam incident at Brewster's angle or using a waveguide geometry. In contrast, L-valley SHG and sum and difference frequency mixing are allowed at normal incidence.

Neglecting depletion and saturation, the second harmonic conversion efficiency is given (in cgs units) by[22]

$$\eta = \frac{128\pi^3}{n\kappa c^3}[\omega\chi^{(2)}_{2\omega}L']^2\frac{\sin^2(\pi L'/L_c)}{(\pi L'/L_c)^2}I_1, \tag{6}$$

where κ is the dielectric constant, ω is the photon frequency of the pump beam, I_1 is the intensity of the pump beam, L_c is the coherence length, $L' = L/\cos\theta$ is the propagation length, L is the thickness of the active layer, and θ is the internal angle of incidence. For a three-level system, the second-harmonic generation coefficient is given by[22]

$$\chi^{(2)}_{2\omega} \approx \frac{Fn^2e^3Nz_{12}z_{13}z_{23}\sin^3\theta}{\kappa(\hbar\omega - E_{12} - i\Gamma)(2\hbar\omega - E_{13} - i\Gamma)}. \tag{7}$$

Here F is the fill factor (ratio of quantum well thickness to total thickness of each period), and N is the three-dimensional electron concentration in each quantum well. The dipole matrix element for optical transitions between subbands i and j is $z_{ij}\sin\theta$, where $z_{ij} \equiv < i|z|j >$ is its value for waveguide geometry.

The double resonance condition for SHG is easily accommodated for a wide range of wavelengths by varying the GaSb well width (d_1), the $Al_xGa_{1-x}Sb$ alloy composition and the Al_xGa_{1-x} step width (d_2). With a broadening parameter of Γ = 7meV and $N_s = 1.6 \times 10^{12}$cm^{-2} per well, Xie et al.[23] have shown that for $2\hbar\omega = 5.5\mu$m, $\chi^{(2)}$ is optimized at a value of 9.1×10^{-8}m/V when $d_1 \approx 30$Å, $d_2 \approx 49$Å, and $x \approx 0.14$. Despite smaller matrix elements for the L-valley transitions, the result compares favorably to the largest $\chi^{(2)}$ for GaAs-based and InP-based quantum wells[16,17,18,19,21] if one properly accounts for the relevant fill factors and optimum internal angle of incidence. The favorable $\chi^{(2)}$ are due in part to the higher practical doping levels which are enabled by the much greater L-valley density of states. We finally note that modulation of the SHG can be achieved by varying an external voltage applied across the active region.[24]

MWIR DIODE LASERS

While III-V semiconductor heterostructure and quantum well diode lasers currently emit high powers at ambient temperature in the visible and near IR, there are several fundamental mechanisms limiting the performance[25,26,27,28] at MWIR wavelengths beyond 3μm. These include inadequate electrical confinement due to small conduction and/or valence band offsets, and the increasing predominance of Auger recombination when the energy gap is lowered and the temperature raised. The nonradiative decay has tended to be dominated by the so-called CHHS Auger process, in which the conduction-to-heavy-hole (CH) recombination is accompanied by a heavy-to-split-off-hole (HS) transition. In InAs-rich alloys such as InAsSb, InAsSbP, and InGaAsSb, both momentum and energy are easily conserved in this process because the energy gap E_g is nearly equal to the split-off gap Δ_0.[25]

Type-II heterostructures employing the InAs/GaSb/AlSb family have recently been proposed[1,29,30] as a promising new material system for MWIR lasers. InAs/$Ga_{1-x}In_xSb$ superlattices are known to display a large interband absorption coefficient when the layers are made thin enough to allow significant overlap of the electron and hole wavefunctions, and the same Type-II structures should clearly produce substantial gain if the nonradiative lifetime is long enough that a population inversion can be established. Miles and co-workers at Hughes have recently demonstrated stimulated emission in the 3-4 μm range from electrically-pumped[30] lasers with active regions consisting of two-constituent Type-II InAs/$Ga_{1-x}In_xSb$ superlattices.

The structures considered in Refs. 29-30 are non-optimal, however, in that the electrons in the superlattice (SL) have strong energy dispersion along all three coordinate axes. It is well known that quantum well (QW) lasers with quasi-2D electron and hole populations tend to significantly outperform double heterostructure lasers with 3D bulk carriers once a given fabrication technology has matured, primarily because the more concentrated 2D density of states yields much higher gain per injected carrier at threshold.

Figure 4 illustrates the conduction, valence, and split-off band profiles, along with the calculated energy levels and wavefunctions for a four-constituent Type-II multiple quantum well (InAs/$Ga_{1-x}In_xSb$/InAs/$Ga_{1-x}Al_xSb$) which preserves the large optical matrix elements of the InAs/$Ga_{1-x}In_xSb$ SL but has 2D dispersion relations for both electrons and holes.[31] Note first that even though the electron wavefunctions (solid curves) have their maxima in the InAs layers and the hole wavefunctions (dashed curves) are centered on the $Ga_{1-x}In_xSb$, their overlap is sufficient to yield interband optical matrix elements more than 70% as large as those in typical Type-I heterostructures.

We find that the resonance between E_g (the separation of E1S and H1) and Δ_0 (the difference between H1 and S1) can be completely removed by the Type-II band alignment. Furthermore, by analogy to the Type-II SL considered by Grein *et al.*,[29] for these particular layer thicknesses the energy gap does not resonate with any intervalence transitions involving H1 near its maximum (it falls approximately halfway between H1-H2 and H1-H3). Moreover, even the rate for CCCH events (in which the CH recombination is accompanied by an electron transition to a higher-energy conduction-band state) is suppressed by the small in-plane mass for H1 holes near the band extremum. On the basis of detailed Auger rate calculations, Grein *et al.* predict that for a properly-engineered $InAs/Ga_{1-x}In_xSb$ superlattice, the current density required for non-radiative loss (j_{NR}) can be made much less than the radiative contribution (j_R) for all temperatures up to 300 K.[29] Youngdale *et al.* have recently demonstrated experimentally that at 77 K, $InAs/Ga_{1-x}In_xSb$ SLs can display Auger lifetimes which are two orders of magnitude longer than those in $Hg_{1-x}Cd_xTe$ alloys with the same energy gap.[32] Note also that electrical confinement ceases to be an issue, because the AlSb provides large offsets for both the conduction and valence bands.

Figure 5 illustrates calculated results[31] for the optical gain, $g(\hbar\omega)$, at 300 K, where two different current densities are shown for both the SL and QW structures at 300 K. As expected, the 2D density of states in the QW leads to a much narrower spectrum. Although the radiative lifetime at fixed N is slightly longer in the SL, for a given j_R the QW nonetheless yields a significantly larger maximum gain $g_{\max}$.

Figure 6 plots the increase of the maximum gain with current density at 77 K and 300 K. Although the carrier concentrations required to achieve transparency in the active region are smaller in the QW at both temperatures, the longer τ_R in the SL leads to a slightly smaller j_R for transparency at low temperatures. However, for the thin active regions required for minimization of the threshold current density, the optical confinement factor is small and a relatively large gain is required to overcome parasitic losses due to free carrier absorption in the cladding layers, reflection, etc. We estimate that $g_{\max}$ on the order of 500 cm^{-1} will be required to achieve optimized laser operation, for which the QW with its much steeper slope has a clear advantage at all temperatures. The larger $\partial g/\partial N$ in the QW also leads to a significantly smaller linewidth enhancement factor (≈ 1.7, vs ≈ 4.2 in the SL for $g_{\max} = 500$ cm^{-1} at 300 K) and hence reduced filamentation.

We obtain extremely attractive threshold currents at 300 K (71 A/cm^2 for the QW and 162 A/cm^2 for the SL) and characteristic temperatures T_0 (350 K for the QW and 250 K for the SL). The analysis thus predicts performance comparable to that attainable from GaAs/Al$_x$Ga$_{1-x}$As QW lasers. In contrast, there have thus far been no reports of stimulated emission at 300 K for other III-V diode lasers emitting at wavelengths beyond 3 μm, and to our knowledge the highest T_0 for $T > 150$ K has been on the order of 30 K.

While up to this point we have employed the prediction[29] that optimized structures are radiative-limited up to 300 K, it is useful to examine the opposite "worst-case" limit, in which we take the Auger coefficient to be no better than what has already been observed at 300 K: $\gamma_3 = 5 \times 10^{-27}$ cm^6/s, as recently measured[33] for a non-optimized three-constituent InAs/Ga$_{1-x}$In$_x$Sb/Ga$_{1-x}$Al$_x$Sb multiple quantum well with photoluminescence emission at 4.8 μm. This upper bound for the Auger coefficient leads to $j_{NR} \approx 4000$ A/cm^2 for $g = 500$ cm^{-1} at 300 K, which is much less attractive than the j_R from Fig. 6 but is nonetheless more than an order of magnitude lower than values extrapolated from the best current MWIR ($\lambda \geq 3$ μm) thresholds.[27] The temperature dependence yields $T_0 = 59$ K, which is roughly a factor of two higher than any observed to date for diode pumping at $\lambda \geq 3$ μm.

CONCLUSIONS

Opportunities for the development of MWIR and LWIR devices based on bandstructure engineered InAs/GaSb/AlSb quantum heterostructures has been reviewed.

We have described ADQW structures in which an applied bias transfers virtually the entire electron population from Γ states to L states. The modulations of both the absorption coefficient and the refractive index are particularly strong because the resonances are effectively turned on or off by the applied field rather than simply being shifted to a different energy. This high degree of control and tunability provides all of the elements required for a wide range of EO devices operating in both normal-incidence and waveguide geometries.

An effective mechanism for surface-emitting SHG utilizing L-valley intersubband transitions in stepped AlSb/GaSb/Ga$_{1-x}$Al$_x$Sb/AlSb QW has been presented. Besides the considerable convenience of a normal-incidence device geometry, the predicted $|\chi^{(2)}_{zzz}(2\omega)|$s are comparable to the largest observed in Γ-valley processes in GaAs/Al$_x$Ga$_{1-x}$As and In$_{1-x}$Ga$_x$As/In$_{1-x}$Al$_x$As quantum wells. Furthermore, the large GaSb/AlSb conduction band offset of ≈ 1 eV enables the generation of second-harmonic wavelengths as short as 1.8 μm.

Finally, we have proposed a Type-II multiple quantum well design for high-efficiency ambient-temperature MWIR diode laser operation. InAs/Ga$_{1-x}$In$_x$Sb heterostructures currently appear to have the most favorable prospects for the significant suppression of Auger recombination, even if the mechanism never becomes altogether negligible at 300 K. Furthermore, the large band offsets effectively eliminate the electrical confinement difficulties that currently limit many of the other systems now being studied. We finally note that as for the intersubband quantum cascade laser,[34] the emission photon energy for the Type-II heterostructure is controlled almost entirely by quantum confinement rather than the energy gaps of the constituents, and can in principle be tuned from zero to more than 1 eV.

ACKNOWLEDGMENTS

Work on EO and NLO devices was supported by ONR. The MWIR laser research was supported by Air Force/Phillips Laboratory. We thank Hui Xie, Wen Wang, Greg Dente, Mike Prairie, Mike Tilton, and Richard Miles for valuable discussions, and Quantum Semiconductor Algorithms for use of the multi-band FEM software.

REFERENCES

1. L. R. Ram-Mohan and J. R. Meyer, J. Nonlinear Opt. Phys. Mat. 4, 191 (1995).
2. H. Xie, J. Piao, J. Katz, and W. I. Wang, J. Appl. Phys. 70, 3152 (1991).
3. P. F. Yuh and K. L. Wang, IEEE J. Quant. Electron. 25, 1671 (1989).
4. D. A. Holm and H. F. Taylor, IEEE J. Quant. Electron. 25, 2266 (1989).
5. Y. J. Mii, R. P. G. Karunasiri, K. L. Wang, M. Chen, and P. F. Yuh, Appl. Phys. Lett. 56, 1986 (1990).
6. N. Vodjdani, B. Vinter, V. Berger, E. Bockenhoff, and E. Costard, Appl. Phys. Lett. 59, 555 (1991).
7. E. Martinet, F. Luc, E. Rosencher, Ph. Bois, and S. Delaitre, Appl. Phys. Lett. 60, 895 (1992).
8. V. Berger, E. Dupont, D. Delacourt, B. Vinter, N. Vodjdani, and M. Papuchon, Appl. Phys. Lett. 61, 2072 (1992).
9. E. B. Dupont, D. Delacourt, and M. Papuchon, Appl. Phys. Lett. 63, 2514 (1993).
10. F. Capasso, C. Sirtori, and A. Y. Cho, IEEE J. Quant. Electron. 30, 1313 (1994).
11. B. F. Levine, J. Appl. Phys. 74, R1 (1993).
12. E. R. Brown, S. J. Eglash, and K. A. McIntosh, Phys. Rev. B 46, 7244 (1992).
13. L. A. Samoska, B. Brar, and H. Kroemer, Appl. Phys. Lett. 62, 2539 (1993).
14. Y. Zhang, N. Baruch, and W. I. Wang, Appl. Phys. Lett. 63, 1068 (1993).
15. Q. Du, J. Alperin, and W. I. Wang, Appl. Phys. Lett. (in press).
16. M. M. Fejer, S. J. B. Yoo, R. L. Byer, A. Harwit, and J. S. Harris, Jr., Phys. Rev. Lett. 62, 1041 (1989).

17. S. J. B. Yoo, M. M. Fejer, and R. L. Byer, Appl. Phys. Lett. 58, 1724 (1991).
18. E. Rosencher, P. Bois, J. Nagle, and S. Delaitre, Electron. Lett. 25, 1063 (1989).
19. P. Boucaud, F. H. Julien, D. D. Yang, J.-M. Lourtioz, E. Rosencher, P. Bois, and J. Nagle, Appl. Phys. Lett. 57, 215 (1990).
20. C. Sirtori, F. Capasso, D. L. Sivco, A. L. Hutchinson, and A. Y. Cho, Appl. Phys. Lett. 60, 151 (1992).
21. Z. Chen, M. Li, D. Cui, H. Lu, and G. Yang, Appl. Phys. Lett. 62, 1502 (1993).
22. Y. R. Shen, *The Principles of Nonlinear Optics* (Wiley, New York, 1984).
23. H. Xie, W. I. Wang, J. R. Meyer, and L. R. Ram-Mohan, Appl. Phys. Lett. 65, 2048 (1994).
24. J. R. Meyer, C. A. Hoffman, F. J. Bartoli, and L. R. Ram-Mohan, Appl. Phys. Lett. 67, 608 (1995).
25. M. Aidaraliev, N. V. Zotova, S. A. Karandashev, B. A. Matveev, N. M. Stus', and G. N. Talalakin, Fiz. Tekh. Poluprov. 27, 21 (1993) [Sov. Phys. Semicond. 27, 10 (1993)].
26. S. R. Kurtz, R. M. Biefeld, L. R. Dawson, K. C. Baucom, and A. J. Howard, Appl. Phys. Lett. 64, 812 (1994).
27. H. K. Choi, S. J. Eglash, and G. W. Turner, Appl. Phys. Lett. 64, 2474 (1994).
28. H. K. Choi, G. W. Turner, and Z. L. Liau, Appl. Phys. Lett. 65, 2251 (1994).
29. C. H. Grein, P. M. Young, and H. Ehrenreich, J. Appl. Phys. 76, 1940 (1994).
30. R. H. Miles, D. H. Chow, and Y.-H. Zhang, Proc. 7th Int. Conf. Narrow Gap Semicond. (Santa Fe, in press).
31. J. R. Meyer, C. A. Hoffman, F. J. Bartoli, and L. R. Ram-Mohan, Appl. Phys. Lett. 67, 757 (1995).
32. E. R. Youngdale, J. R. Meyer, C. A. Hoffman, F. J. Bartoli, C. H. Grein, P. M. Young, H. Ehrenreich, R. H. Miles and D. H. Chow, Appl. Phys. Lett. 64, 3160 (1994).
33. E. R. Youngdale, J. R. Meyer, C. A. Hoffman, B. R. Bennett, J. R. Waterman, B. V. Shanabrook, and R. J. Wagner, unpublished data.
34. J. Faist, F. Capasso, D. L. Sivco, C. Sirtori, A. L. Hutchinson, and A. Y. Cho, Science 264, 553 (1994).

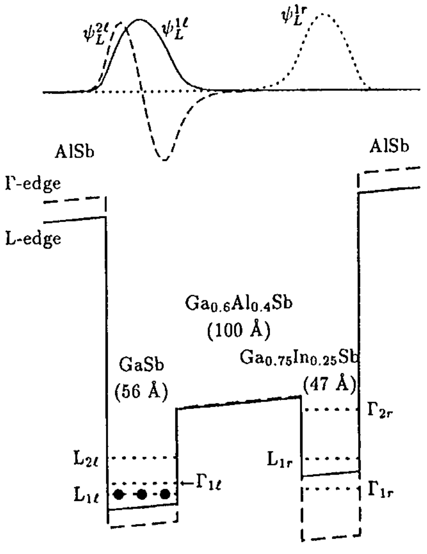

(a) $F = +50$ kV/cm

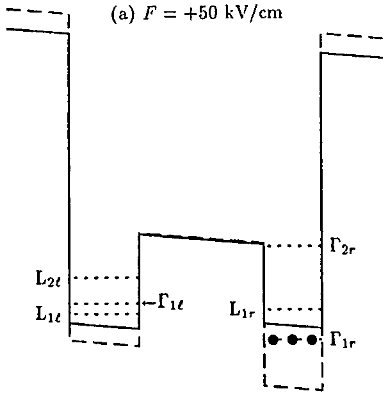

(b) $F = -50$ kV/cm

Figure 1. Γ-point (dashed) and L-point (solid) conduction band profiles, quantized energy levels, and wavefunctions (L-point at positive field only) for an ADQW at applied fields of (a) +50 kV/cm and (b) −50 kV/cm.

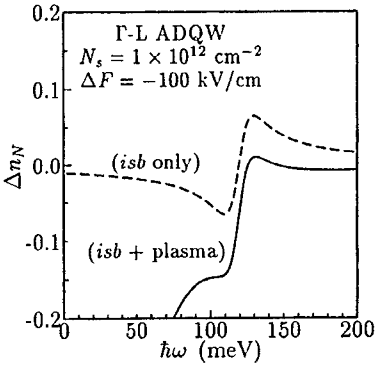

Figure 2. Field-reversal shift of the normal-incidence refractive index vs photon energy at $T = 77$ K for the ADQW from Fig. 1. The dashed curve is the resonant intersubband contribution alone, while the solid curve also includes the free-carrier plasma contribution.

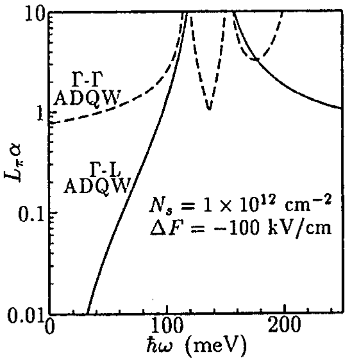

Figure 3. Sample length required to achieve a phase shift of π (normalized by the absorption depth) vs photon energy, for the Γ-L ADQW at normal incidence (solid curve) and a conventional InGaAs/InAlAs Γ-Γ ADQW in waveguide geometry (dashed curve).

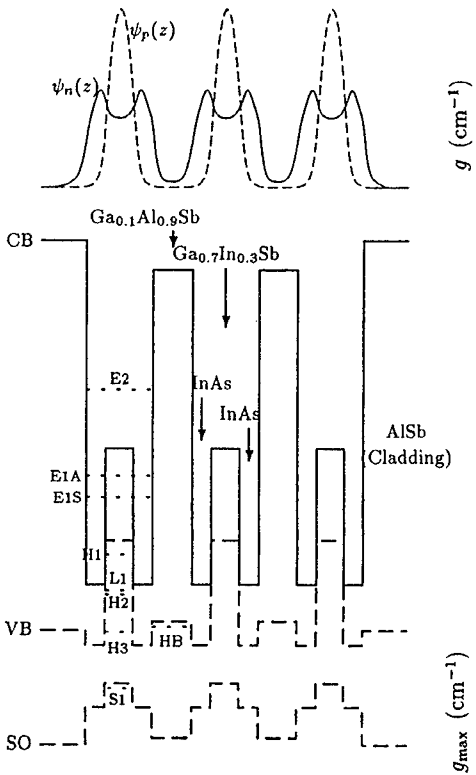

Figure 4. Conduction, valence, and split-off band profiles for the InAs(21Å)/GaInSb(31Å)/InAs(21Å)/GaAlSb(43Å) Type-II multiple quantum well. Also shown are electron (solid) and hole (dashed) wavefunctions, along with energy extrema for the various conduction and valence subbands.

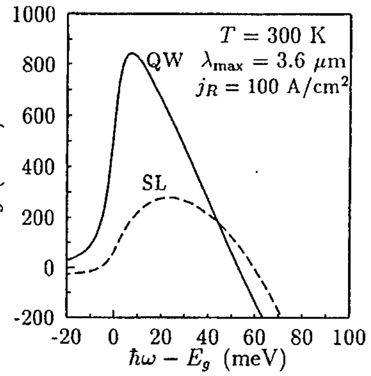

Figure 5. Calculated gain (averaged over both wells and barriers) vs photon energy relative to the energy gap for the superlattice (dashed) and multiple quantum well (solid) at a radiative-limited current density of 100 A/cm^2.

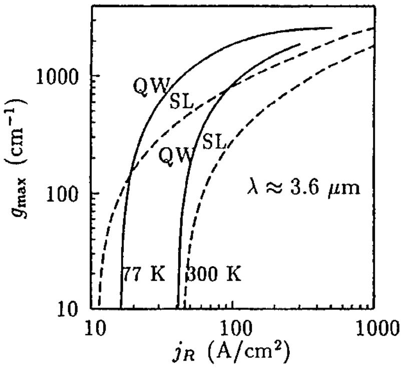

Figure 6. Maximum gain vs current density at 77 K and 300 K for the superlattice (dashed curves) and multiple quantum well (solid curves), assuming $L = 1400$ Å and $j = j_R$.

NOISE MEASUREMENTS ON A BOUND-TO-CONTINUUM QWIP DETECTOR

D.K. Sengupta, A.P. Curtis, H.C. Kuo, J.I. Malin, W.C. Fang, N.F. Gardner,
S.L. Jackson, P.J. Mares, T.U. Horton, S.L. Chuang, K.C. Hsieh, A. Kar, J. Mazumder,
M. Feng, H.C. Liu[†], K.K. Choi[††], I. Bloom[†††], and G.E. Stillman

Department of Electrical and Computer Engineering, Center for Compound
Semiconductor Microelectronics, Coordinated Science Laboratory, and Material Research
Laboratory, University of Illinois, Urbana, Il, 61801

[†]N.R.C., Ottowa, Canada, K1A0R6
[††]U.S. Army Research Labs, Fort Monmouth, NJ 07703
[†††]I.I.T. Technion, Haifa, Israel 32000

ABSTRACT

Noise measurements between 200 Hz and 15 KHz were carried out on a bound-to-continuum III-V quantum well infrared photodetector (QWIP). Two experiments were conducted on the QWIP. In the first experiment, the device was held at the design temperature of 60K and the bias current was varied. The noise current of the QWIP was found to increase as expected under G-R noise limited operation. In the second experiment, the detector bias current was held constant and the noise current was found at three different operating temperatures, 60K, 70K, and 80K.

INTRODUCTION

In the past few years there has been increasing interest in the development of infrared detectors using quantum wells as an alternative to photodetectors based on narrow-gap semiconductor materials[1]. An immediate advantage to using quantum wells can be seen because the peak response wavelength of the QWIP corresponds to the intersubband transition within the well and thus can be altered to suit the application by merely adjusting the well width and barrier height. Many papers have recently been published discussing the structure, performance, and feasibility of the QWIP. The use of the QWIP rather than the conventional mercury cadmium telluride (MCT) detector is advantageous for the following reasons. First, QWIPs are fabricated using AlGaAs/GaAs quantum well superlattices which are significantly less expensive and can be more uniform than MCT. Second, standard high yield GaAs integrated circuit fabrication techniques may be used, paving the way for advanced sensor arrays and their cost effective manufacture with existing infrastructure. The disadvantages to using QWIPs are the lower quantum efficiency and higher dark currents than ideal narrow-gap detectors, such as HgCdTe[2], and the requirement that either incident radiation be polarized or that gratings must be incorporated for normal radiation detection. Despite these disadvantages, however, QWIPs remain strong candidates for infrared detection in the 8-14 µm range.

DEVICE DESCRIPTION

The QW detector structure is shown in figure 1. It consists of a 32 period superlattice of 65Å thick GaAs quantum wells (δ doped at $n=5\times10^{11}$ cm^{-2}) and 350Å thick $Al_{0.22}Ga_{0.78}As$ barriers sandwiched between a 0.4 µm top contact layer and a 0.8 µm bottom contact layer, both doped at $n=1.5\times10^{18}$ cm^{-3}.

A 120 µm x120 µm square mesa was fabricated by etching through both the upper contact layer and the multi-QW structure down to the bottom contact layer. Metallization was subsequently performed by evaporation and alloying of standard AuGe/Ni/Au contacts. Dark current measurements were performed on the discrete detector using a continuous-flow He-Tran system with both full cold shielding and a 2πSr 300K background.

Figure 2 shows the dark current versus voltage characteristics for the QWIP as a function of temperature for the two different background conditions. The I-V data was collected by an HP 4145 Semiconductor Parameter Analyzer. As the figure shows, for temperatures below 80K and applied biases below approximately 4.5 volts, the noise current for the QWIP with full cold shielding was lower than for the 300K background, as expected. Hence, under the operating conditions used in these experiments, 60K and low bias, the QWIP dark current is background limited.

The spectral response, shown in figure 3, was measured using a Glowbar source and a Spex monochrometer. The substrate was polished to a 45° angle in order to properly illuminate the device. The sample was mounted in the dewar with a KRS-5. The light from the IR source was chopped and the AC signal produced by the QWIP was amplified by a low noise preamp and measured with a lock-in detector. This system spectral response was characterized by a pyroelectric detector assumed to have a flat spectral response.

EXPERIMENTAL TECHNIQUE

The experimental setup used for measuring the noise current is shown in figure 4, and figure 5 shows the circuitry involved in both the photoresponse and noise current measurements. The QWIP (or resistor standard) is placed in series with a load resistor and biased by a variable battery source. The output of the QWIP is amplified by a preamp and then measured with a Fast Fourier Transform analyzer. This gives a plot of the noise amplitude versus frequency. Only the frequency independent noise (white noise), which arises from thermal fluctuations, shot noise, and G-R noise is of interest in these experiments.

There are several precautions that are taken in order to reduce the background noise of the system. Batteries are used to power the detector and preamp to keep the noise low. High precision, metal film resistors must be used, and these and the detector are placed in protective shielding. Finally, all BNC cables are kept as short as possible and even then, corrections for the remaining capacitance are made using the spectrum obtained. Care must also be taken when choosing the load resistor so that its Johnson noise is less than the detectors Johnson noise. Since this noise component is given by the following,

$$I_{johnson} = \sqrt{4k_BT/R}, \qquad (1)$$

for a detector at 60K and the load resistor at room temperature, this requires that,

$$\frac{T_D}{R_D} > \frac{T_L}{R_L} \quad or \quad R_L > 5R_D \qquad (2)$$

Where R_D is the differential resistance of the QWIP at the desired detector bias.

The noise output from a resistor matched to the differential resistance of the detector at the operating voltage was measured to verify the noise measurements.

The measured noise spectrum contains components due to the load resistor and preamp as well as the capacitative effects mentioned above. The noise voltage for the standard resistor spectrum, as limited by the capacitance, is given by,

$$V^2_{measured} = \frac{R_{\parallel}^2\left(i_R^2 + i_L^2\right)}{1 + (2\pi f R_{\parallel} C)} + V^2_{preamp}, \qquad (3)$$

where $R_{\parallel}$ is the ac resistance due to the parallel combination of the load resistor and standard resistor, C is the capacitance of the circuit, f is the measurement frequency, i^2_R is the Johnson noise of the standard resistor, i^2_L is the Johnson noise of the load resistor, and V^2_{preamp} is the noise from the preamp. The analogous equation for the detector noise is given by,

$$V^2_{measured} = \frac{R_{\parallel}^2\left(i_n^2 + i_L^2\right)}{1 + (2\pi f R_{\parallel} C)} + V^2_{preamp}, \qquad (4)$$

where i^2_n includes both the Johnson noise and the G-R noise. In the frequency range and source resistances of interest in this experiment, the noise due to the, V^2_{preamp}, preamp is <4nV/Sqrt(Hz) which is negligible compared to the noise due to the load and detector/standard resistor thermal noise. The effect of the capacitance can therefore be obtained by fitting the resistor standard noise spectrum to the above equation with $R_{\parallel}C$ and $\sqrt{R_{\parallel}^2\left(i_R^2 + i_L^2\right)}$ as parameters. Once these are obtained, the detector noise spectrum can be analyzed using the $R_{\parallel}C$ parameter to find the total white current noise of the detector by subtracting the theoretical Johnson noise of the load resistor.

EXPERIMENTAL RESULTS AND DISCUSSION

The measured noise power spectral density (PSD) of the QWIP, whose differential resistance (R_{ac}) at 26.7 µA is 42.2kΩ, and a 42kΩ standard resistor are shown in figure 6. In this frequency range the noise spectral density is affected by the RC parasitic effect, but after corrections are made a frequency independent noise level results. Table I shows the fitting parameters for the standard resistor noise spectrum shown in figure 6. The Johnson noise of the parallel combination of the load resistor at 300K and the standard resistor at 60K is evaluated using the expression:

$$V_N = \sqrt{4k(R_L T_R + R_R T_L) \bullet \Delta f \bullet \left(\frac{R_L R_R}{R_L + R_R} \right)^2} \qquad (5)$$

where R_L is the load resistance, R_R is the standard resistor resistance, T_L is the temperature of the load resistor, , T_L is the temperature of the standard resistor, and Δf is the bandwidth, which is normalized to 1 Hz.

As seen in the table, the value obtained for the parasitic time constant $R_{||}C$ from the standard resistor spectrum was 5.1 µs. Using this result and repeating the fitting procedure for the detector noise spectrum, $\sqrt{R_{||}^2 (i_N^2 + i_L^2)}$ is extracted and i^2_n may be found.

Figures 7 and 8 show the noise current of the QWIP as functions of bias current and detector temperature respectively. The G-R noise current is expected to vary as the square root of the applied biasing current,

$$i_n^2 = 4qIG(\Delta f) \qquad (6)$$

$$i_n \propto \sqrt{I} \qquad (7)$$

and therefore, the data shown below, as well as previous data[1], exhibit this trend. The results presented here of the magnitude of the noise current also agree well with the predictions from Levine et al.[1]. However, if the noise current is truly G-R limited, it is also expected that the noise current should not vary as a function of temperature at a given biasing current. The results presented below are not consistent with this prediction. It may be speculated that this is due to changes in the noise gain with temperature[3]. Further experiments are in progress to address this issue.

CONCLUSION

This paper has presented noise studies on a bound-to-continuum QWIP under various temperatures and biasing conditions. For frequencies between 200 Hz and 15 KHz, the noise measured is consistent with the results obtained for G-R limited noise, however further studies need to be undertaken to ascertain the effect of temperature on the noise characteristics of QWIPs.

ACKNOWLEDGMENTS

The authors would like to gratefully acknowledge the help of the following for discussions and technical assistance: L. Lundqvist, M. Dodd, A. Mahajan, and the members of the Semiconductor Research Group.

REFERENCES

1. B.F. Levine, J. Appl. Phys., **74**, R1 (1993)
2. M.A. Kinch and A. Yariv, Appl. Phys. Lett., **55**, 2093 (1989)
3. K.K. Choi, Private communication

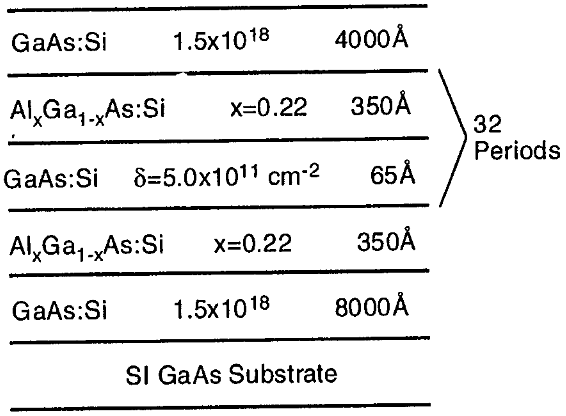

Fig. 1. QWIP device structure

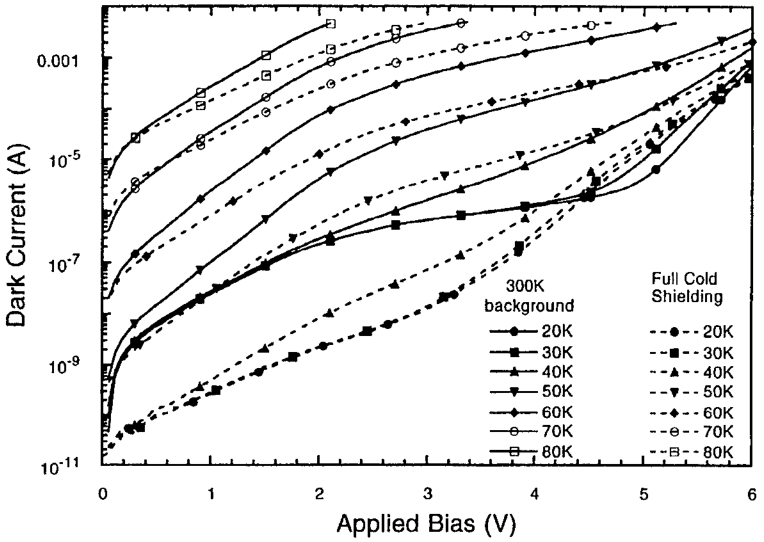

Fig. 2. Dark current as a function of applied bias at temperatures used in this experiment for both full cold shielding and 300K background cases

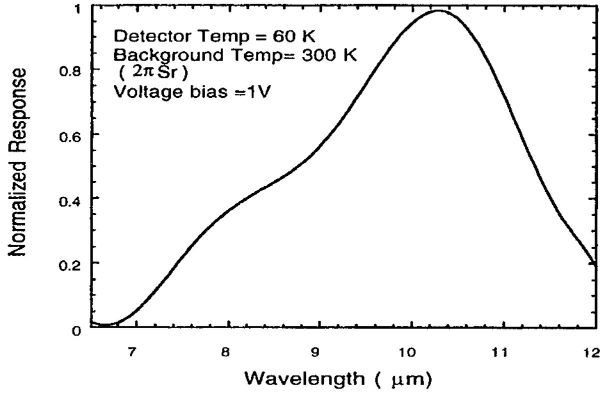

Fig. 3. Normalized response of the QWIP detector

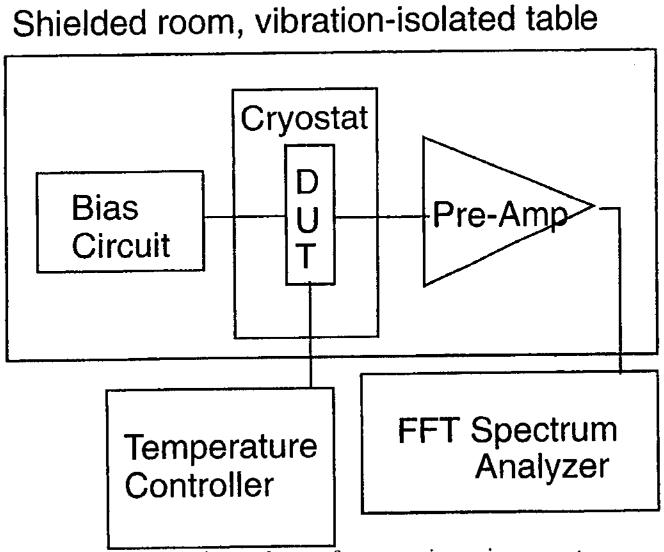

Fig. 4. Experimental setup for measuring noise current

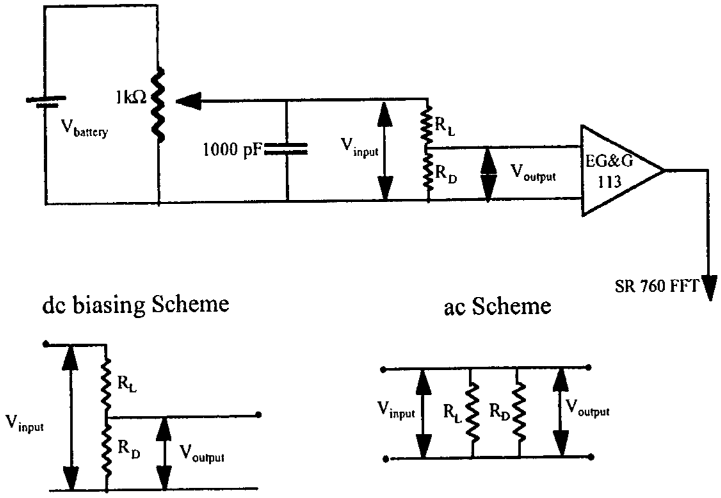

Fig. 5. Circuitry schematic for photoresponse and noise measurements

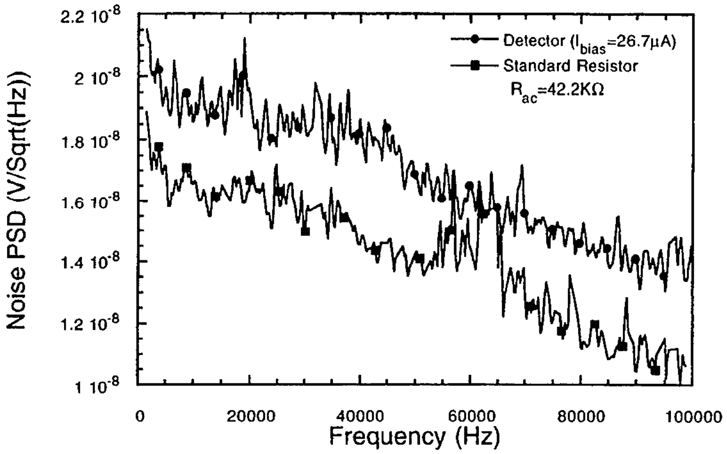

Fig. 6. Noise PSD as a function of frequency for the standard resistor and QWIP

Table I. Fitting parameters used for the spectra of figure 6 above

UIUC	*Standard Resistor 42.2 KΩ*	*Detector R_{ac}=42.2 KΩ*
Fit Frequency minimum	*2 KHz*	*2 KHz*
Fit Frequency maximum	*13 KHz*	*15 KHz*
Fitted $R_{\parallel}C$	*5.1 μs*	*5.1 μs*
Fitted $\sqrt{R_{\parallel}^2(i_R^2+i_L^2)}$	*17.2 nV*	*20.1 nV*
Calculated $\sqrt{R_{\parallel}^2(i_R^2+i_L^2)}$	*12.1 nV*	
Calculated i_n		*0.17 pA*

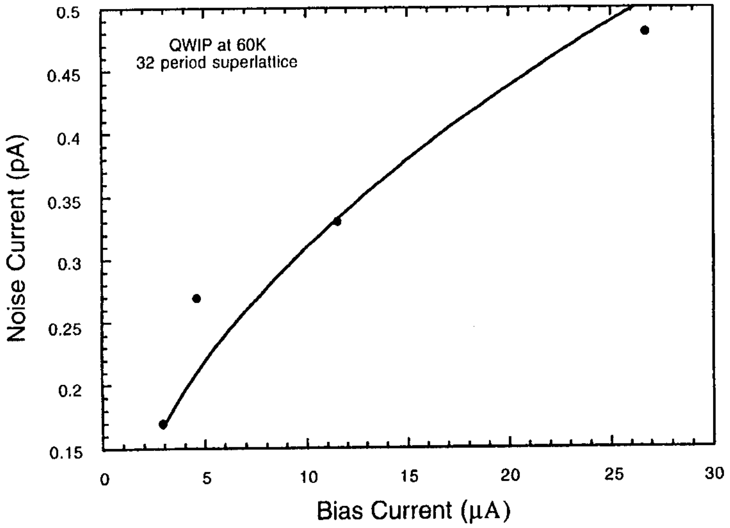

Fig. 7. Dark current as a function of applied bias current

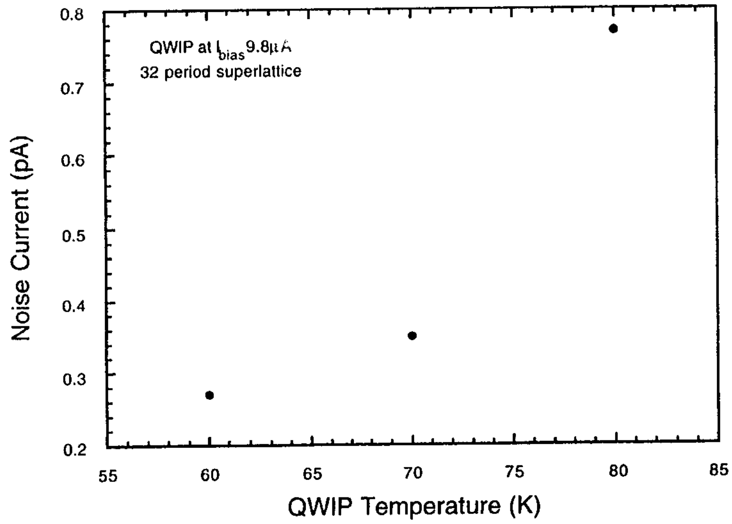

Fig. 8. Dark current as a function of QWIP temperature

SPONTANEOUS PULSING IN SEMICONDUCTOR HOMO AND HETEROSTRUCTURES FOR IR DETECTION

A. G. U. Perera, S. G. Matsik and M. H. Francombe
Department of Physics & Astronomy
Georgia State University, Atlanta
GA 30303, 404-651-3221
phyuup@gsusgi1.gsu.edu

Experimental pulsing data obtained at 4.2 K, with Si p^+-n-n^+ structures, (showing a rich spectrum of nonlinear behavior) working as infrared detectors without preamplifiers, will be discussed. Device physics, starting with the current-voltage relations and space charge accumulation leading to spontaneous pulsing in GaAs/AlGaAs quantum well structures will be introduced. Photoionization will be added to the model to get the infrared response. This can lead to novel IR detectors operating above 77 K which will not require any preamplification. The wavelength tunability, and the temperature dependence are also studied.

INTRODUCTION

Recent developments in novel infrared sensors have involved an increasing focus on materials systems based on Si and GaAs, since these offer greatly enhanced stability and processing advantages (e.g. over HgCdTe), particularly in the areas of large -array and integrated focal plane technology. In these large bandgap semiconductors, increase of the optical absorption wavelengths to regions extending from the near infrared to the far infrared (depending on the composition and structure adopted) have been demonstrated through the use of special barrier (or junction) and heterostructure configurations.(1) Typical examples include photoemissive (silicide) detectors, bolometers, charge couple devices etc,. More recent developments include combinations of the basic principles with new improvements such as blocked impurity band detectors(2), charge storage mode(3), homojunction and heterojunction internal photoemission detectors(1,4,5), and multiquantum well detectors.(6) All of these detectors need the use of preamplifiers or lockin amplifiers due to the very small photocurrent signals. Here, we will discuss a detector which does not need any amplifiers for the detection of infrared radiation.

In previous publications(1,7) we have developed a detailed device physics model to describe the spontaneous pulsing in (dc) forward biased Si p^+-n-n^+ structures at 4.2 K. The mechanism is based on the space charge accumulation due to the impact ionization in the n-region which leads to breakdown. The space charge neutralization will reset the diode, starting the process again, functioning similarly to a relaxation oscillator. Pulse heights from about few volts to tens of volts have been observed. Although the heights remained roughly the same for each pulse in the spiketrain, the interpulse time intervals (IPTIs) had very interesting patterns depending on various device and circuit parameters, and also on incident electromagnetic radiation. The power spectra obtained from IPTIs showed peaks corresponding to Farey fractions. By changing the bias conditions different IPTI patterns were obtained showing various periodicities.

Low temperatures permit n-region impurities (for example, phosphorus with 45 meV ionization energy) to act as traps with long lifetimes. Impact ionization and IR photoionization of these n-region impurities result in an increase in space charge. The cumulative (integrated) effect of this buildup triggers a large injection current, i.e., the firing of the integrate-and-fire detectors. The R_LC_L load in Fig. 1 cuts off the injection current shortly after it is initiated so that the output consists of injection current pulses. If the injected current neutralizes all of the space charge in the n-region, (see Fig. 2) initial conditions will be the same at the start of each cycle and the injection pulses should then occur periodically. However, depending on the device and circuit parameters, injection pulses may neutralize only a portion of the n-region space charge. This can give rise to different initial conditions and temporal patterns in the output pulse train.

In the absence of IR radiation, the rate of change of space charge in the n-region can be expressed as

$$\frac{d\rho}{dt} = n\sigma_i\, j \qquad [1]$$

where σ_i is the impact ionization cross section, (8,9) ρ is the space charge density and n is the concentration of unionized traps. From Gauss's law, the field at the n$^+$-n interface is given by

$$F = \frac{V - V_0}{D} + \frac{1}{D\varepsilon}\int_0^D x\rho(x)\, dx, \qquad [2]$$

where V is the voltage across the diode, D is the n-region thickness and V_0 accounts for the Fermi level difference between the p and n impurity bands. For simplicity, we assume that the space charge is uniform over the diode thickness.

The Richardson-Dushman equation for the injection current density(10) becomes

$$j = A^* T^2 e^{-(\Delta - edF)/kT} \qquad [3]$$

where d is an interface thickness parameter, Δ is the barrier height, A^* the Richardson constant. Combining the above equations, we get an expression for the variation of current density with time as

$$j(t) = \frac{j(0)}{1 - t/\tau_0}$$

where $j(0)$ and τ_0 are device and circuit dependent constants.(1) This is a very simplified model, where the sharp rise in the current density is interpreted as the onset of pulsing and the fall phase of the current density is completely ignored. A more detailed discussion is given elsewhere.(7,11) By analyzing the interpulse time intervals (IPTIs) of the spiketrain outputs using nonlinear dynamic techniques, several interesting phenomena were discovered. Several periodic patterns of spiketrain firing are recorded with a strong period 2 pattern(12) which parallels large-small (LSLSLS......) amplitude modulation patterns observed in the Belousov-Zhabotinski (BZ) reaction.(13) The variable parameter in the BZ reaction, the flow rate, is parallel to the dc bias in the p^+-n-n^+ situation. Power spectra showed peaks corresponding to Farey fractions showing 115 out of the possible 129 of the Farey sequence of order 20.(14)

Effect of Infra Red on Pulsing

When infrared radiation is incident on the p^+-n-n^+ structure, experimental and modeling results show that the IPTI patterns will undergo a change consisting of a change in the rate, mostly a rise and a change in the temporal pattern. This faster firing is due to the additional space charge created by the photoionization of the n-region impurity atoms. This additional space charge buildup in the detector n-region (see Fig. 2 showing band bending due to space charge) can be described by adding space charge generation due to the incident IR radiation.

$$\frac{d\rho}{dt} = n\sigma_i\, j + \frac{e\sigma_p n I}{h\nu} \qquad [4]$$

where σ_p is the photoionization cross section,(15) I is the intensity of the source, $h\nu$ is the energy of the IR photon.

Combining the new space charge generation equation with the field equation 2 and equation 3, we get

$$j(t) = \frac{bc}{n\sigma_i[(c + be^{-a\rho_0})e^{-abt} - c]} \quad , \qquad [5]$$

where $c = n\sigma_i A^* T^2 \exp(-\Delta + ed(V - V_0)/D)/kT$, $b = \sigma_p n I e/h\nu$, and $a = edD/2\varepsilon kT$.

From the above equation, we see that the firing occurs when $[c + b\exp(-a\rho_0)] \times \exp(-abt) = c$ which gives

$$f = f_{dark} \frac{I/I_0}{\ln(1 + I/I_0)} \qquad [6]$$

where

$$f_{dark} = \frac{edDc}{2\varepsilon kT} \exp(a\rho_0) \qquad [7]$$

and

$$\frac{1}{I_0} = \frac{e\sigma_p \exp(-a\rho_0)\exp(\Delta/kT)}{h\nu\sigma_i A^* T^2 \exp[ed(V - V_0)/DkT]}$$

Responsivity and Specific Detectivity (D^*)

Current responsivity (R) is given by $q\,df/dI$, where q is the charge per pulse, df is the change of frequency of the output pulse rate and dI is the change of incident IR flux. Responsivity has been observed to be 9.2 A/W or 9×10^9 Hz/W with power incident on the diode being 2×10^{-2} W/m^2.(16) For high intensities (i.e. $I/I_0 >> 1$) the frequency responsivity df/dI becomes

$$\frac{df}{dI} = \frac{f_{dark}}{I_0} \frac{\ln(I/I_0) - 1}{[\ln(I/I_0)]^2}$$

Noise equivalent power is given by $A(dI/df)(\delta f)$, where A is the area of the device, (dI/df) is the frequency responsivity, and δf is the variation of the dark pulse rate.

Specific detectivity (D^*) can be obtained from noise equivalent power. For example, for a particular (nonoptimized) detector at 16.5 V bias, we have observed a dark pulse rate of 0.14 Hz over a 50-second interval with a $\delta f = 0.005$ Hz which corresponds to $D^* = 3 \times 10^{12}$ cm $\mathrm{Hz}^{1/2}$ W^{-1} for the 27 μm region, where the Si:P detector has its highest sensitivity.

Mode Locking

By adjusting circuit parameters, the pulsing patterns could be locked in to certain periodic patterns under IR illumination which is termed "mode locking".(17) Within the mode locked regime, the pulse rate remains sensitive to changes in IR intensity and fluctuations in the pulse rate are small. Since the electrical background noise in these pulsing structures is negligibly small compared to the size of the pulses, the relevant noise is contained within the fluctuations in the IPTIs. However, not all of the IPTI fluctuations reflect noise. Studies on nonlinear dynamics indicates that fluctuations in nonlinear systems can have a deterministic relationship to the parameters of the nonlinear system.(18) This suggests that for the devices under consideration, a sizable component of the fluctuations in the temporal pattern could be deterministically related to parameters like IR intensity and bias voltage, and unrelated to true performance limiting noise.

The distinction between deterministic fluctuations and true noise, together with recently achieved understanding of nonlinear systems, could lead to significant advances in IR detector performance. Mathematical models of nonlinear systems provide some guidance and understanding in this area. Many of the models are formulated in terms of iterative maps. A spiketrain can be regarded as a physical representation of a time series $t_1, t_2, t_3, \ldots$. An example for this pulsing structure can be considered as:

$$t_{r+1} = f(t_r, \mu), \qquad [8]$$

where f is a nonlinear function which relates successive terms in a time series t_r with $r = 1, 2, 3, \ldots$, and μ indicates circuit and device parameters. The explicit form of f is associated with the dynamical system. For a particular device in a fixed circuit under fixed bias conditions μ, can be regarded as the incident IR intensity.

If time series information including deterministic fluctuations were fully utilized, and one had sufficient knowledge about f, one could pin down the parameters of f quite precisely. This is equivalent to decoding the time series to obtain information about the parameters of the iterative mapping. The decoding problem is in some sense the inverse of the mapping problem. Since IR intensity is a sought after parameter, and bias voltage is a known adjustable parameter, one can regard IR detection as a special type of decoding, or inverse mapping problem. In a region of parameter space where mapping generates a chaotic time series the decoding problem is difficult, while in a periodic regime the decoding problem is simple. If an injection mode detector output is periodic with period P, i.e. $t_r = t_{r+P}$ for a range of IR intensities, then decoding simply involves empirical determination of the relationship between the IR intensity and P successive time intervals.

The existence of narrow peaks in the injection mode detector power spectra (see Figs. 3 and 4) supports the view that injection mode detectors are deterministic systems. The power spectra are associated with Fourier transforms over the time series index r. Period P is associated with peaks at a frequency $1/P$ and harmonics thereof.

In Figs. 3 and 4, the detector is passing through mode locked regimes as a function of IR source temperature, with a fixed bias voltage. The large, narrow peaks indicate closeness to the ideal situation of perfectly periodic, noise-free output. For a range of source temperatures, the detectors lock onto nearly periodic modes of pulsing. Fig. 5 shows return maps which also indicate the nearly periodic behavior and display the fluctuations. From Fig. 5, it can be seen that the 107K data is more nearly periodic than the 102K data. Similar mode locking regions are observable as a function of bias voltage.

Based on the variations observed for a 5K IR source, and using an eigenvalue analysis on the periodic IPTI data sets, resulting in a weighted averaging technique, Coon and Perera calculated(17) a minimum resolvable temperature of 0.01K. The corresponding unweighted averaging resulted in a value of 0.03K for the same data sets. This technique shows the application of nonlinear dynamic techniques to improve detector performance.

Due to the high amplitude of the pulse, this IR detector can be used without any preamplifier; However, it has its disadvantages too. The low operating temperature is the main concern. With deeper impurity levels, the operating temperature could be increased. However, a better solution will be to implement this idea in multi-quantum well (MQW) structures. A necessary condition for pulsing, the s-type negative differential conductivity, has been observed in GaAs/AlGaAs MQW structures at room temperatures.(19)

PULSING IN MQW STRUCTURES

The single-quantum well structure studied for pulsing is δ doped with silicon between highly doped contact regions driven by a constant current as seen in Fig. 6. As charge builds up in the input capacitor, electrons are injected into the device at the load end. These electrons interact with the electrons in the well causing ionization in the well. This leads to an increase in the electric field at the injection contact causing an increased current that leads to a pulse. This discharges the input capacitor and charges the output capacitor. When this occurs the field at the input end of the device changes sign causing electrons to be trapped and neutralizing the charge in the well. The load capacitor then discharges through the load resistance, resetting the system for the next pulse. We have assumed w = 500 Å GaAs well and 697 meV high (ΔE) AlAs barrier of b = 1000 Å, unless noted otherwise, throughout our modeling exercise. The doping concentration in the well is 3.75×10^{12} cm^{-2} and the contacts will be doped to 1×10^{19} cm^{-3}. The circuit parameters will be input capacitance $C = 80$ pF, load capacitance $C_L = 100$ pF and and load resistance $R_L = 3$ MΩ.

The calculations done include four parts,(20) which will then be combined to obtain the output pulse. They include 1) The fields at the emitter and collector for a given bias and charge in the well 2) the injected current as a function of the field at the emitter 3) the impact ionization rate for electrons in the well and 4) the tunneling current for electrons out of the well. The fields at the emitter and collector are given by

$$F_e = \frac{V_i - V_L}{2b + w} + \frac{\sigma}{2\epsilon} \qquad [9]$$

$$F_c = \frac{V_i - V_L}{2b + w} - \frac{\sigma}{2\epsilon} \qquad [10]$$

respectively, where V_i and V_L are the input and load voltages, b is the barrier width, w is the well width, σ is the surface charge density in the well and ϵ is the permittivity of the well.

The injection current density $j_{(inj)}$ is calculated from the following equation

$$j_{(inj)} = q\int_0^{\infty} n_e(E_x)T(E_x, F_e)dE_x \qquad [11]$$

where q is the electron charge, n_e is the number of electrons per unit area per unit energy per unit time incident on the barrier with energy E_x and $T(E_x, F_e)$ is the transmission probability for the incident electrons with energy E_x and electric field F_e. We have followed Gundlach(21) for $T(E_x, F_e)$. The incident electron distribution is simply the standard Fermi distribution integrated over the directions parallel to the plane of the well giving $n_e = \frac{4\pi mkT}{h^3}\ln(1+e^{E_x/kT})$.

The tunneling current (Eq. 12) is calculated using the same procedure except that the electron distribution is replaced by the corresponding distribution in the well $n_w = \frac{4\pi mkT}{h^2 w}\sqrt{\frac{E_i}{2m}}\ln(1+e^{(E_i-E_F)/kT})$ where E_F is the Fermi energy in the well and w is the well width. Because the energy levels are now discrete the integral is replaced by the sum

$$j_{(tun)} = q\sum_{i=0}^{N} n_w(E_i)T(E_i, F_c) \qquad [12]$$

where there are $N+1$ levels in the well.

The impact ionization current was calculated using the method of Chuang and Hess(22) with tunneling of the excited electrons included. This involves integrating the probability of both electrons escaping after a collision of a hot electron with a cold electron in the well over the distribution of electrons. When this was done it was found that the effects of impact ionization are negligible when compared to the tunneling component, so we omit them for the rest of the calculation.

The input (C) and load (C_L) capacitors obey the following relationships

$$\frac{dV_i}{dt} = \frac{I - jA}{C} \qquad [13]$$

$$\frac{dV_L}{dt} = \frac{jA}{C_L} - \frac{V_L}{R_L C_L} \qquad [14]$$

where I is the driving current, A is the device area, C and C_L are the input and load capacitors and R_L is the load resistor. The final equation needed is the rate of generation of space charge in the well. This is just

$$\frac{d\sigma}{dt} = j_{(tun)}, \quad F_c > 0 \qquad [15]$$

$$= -j_{(inj)}, \quad F_c < 0 \qquad [16]$$

This system of equations can be integrated numerically with V_L being the output signal that would be measured experimentally. For the parameters given, a pulse is produced as seen in Fig. 7 at 300 K. Also calculated was the fraction of the electrons that have escaped from the well. At 300 K this also shows a maximum indicating that the pulse is being driven by the space charge. At 280 K the space charge increases to a maximum at the pulse but there is no recombination indicating that the transient associated with the input capacitor charging is now becoming important although space charge is also contributing. At 260 K this is now reaching a steady state after the pulse indicating that the space charge is not generating the pulse in this case but rather the transient associated with charging the input capacitor.

IR DETECTION WITH PULSING QUANTUM WELL STRUCTURES

This spontaneous pulsing in quantum well structures can be used for IR detection when operated at a reduced temperature. The rate of generation of space charge is sensitive to the population distribution of electrons in the well. Reducing the temperature reduces the population in the higher energy levels that contribute to the tunneling, leading to reduced space charge generation rates. This precludes pulsing until IR radiation is present which increases the ionization rate, either by direct photoionization or by photoexcitation and subsequent tunneling, back to that at the spontaneous pulse operating temperature (300K). Thus pulsing occurs only when IR radiation is incident on the structure. We will show results demonstrating the emergence of a pulse at 260 K due to the incident radiation(see Fig. 7) Adjusting the device parameters will lead to wavelength tunable IR detectors operating at elevated temperatures.

The effects of photoionization on pulsing were introduced by including a term in the space charge generation rate that was independent of the field. This term is equal to the quantum efficiency (η) of the well times the rate at which photons are incident on the device. Initially this rate was varied to determine its effects on the pulsing behavior and to determine the threshold for effects to occur. For low photoionization rates ($\leq$ 10% of the electrons/sec) there was minimal effect on the pulsing. Above this limit two effects were observed. First for systems that showed pulsing, the time to pulse could be decreased slightly, or if the photoioization rate was increased still further, the pulse could be prevented. This is seen in fig. 7(a) in which the pulse is initially accelerated and then as seen for the dashed line it is blocked. Secondly, for the case in which the structure was close to pulsing but was not quite pulsing the introduction of photoionization could trigger a pulse. Here the pulse is a true pulse with space charge neutralization occurring after the peak is reached.

This indicates that the photoionization by IR radiation can produce a detectable effect on the pulsing structure. The next step is to connect the abstract ionization rate used in the model to the device structure. This is done by determining η of the structure and the rate of incident photons. The η is given by

$$\eta = 1 - e^{-\alpha L} \qquad [17]$$

where α is the absorption coefficient for the structure and L is the thickness of the structure. The absorption was determined from the dipole approximation. Line broadening is introduced by assuming a Lorentzian probability distribution for the transitions

$$f(E, E_{ij}) = \frac{1}{\pi} \frac{\Gamma}{(E - E_{ij})^2 + \Gamma^2} \qquad [18]$$

where Γ is the line halfwidth and E_{ij} is the energy difference between the i-th and j-th states. Because the escape probability for the states below the uppermost excited state are significantly reduced the absorption can be calculated using only those transitions to this state j. The absorption is then given by

$$\alpha = \left(\frac{\pi e^2 \hbar^3}{2 m_e^2 c \epsilon_0 E}\right) \sum_{i<j} n_i |T_{ij}|^2 f(E, E_{ij}) \qquad [19]$$

where m_e = free electron mass, ϵ_0 = permittivity of the vacuum and n_i = number of electrons in the i-th energy level. The photoexcitation matrix element is given by

$$|T_{ij}| = |\int_{-\infty}^{\infty} \frac{m_e}{m^*(z)\sqrt{n(z)}} u_j^*(z) \frac{\partial U_i(z)}{\partial z} dz|. \qquad [20]$$

In the above calculation a number of effects have been ignored. In particular, the energy levels have been calculated using the single isolated quantum well model. This ignores any exchange effects or distortion of the well by the applied field.

The calculated peak absorptions are very low, leading to quantum efficiencies on the order of 10^{-13}. This is due in large part to the large difference in energies in the transition which is from the second excited state to the 17th excited state for the peak absorption. This reduces the absorption in two ways, the matrix element is reduced by the large wavelength difference for the wavefunctions and the $1/E$ term also causes the absorption to be reduced. The efficiency can be improved by optimizing the device for absorption. Plots of peak absorption and energy versus well width and barrier height are shown in Fig. 8. From these we can see that reducing the barrier height increases the absorption. By adjusting the conditions to produce pulsing at the lowest possible barrier height it should be possible to improve the quantum efficiency of these structures. Adding additional wells to the structure may also improve the efficiency. The extra path length for photoionization may lead to an increased efficiency provided the electrons are not trapped in some later well.

CONCLUSION

In conclusion, we have experimentally shown that IR detection without any preamplifiers is possible by utilizing spontaneous pulsing frequency in silicon homojunction structures. Non linear dynamics tools have improved the sensitivity of the detectors. Our modeling exercises show that spontaneous pulsing can be obtained in quantum well structures and this could be used to increase the low operating temperatures of the previous spontaneous pulsing detectors. Although our calculated efficiencies are low, selecting different parameters can give rise to much better performance as shown in Fig. 8. Further modeling studies and experimental confirmation will be needed for the improvement of this type of IR detector.

ACKNOWLEDGMENT

The work is supported in part by the US NSF under grant # 94-12248.

REFERENCES

1. A. G. U. Perera, Physics and Novel Device Applications of Semiconductor Homo Junctions , Academic Press **The Physics of Thin Films, Vol 21** in Press.
2. M. D. Petroff, M. G. Stapelbroek and W. A. Kleinhans, Appl. Phys. Lett. **51**, 406 (1987).
3. D. D. Coon, S. D. Gunapala, R. P. G. Karunasiri and H.-M. Muehlhoff, Solid State Commun. **53**, 1144 (1985).
4. T. L. Lin and J. Maserjian, Appl. Phys. Lett. **57**, 1422 (1990).
5. H. C. Liu, J.-P. Noel, Lujian Li, M. Buchanan, and J. G. Simmons, Appl. Phys. Lett. **60**, 3298 (1992).
6. B. F. Levine, J. Appl. Phys. **74**, R1 (1993).
7. A. G. U. Perera and S. Matsik, Appl. Phys. Lett. **64**, 878 (1994).
8. N. F. Mott, *Metal-Insulator Transitions*, Barnes and Noble, New York, 1974.
9. A. G. Milnes, *Deep Impurities in Semiconductors*, John Wiley & sons, N. Y, 1973, page 379.
10. Y. N. Yang, D. D. Coon and P. F. Shepard, Appl. Phys. Lett. **45**, 752 (1984).
11. D. D. Coon and A. G. U. Perera, Neural Networks **2**, 143 (1989).
12. A. G. U. Perera and S. G. Matsik, Physica D **84**, 615 (1995).
13. J. Maselko and H. L. Swinney, Phys. Scr. **T9**, 35 (1985).
14. D. D. Coon, S. N. Ma and A. G. U. Perera, Phys. Rev. Lett. **58**, 1139 (1987).
15. D. D. Coon and R. P. G. Karunasiri, Solid State Electronics **26**, 1151 (1983).
16. D. D. Coon and A. G. U. Perera, Appl. Phys. Lett. **51**, 1711 (1987).
17. D. D. Coon and A. G. U. Perera, Appl. Phys. Lett. **51**, 1086 (1987).
18. R. M. May, Nature **216**, 459 (1976).
19. Zh. I. Alferov, O. A. Mexrin, M. A. Sinitsyn, S. I. Troshkov and B. S. Yavich, Sov. Phys. Semicond. **21**, 304 (1987).
20. A. G. U. Perera and S. G. Matsik, Appl. Phys. Lett **67**, 962 (1995).
21. K. H. Gundlach, Solid-State Electronics **9**, 949 (1966).
22. S. L. Chuang and K. Hess, J. Appl. Phys. **61**, 1510 (1987).

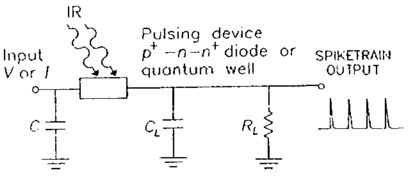

Figure 1: Circuit diagram showing a dc forward biased p^+-n-n^+ diode and the pulse output. The load impedance consists of R_L = 50 kΩ and C_L = 200 pF. This simple circuit eliminates the need for a preamplifier and it performs IR intensity-to-frequency conversion.

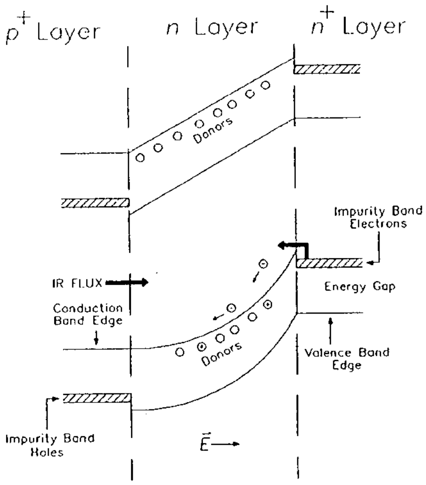

Figure 2: Band diagram of a forward biased p^+-n-n^+ diode at low temperatures. Top: before any accumulation of space charge. Bottom: after accumulation of space charge. Carriers remain trapped in n-region phosphorus impurities until photoionization or impact ionization occur. Excited carriers are swept out by the electric field leaving an ionized atom creating a space charge. Fermi levels in the p^+ and n^+-layers are offset from the valence and conduction-band edges due to the formation of impurity bands. The band bending (due to space charge) at the interface is stronger at the interface due to the high concentration of ionized donors.

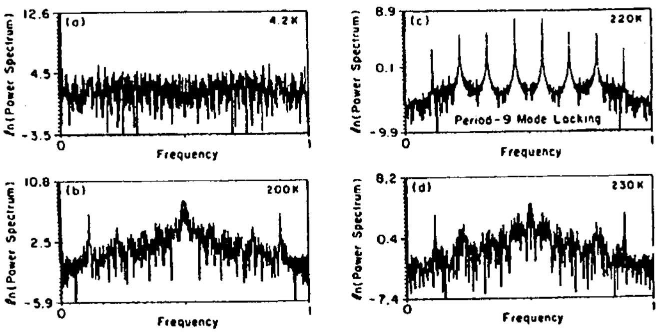

Figure 3: Power spectra obtained from 1024 measured interpulse time intervals at 9.138V bias for different blackbody source temperatures: a) 4.2K b) 200K c) 220K d) 230K. The vertical axis has a logarithmic scale. The frequency variable on the horizontal axis is the inverse of the time series periodicity.(17)

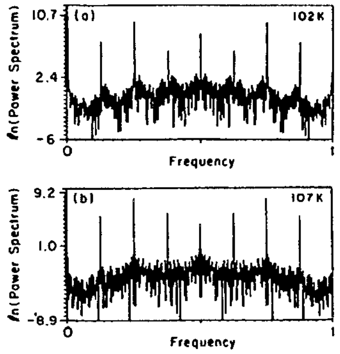

Figure 4: Power spectra obtained from 1024 interpulse time intervals at 8.886V for two different blackbody temperatures. a) 102K b) 107K.(17)

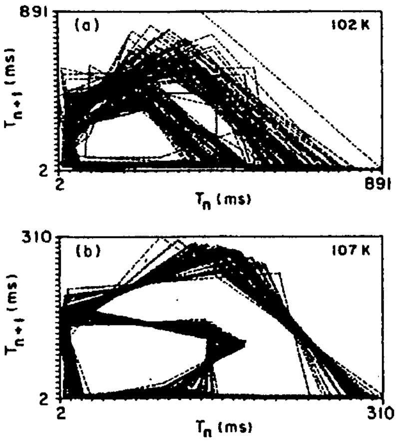

Figure 5: Return maps for 500 measured interpulse time intervals at a) 102K b)107K for constant bias voltage , for the data shown in Fig. 4. Even though the 2 power spectra are similar the return maps indicate a better resolution for the mode-locking phenomena.(17)

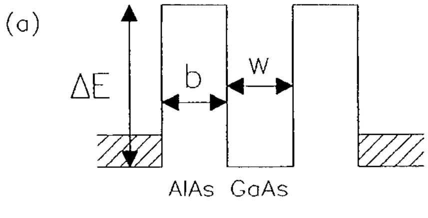

Figure 6: The quantum well structure used in the model. The corresponding parameter values, well width w = 500 Å, barrier width b = 1000 Å, and barrier height ΔE = 697 meV are also shown.

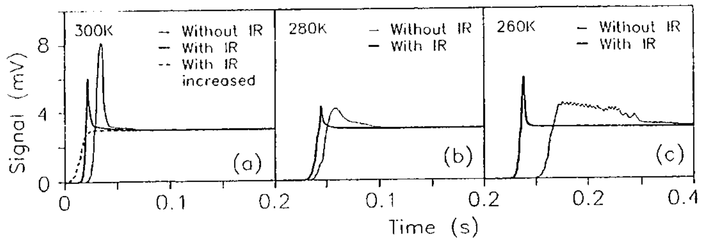

Figure 7: The calculated output signal without IR radiation (normal line) and with IR radiation (heavy line) for (a) 300K, (b) 280K and (c) 260K. The dashed curve at 300K shows the suppression of the pulse when the radiation is increased by a factor of 10.

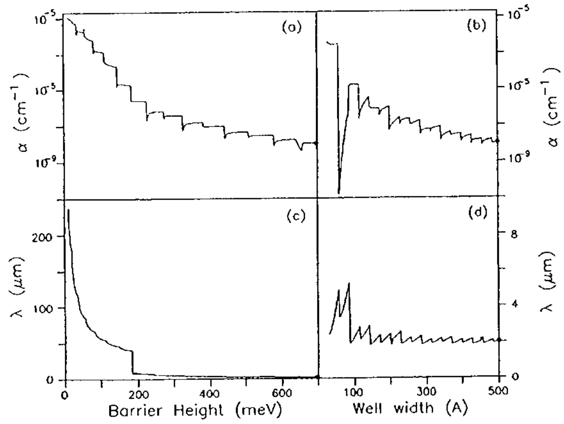

Figure 8: The absorption coefficient (a), (c) and the peak transition wavelength (b), (d) for a single well structure plotted vs barrier height and well width respectively. The observed rapid drops are related to the changes in the number of energy levels present in the well. The absorption is improved by reducing the barrier height to a minimum consistent with pulsing. The parameters corresponding to our structure in the modeling effort is indicated by the dark point marked in all four figures.

BACKGROUND LIMITED PERFORMANCE IN P-DOPED GAAS / GA$_{0.71}$IN$_{0.29}$AS$_{0.39}$P$_{0.61}$ QUANTUM WELL INFRARED PHOTODETECTORS

J. Hoff, C. Jelen, S. Slivken, M. Erdtmann, G.J. Brown*,
E. Bigan, and M. Razeghi

Center for Quantum Devices,
Department of Electrical Engineering and Computer Science,
Northwestern University, Evanston, Illinois 60208

*Wright Laboratory, Materials Directorate, .
WL/MLPO, Wright Patterson AFB, Ohio 45433-7707

Background limited infrared photodetection has been achieved up to sample temperatures of 100 K with p-type GaAs/Ga$_{0.71}$In$_{0.29}$As$_{0.39}$P$_{0.61}$ quantum well intersubband photodetectors grown by low-pressure metalorganic chemical vapor deposition. Normal incidence photoresponse covers a wavelength range of 2.5 μm to 7 μm. An asymmetric quantum well profile caused by zinc dopant distribution is evidenced by a photovoltaic effect, a non-linear responsivity versus bias, and an asymmetric dark current versus bias. The cut-off wavelength also increases with bias due to tunelling.

INTRODUCTION

There has been considerable effort directed towards the development of Long Wavelength Infrared (LWIR) photodetectors from multi-quantum well epitaxial structures (1). These quantum well intersubband photodetectors (QWIPs) offer numerous potential benefits since they can be engineered from robust III-V semiconductor materials to detect in wavelength ranges traditionally visible only to narrow bandgap II-VI materials. Most of the effort directed towards QWIPs thus far has been placed on n-type GaAs/Al$_x$Ga$_{1-x}$As heterostructures and the results have been good. Nevertheless, it is possible that improvements to QWIP devices can be made through changes in two areas. First, polarization dependent quantum mechanical selection rules make normal incident detection inefficient in n-type QWIPs without external coupling systems regardless of the material system in which the QWIPs are grown. Second, Al$_x$Ga$_{1-x}$As has material problems which limit its effectiveness as a barrier. While highly successful QWIPs have been demonstrated using GaAs/Al$_x$Ga$_{1-x}$As quantum wells, performance improvements may be possible through changes in doping flavor and material system.

To research QWIP alternatives, our efforts have been directed towards p-type In$_x$Ga$_{1-x}$As$_y$P$_{1-y}$ compounds. p-type QWIPs inherently photorespond to normally incident light due to valence band anisotropy and the admixture of the spherically symmetric conduction band into the quantum well states away from zone center (2,3) The Aluminum-free compounds should provide improvements in electrical properties as well as ease of fabrication (4).

Recent studies have demonstrated normal incidence detection in p-type GaAs/$Ga_{0.49}In_{0.51}P$ QWIPs (5). However, cutoff wavelengths were short due to the large valence band discontinuity (~360 meV). It was shown that 8-12 μm detection could be achieved only with very narrow quantum wells. In order to achieve LWIR detection with wider wells and therefore improved manufacturability, the barrier height must be lowered. Furthermore, Liu *et al* demonstrated that there is an optimal position for the resonant state in bound-to-continuum absorption implying that for a particular cutoff wavelength, there is an optimal well width-barrier height combination (6). This point was also demonstrated for p-type GaAs/$Al_{0.3}Ga_{0.7}As$ by Szmulowicz and Brown (2). Therefore, to achieve 8-12 μm photodetection, it is necessary to introduce the appropriate quaternary material into the superlattice to reduce the barrier height and then to optimize the well width for best performance.

The first step in this optimization is simply to introduce any quaternary material into the barrier. Once its effect has been determined then predictions can be made concerning the barrier height and composition of the appropriate quaternary barrier material for LWIR detection. In this paper, we report the realization of this first step towards longer cutoff wavelength. An aluminum-free GaAs/$Ga_{0.71}In_{0.29}As_{0.39}P_{0.61}$ superlattice was grown by low pressure metalorganic chemical vapor deposition (LP-MOCVD). The resultant device was background limited up to sample temperatures of 100K. In this paper we report on the characterization of this device.

AL$_X$GA$_{1-X}$AS VERSUS GA$_{1-X}$IN$_X$AS$_Y$P$_{1-Y}$

The $Al_xGa_{1-x}As$ system has been a material system of choice for optoelectronic design for many years. An alloy of GaAs (Eg=1.42 eV;a=5.653 Å) and AlAs (Eg≈3.0 eV; a=5.66 Å), $Al_xGa_{1-x}As$ remains lattice matched to GaAs substrates over a wide range of bandgaps eliminating the concern over lattice mismatch. However, there are some aspects of $Al_xGa_{1-x}As$ that are less than desirable. First, $Al_xGa_{1-x}As$ has a high reactivity with oxygen (4,7) mainly due to the presence of Aluminum in the alloy. This oxidation results in processing and reliability problems and requires the extra processing steps necessary to passivate devices. Aluminum oxidation also restricts fabrication methods, such as epitaxial regrowth. Elevated deposition temperatures must be used to get device-quality material, resulting in undesirable dopant diffusion. Furthermore, the electrical properties of $Al_xGa_{1-x}As$ are affected by oxygen-related defects (4,7,8). Therefore, while $Al_xGa_{1-x}As$ may be capable of producing optoelectronic quality devices, it is not the perfect material system.

$Ga_{1-x}In_xAs_yP_{1-y}$ on the other hand is far superior. $Ga_{1-x}In_xAs_yP_{1-y}$ lattice matched to GaAs covers the same bandgap range as direct bandgap $Al_xGa_{1-x}As$ (1.42 eV to 1.92 eV), and device quality material can be deposited at a lower temperature, reducing undesirable dopant diffusion. Extremely high electron mobilities have been demonstrated in two-dimensional GaAs-$Ga_{0.51}In_{0.49}P$ heterostructures (9). Dislocation and impurity motion is much lower than in $Al_xGa_{1-x}As$ because of the large difference in atomic size between Indium and Gallium. This facilitates growth on silicon substrates and future monolithic optoelectronic integration. Surface and interface recombination velocities are lower than for AlGaAs, translating into improved device performance (10). Finally, and of great importance to QWIPs, high-field transport properties of $Ga_{1-x}In_xP$ are much improved over those of $Al_xGa_{1-x}As$ for $x \geq 0.3$ (the most widely used $Al_xGa_{1-x}As$ mole fraction) (7). Therefore, $Ga_{1-x}In_xAs_yP_{1-y}$ appears to be a good candidate to improve apon the work already done with $Al_xGa_{1-x}As$ QWIPs.

THE MATERIAL IN THIS STUDY

The sample was grown by low-pressure metalorganic chemical vapor deposition (LP-MOCVD), and the growth conditions have been detailed elsewhere (11). The superlattice consists of fifty 30 Å wide GaAs quantum wells separated by 280 Å wide $Ga_{0.71}In_{0.29}As_{0.39}P_{0.61}$ barriers ($Eg \approx 1.83$ eV @77K). The superlattice was sandwiched between thick GaAs layers for top (0.5 µm) and bottom (1.0 µm) contacts. X-ray diffraction and photoluminescence measurements confirmed the nominal thicknesses (see Figure 1). The bandgap of the barrier was also confirmed by photoluminescence measurement. The large number of superlattice sattelite peaks and the symmetry of the X-ray scan shown in Figure 1 indicate the lack of strained interfacial layers in the superlattice (12).

All the GaAs layers (wells and contacts) were doped with Zinc to a net acceptor concentration of 3×10^{18} cm^{-3}. The barriers were left undoped. No dopant-free spacers at the interfaces of the wells were used in this growth.

The sample was processed into 400 µm x 400 µm mesa structures using standard photolithographic techniques and selective wet chemical etching. Finally, 100 µm x 100 µm Ti/Pt/Au contacts were formed by electron beam evaporation and lift-off.

DEVICE CHARACTERIZATION

Photoresponse

Photoresponse spectra were measured at 77K for various biases using a Fourier Transform Infrared spectrometer. Measurements were taken across a 40kΩ load resistor which is negligible compared to the QWIP differential impedance (> 1GΩ) and the capacitive impedances of cables. Results are shown in Figure 2a for +9 V, 0 V, and -9 V.

Clearly, a photovoltaic effect is observed since there is responsivity at zero bias. Furthermore, the cut-off wavelength is a function of bias and that function is not symmetric with respect to zero bias for moderate voltages (-15V to +15V). As can be seen in Figure 2b, near equivalent cutoff wavelengths for equal and opposite biases is restored by ±18V.

Blackbody Responsivity

Blackbody responsivity was measured as a function of bias using a chopped 800K blackbody radiation source and conventional lock-in detection techniques. The results are shown in Figure 3. Here again the signal was measured across a 40kΩ load resistor. Photoresponse goes to zero for approximately 1.5 V, consistent with the observation of a photovoltaic effect. For negative biases between 0 V and -10 V, responsivity increases at a lower rate than for positive biases. For larger negative biases, the responsivity increases rapidly and reaches a similar magnitude for +18 V or -18 V.

Dark Current

Dark current was measured with the detector mounted in a cryostat surrounded by a copper cold shield maintained at the same temperature as the detector itself. Figure 4a shows the shielded dark current versus bias for temperatures from 77K to 300K. Once again, the photovoltaic effect is observed in the low temperature curves in which the current minima do not occur at zero bias. This effect decreases with increasing temperature. Note also that the dark current curves are asymmetric with respect to zero bias.

Arrhenius plots of the dark current versus inverse temperature are shown in Figure 4b. The slopes of these plots are indicative of thermionic activation energy and, by the direct relationship between thermionic activation energy and photonic cut-off energy, they are also indicative of the cut-off wavelength of the QWIP. There is a close relationship between the activation energy for a particular bias and the cut-off wavelength of the QWIP at that bias.

AN ASYMMETRIC WELL PROFILE

The GaAs/$Ga_{0.71}In_{0.29}As_{0.39}P_{0.61}$ QWIP demonstrates several features not present in the theoretically ideal QWIP. First, it has a photovoltaic effect. Second, it has a non-linear responsivity versus bias curve. Third, it has an asymmetric dark current versus bias curve. All three phenomena can be considered related through an asymmetric quantum well potential profile such as shown in Figure 5 (8,13).

The lower rate of increase in responsivity with negative biases (Figure 3) indicates a larger photo-excited carrier capture probability, which results from the asymmetry in the quantum well profile. At higher biases, this asymmetry no longer plays a significant role because the photo-excited carriers gain enough energy from the electric field so that they are less sensitive to the actual well potential profile.

Tunnelling through the triangular tip of a barrier under bias is expected. Therefore, an increase in cut-off wavelength with bias is also expected. However, in the theoretically ideal QWIP, the barrier is identical at either interface. Therefore equal but opposite biases should give the same cutoff wavelength. However, note from Figure 5 b and c the barrier height seen by a charge carrier is different for positive and negative biases in an asymmetric well. Therefore, the cut-off wavelength for equal and opposite biases will not be the same. As is the case with blackbody responsivity, though, at high biases, the photo-exicted carriers gain enough energy from the electric field so that they are less sensitive to the potential profile and the equality of cut-off wavelengths for equal and opposite biases is restored.

An asymmetric well profile can occur in one of two ways. First, to the MOCVD, the $Ga_{1-x}In_xAs_yP_{1-y}$-GaAs (lower) interface is different than the GaAs-$Ga_{1-x}In_xAs_yP_{1-y}$ (upper) interface. Therefore, if the growth is imperfect, it is possible that interfacial layers can occur. However, in the $Ga_{1-x}In_xAs_yP_{1-y}$ system such interfacial layers would be lattice mismatched and strained and such layers would effect the X-ray scan in Figure 1. This is not the case. Figure 1 reveals little strain.

A more reasonable explaination of the asymmetric well profile comes from the zinc memory effect in MOCVDs. It is likely, since no dopant-free spacers were used in the wells of this growth, that there are no dopants across the lower interface, but that there are dopants across the upper interface. Holes in the barrier would travel into the well leaving a potential spike at the upper interface. Such a potential spike would not effect the X-ray scan.

BACKGROUND LIMITED PERFORMANCE

Similar to the GaAs/$Ga_{0.51}In_{0.49}P$ QWIPs in Reference 5, this device was background limited. To demonstrate this, the device current was measured with the detector mounted in a stainless steel cryostat with a ZnSe window. This window provided a 60° field of view through which 300 K background radiation was incident on the device. There was additional radiation from the walls of the cryostat which were also at 300 K. The results of this unshielded measurement as well as the previous shielded dark current measurements are shown in Figure 6. At 77 K, the photodetector is clearly background-limited as the unshielded, 300 K background photocurrent exceeds the dark current by about two orders of magnitude. The device remains background-limited up to a detector temperature of 100 K for biases between -7.5 V and +2.5 V. To the best of our knowledge, there has been only one other report of BLIP operation in QWIPs at such high temperature (14). The 77 K unshielded I(V) curve reaches its minimum at around +0.2 V. This is a result of the photovoltaic response of the device. This is confirmed by increasing the level of infrared illumination using a blackbody source. At higher illumination, the I(V) curve moves up and reaches a minimum at a voltage that approaches +1.5 V asymptotically.

Combining the measured blackbody responsivity and the photoresponse spectra with Planck's law for spectral exitance, we computed the expected photocurrent in the presence of 300K background radiation (15). The computed photocurrents for a 180° field of view are 130pA, 126pA, and 403pA for biases of -6 V, -3 V and 6 V, respectively. These values compare favorably with the measured unshielded I(V) curve given in Figure 6, and further confirm that this detector is background limited.

CONCLUSION

In conclusion, we have demonstrated a p-type GaAs-$Ga_{0.71}In_{0.29}As_{0.39}P_{0.61}$ Quantum Well Intersubband Photodetector operating under normal incidence with background limited performance up to 100K operating from 2.5 μm up to 7.0 μm. The detector demonstrates all the characteristics of a QWIP with an asymmetric quantum well potential profile including a photovoltaic effect and asymmetric dark current and responsivity versus bias curves.

ACKNOWLEDGMENTS

The work at Northwestern University was supported by Air Force Contract No. F33615-93-C5382 through Kopin Corporation. The authors would like to acknowledge Dr. Gerald L. Witt from the US Air Force Office of Scientific Research (AFOSR) for his encouragement.

REFERENCES

1. B. F. Levine, J. Appl. Phys. **50**, R1 (1993)
2. F. Szmulowicz and G. Brown, Appl. Phys. Lett., **66**, 1659 (1995)
3. Yia-Chung Chang and R.B. James, Phys. Rev. B **39**, 12672 (1989)
4. Manijeh Razeghi, Nature **369**, 631 (1994)
5. J. Hoff, X. He, M.Erdtmann, G. Brown, E. Bigan, M. Razeghi, J. Appl. Phys **78**, 2126 (1995)
6. H.C. Liu, J. Appl. Phys **73**, 3062 (1993)
7. C. Besikci and M. Razeghi, IEEE Trans. Elec. Dev., **41**, 1066 (1994)
8. K.L. Tsai, C. P. Lee, K. H. Chang, D. C. Liu, H. R. Chen, and J. S. Tsang, Appl. Phys. Lett., **64**, 2436 (1994)
9. M. Razeghi, M. Defour, F. Omnes, M. Dobers, J.P. Vieren, and Y. Guldner, Appl. Phys. Lett., **55**, 278 (1989)
10. M. Fukuda, J. Appl. Phys. **59**, 4172 (1986)
11. F. Omnes and M. Razeghi, Appl. Phys. Lett. 59, 1034 (1991)
12. X. G. He, M. Erdtmann, R. Williams, S. Kim, and M. Razeghi, Appl. Phys. Let. **65**, 2812 (1994)
13. H. Schneider, K. Kheng, M. Ramsteiner, J.D. Ralston, F. Fuchs, and P. Koidl, Appl. Phys. Lett, **60**, 1471 (1992)
14. Y.H. Wang, Sheng S. Li, J. Chu, and Pin Ho, Appl. Phys. Lett. 64, 727 (1994).

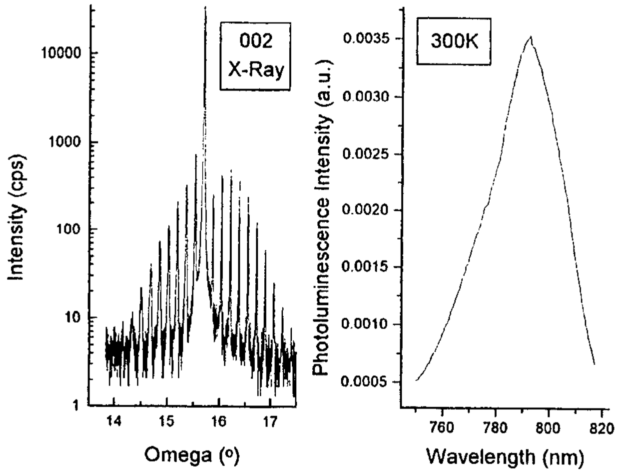

Figure 1: a) 002 X-ray scan for the GaAs/GaInAsP superlattice. The symmetry of the scan reveals a lack of strain at the interfacial layers. b) The peak position and the narrowness of the photoluminescence spectra reveal the quality of the growth.

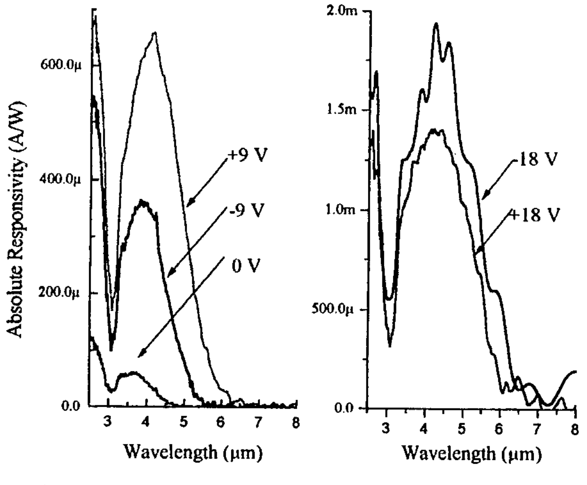

Figure 2: a)Absolute responsivity versus wavelength for different biases across the GaAs/GaInAsP QWIP. b) Absolute responsivity versus wavelength for +18 and -18 V bias. The cutoff wavelength for each are now approximately the same.

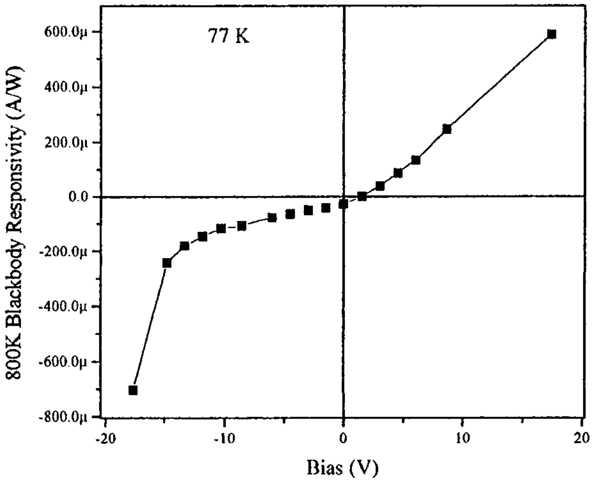

Figure 3: Absolute Blackbody responsivity versus bias. Responsivity goes to zero for approximately 1.5V in keeping with the photovoltaic effect.

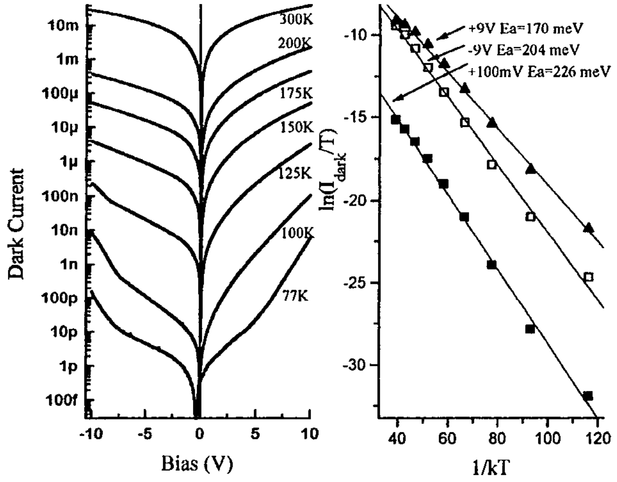

Figure 4: a)Dark current versus bias for temperatures between 77K and 300K b) Arrhenius plots versus inverse temperature for different biases

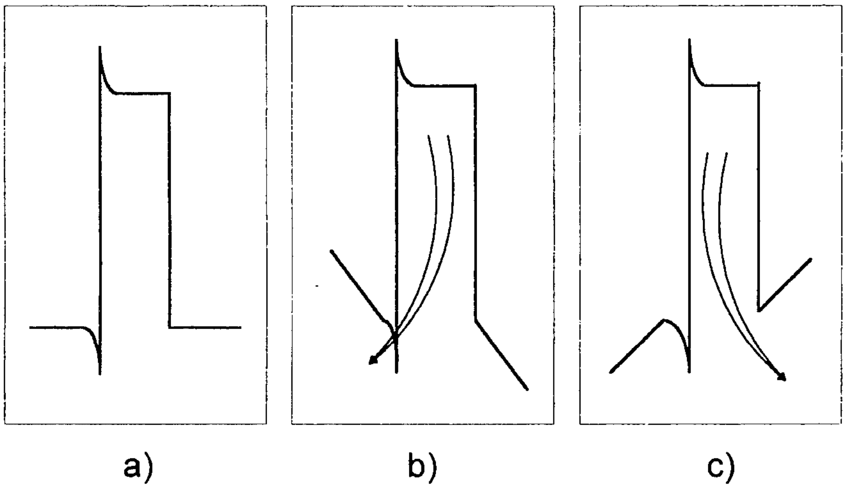

Figure 5: An asymmetric quantum well potential profile under a) zero bias b) forward bias and c) reverse bias.

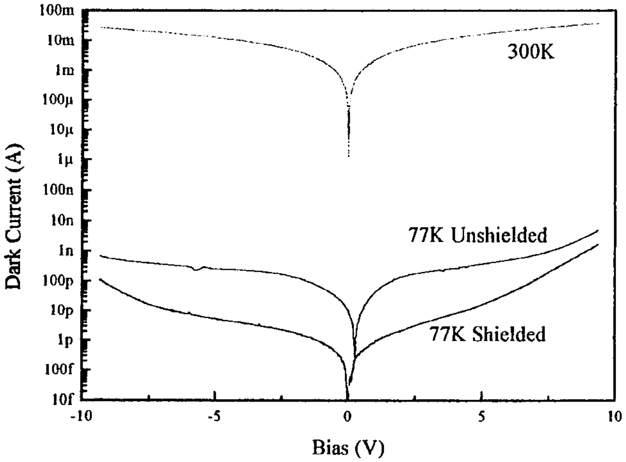

Figure 6: A simple demonstration of background limited performance. The device current increases by approximately 2 orders of magnitude between the shielded and unshielded configurations at a samples temperature of 77K.

CHARACTERIZATION OF A P-DOPED GaAs/$Ga_{0.51}In_{0.49}P$ QUANTUM WELL INTERSUBBAND PHOTODETECTOR

J. Hoff, S. Kim, M. Erdtmann, R. Williams, J. Piotrowski, E. Bigan, and M. Razeghi
Center for Quantum Devices, Department of Electrical Engineering and Computer Science,
Northwestern University, Evanston, Illinois 60208
G. J. Brown
Wright Laboratory, Materials Directorate, WL/MLPO, Wright Patterson AFB, Ohio 45433-7707

A p-doped GaAs/$Ga_{0.51}In_{0.49}P$ quantum well intersubband photodetector was grown by low-pressure metalorganic chemical vapor deposition. The device operates at normal incidence with background-limited performance up to 120 K in the 2 to 5 µm wavelength range. At low bias, the dark current increases exponentially with temperature, and the corresponding activation energies are in good agreement with photoresponse cut-off wavelengths. The blackbody responsivity increases linearly with bias. At high bias, the dark current exhibits a weaker temperature dependence and oscillations are observed in the differential dark conductivity as well as the blackbody responsivity versus bias. We tentatively explain this oscillatory behavior by the formation of a high field domain induced by tunneling and interband avalanche.

INTRODUCTION

Quantum Well Intersubband Photodetectors (QWIPs) are long-wavelength devices based on robust, mature, and uniform III-V semiconductors. Most of the previous work has focused on n-doped GaAs/GaAlAs quantum wells. Only limited work has been done using p-doping which presents the advantage of normal incidence absorption, or using different material systems which present better electrical characteristics and/or metallurgical properties (1). $Ga_{0.51}In_{0.49}P$ is immune to defects induced by the presence of aluminum in GaAlAs (2). In this work, we present the dark current and photoresponse characteristics of a p-doped GaAs/$Ga_{0.51}In_{0.49}P$ QWIP grown by low-pressure metalorganic chemical vapor deposition. This normal incidence detector operates at wavelengths below 5 µm and is background-limited up to a temperature of 120 K. An oscillatory behavior is observed in both the blackbody photoresponse and the differential dark conductance versus bias. We tentatively explain these oscillations by the formation of a high field domain induced by interband avalanche multiplication.

EXPERIMENTAL METHODS AND RESULTS

Device Fabrication

The sample was grown by low-pressure metalorganic chemical vapor deposition (MOCVD). The superlattice consists in 50 periods of 20 Å wide GaAs quantum wells separated by 260 Å wide $Ga_{0.51}In_{0.49}P$ barriers. It is sandwiched between thick GaAs layers for top (0.5 µm) and bottom (1.0 µm) contacts. All GaAs layers are doped with Zinc to a net acceptor concentration of 3 x 10^{18} cm^{-3}. The barriers are left undoped. The sample was processed into 400 µm x 400 µm mesa structures using standard photolithographic techniques and wet chemical etching. Finally, 150 µm x 150 µm Ti/Pt/Au contacts were formed by electron beam evaporation and lift-off. Cleaved chips were indium-bonded to copper heat sinks and front illuminated under normal incidence.

Photoresponse spectra

Photoresponse spectra were measured at 77 K for various biases using a Fourier Transform Infrared (FTIR) spectrometer and are shown in Figure 1. The spectra peak outside the experimental wavelength range because of the large valence band discontinuity, but the long wavelength cut-off is clearly visible. This cut-off increases from 3.5 µm at -3 V (mesa top negative) up to 5.5 µm for biases larger than -15 V. Comparable photoresponse spectra are obtained for positive biases and are not shown here for clarity. A small photovoltaic effect was also observed. Beyond 15 V, the photoresponse spectrum shape and magnitude remains unchanged but the noise increases sharply, as can be seen on the -18 V spectrum. The increase in cut-off wavelength is typical of QWIPs, and results from a reduction of the effective barrier height for carriers escaping the quantum wells.

Dark current

Dark current was measured as a function of bias for different temperatures, cold-shielded from 300 K background radiation. For comparison, the unshielded detector current was also measured. Results (Figure 2) show that the detector is background-limited up to a detector temperature of 120 K. For biases below around 10 V, the dark current increases exponentially with temperature. At the lowest temperatures, the minimum in shielded current does not occur at zero bias. We believe this is due to instrumental limitations in measuring such low currents, because similar effects are observed when measuring the open-circuit current versus voltage. Disregarding these lowest currents, we have used Arrhenius plots of the logarithm of the dark current normalized to temperature versus inverse temperature in order to determine the barrier height for carriers escaping from the quantum well (1). These plots are shown in Figure 3. The corresponding activation energies agree with the cut-off wavelengths measured in the FTIR spectrometer. For higher biases (above around 15 V), the dark current increases sharply with bias, and its temperature dependence decreases as can be seen on Figure 2. This soft breakdown is more prominent for negative biases. A closer look at the differential conductance in this regime reveals an oscillatory behavior as is seen on Figure 2. The period of these oscillations is 0.85 V. Similar oscillations are observed in the photoresponse, as described below.

Blackbody Responsivity

Blackbody responsivity was measured as a function of bias using a chopped 1000 C blackbody radiation source and conventional lock-in detection techniques, and is shown in Figure 4 for two chopper frequencies. The blackbody responsivity increases with bias up to 15 V bias. For negative biases in excess of 15 V, the blackbody responsivity reveals even sharper oscillations than observed in the differential dark conductivity. For positive biases in excess of 15 V, the blackbody responsivity first saturates, then increases again. For both bias directions, the excess blackbody responsivity for biases in excess of 15 V shows a slow frequency response, as is seen by comparing the data obtained at chopper frequencies of 390 Hz and 3.85 kHz. The signal was measured across a 10 kΩ load resistor, and the time constant associated with this load and the total capacitance of the cables (200 pF) is 2 μsec, which has negligible effect in this frequency range. The amplitude of the oscillations decreases with increasing temperature, but 12 oscillations remain clearly visible between -15 V and -25 V up to 100 K. The bias was not increased beyond -25 V to avoid destruction of the sample. Careful analysis of the photoresponse spectra in this bias regime reveals no significant change with bias, but it should be noted that FTIR measurements correspond to electrical frequencies of several kHz for which the oscillatory photoconductivity mechanism is damped.

DISCUSSION

Hypothesis for high field domain formation

In this section, we attempt to give a plausible explanation for this oscillatory behavior. The oscillation voltage period (0.85 V) either drops uniformly across the superlattice, or drops across a limited number of superlattice periods (high field domain).

A 0.85 V uniform voltage drop across the 50 period superlattice corresponds to a 17 meV potential energy drop per period. We believe this is unlikely to result in sharp oscillations because first, 17 meV does not correspond to any resonant energy loss mechanism (it does not correspond to the optical phonon energy which is 36 meV in GaAs, slightly higher in $Ga_{0.51}In_{0.49}P$), and second, 17 meV is only slightly higher than the thermal energy (8 meV at 100 K) which is incompatible with the observation of such sharp oscillations.

We now consider the hypothesis of field domains. High field domains may occur when the structure exhibits negative differential resistance, i.e. when the same current can be sustained for different electric fields. Oscillatory conductivity and photoresponse has been observed at low bias in n-doped superlattices as a result of high field domain (HFD) formation (3). Conductivity increases first with bias through miniband conduction. When the potential drop over one period reaches the miniband width, miniband conduction is impeded and the conductivity decreases, until the electric field reaches a value such that electrons can tunnel from the ground state to an excited state of the neighboring well. As a result, a low field region in which miniband conduction occurs may coexist with a high field region in which conduction occurs through sequential tunneling from the ground state to the first excited state of the neighboring well.

Here oscillations appear beyond -15 V, which corresponds to a 0.3 eV potential drop per period. 0.3 eV is comparable to the spacing between the ground state and the top of the barrier. A possible explanation for the sharp increase in conductivity is that holes in the ground state can tunnel to an excited state of the neighboring well. It has been shown that valence band mixing can result in comparable tunneling times for electrons and holes (4), so that tunneling may be significant even for p-doped structures. For larger reverse biases this conduction mechanism is impeded (negative differential resistance). The superlattice may then break into a "low" (around 100 kV/cm in our case) electric field domain, and a high field domain. Oscillations are observed in the conductance as the number of superlattice periods in the high field domain increases. In previous observations of HFDs, the conductivity mechanism in the HFD was tunneling from the ground state to an excited state of the neighboring well, so that the oscillation period corresponded to the energy spacing between two energy levels. In our case, this spacing is 0.85 eV which is too large to be explained this way. Instead of tunneling, we propose that the excess potential drop of 0.85 eV is what is required to induce interband avalanche multiplication. A photo-excited hole on top of the barrier gains a kinetic energy of $(eFL_p)_0+\delta(eFL_p)$ by ballistic transport over the barrier. Here e is the electronic charge, F the electric field, L_p is the superlattice period, $(eFL_p)_0 = 0.3$ eV is the potential drop per period for 15 V bias, and $\delta(eFL_p) = 0.85$ eV is the excess potential drop across one period. When the hot hole crosses the next quantum well, it has a high probability of being captured to the ground state, thus losing an energy equal to $(eFL_p)_0+\delta(eFL_p)+V_b$, where V_b is the confinement barrier height for holes in the quantum well ($V_b \approx 0.3$ eV from photoresponse spectra). If this excess energy reaches the electron-to-heavy hole interband transition energy ($E_{e-h} = 1.57$ eV from photoluminescence measurements), it can be lost by raising an electron from the valence band into the conduction band. This avalanche mechanism produces excess carriers and thus increases the conductivity. The expected required potential drop $\delta(eFL_p)$ is equal to $E_{e-h}-(eFL_p)_0-V_b \approx 0.97$ eV. This is higher than the measured value of 0.85 eV but it should be noted that the electric field corresponding to a potential drop of $(eFL_p)_0+\delta(eFL_p)\approx 1.15$ eV per period, is 400 kV/cm. Under such very large electric fields, the quantum-confined Stark effect is expected to reduce the interband transition energy by approximately the potential drop over the well, which is about 0.1 eV, which brings the expected excess potential drop in reasonable agreement with the measured one. Tunneling and interband avalanche may thus explain the formation of a high field domain in the superlattice.

There is a charge accumulation or depletion at the boundary between the low and high field domains. The corresponding two-dimensional carrier density computed from Poisson equation is 2×10^{12} cm^{-2}, which is comparable to the doping density in the well. Whether there is charge accumulation or depletion depends on the spatial distribution of the field domains (5).

Influence of Bias Direction

Can this mechanism explain the fact that these oscillations are seen in only one bias direction? Negative differential resistance (explained by tunneling) is required for HFD formation. Due to an asymmetric quantum well potential profile, it is possible that tunneling be enhanced for one bias direction. X-ray diffraction did not reveal any significant structural asymmetry in the superlattice. The other possibility is an asymmetric zinc dopant distribution. The residual zinc concentration in the barrier is expected to be higher near the upper GaAs/GaInP interface because of the zinc memory effect. As a result, holes are transferred into the quantum well and there is a potential spike at the upper interface resulting in a thinner and lower effective barrier for hole tunneling out of the well. Tunneling should be enhanced for negative biases, which is consistent with the observation of oscillations for negative bias only.

Moreover, avalanche ionization is highly dependent on potential singularities (6). It is also possible that the avalanche ionization probability across the quantum well be enhanced for negative bias.

Speed of Response

Can it explain the very slow speed of response of the excess photoconductivity? Generally speaking, avalanche multiplication can be slow if electron and holes have similar ionization coefficients, because following light excitation excess carriers can be recycled (7). Bulk III-V semiconductors have comparable ionization coefficients for electrons and holes. We cannot ascertain the exact value of this ratio for the present superlattice, but it is plausible that ionization coefficients be comparable for electrons and holes.

CONCLUSION

In conclusion, we have investigated the dark current and photoresponse properties of a p-type GaAs-$Ga_{0.51}In_{0.49}P$ Quantum Well Intersubband Photodetector operating under normal incidence with background limited performance up to 120K. We have observed an unusual oscillatory behavior in the differential conductivity and blackbody responsivity, which we have tentatively explained in terms of high field domain formation induced by tunneling and interband avalanche multiplication.

ACKNOWLEDGMENTS

The work at Northwestern University was supported by Air Force Contract No. F33615-93-C5382 through Kopin Corporation.

REFERENCES

---

1. B.F. Levine, J. Appl. Phys., **50**, R1 (1993).
2. M. Razeghi, Nature, **369**, 631 (1994).
3. L. Esaki and L.L. Chang, Phys. Rev. Lett., **33**, 495 (1974).
4. E.T. Yu, M.K. Jackson, and T.C. McGill, Appl. Phys. Lett., **55**, 744 (1989).
5. H.T. Grahn, H. Schneider, and K. von Klitzing, Phys. Rev.B, **41**, 2890 (1990), A. Shakouri, I. Grave, Y. Xu, A. Ghaffari, and A. Yariv, Appl. Phys. Lett., 1101 (1993).
6. F. Capasso, IEEE Trans. Electron. Devices, **ED-30**, 38 (1983).
7. G.E. Stillman and C.M. Wolfe, "Avalanche Photodiodes", in Semiconductors and Semimetals, vol. 12, R.K. Willardson and A.C. Beer , editors, Academic Press, New York, 1977.

FIGURES

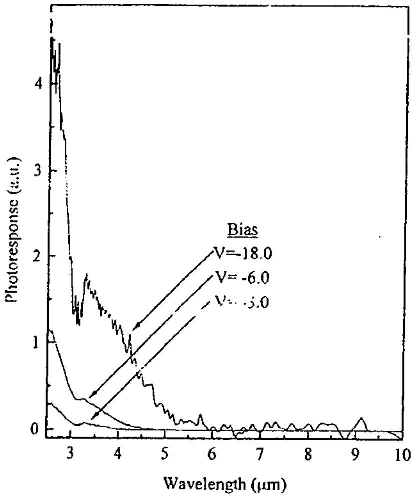

Figure 1: 77K Photoresponse spectra for different negative (mesa top negative) biases.

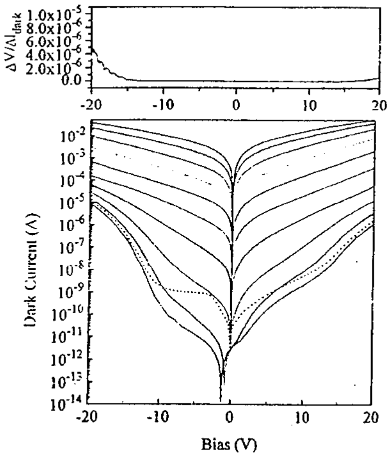

Figure 2: Bottom: Dark current versus bias. Solid lines: Detector with cold shield for temperatures of 77, 100, 125, 150, 175, 200, 225, 250, 275, and 300 K. Dashed line: Detector at a temperature of 77 K exposed to 300 K background radiation without cold shield. Top: Differential conductivity versus bias at 77K.

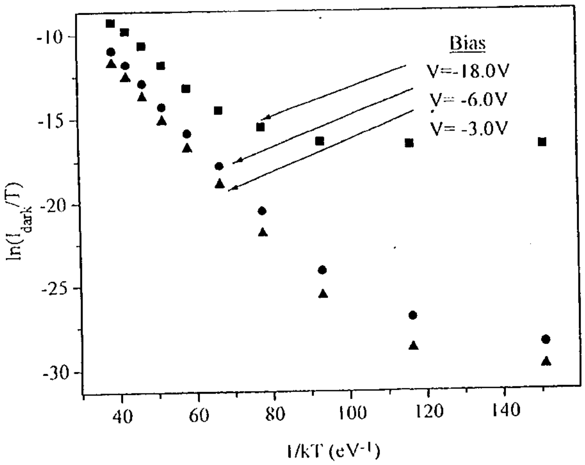

Figure 3: Arrhenius plots of the normalized dark current versus inverse temperature, for three different biases. Activation energies extracted from the linear regime are 260, 230, and 209 meV for -3, -6, and -18 V, respectively.

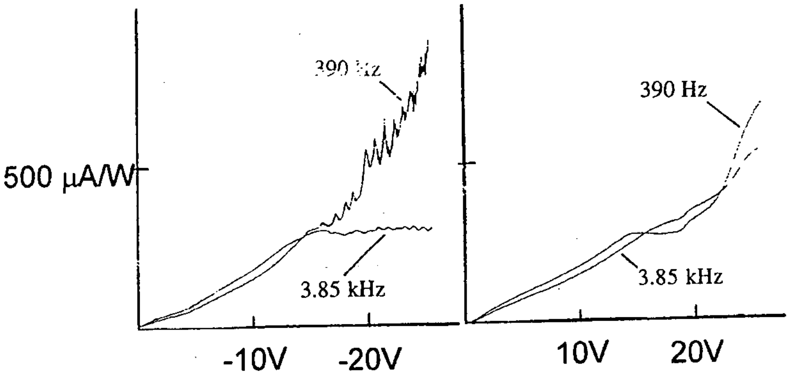

Figure 4: 1000 C blackbody responsivity versus bias, for two chopper frequencies of 390 Hz and 3.85 kHz. The detector temperature is 77K. Left: negative bias. Right: positive bias.

A NEW COMPRESSIVELY STRAINED InGaAs/AlGaAs P-TYPE QUANTUM WELL INFRARED PHOTODETECTOR WITH ULTRA-LOW DARK CURRENT AND DETECTIVE PEAKS IN THE LWIR AND MWIR BANDS

J. Chu, Sheng S. Li, and Y. H. Wang
Department of Electrical and Computer Engineering
University of Florida
Gainesville, FL 32611

Pin Ho
Electronics Laboratory
Lockheed Martin Corporation
Syracuse, NY 13221

Recently, great strides have been made in the development of quantum well infrared detectors (QWIPs) for long wavelength infrared imaging applications. While most of the research has been focussed on n-type QWIPs, progress is also being made in p-type QWIPs. A normal incidence p-type compressively strained layer (PCSL) InGaAs/AlGaAs QWIP grown on semi-insulating (SI) GaAs by molecular beam epitaxy (MBE) has been developed and characterized in this work. This p-type CSL-QWIP structure achieved two-color detection with detection peaks at 7.4 μm in the long wavelength infrared (LWIR) band and 5.5 μm in the mid-wavelength infrared (MWIR) band. This detector exhibits an ultra-low dark current characteristic, and is under background limited performace (BLIP) conditions at T=63 K for applied biases from -2.7 V to +3 V. The measured peak responsivities were found to be 37 mA/W and 7 mA/W at the LWIR and MWIR peaks, respectively. A detectivity of 1.06 $\times 10^{10}$ cm$\sqrt{Hz}$/W was obtained at λ_p = 7.4 μm, T=81 K and V =1.0 V.

INTRODUCTION

In the last few years, n-type QWIPs have been extensively investigated using III-V semiconductor material systems [1]. Because of the small electron effective mass and high electron mobilities, n-type GaAs/AlGaAs QWIPs offer excellent IR detection properties. These n-type QWIPs have utilized the bound-to-continuum

[1-3] and bound-to-miniband [4] transition schemes in the 8-14 μm LWIR and 3-5 μm MWIR bands, to achieve reasonable detectivities and dark current characteristics. However, quantum mechanical selection rule for intersubband transitions requires that the electric field of the incident IR radiation has a component perpendicular to the quantum well plane in order to induce intersubband absorption in the quantum wells. Therefore, for n-type QWIPs. it is necessary to use either planar metal or dielectric grating structures to couple the normal incidence radiation into absorbable angles in the quantum wells [6-7].

In contrast, p-type QWIPs allow the absorption of normal incidence IR radiation due to the band mixing between the heavy-hole and light-hole states. In p-type quantum wells, intersubband transitions under normal incidence illumination are induced by the linear combination of p-like valence band Bloch states which provides a nonzero coupling between these components and the normal radiation field. The strong mixing between light-hole and heavy-hole states for $k_{\|} \neq 0$ greatly enhances the normal incidence intersubband absorption. However, in the unstrained lattice matched GaAs/AlGaAs and InGaAs/InAlAs quantum well systems recently demonstrated [8-10], the intersubband transitions occur between the heavy-hole ground state and the upper heavy-hole excited states. Due to the large heavy-hole effective mass, weak absorption and low responsivity are expected for the unstrained p-QWIPs. By utilizing biaxial strain confined in the quantum wells of the QWIP, we can increase the responsivity and the BLIP temperature, which offers more flexibility in the design and fabrication of p-QWIPs. Here we present a new normal incidence p-type compressively strained-layer (PCSL) $In_{0.2}Ga_{0.8}As/Al_{0.15}Ga_{0.85}As$ QWIP grown on SIGaAs by molecular beam epitaxy. In this QWIP structure, the intersubband utilizes a bound to continuum transition between the ground heavy-hole (HH1) state to the second extended heavy-hole (HH3) state for LWIR detection. The MWIR detection peak is due to the intersubband transition from the HH1 state to the first continuum heavy-hole (HH4) state.

THEORY

In general, strain effects induced by the lattice mismatch between the well and barrier layers in a multiquantum well structure can modify the energy bandgap of the quantum well/superlattice, split the degeneracy of the heavy- and light-hole bands at the center of the Brillouin zone, and modify the carrier transport properties [11]. Matthews and Blakeslee [12] reported that high quality coherently strained layers can be grown if the individual layer thickness of the system is less than its critical thickness. Osbourn [13] also demonstrated the ability of coherently strained-layer superlattices (SLS) for use in a wide variety of novel optoelectronic devices including lasers, modulators, enhanced-mobility field effect transistors, light emitting diodes, and photodetectors.

When a biaxial strain is applied between two thin superlattice layers, coherent heterointerfaces can be obtained if the individual layer thickness is within the critical thickness. In this case the misfit due to the lattice constant mismatch is totally accomodated by the elastic strain. The applied biaxial strain can be either compressive or tensile depending on the lattice constants and the layer growth direction. Based upon the force balance model [12], the equilibrium critical layer thickness, h_c, for an epilayer with a lattice constant, a, grown on a substrate with a lattice constant of a_s is given by

$$h_c = \left(\frac{a}{\sqrt{2}\delta_o}\right) \frac{1 - \nu \cos^2 \Theta}{8\pi(1+\nu)\cos\alpha} \left[1 + \ln(h\sqrt{2}/a)\right] \tag{1}$$

where h is the epilayer thickness, Θ is the angle between the dislocation line and the Burges' vector, α is the angle between the slip direction and the layer plane direction, δ_o is the lattice mismatch or the in-plane strain, and ν is the Poisson ratio. δ_o is defined as $\delta_o = (a - a_s)/a$, where $\delta_o > 0$ for tensile strain and $\delta_o < 0$ for compressive strain. Similarly, ν is defined as, $\nu = -C_{12}/C_{11}$. Here the C_{ij}'s are elastic constants.

For a coherently strained QWIP structure, the multiple layers can also be grown without misfits if the substrate lattice constant $a_s = a_{\|}$, where $a_{\|}$ is the equilibrium in-plane lattice constant for the multiple layers. It can be calculated from [12]

$$a_{\|} = \frac{a_1 \xi_1 L_1 + a_2 \xi_2 L_2}{L_1 \xi_1 + L_2 \xi_2} \tag{2}$$

where $a_{1,2}$ and $L_{1,2}$ are the individual layer lattice constants and thicknesses, respectively. ξ is the shear modulus, and is given by $\xi = (C_{11} + C_{12} - 2C_{12}^2/C_{11})$. When $a_{\|} \neq a_s$, the coherently strained superlattice is no longer in equilibrium with the substrate. If the lattice constant of the barrier layers is equal to that of the substrate, then the strain will be totally accomodated in the well layers with no strain in the barrier layers. However, Hull et al. [14] showed that if the individual layer thicknesses in the superlattice are less than the critical thickness, even though $a_{\|} \neq a_s$, the loss of coherence only occurs at the interface between the whole superlattice and the substrate, while the superlattice itself remains coherent.

If the coherently strained layer structure is grown in the [100] direction, the components of the strain tensor [e] are simplified to

$$e_{xx} = e_{yy} = e_{\|} = \frac{a_s - a_{\|}}{a_{\|}}$$

$$
\begin{aligned}
e_{zz} &= -e_{\|}\left(\frac{2C_{12}}{C_{11}}\right) \\
e_{xy} &= e_{yz} = e_{zx} = 0.
\end{aligned}
$$

In addition to altering and limiting the physical properties of the QWIP, lattice strain can also induce energy band shifts. These shifts can be used to improve the absorption characteristics of the device. The strain induced energy band shifts for the conduction band ΔE_c, the heavy-hole valence subband ΔE_{hh}, and the light-hole valence subband ΔE_{lh} at **k**=0 can be expressed as

$$
\begin{aligned}
\Delta E_c &= 2c_1 \frac{C_{11} - C_{12}}{C_{11}} \delta_o &\quad (3) \\
\Delta E_{hh} &= b \frac{C_{11} + C_{12}}{C_{11}} \delta_o &\quad (4) \\
\Delta E_{lh} &= -\Delta E_{hh} + \frac{(\Delta E_{hh})^2}{2\Delta_o} &\quad (5)
\end{aligned}
$$

where c_1 is the combined hydrostatic deformation potential which characterizes the splitting of the Γ_8 valence band under strain, b is the shear deformation potential, and Δ_o is the spin orbit split-off energy. The total hydrostatic deformation potential ($c_1 + V_v$, where V_v is the valence band deformation potential, can be shown to be [19]

$$
c_1 + V_v = -\frac{1}{3}(C_{11} + 2C_{12})\frac{dE_g^o}{dP}, \quad (6)
$$

where dE_g^o/dP is the unstrained energy bandgap change with respect to unit pressure.

To fully describe the optical and electronic properties of a coherently strained layer structure, the multiband effective-mass **k**·**p** model based upon the pertubation approximation can be used. In the **k**·**p** model, the interactions of the s-p type coupling among the conduction band (CB), heavy-hole (HH), light-hole (LH), and spin-orbit (SO) states combined with spin-orbit like coupling are taken into consideration in the derivation of the band structure. This results in an 8×8 **k**·**p** Hamiltonian and momentum matrix elements. Under the perturbation approximation, a set of wavefunctions of $S_{1/2}$: ($|1/2, \pm 1/2>_c$), $P_{3/2}$: ($|3/2, \pm 3/2>$; $|3/2, \pm 1/2>$), and $P_{1/2}$: ($|1/2, \pm 1/2>$) are used to represent the unperturbed and unstrained basis in the $|J, m_J>$ presentation [15]. $m_J = \pm 1/2$ represents the light-particle states (either electron or light-hole), while $m_J = \pm 3/2$ denotes the heavy particle states (HH). A slightly simplified 6×6 **k**·**p** Hamiltonian can be used to roughly predict the P-like properties of the coherently strained layers by considering the S-like conduction band states as a perturbation, if a large enough bandgap exists, as in the InGaAs and AlGaAs layers. The wavefunctions of the coherently strained superlattice at the Brillouin zone center (k=0) are given by [16],

$$
\begin{aligned}
&|3/2, \pm 3/2> && \text{HH states} && (7)\\
\gamma|3/2, \pm 1/2> + \; &\beta|1/2, \pm 1/2> && \text{LH states} && (8)\\
-\beta|3/2, \pm 1/2> + \; &\gamma|1/2, \pm 1/2> && \text{SO states} && (9)
\end{aligned}
$$

where γ and β are constants depending on the strain parameters. Note that the heavy-hole states, $|3/2, \pm 3/2>$, are still decoupled from the other valence band state even under biaxial stress at the zone center; while the light-hole and spin-orbit split off states are coupled at k=0. However, the HH, LH, and SO states are mixed in the coherently strained superlattice if $k \neq 0$ [17]. The mixing between states with different m_j's is due to the boundary conditions across the interface of the quantum well layers. By examining the $\mathbf{k}\cdot\mathbf{p}$ matrix, we can see that the interaction between different m_j states is proportional to the transverse components of the wave vector, $k_{x,y}$, so that the HH states are decoupled when $k_{x,y}=0$. Note that the $k_{x,y}$'s are conserved across the interfaces since the interface potential depends only on z, the quantum well growth direction. Thus, the band mixing can be significant if the Γ-bandgap is small and the LH and SO bands involved have a large k_z value [18].

Since the heavy-hole and light-hole valence band subbands are non-degenerate when strain is introduced into the growth layers, a simpler method can be used to determine the transmission probability and the allowed states of the individual subbands. By using the parabolic band approximation at and near the valence band zone center, and knowing the energy shifts due to biaxial strain in the conduction band, heavy-hole valence subband, and light-hole valence subband, we can utilize the simpler two-band Hamiltonian for electrons by simply altering the carrier effective mass (e.g. use either the LH or HH effective mass) and the corresponding barrier height for each carrier type. Although this does not allow simultaneous prediction of allowed states for both carrier types, it does allow for a reasonably accurate estimation of each individual carrier type in relation to its local subband minimum near the zone center. When compared with the results of the direct calculation [20], the simpler two-band approximation yields accurate results. One limitation of the tranfer matrix method (TMM) [21], is the inability to locate the states above the quantum well. This limitation is not very critical, since most p-type QWIP designs call for transitions from the bound states to the state in resonance with the barriers, and it can be overcome by using the Kronig-Penney approximation to determine the location of the extended states in the continuum states.

P-TYPE COMPRESSIVE-STRAINED LAYER QWIP DESIGN

Compressive strain is introduced in the $In_{0.2}Ga_{0.8}As$ quantum wells of the QWIP, while no strain is present in the $Al_{0.15}Ga_{0.85}As$ barrier layers, which is lattice matched with the semi-insulating (SI) GaAs substrate. The induced strain pushes the heavy hole states upwards and the light hole states downwards relative increasing electron energy in the InGaAs quantum wells. Thus the heavy- and light-hole bands are split in the quantum wells, but remain degenerate in the AlGaAs barrier regions at the Brillouin zone center.

The $In_{0.2}Ga_{0.8}As/Al_{0.15}Ga_{0.85}As$ p-type CSL QWIP was grown on a (100) SI GaAs substrate by molecular beam epitaxy. The structure consists of twenty periods of 48 $\AA$ $In_{0.2}Ga_{0.8}As$ quantum wells spaced with 500 $\AA$ wide $Al_{0.15}Ga_{0.85}As$ barriers. The wells were Be-doped to a density of 2×10^{18} cm^{-3}, while the barriers were undoped. A 0.3 μm cap layer and a 1.0 μm thick buffer layer of GaAs each Be-doped to 5×10^{18} cm^{-3} were also grown to serve as ohmic contacts. In addition, a 600 $\AA$ wide $Al_{0.15}Ga_{0.85}As$ barrier layer were grown between the contact layers and the multi-quantum well structure to reduce the large tunneling current from the triangle potential formed from the heavily doped, large bandgap ohmic contact regions. In our design, the barrier and substrate are lattice matched and the well regions are in biaxial compression due to a lattice mismatch of -1.4%. The ground subband energy levels confined in the quantum wells are the highly populated heavy hole states, E_{HH1}. The mobility of the heavy hole is enhanced by the compressive strain in the InGaAs quantum wells by the reduction of the heavy hole effective mass [22]. Another improvement which results from the introduction of compressive strain in the quantum wells is the reduction in the density of states in the InGaAs layers. Because of this, more free holes will reside in higher energy states, which implies that the Fermi level is elevated when compared with the unstrained case. The elevation of the Fermi level will result in an increase of the number of off zone center (i.e., $k \neq 0$) holes with less effective mass. Therefore, a larger intersubband absorption under normal incidence infrared radiation can be expected.

As seen in Figure 1, the intersubband transition occurs from the highly populated ground heavy hole state (E_{HH1}) to the upper heavy hole bound state (E_{HH3}) and the first extended heavy hole state (E_{HH4}) for the 7.4 μm LWIR and 5.5 μm MWIR detection peaks, respectively. Since the upper heavy hole bound state (E_{HH3}) is slightly below the barrier valence band maximum, we expect a maximum in the absorption oscillation strength; whereas the first extended heavy hole state (E_{HH4}) is above the barrier, which predicts a weaker aborption.

RESULTS AND DISCUSSION

To facilitate the characterization of this p-QWIP, a 216 × 216 μm^2 mesa was etched onto the wafer by wet chemical etching. After patterning with a contact mask, a thin film of 120 Å of Cr was deposited by E-beam evaporation. This layer was topped off with a 1000 Å layer of Au to create both the top and bottom ohmic contacts. The top ohmic contact consists of a ring type structure around the edge of the mesa with a 50 × 50 μm^2 contact pad for electrical connection.

Figure 2 shows the dark I-V characteristics of the InGaAs/AlGaAs compressively strained p-QWIP. As can be seen in this figure, the device is under BLIP at temperatures below 63 K for applied biases between -3 V and +3 V. A BLIP temperature of 70 K can also be achieved when the applied bias is less than 1 V. Like all of the previously studied p-QWIPs, the dark current characteristic is slightly asymmetric. This can be attributed to the doping migration effect of the Be dopant during layer growth [5].

The responsivity of the p-QWIP was measured under normal incidence illumination as a function of temperature, applied bias, and incident IR radiation wavelength by using a blackbody radiation source running through an automatic PC-controlled single grating monochrometer with the appropriate IR filters attached. The output of the QWIP was measured with a Princeton Applied Research 5210 lock-in amplifier and converted to responsivity by calibrating the output with a pyroelectric detector. Figure 3(a) and 3(b) show the results of these measurements. A single LWIR peak was found at λ_{p1} = 7.4 μm and T=77 K with an applied bias of 5 V. Given a rather broad LWIR peak and a cut-off wavelength of approximately at 10 μm; this corresponds to a half-peak spectral bandwidth of $\Delta\lambda/\lambda_{p1}$ = 30 %. The responsivity was determined to be 37 mA/W at 7.4 μm peak wavelength. A single MWIR peak was also found at λ_{p2} = 5.5 μm under the same conditions previously mentioned. The MWIR peak has a bandwidth ranging from approximately 4 to 6 μm. For a cut-off wavelength of 6 μm, we derive a spectral bandwidth of $\Delta\lambda/\lambda_{p2}$ = 27 %, which is again a rather wide peak. The asymmetrical responsivity around the MWIR spectral peak is attributed to the long-pass filter characteristic which has a cut-on at λ_{on} = 6.7 μm. As seen in Fig. 4(a) and 4(b), the responsivity is linearly proportional to the applied bias and that variation with respect to device temperature is minimal for both detection peaks.

Noise characterization was also performed on the p-type CSL QWIP using standard noise measurement procedures [23]. A Brookdeal 5004 low noise amplifier (LNA) which has an input reference current noise, $S_{ia} \approx 4 \times 10^{-27} A^2/Hz$, was used to amplify the signal generated by the QWIP. The spectral density from the output of the LNA was measured using a HP 3561A spectrum analyzer which has a bandwidth of 100 kHz and allows for data collection via computer. In order to extract the device parameters, all the measurements were carried out at temperatures higher than the device BLIP temperature of 67 K.

The noise spectral density measured with an applied bias of $V_b = 1.0$ V and $T = 81$ K was found to be 6.5×10^{-28} A^2/Hz. Given a device area of 216×216 μm^2, and a measured current responsivity, $R_A = 12.5$ mA/W under the previously mentioned conditions, we calculated a detectivity of, $D^* = 1.06 \times 10^{10}$ $cm\sqrt{Hz}/W$ at the 7.4 μm peak wavelength. As the applied bias is increased, the detectivity decreases due to the increase in dark current and the corresponding increase in noise spectral density; even though the current responsivity increases linearly. The calculated D^* values at $V_b = 2$ and 3 V are 6.3×10^9 and 3.2×10^9 $cm\sqrt{Hz}/W$, respectively. The noise spectral density of this PCSL QWIP as a function of temperature and applied bias voltage is shown in Fig.5. As shown in this figur, at a low bias voltag the number fluctuation noise translates into current fluctuation noise via the diffusion mechanism. As the applied bias increases, charge transport becomes drift dominant and the number fluctuation noise couples to current noise via the hole drift mechanism; which results in a strong current dependence [23].

CONCLUSION

We have demonstrated a new normal incidence p-type compressively strained-layer (PCSL) InGaAs/AlGaAs QWIP grown on SI GaAs for MWIR and LWIR two-band two color detection. The intersubband absorption and photoresponse of this normal incidence PCSL QWIP were enhanced by using compressive biaxial strain in the InGaAs quantum well layers. Since the total layer thickness of this PCSL QWIP is greater than the strained layer critical thickness, certain strain relaxation might occur, which may result in a lower photoresponse and higher dark current characteristic than expected; even though the individual layer thicknesses are within the critical layer thickness criteria. Although the LWIR detection peak for this QWIP is shorter than that required for most staring focal plane array (FPA) applications and the MWIR detective peak is slightly longer than required, we can shift the MWIR and LWIR detection peaks into more useful regions in addition to maintaining or improving the responsivity and dark current characteristics the PCSL QWIPs for FPA applications by further optimizing the quantum well dopant density and the biaxial strain strength, changing the well and barrier thicknesses as well as the In and Al compositions of the well and barrier layers.

ACKNOWLEDGEMENTS

The authors would like to thank Daniel Wang for the noise measurments on the PCSL QWIP reported in this work. The research performed at the University of Florida and was supported by the Advanced Research Projects Agency and monitored by the Office of Naval Reseach under ASSERT grant No.N00014-93-1-0827. This work was also supported in part by Phillips Lab, Kirtland AFB under contract No. F29650-94-W-0774.

REFERENCES

1. B. F. Levine, *et al.*, Appl. Phys. Letts., **56**, 851 (1990).
2. Y. H. Wang, S. S. Li, J. Chu, and Pin Ho, Appl. Phys. Letts., **64**, 727 (1994).
3. Y. H. Wang, S. S. Li, J. Chu, and Pin Ho, Appl. Phys. Letts., **76**, 2538 (1994).
4. L. S. Yu and S. S. Li, Appl. Phys. Letts., **59**, 1332 (1991).
5. H. C. Liu, Z. R. Wasilewski, and M. Buchanan, Appl. Phys. Letts., **63**, 761 (1993).
6. Y. C. Wang and S. S. Li, J. Appl. Phys. **74**, 2192 (1993).
7. J. Y. Andersson and L. Lundqvist, J. Appl. Phys. **71**, 3600 (1992).
8. J. Katz, Y. Zhang, and W. I. Wang, Electron. Letts. **28**, 932 (1992).
9. B. F. Levine, S. D. Gunapala, J. M. Kuo, and S. Hui, Appl. Phys. Letts. **59**, 2864, (1991).
10. W. S. Hobson, A. Zussman, B. F. Levine, and J. deJong, J. Appl. Phys. **71**, 3642 (1992).
11. G. E. Bir and G. E. Pikus, "Symmetry and Strain-Induced Effects in Semiconductors", J. Wiley, New York (1974).
12. J. W. Matthews and A. E. Blakeslee, J. Cryst. Growth **27**, 118 (1974); **29**, 273 (1975); **32**, 265 (1976).
13. G. C. Osbourn, J. Appl. Phys. **53**, 1586 (1982).

14. R. Hull, J. C. Bean, F. Cerdeira, A. T. Fiory, and J. M. Gibson, Appl. Phys. Letts. —bf 48, 56 (1988).

15. E. O. Kane, "Semiconductors and Semimetals," ed. R. K. Willardson and A. C. Bear, **1**, 75 (1966).

16. F. H. Pollack, "Semiconductors and Semimetals," ed. T. P. Pearsall, **32**, 17 (1990).

17. P. Man and D. S. Pan, Appl. Phys. Letts. **61**, 2799 (1992).

18. S. H. Pan, H. Shen, Z. Hang, F. H. Pollack, W. Zhuang, Q. Xu, A. P. Roth, R. A. Masut, C. Lacelle, and D. Morris, Phys. Rev. **B-38**, 3375 (1988).

19. G. Ji, D. Huang, U. K. Reddy, T. S. Henderson, R. Houre, and H. Morkoç, J. Appl. Phys. **62**, 3366 (1987).

20. H. Xie , J. Katz, and W. I. Wang, Appl. Phys. Letts. **59**, 3601 (1991).

21. A. K. Ghatak, K. Thyagarajan, and M. R. Shenoy, IEEE J. Quantum Electron. **24**, 1524 (1988).

22. K. Hirose, T. Mizutani, and K. Nishi, J. Crystal Growth **81**, 130 (1987).

23. D. C. Wang, G. Bosman, Y. H. Wang, and S. S. Li, J. Appl. Phys. **77**, 1107 (1995).

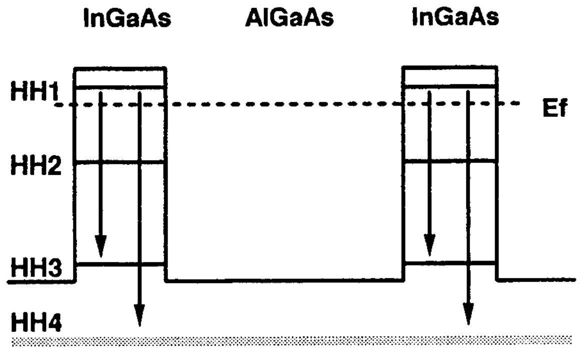

Figure 1: Schematic energy band diagram for the p-type CSL InGaAs/AlGaAs QWIP showing the intersubband transitions.

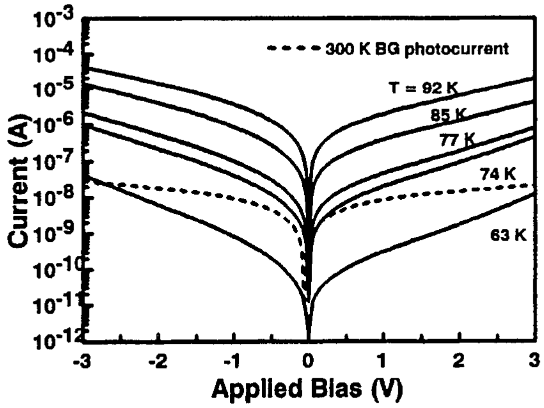

Figure 2: Dark current characteristic for the p-type InGaAs/AlGaAs CSL QWIP.

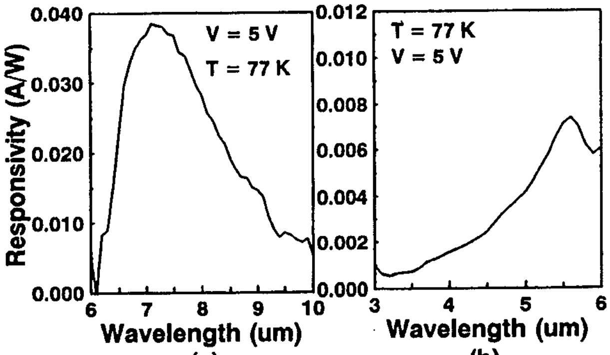

(a) (b)

Figure 3: (a) LWIR responsivity and (b) MWIR responsivity for the p-CSL QWIP.

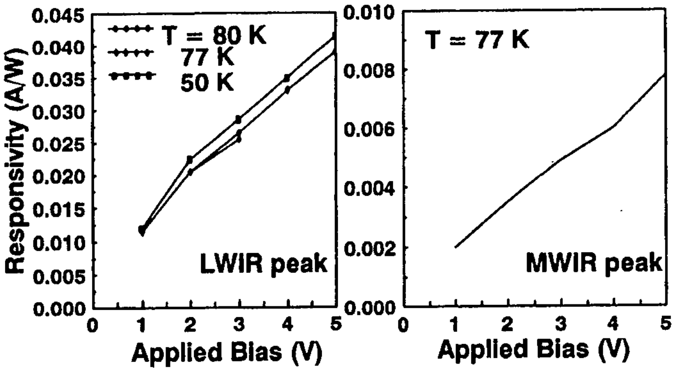

(a) (b)

Figure 4: Responsivity versus bias and temperature for the (a) LWIR and (b) MWIR peaks.

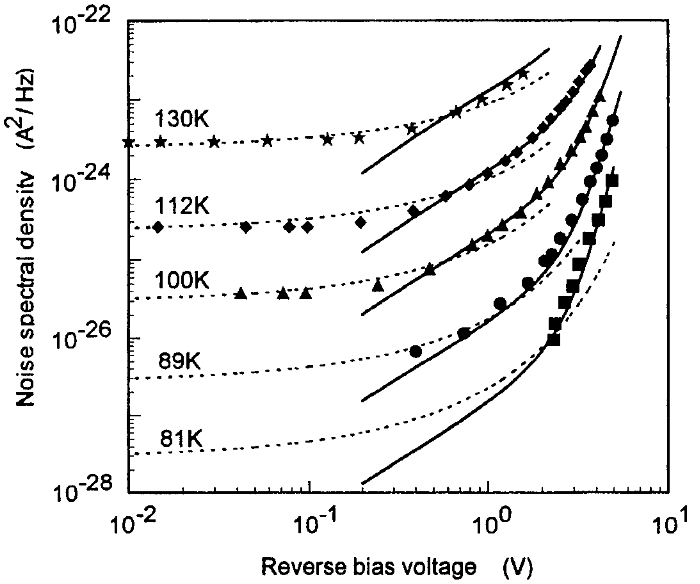

Figure 5: Noise spectral density of the p-type CSL QWIP as a function of bias and temperature.

NOISE PERFORMANCE OF P-TYPE STRAINED LAYER QUANTUM WELL INFRARED PHOTODETECTORS

D. C. Wang, G. Bosman, S. S. Li and J. Chu
Department of Electrical and Computer Engineering
University of Florida
Gainesville, FL 32611

Dark current noise measurements between 10^1 and 10^5 Hz were carried out on a compressively strained p-type InGaAs/AlGaAs quantum well infrared photodetector (QWIP) as a function of temperature and bias voltage. The measured noise can be attributed to number fluctuation noise associated with the generation and recombination of holes from and to the quantum well bound states and the extended valence band states. At low bias the number fluctuation noise translates into current fluctuation noise via hole diffusion, where as at higher bias values the coupling is via the hole drift current component. A value for the capture coefficient for hole trapping is determined and interpreted in terms of the Be-acceptor characteristics. Our measurements indicate that the field induced barrier lowering and the Schottky image effect strongly influence the device characteristics. In addition we observe that the thermally generated heavy holes diffuse, at low fields, on the average to the nearest neighboring quantum well where they subsequently recombine. The current-voltage and noise behavior of the QWIP at low bias can be explained by a model of N statistically independent device sections, each section consisting of a barrier region with two quantum well contacts supplying the holes.

INTRODUCTION

In this paper, detailed noise measurements are reported on a compressively strained p-type InGaAs/AlGaAs QWIP for different bias voltages and operating temperatures. The measurement results show that generation-recombination (g-r) noise is the dominant noise source down to 10 Hz. By applying a wide range of bias voltages, both the diffusion and drift dominant regimes of operation could be investigated.

In stead of using the in general unknown phenomenological parameters such as noise gain and well capture probability, we developed a model based on a priori known quantities such as the electric field and the quantum well features to explain the observed noise levels in the diffusion and drift regimes. Based upon this model, values for the low field hole diffusion length and for the hole capture coefficient for trapping in the quantum wells can be extracted from the noise data.

DEVICE DESCRIPTION

The p-type QWIP under study was grown on a semi-insulating GaAs substrate by molecular beam epitaxy. This QWIP consists of 20 periods of Be-doped $In_{0.2}Ga_{0.8}As$ quantum wells of 48 Å in width with dopant density $2 \times 10^{18} cm^{-3}$, separated by 500 Å undoped $Al_{0.15}Ga_{0.85}As$ barriers. A 0.3 μm cap layer and a 1.0 μm buffer layer of Be-doped GaAs with a dopant density of $5 \times 10^{18} cm^{-3}$ were also grown to serve as top and bottom ohmic contacts. The $In_{0.2}Ga_{0.8}As$ quantum wells are in biaxial compression with a lattice mismatch of nearly -1.4%. A 100 Å undoped barrier layer of $Al_{0.15}Ga_{0.85}As$ was grown between the contact layer and the QWIP structure to reduce the dark current tunneling through the contact.

The hole transition was designed to be from the heavy hole ground state (HH1) to the third heavy hole state (HH3). The HH1 and HH3 are located 24 meV and 190 meV below the quantum well valance band edge, respectively. The experiments were performed on a $216 \times 216 \mu m^2$ mesa formed by wet chemical etching.

MEASUREMENT SETUP

Measurements were carried out using standard noise measurement procedures.[1] A Brookdeal 5004 low noise amplifier (LNA) which has an input referred current noise $S_{i_a} \approx 4 \times 10^{-27} \frac{A^2}{Hz}$ was used to amplify the signal generated by the device. Due to the low current noise and high dynamic resistance of this p-type QWIP under low bias conditions, our detection was limited by this amplifier current noise component. The spectral density of the output of the LNA was measured using a HP3561A spectrum analyzer which has a bandwidth of 100 kHz and allows data collection via a computer.

During the measurements, the device was placed in a nitrogen flow cryostat which allows for temperature variation between 80K and room temperature. This cryostat also acted as an external noise shield. In order to extract the device parameters, all the measurements were carried out at temperatures higher than the device BLIP temperature of 63K.

EXPERIMENTAL RESULTS

The dark currents under both forward and reverse bias voltages were measured using a HP4145B semiconductor parameter analyzer and are shown in Figure 1 for different temperatures. Current noise spectra were measured in the reverse bias range which is used for IR detection. Our temperature range was determined by the lowest temperature that we could achieve with this setup (80K) and on the high side by the maximum DC current (2 mA) that we allowed to flow through the device. The latter limited our temperature to 130K. Noise spectra were measured from 10 Hz to 100 kHz. Typical current noise density spectra are shown in Figure 2. In the high frequency range ($f >$ 1KHz), the noise spectral density is affected by RC parasitic effects, but after corrections are made, frequency independent noise levels result. The noise plateaus are attributed to hole trapping and detrapping in the quantum well bound states.

The measured data indicate that most of the current spectra are frequency independent down to 10 Hz. Only at high bias voltage conditions, eg. $|V_{bias}| > 4$V, excess noise shows up in the spectra for frequencies below 100 Hz.

Figure 3 shows the noise plateau values plotted as a function of dark current for three selected temperatures. From this plot, two different regimes of operation can be recognized. In the low field diffusion dominant regime, noise values are nearly independent of DC current. The observed low bias noise values agree with the values calculated from the Nyquist expression at zero applied bias voltage for all the measured temperatures. In the high field, drift dominant regime, however, noise values become strongly current dependent. This general behavior is quite similar to what Rose predicted for traditional photoconductive devices.[2]

DISCUSSION

Noise Mechanism

If the hole lifetime in the valence band is τ_0 and in the quantum well bound state is τ_s, then the particle number spectral density is given by[3]

$$S_P(f) = 4\overline{G}\frac{\tau^2}{1+\omega^2\tau^2} \qquad [1]$$

where $\tau^{-1} = \tau_0^{-1} + \tau_s^{-1}$ and G is the hole generation rate from the quantum well ground states to the valence band extended states. In equilibrium, the average number of holes generated from the quantum well ground states per unit time should equal the average number of holes recombining from the valence band extended states per unit time. Assuming the total number of holes in the valence band is P_0 and in the quantum well bound state is P_s, We have

$$\frac{P_s}{\tau_s} = \overline{G} = \overline{R} = \frac{P_0}{\tau_0} \qquad [2]$$

At low temperatures, the total number of holes in the valence band extended states is much smaller than the number of holes in the quantum well ground states of our undoped barrier QWIP device. Therefore, τ_0 is much smaller than τ_s resulting in $\tau \approx \tau_0$. This implies that the particle number spectral density at low frequencies becomes

$$S_P \approx 4\overline{G}\tau_0^2 \qquad [3]$$

In our p-type QWIP with undoped barriers, the number of mobile holes is equal to the total number of holes excited from the quantum well ground states. The dark current, I_d, can be expressed as

$$I_d = q\bar{v}pA = q\bar{v}\frac{P_0}{L} \qquad [4]$$

where $\bar{v}$ is the average hole velocity, p is the hole density in the valence band, A is the device cross-sectional area, and L is the device length. Then, the noise current spectral density can be expressed in terms of S_P as

$$S_i = \left(\frac{q\bar{v}}{L}\right)^2 S_P \qquad [5]$$

In the absence of an applied field, the diffusion length, L_D, is the distance a free carrier diffuses before recombining into quantum well ground states. Therefore, the current noise in the diffusion dominant regime can be expressed as

$$S_i = 4q^2\overline{G}\left(\frac{\tau_0\bar{v}}{L}\right)^2 = 4q^2\overline{G}\left(\frac{L_D}{L}\right)^2 \qquad [6]$$

When a sufficiently large electric field is applied, the transport mechanism becomes drift dominated and Eq. [6] is no longer valid. By using Eq. [2], Eq. [4], and Eq. [5], the current noise spectral density can then be expressed as

$$S_i = \frac{4q^2}{\overline{G}}\frac{P_0^2}{(\frac{L}{\bar{v}})^2} = \frac{4I_d^2}{\overline{G}} \qquad [7]$$

As a result, the current noise in the drift dominant regime is proportional to the dark current squared and inversely proportional to the total hole generation rate.

Hole Generation Rate

Considering quantum well ground states as the trap states for the holes in the valence band extended states, the generation rate density, $\overline{g}$, can be expressed as

$$\overline{g} = N_a v_{th} \sigma_p N_v e^{(-\frac{E_v - E_0}{kT})} = Ce^{(-\frac{E_v - E_0}{kT})} \qquad [8]$$

where N_a is the doping density in the quantum well, nearly equal to the trapped hole concentration, v_{th} is the hole thermal velocity, σ_p is the cross-sectional area for hole trapping into the quantum well ground states, and N_v is the effective density of states of the valence band. E_v and E_0 are the valence band extended state energy and quantum well ground state energy, respectively. For a p-type QWIP with doped quantum wells and undoped barriers, the total hole generation rate can be expressed in terms of generation rate density as $\overline{G} = NAL_w\overline{g}$, where L_w is the width of a quantum well, and N is the total number of quantum well.

In equilibrium, the energy barrier seen by the holes in the quantum well ground states is $E_b = E_v - E_0$. With an electric field present in the well, the energy band diagram will be tilted and the effective energy barrier on the cathode side of the quantum well will be reduced by approximately $\Delta E_{\mathcal{E}} = q\mathcal{E}L_w$, where $\mathcal{E}$ is the electric field in the well. This barrier lowering effect due to the electric field will cause an increasing in the hole generation rate when a bias voltage is applied to the device.

In addition, the image-force-induced barrier lowering should be taken into account because of the highly doped state of the quantum wells. A hole in the barrier region is subject to an image force. When an external field $\mathcal{E}$ is applied, the Schottky barrier lowering $q\Delta\phi$ is given by[4]

$$q\Delta\phi = q\sqrt{\frac{q\mathcal{E}}{4\pi\epsilon_0\epsilon_r}} \qquad [9]$$

To have a significant Schottky effect, holes inside the quantum well must be able to form a charge plane (image plane) during the hole escape process.[5] Therefore, the dielectric relaxation time, τ_{rel}, in the quantum well Fermi sea must be much smaller than the hole escape time, τ_{esc}, i.e.,

$$\tau_{esc} \gg \tau_{rel} = \epsilon_0\epsilon_r\rho = \frac{\epsilon_0\epsilon_r}{q\mu p} \qquad [10]$$

where ρ is the resistivity and μ is the hole mobility.

For our p-type QWIP with a quantum well doping concentration of $2 \times 10^{18} cm^{-3}$, the dielectric relaxation time for an hole is approximately $7 \times 10^{-15} sec$ by assuming bulk GaAs hole parameter values. On the other hand, the escape time can be estimated from the time it takes an hole to pass through a single barrier region.

$$\tau_{esc} \approx \frac{L_b}{v_{th}} \qquad [11]$$

where $v_{th} = \sqrt{\frac{3kT}{m}}$ is the average hole thermal velocity. With a 500 Å barrier width, the escape time is approximately $6 \times 10^{-13} sec$ at 80K and $5 \times 10^{-13} sec$ at 130K by assuming, again, bulk GaAs parameter values. This first order calculation shows that τ_{rel} is roughly two order of magnitude smaller than τ_{esc} indicating that indeed the Schottky effect needs to be accounted for.

The total energy barrier lowering ΔE, including both the electric field effect and the Schottky image effect, becomes

$$\Delta E = q\Delta\phi + q\mathcal{E}L_w \qquad [12]$$

The total hole generation rate is then

$$\overline{G} = NAL_w\overline{g} = NAL_wCe^{(-\frac{E_b-\Delta E}{kT})} \qquad [13]$$

In the following we will neglect a possible weak temperature or field dependence of the parameter C.

Comparison between Current Noise Expressions and Experimental Data

The expression for the noise current plateau values in the drift dominant regime can be written, using Eq. [7] and Eq. [13], as

$$S_i = \frac{4I_d^2}{NAL_wCe^{(-\frac{E_b-\Delta E}{kT})}} \qquad [14]$$

Assuming a position independent electric field, the hole generation rate constant, C, was found by fitting Eq. [14] to the measured noise data in the drift dominant regime resulting in $C = 9.4 \times 10^{30} cm^{-3}s^{-1}$. Fig. 4 shows the measured noise plateau values versus applied reverse bias voltage for different temperatures and the results of our fit (solid lines).

Once the generation rate constant has been determined, the noise current spectral density in the diffusion dominant regime, written as

$$S_i = 4q^2 NAL_w Ce^{(-\frac{E_b-\Delta E}{kT})}\left(\frac{L_D}{L}\right)^2 \qquad [15]$$

can be used to determine L_D by fitting Eq. [15] to the measured noise data in this regime. The low field diffusion length, L_D, was found to be 450 Å. With this value for L_D, the current noise spectral densities in the diffusion dominant regime were calculated and plotted in Fig. 4, using the dashed lines, for different temperatures showing that there is a good agreement between theory and experiment in terms of noise magnitude and its current dependence for all temperatures considered.

Capture Cross-section for Hole Trapping in the Quantum Well Ground States

From the drift dominant current noise component we found $C = N_a N_v v_{th} \sigma_p = 9.4 \times 10^{30} cm^{-3} s^{-1}$. To explain this value of C and derive a value of σ_p within the context of the hole transport mechanism and the quantum well characteristics we propose the following model.

The thermally generated heavy holes will move via drift or diffusion in the barrier region to a neighboring quantum well. These quantum wells are doped with Beryllium acceptors to a concentration of $2 \times 10^{18} cm^{-3}$, which results in an inter acceptor spacing of about 100 Å. Since the well width L_w is only 48 Å, these acceptors basically form a monolayer thin plane of nearly neutral charge centers. The holes approaching this monolayer with a thermal velocity determined by barrier parameters will interact with these Be-centers triggering a recombination process which results in the holes reaching the HH1 bound states. Assuming ineffective screening of the Be nuclei due to the two dimensionality of the surrounding electron gas, we approximate the Be perturbation potential by[6] $\frac{Zq}{4\pi\epsilon_0\epsilon_r r}$ where Z is the atomic number of Be, equal to 4. The holes impinging on the Be-centers gain kinetic energy by crossing the barrier/well interface. Hence to determine the effective scattering cross-section, σ_p, of the Be-centers embedded in the quantum wells we equate

$$\frac{Zq^2}{4\pi\epsilon_0\epsilon_r r} = E_b + E_{th} \qquad [16]$$

from which $\sigma_p = \pi r^2$ can be calculated. $E_{th}=kT$ is the thermal energy of the holes in the barrier region. This equation reflects that holes with energy less than the total energy, stated in the right hand side of Eq. [16], are subject to scattering, triggering a recombination process whereas holes with energies higher than the energy stated do not sense the perturbation potential and continue their path unperturbed.

Selecting a temperature near the middle of our temperature range, we calculate, at T=100K, that $\sigma_p(100K) = 1.9 \times 10^{-13} cm^2$. The measured value for σ_p follows from $C = N_a N_v v_{th} \sigma_p = 9.4 \times 10^{30} cm^{-3} s^{-1}$. Using $N_a = 2 \times 10^{18} cm^{-3}$ and bulk GaAs values for N_v and v_{th}, we find at 100K

$$\sigma_{p_{exp}} = 2.6 \times 10^{-13} cm^2$$

which is in good agreement with the predictions of the model outlined above.

Low Bias Device Operation

From the noise data presented above the following picture emerges for the operation of QWIPs at zero bias. Holes are being thermally generated from the quantum well bound states into the extended states of the device with, in equilibrium, equal probabilities for transferring to the next neighboring quantum well on the anode or cathode side. The hole lifetime in the bound states is large compared to the barrier transit time, allowing the holes to fully thermalize in the wells. This thermalization process decouples the statistical fluctuations in hole transport through a barrier from one period to the next. As a result the QWIP can be thought of as consisting of N statistically independent sections made up of a barrier region with two contacts from which the holes are emitted. In equilibrium the net hole current through any cross-sectional plane is zero which results from the detailed balance between two opposing currents I_0. Assuming full shot noise in each current, the current noise spectral density of a single section becomes

$$S_{i(section)} = 4qI_0 \qquad [17]$$

The measured noise from N sections in series is then

$$S_i = \frac{S_{i(section)}}{N} = \frac{4qI_0}{N} = S_{i(Nyquist)} \qquad [18]$$

Table I shows the I_0-values calculated from Eq.[18] and the relevant parameters for different temperatures.

Table I. Parameters for p-type QWIP in thermal equilibrium

T (K)	$R_{(ac)}$ (Ω)	$S_{i(Nyquist)}$ (A^2/Hz)	I_0 (A)
80	16.8 M	2.6×10^{-28}	8.1×10^{-9}
89	1.65 M	3.0×10^{-27}	9.4×10^{-8}
100	145 K	3.8×10^{-26}	1.2×10^{-6}
112	21.6 K	2.9×10^{-25}	9.1×10^{-6}
130	2.25 K	3.2×10^{-24}	1.0×10^{-4}

When an electric field is present producing a voltage drop V_b across a section, the total current becomes

$$I = I_s[1 - \exp(-\frac{qV_b}{kT})] \qquad [19]$$

where I_s is the saturation current. In equilibrium, the saturation current is equal to I_0 and the total current will be zero. With an electric field present, the saturation current will increase due to field induced barrier lowering and the image effect. Hence,

$$I_s = I_0 \exp(\frac{\Delta E}{kT}) \qquad [20]$$

Using the I_0-values extracted from the Nyquist noise levels, the dark current under low bias voltage can be calculated. The measured dark current and our calculated results based on Eq. [19] are shown in Fig. 5 for different temperatures.

CONCLUSION

The dark current noise measurements show that the noise of the p-type QWIP under study can be attributed to number fluctuation noise associated with the generation and recombination of holes from and to the quantum well ground states and the valence band extended states. At low bias voltage, the number fluctuation noise translates into current fluctuation noise via the diffusion mechanism. When the applied bias increases, charge transport becomes drift dominant and the number fluctuation noise couples to current noise via the hole drift mechanism resulting in a strong current dependence.

In addition, we found that the stress in the device does not generate a significant amount of excess noise. Inspection of the measured spectra indicates that the excess corner frequency lies below 100 Hz for the QWIP under study. Using the model presented in this paper, the low field diffusion length was extracted to be 450 Å which indicates that holes thermally generated in a quantum well travel, on average, one period before they trap into nearest neighbor quantum wells. The good agreement between calculated and measured dark current using the model of N statistically independent sections also supports this statement.

ACKNOWLEDGMENTS

The QWIP sample used in this study was grown by Dr. Pin Ho of the Electronics Laboratory, Martin Marietta, Syracuse, NY.

REFERENCES

1. Daniel C. Wang, Gijs Bosman, Yeng H. Wang, and Sheng S. Li, J. Appl. Phys. **77**, 1107 (1995).
2. A. Rose, *Concepts in Photoconductivity and Allied Problems* (Wiley-Interscience, New York, 1963).
3. Aldert van der Ziel, *Noise in Solid State Devices and Circuits* (Wiley-Interscience, New York, 1986).
4. S. M. Sze, *Physics of Semiconductor Devices* 2nd Edition (Wiley-Interscience, New York, 1981).
5. S. R. Andrews and B. A. Miller, J. Appl. Phys. **70**, 993 (1991).
6. R. H. Bube, *Electronic Properties of Crystalline Solids* (Academic Press, New York, 1974).

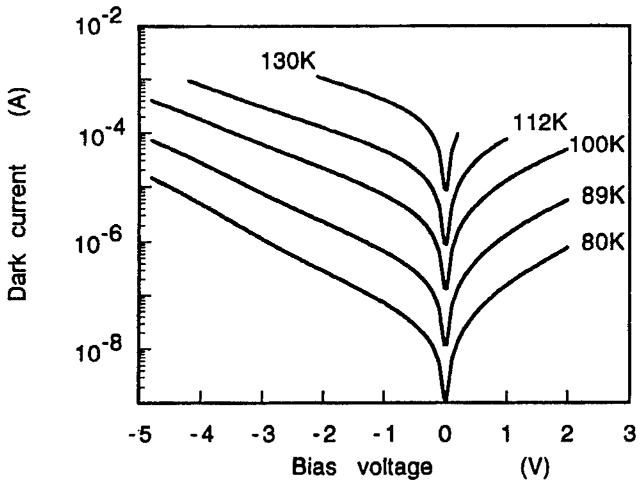

Figure 1. The dark current versus applied bias voltage for different temperatures.

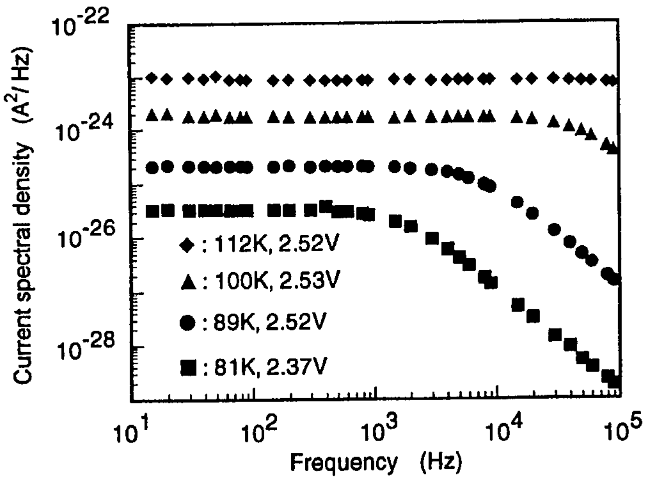

Figure 2. Current noise spectral density versus frequency at different bias voltages and temperatures.

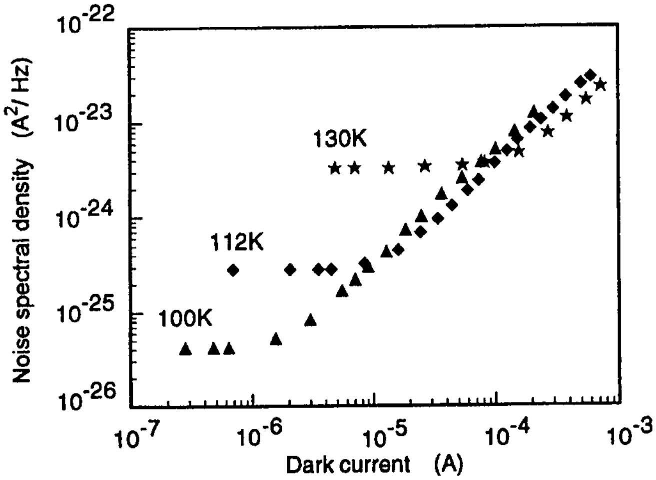

Figure 3. Current noise spectral density versus dark current for various temperatures.

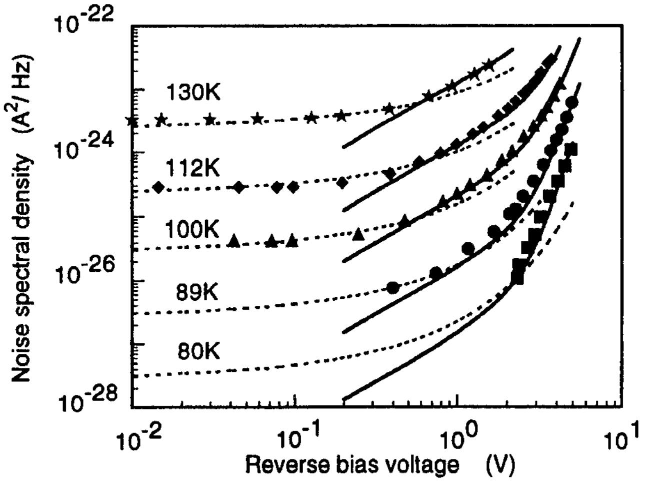

Figure 4. Experimental and theoretical current noise spectral density versus reverse bias voltage for various temperatures.

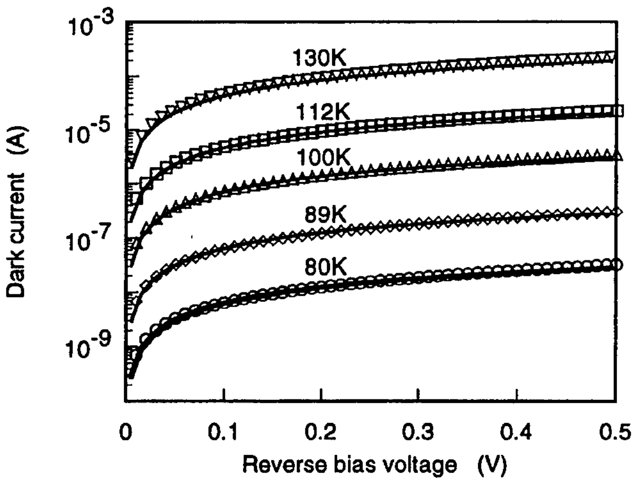

Figure 5. Measured and calculated dark currents at low bias voltage for different temperatures.

Normal incidence interband and intersubband optical transitions in GaSb/InAs superlattices

Y. K. Su, S. M. Chen and C. F. Yu*
Department of Electrical Engineering
National Cheng Kung University
Tainan, Taiwan, Republic of China

*Electrical Engineering Department
National Kaohsiung Institute of Technology and Commerce
Kaohsiung, Taiwan, Republic of China

Abstract

Two novel interband and intersubband optical transitions in the range of infrared wavelength were demonstrated using a type II GaSb/InAs superlattice structure. The intersubband transition, which is a result of the strong mixing of the heavy-hole band and the light-hole band, was achieved by using InAs n-type cap and buffer layers. On the other hand, the interband transition results from the coupling between the wave-functions of the first conduction and the first heavy-hole subband when Zn-doped GaSb p-type cap and buffer layers are used. The wavelengths of interband and intersubband transitions is in the ranges of 3-5 μm and 8-14 μm, respectively. Consequently, there is a possibility of fabricating infrared photodetectors with the GaSb/InAs superlattices.

The GaSb/InAs superlattices have attracted a lot of attention recently due to the possibilities of infrared (IR) applications (3-5 and 8-14 μm).[1-5] Previous reports usually use n-type quantum well and superlattice structures as possible infrared devices.[6,7] In these structures, the selection rules forbid intersubband transitions induced by normal incidence light. However, B. F. Levine and K. K. Choi *et. al.*[1,2] proposed that taking into account the effect of mixing between the subbands would lead to the intersubband transition for small *k's* (wave vector) near the Γ point. A large absorption coefficient was also proposed and has been demonstrated for GaSb/InAs superlattice structures.[4,5] In this letter, the interband transition with an absorption wavelength in the range of 3-5 μm is observed on a similar structure with Zn-doped GaSb p-type cap and buffer layers. This concept of the interband transition is similar to one of our previous papers.[8] On the other hand, an intersubband transition between light-hole and heavy-hole subbands is successfully observed in a GaSb/InAs superlattice sandwiched between InAs n-type cap and buffer layers at room temperature. The superlattice yields an absorption peak in the range of 8-14 μm. Consequently, different types of transitions can be determined by using different doped cap and buffer layers.

Our 50-period GaSb/InAs superlattice samples were grown on GaSb(100) substrates by low pressure metalorganic chemical vapor deposition (MOCVD) at 500 ℃. The reaction gases TEGa (triethylgallium), TMSb (trimethylantimony), TMIn (trimethylindium) and AsH_3 (arsine, 15 percent) were studied with temperatures fixed at 10℃, -14℃, 20℃ and room temperature, respectively. The dopant gases were DEZn (diethylzinc, temperature fixed at -18 ℃) and SiH_4 (silane, 500ppm). The mole fractions of TEGa, TMSb, TMIn, AsH_3, DEZn and SiH_4 were about 2×10^{-5}, 9×10^{-4}, 4×10^{-5}, 3×10^{-3}, $10 \times ^{-7}$ and $10 \times ^{-6}$, respectively. The thicknesses of InAs and GaSb layers of the superlattice were measured by high resolution transmission electron microscope (HRTEM).

The energy diagrams of GaSb/InAs (18/24Å) superlattice sandwiched between the various type cap and buffer layers are shown in Fig. 1 (a) and (b). For intersubband transition, the Fermi level (E_f) of the GaSb/InAs superlattice will be pinned by the InAs layers when the superlattice is sandwiched between thick InAs n-type cap and buffer layers as shown in Fig. 1 (a). One part of electrons will transport from InAs cap and buffer layers into the GaSb/InAs superlattice because the Fermi level must be constant through this sample. Then the Fermi-Dirac distributions of GaSb and InAs layers in the GaSb/InAs superlattice will be adjusted by the final distribution of the electrons. If the E_f is pinned between the first heavy-hole subband (HH1) and the first light-hole subband (LH1), the HH1 is mainly empty and the LH1 is mainly occupied. Then the HH1-LH1 transition can occur. To find the energy levels, we performed a theoretical calculation using the tight-binding method with s^*sp^3 orbitals for the anion and cation.[9] Our result was found to be in good agreement with that obtained using a bond-orbital model.[10] The hole and electron subband structure for the GaSb/InAs (18/24Å) superlattice is shown in Fig. 2. Here $k_{//}$ is the in-plane wave vector and the zero for the energy is defined to be at the top of the valence band of the GaSb layer. For $k_{//} \neq 0$, the subbands contain the heavy-hole and the light-hole characteristics due to the band mixing effect.[11] Hence, the HH1-LH1 optical transition could occur at small $k_{//}$ near the Γ point[5] for the superlattice sandwiched between InAs n-type cap and buffer layers. The minimum energy separation between HH1 and LH1 subbands is about 92 meV (13.48μm) at $k_{//}$=0.024(2π/a) as indicated in Fig. 2. The maximum separation in energy (at Γ point) between HH1 and LH1 subbands is calculated for the GaSb/InAs (30/30Å) superlattice and found to be similar to the result of G. Bastard. [12] To generate the HH1-LH1 intersubband transition, the GaSb/InAs (18/24Å) superlattice must be sandwiched between InAs n-type cap and buffer layers. Our 50-period GaSb/InAs (18/24Å) superlattice sample was grown by metalorganic chemical vapor deposition (MOCVD). The thicknesses of and GaSb layers were measured with a high resolution transmission electron microscope. The concentration of InAs cap (0.2μm) and buffer (1.0μm) layers is about $1 \times 10^{16}cm^{-3}$ and E_f (line a) is 55 meV below the bottom of InAs conduction band (205 meV below the top of GaSb valence band) as indicated in Fig. 1 (a). The energies of HH1 and LH1 subbands are 160.9 and 260 meV below the top of GaSb valence band for the GaSb/InAs (18/24Å) superlattice respectively as indicated in Fig. 2. The HH1-LH1 transition can be made to occur by using normal incident light near the Γ point $k_{//} \neq 0$ in this structure as mentioned above. In order to obtain the IR absorption of these samples, a Fourier-transform infrared (FTIR) spectrometer was used. The reflective absorption method was used to reduce the absorption of the substrate. Thus the absorption mainly results from the 50-period GaSb/InAs superlattice. A GaSb bulk sample (without the GaSb/InAs superlattice) was used as a reference for the absorption measurement. The room temperature FTIR spectrum of the sample has an absorption peak at a wavelength of 13.9 μm (89.2 meV) and a fractional half-width (ΔE/E) of about 30 percent as shown in Fig. 3. This is comparable with the 77 K results of J. Katz *et. al.*[4] The HH1-LH1 optical transition is dominant as shown in Fig. 3 when E_f lies between the energies of the LH1 and the HH1 subbands. The absorption peak of the theoretical calculation was found to be at a wavelength of λ_p=13 μm at 300 K. The experimental absorption peak of FTIR which occurs at λ_p=13.9 μm (89.2 meV) at 300 K as shown in Fig. 3, is in excellent agreement with our theoretical calculation.

For a similar GaSb/InAs (18/24Å) superlattice structure, when the E_f is adjusted to the position between C1 (first conduction subband) and HH1 like Fig. 1(b), the C1-HH1 transition will become the dominant optical transition at the Γ point. Under this condition, HH1 and LH1 subbands are occupied and therefore the HH1-LH1 optical transition can not be observed. Thus different optical transitions can be obtained by varying the positions of E_f. Pinning E_f between C1 and HH1 subbands can be achieved by using thick GaSb p-type cap and buffer layers which allows the C1-HH1 transition. The C1-HH1 interband transition energy at the Γ point for this GaSb/InAs (18/24Å) superlattice structure obtained from our theoretical calculation is found to be 295 meV (4.2μm) as shown in Fig. 2. To generate the interband transition, the 50-period GaSb/InAs(18/24Å) superlattice must be sandwiched between the Zn-doped GaSb p-type cap (0.25 μm) and buffer (1.0 μm) layers as shown in Fig. 1 (b). The concentration of holes is about $3 \times 10^{18}cm^{-3}$ and E_f (line b) is 20 meV above the top of the valence band of GaSb as indicated in Fig. 1 (b). As E_f is between the energies of the C1 (134.5 meV above the top of GaSb valence band) and the HH1 (160.9 meV below the top of GaSb valence band), C1 should be mainly empty and HH1 should be almost completely occupied. Hence, the C1-HH1 optical transition at the Γ point can be made to occur by using normally incident light. The normal incidence FTIR spectrum of this sample at 300 K was shown in Fig. 4. The absorption peak of C1-HH1 occurs at λ_p=4.73μm (262 meV) at 300 K which is a result of the coupling between the HH1 wave-function of GaSb layers and the C1 wave-function of InAs layers as shown in Fig. 4. The calculated energy of C1-HH1 transition is 295 meV as indicated in Fig. 2. Meanwhile, the HH1-LH1 optical transition is not observed as HH1 and LH1 subbands are almost completely occupied. The optical transition can be selected by sandwiching the GaSb/InAs superlattice with different doped-type cap and buffer layers as observed from the experimental results. It means that E_f as well as the absorption wavelengths can be modulated by using different types of cap and buffer layers.

In summary, the optical absorptions of different cap and buffer layers of the GaSb/InAs superlattice were measured by normal incidence FTIR absorption. The intersubband absorption results from the mixing of the heavy-hole states and light-hole states and the absorption peak of the HH1-LH1 transition was at 13.9 μm (89.2 meV) at 300 K. The interband absorption was a result of the coupling between the C1 wave-function of InAs layer and the HH1 wave-function of GaSb layer and the absorption peak at 300 K was at 4.73 μm (262 meV). The intersubband and the interband transitions in the ranges of the IR wavelength were demonstrated from the calculated and experimental results when the thickness of the superlattice, the cap and the buffer layers were well controlled. The interesting phenomena of the GaSb/InAs superlattice makes it a promising candidate for practical device applications such as IR photodevices.

Acknowledgments

The authors wish to express their thanks for Dr. C. Cheug for his helpful discussions. This work was supported in part by National Science Council under Contract No. 83-0417-E-006-003.

References

1. B. F. Levine, R. J. Malik, J. Walker, K. K. Choi, C. G. Bethea, D. A. Bleinman, and J. M. Vandenbery, Appl. Phys. Lett. 50, 273 (1987).
2. K. K. Choi, M. Dutta, P. G. Newman, and G. J. Iafrate, Appl. Phys. Lett. 57, 1348 (1990).
3. R. H. Miles, D. H. Chow, J. N. Schulman, and T. C. McGill, Appl. Phys. Lett. 57, 801 (1990).
4. J. Katz, Y. Zhang, and W. I. Wang, Appl. Phys. Lett. 62, 609 (1993).
5. H. H. Chen, M. P. Houng, Y. H. Wang, and Y. C. Chang, Appl. Phys. Lett. 61, 509 (1992).
6. B. F. Levine, K. K. Choi, C. G. Bethea, J. Walker, and R. J. Malik, Appl. Phys. Lett. 50, 1092 (1987).
7. L. S. Yu, S. S. Li, and P. Ho, Appl. Phys. Lett. 59, 2712 (1991).
8. S. M. Chen, Y. K. Su, and Y. T. Lu, IEEE Electron Device Letters, 14, 447 (1993).
9. J. N. Schulman, and Y. C Chang, Phys. Rev. B 27, 2346 (1983).
10. Y. C. Chang, Phys. Rev. B 31, 8215 (1986).

11. Y. C. Chang and J. N. Schulman, Appl. Phys. Lett. 43, 536-8 (1983).

12. G. Bastard and J. A. Brum, IEEE J. Quantum Electron. QE-22, 1625(1986).

LOW NOISE HgCdTe/Al_2O_3 1024x1024 FOCAL PLANE ARRAYS

L.J. Kozlowski
Rockwell Science Center
1049 Camino Dos Rios
Thousand Oaks, CA 91360

W.E. Kleinhans
Valley Oak Semiconductor
31255 Cedar Valley Drive
Suite 314
Westlake Village, CA 91362

ABSTRACT

We report recent results on our 1024x1024 FPA for astronomy and succinctly compare this device's key performance characteristics to those of an alternative 1024x1024. The latter device also has low read noise, but at much higher signal bandwidth. Specifically, we compare the source follower per detector input used in the former FPA to a capacitive transimpedance amplifier scheme used in the latter. Both devices have been shown capable of consistently achieving background-limited sensitivity at very low infrared backgrounds ($\leq 10^{10}$ photons/cm^2-sec) by virtue of their low read noise, low dark current including negligible MOSFET self-emission, and high quantum efficiency. In addition, megapixel hybrid FPA operability has been increased to 99.84% with background-limited $D^*(_{pk})$ of 10^{14} cm-Hz$^{1/2}$/W.

INTRODUCTION

Infrared (IR) FPA development is currently progressing at a rapid rate. One reason is the continuing commitment of the U.S. government to infrared materials development; this support is recently manifest in programs such as IRFPA and MANTECH (1). A second reason is the evolution in silicon readouts fueled by commercial submicron CMOS. Finally, the use of hybrid technology synergistically exploits the ongoing advances in both constituents since each can be individually optimized. As a result, FPA capability has greatly improved even as cost has been reduced.

IR sensor development nevertheless is about four years behind that of incumbent CCD-based visible sensors as shown in Figure 1. The most mature IR sensor material is PtSi, followed by HgCdTe material grown on Al_2O_3 substrates (to 5.5 µm cutoff wavelength), and finally InSb. The first IR FPAs with full TV-compatible resolution, which were fabricated using PtSi in a monolithic configuration, became available in 1987 as compared to 1983 for CCD-based visible imagers (2). As evident in the figure, the sapphire-based HgCdTe FPA technology is the leading high performance IR material for fabricating large FPAs. HgCdTe/Al_2O_3 arrays have been the first high performance IR sensors in the 256x256, 640x480 and 1024x1024 formats (3–7).

In addition to the many attributes of the sapphire-based HgCdTe detector material including relatively large substrate area for processing and mechanical compatibility with the Si-based readouts, the recent progress also is a consequence of the spin-off benefits from CMOS. Our first 640x480 CMOS readouts, for example, were fabricated on 4-inch wafers at TRW Semiconductor in 1.2 μm CMOS with only 11 die per wafer. The latest lot was fabricated on 8-inch wafers on Rockwell's submicron CMOS line with 70 die per wafer and roughly two order-of-magnitude higher yield of defect-free devices.

We are also exploiting the capability of CMOS with respect to on-chip integration of signal processing functions. Though low noise analog circuits cannot approach the device densities possible in digital integrated circuits, IR readouts now have mixed-signal device densities (including MOSFETs and capacitors) exceeding 1 million devices/cm^2. The above 640x480 readout integrated circuit has about 1.25 million transistors on the 18.5 by 15.5 mm^2 die, which is similar to the transistor count on the Intel 80486 or the Motorola 68040. The most recent 1024x1024 readout, which has a capacitive transimpedance amplifier servicing each pixel, has over 4.4 million transistors; the transistor count here is about 1/3 more than the Intel Pentium microprocessor. In addition, the peak mixed-signal device density is 2.3 million/cm^2. This integration level, which is unprecedented for an IR readout integrated circuit, was achieved with both high yield and low noise. The latter will be reported in the next section. Figure 2 shows our experience with respect to mixed-signal device yield vs. density using Rockwell's commercial submicron CMOS line and several foundries including Hewlett-Packard, Texas Instruments, TRW and Orbit Semiconductor.

1024x1024 HgCdTe FPA DATA

Source Follower-Based 1024x1024

Rockwell Science Center and the University of Hawaii developed the first high performance 1024x1024 focal plane array (FPA) for the U.S. Air Force Phillips Laboratory to support their Advanced Electro Optical System (AEOS) 3.67 m telescope project on Haleakala, Maui (8). This device, which is designated Hawaii Astronomical Wide Area Infrared Imager (HAWAII), uses a source follower amplifier at each pixel to interface the detector. It has exhibited excellent performance characteristics from the outset including read noise of 8.5 e-, FPA dark current <0.1 e-/sec, quantum efficiency >50%, and BLIP-limited sensitivity at low-10^9 photons/cm^2-s background and operating temperatures to 120K. The focus of our recent efforts has been on hybridization and packaging to maximize pixel operability and insure hybrid reliability after many thermal cycles.

The HAWAII FPA is structured in four independent quadrants with four outputs. Six CMOS-level clocks, two 5 V power supplies (one analog and digital), one fixed dc bias and one variable dc bias are required for basic operation. The multiplexer architecture has been optimized to minimize MOSFET self-emission stemming from hot carriers; lowest MOSFET "glow" is achieved by lowering the voltages below 5V (9). The signal voltage from each pixel in the array is read through the first stage source follower consisting of a pixel-based driver MOSFET and a current source FET shared among the elements in a column (Fig. 3). The column bus output then drives the output source follower or can be read directly to eliminate output amplifier glow in trade for reduced pixel data rate. The various MOSFET switches are appropriately enabled and disabled to perform the functions of pixel access, reset and multiplexing. A maximum of six externally-supplied clocks is required. Since CMOS logic circuitry is used, the clock levels do not require precise adjustment for optimum performance. The simple architecture also helps maximize fabrication yield of defect-free readouts.

The source follower per detector, also referred to as direct detector integration, is used for interfacing the detector and read out the photo-induced signal. This scheme works very well at low backgrounds and long frame times; the frame rate used to test the HAWAII focal plane arrays is often less than 1 Hz. The circuit is capable of very low read noise due to the small detector capacitance, concomitant high photoconversion gain and high transimpedance. The dominant noise source, expressed in unit of electrons, stems from the integrated amplifier noise:

$$N_{amp} \approx \frac{\sqrt{2}}{S_V}\left[\int^{\Delta f} V_n^2(f)\frac{(1-\cos 2\pi f t)}{\left[1+(2\pi f T_D)\right]}df\right]^{1/2} \quad (1)$$

where $V_n(f)$ is the MOSFET noise as a function of frequency, T_D is the time constant for correlated double sampling (CDS) set by the appropriate Nyquist rate, and S_V is the readout conversion gain in volts per electron (10). Depending upon the detector and its C-V characteristic, there can also be noise due to nonlinear dependence of capacitance on voltage (and thus charge level). This second order noise can be roughly approximated by kTC_{diff} where C_{diff} is the differential capacitance stemming from the photo-induced bias shift.

Very low read noise has been achieved using correlated double sampling invoked by clocking a reset frame followed by two read frames. Using a 300 kHz low-pass electronic filter to match the noise bandwidth to the signal bandwidth, a mean read noise of slightly under 15 e- was achieved at 0.5 V detector bias. The mean read noise was reduced to 8.6 e- by increasing the detector bias to 1.0 V and thus maximizing the transimpedance. The measured data are in reasonable agreement with those predicted using nominal parameters. For example, we predict a read noise of 4 e- with CDS and 84 e- without if we assume a 1 s integration time, 22 fF detector capacitance, external noise of 35 µV rms and FET noise consistent with the measured MOSFET noise spectral density of 2 $\mu V/Hz^{1/2}$ at 1 Hz (11).

The low read noise translates to background-limited sensitivity. Figure 4 is a histogram of the peak D* for a recent device with 2.5 µm detector cutoff at 78K. The mean of 1.08×10^{14} cm-$Hz^{1/2}/W$ is background limited for the 5.92×10^{9} photons/cm^2-sec test background and measured quantum efficiency of 64.8%; the pixel operability of 99.84% is the highest yet achieved for a megapixel hybrid FPA.

CTIA-based 1024x1024.

Since the source follower-based design cannot manage TV-like frame rates, a second 1024x1024 was developed having a capacitive transimpedance amplifier servicing each pixel. The minimum noise of the CTIA is limited by the composite broadband channel noise and 1/f noise. Assuming large open-loop gain, the total broadband noise of the capacitive transimpedance amplifier can be approximated:

$$N_{channel}^2 = \frac{nkTC_{fb}}{q^2}\left[\frac{C_{\text{det}} + C_{fb}}{C_L(C_{fb} + C_{\text{det}}) + C_{fb}C_{\text{det}}}\right] \tag{2}$$

where the prefactor n is approximately one to two, C_{fb} is the feedback or integration capacitance, and C_L is the load capacitance (12). The load capacitor is used to optimize the CTIA bandwidth for minimum noise.

The amplifier 1/f noise component is approximately:

$$N_{amp,1/f} \approx \frac{C_{\text{det}}\, V_{1/f}(1\text{Hz})\sqrt{2}}{q}\left[\ln\frac{5t_{\text{int}}}{\tau_{\text{amp}}}\right] \tag{3}$$

where t_{int} is the integration time, $V_{1/f}$ is the MOSFET noise spectral density at 1 Hz if classical 1/f noise is assumed; and τ_{amp} is the amplifier time constant. The amplifier is band-limited to the maximum needed signal bandwidth to minimize aliasing of amplifier noise. Both the white and low frequency noise are directly proportional to the detector capacitance. Owing to the very low detector capacitance, however, the critical detector parameter at the target operating temperatures is the detector R_0A product. Figure 5 shows the predicted read noise, amplifier 1/f noise, broadband channel noise, composite detector noise and input-referred post-FPA noise, as a function of detector R_0A product. For detector R_0A's greater than about $10^7\Omega$ -cm^2, total output noise of about 20 e- is predicted. We measured a minimum read noise of 114 µV at an integration time of 0.336 seconds; this corresponds to 27 e- rms, which is in good agreement with that predicted.

Very low FPA 1/f noise has been measured, confirming that the composite 1/f noise is very low. Figure 6 is the noise spectrum for a typical pixel of an 3.2 µm 1024x1024 FPA at 115K operating temperature.. The mean white noise spectral density of 209 µV/Hz is consistent with the folded background noise. The absence of a distinct 1/f characteristic suggests an upper limit of $6.54\text{x}10^{-15}$ A/Hz$^{1/2}$ at 1 Hz. Other data has since shown the 1/f noise at 1 Hz to be on the order of 10^{-18}A/Hz$^{1/2}$ at 115K and 10^{-21}A/Hz$^{1/2}$ at 80K.

The low read noise achieved with both devices agrees with both theory and our experience. Figure 7 is a plot of read noise vs. input capacitance for several source follower and CTIA designs including both 1024x1024 devices.

CONCLUSION

A pair of 1024x1024 FPAs have been developed for high performance applications. The hybrid focal plane arrays consist of photovoltaic HgCdTe/Al_2O_3 detector array, having cutoff wavelength that can be optimized for each specific application, hybridized to either of two silicon CMOS readouts. Using the readout with source follower input, a minimum read noise of 8.7 e- was achieved at 300 kHz output bandwidth. A mean $D^*(_{pk})$ of 1.08×10^{14} cm-$Hz^{1/2}$/W was achieved, which is background limited for the 5.92×10^9 photons/cm^2-sec test background and measured quantum efficiency of 64.8%; the pixel operability of 99.92% is the highest yet achieved for this class of IR FPA. Using the readout with CTIA input, a minimum read noise of 27 e- was measured at 2 MHz bandwidth. Hybrid reliability is continually being continually addressed with both devices. We have thus far demonstrated that interconnect loss can be <0.2% after 100 thermal cycles.

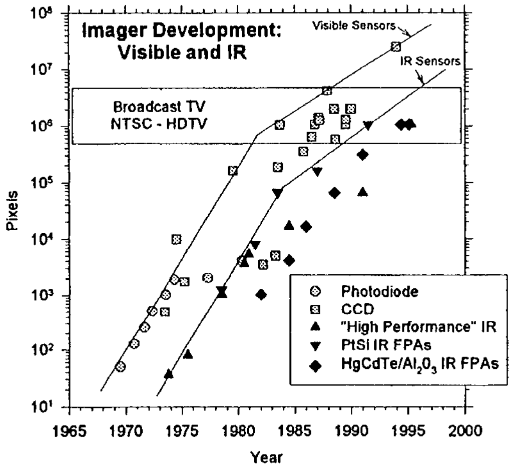

Fig. 1 Chronology of Visible and IR Imager Development

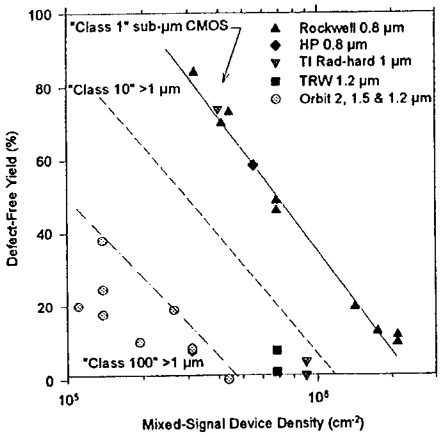

Fig. 2 Defect-free yield versus mixed-signal device density for IR readout integrated circuits.

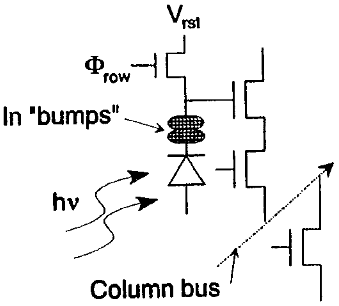

Fig. 3 Schematic diagram showing pixel circuitry, column bus and current source shared among all the pixels along the column bus.

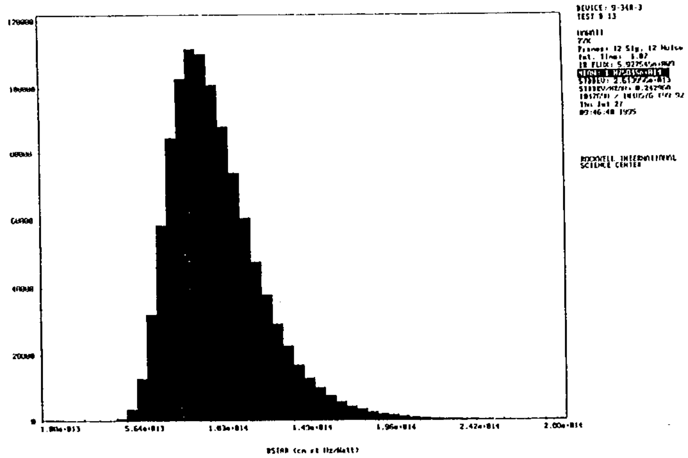

Fig. 4 Histogram of peak D* at 5.92×10^9 photons/cm^2-sec test background

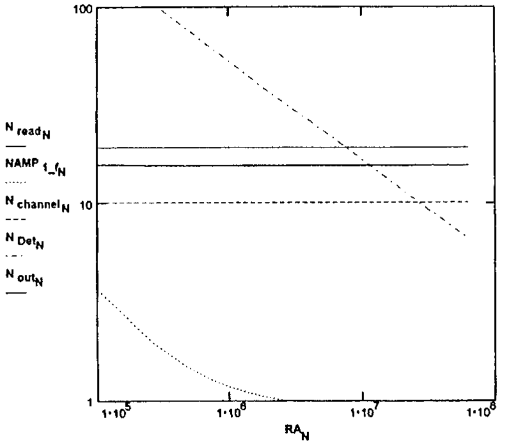

Fig. 5 Predicted Noise Levels vs. Detector R_0A Product.

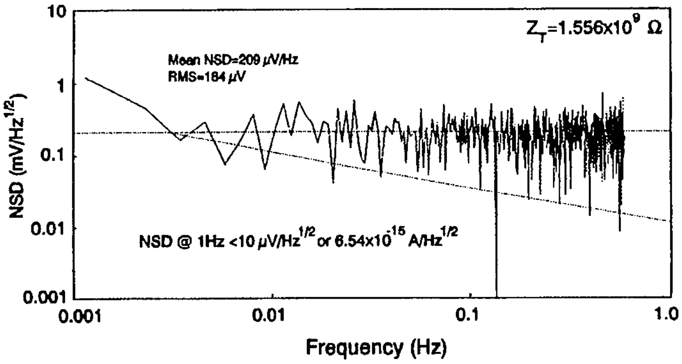

Fig. 6 Noise Spectrum for Typical CTIA-based FPA Pixel at 115K.

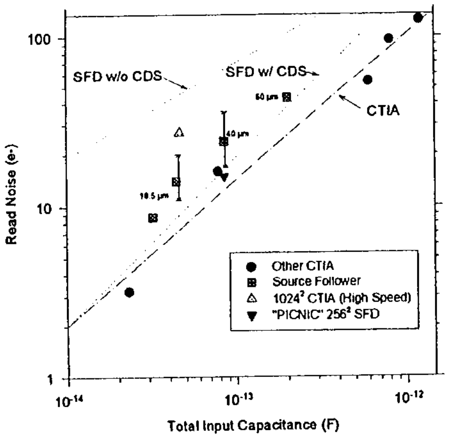

Fig. 7 Read noise vs. total input capacitance for source follower and CTIA FPAs.

REFERENCES

1. For example, SPIE Proceedings **2274**, (1994).
2. M. Kimata, M. Denda, N. Yutani, S. Iwade, and N. Tsubouchi, IEEE J. Solid State Circuits, **SC-22**, No. 6, pp. 1124–1129 (1987).
3. E.R. Gertner, W.E. Tennant, J.D. Blackwell, and J.P. Rode, J. Cryst. Growth, **72**, 465 (1985).
4. R.B. Bailey, L.J. Kozlowski, W.E. Tennant, IEEE Trans. ED, **38**, No. 5, May 1991
5. K. Vural, L.J. Kozlowski and R.W. Rasche, in Int. Mtg. on Infrared Technology and Applications, SPIE **1320**, 107 (1990).
6. L.J. Kozlowski, R.B. Bailey, D.E. Cooper, K. Vural, E.R. Gertner, W.E. Tennant, SPIE **1540**. 250 (1991).
7. L.J. Kozlowski, K. Vural, S.C. Cabelli, A. Chen, D.E. Cooper, D.M. Stephenson and W.E. Kleinhans, SPIE **2268**, (1994).

8. Ibid.

9. A.L. Lacaita, F. Zappa, S. Bigliardi, and M. Manfredi, IEEE Trans. ED, 40, No. 3, 577, (1993).

10. J.R. Janesick, T.Elliott, S. Collins and H. Marsh, SPIE **501**, (1984).

11 L.J. Kozlowski, K. Vural, D.Q. Bui, R.B. Bailey, D.E. Cooper and D.M. Stephenson, SPIE **1946**, 148 (1993).

12. L.J. Kozlowski, S. A. Cabelli, D.E. Cooper and K. Vural, SPIE **1946**, 199 (1993).

Fourier Transform Infrared Spectroscopy for InAsSb/GaSb type II superlattices

F. S. Juang, Y. K. Su* and S. M. Chen*

Electro-Optics Department
National Yunlin Polytechnic Institute
Huwei, Yun-Lin, Taiwan, R.O.C.

*Department of Electrical Engineering
National Cheng Kung University
Tainan, Taiwan, R.O.C.

ABSTRACT

The absorption energies for InAsSb/GaSb type II superlattices were characterized by Fourier Transform Infrared (FTIR) spectroscopy. The absorption wavelength is modulated by the solid composition of the layer. The transition energies measured from FTIR spectroscopy were found to decrease with increasing well ($InAs_{1-x}Sb_x$)thickness. The first conduction to heavy-hole (C1-hh1) and conduction to light-hole (C1-lh1) transition energies increased as the dopant concentration in inner bulk layer increased. The effects of the thickness of inner bulk and outer bulk layers has been studied in detail. If the bulk layers which sandwiched the superlattices were too thin, the fermi level will be decided not only by the bulk layer but also by the substrate. Then, the fermi level will be located at an inappropriate position. The p-type superlattice was also formed to study the interband transitions. A strong response in the range of 3-5μm has been found.

INTRODUCTION

AlGaAsSb and InGaAsSb are the promising candidates to be used to manufacture long wavelength (1.24-4.3μm) optical devices[1-4]. Furthermore, the n-type InAsSb/GaSb superlattice has been proposed to be the promising structure for fabrication of long wavelength devices due to the strong hh1-lh1 intervalence subband optical transition elements. In recent years, bulk layers of InAsSb have been deposited by metal organic chemical vapor deposition (MOCVD)[5-6] or by metal organic molecular beam epitaxy (MOMBE)[7,8]. The InAsSb/InSb strained quantum well[9-10] and InAsSb/InSb strained layer superlattice[10,11-14] have been studied in detail. S. R. Kurtz has developed the high detectivity InAsSb strained layer superlattice (SLS) photo-voltaic infrared detector[12]. G.C. Osbourn suggested the $InAs_{0.39}Sb_{0.61}/InAs_{1-x}Sb_x$ strained layer superlattice can be used for long wavelength detectors[15]. In 1993, S. Eliest proposed the used of lattice matched InAsSb bulk layer grown on GaSb[16]. In this study, the absorption energy and the quality of the different SLS structures were characterized by Fourier Transform Infrared (FTIR) spectroscopy. The envelope function scheme was used to predict the subband energies. The effects of well width, bulk layer dopant concentration and thickness on FTIR spectroscopy were studied. The comparision between n-type and p-type InAsSb/GaSb superlattice is also presented.

EXPERIMENTS

There are two designations that have been proposed, one is n-type and the other is p-type superlattices grown by metal organic chemical vapor deposition(MOCVD). It is necessary to growth a defect-free buffer layer (GaSb) on GaSb substrates in the beginning of the growth procedure. The buffer layer thickness was fixed at 1250Å for all the samples in this study. There was a 30 second interruption after the buffer layer. In the n-type superlattices, a thick InAs silicon doped layer was deposited above the buffer layer. In the p-type superlattices, a thick GaSb zinc doped layer was grown above the buffer layer. After the inner bulk layer had been deposited, there was a 30 second interruption. After the interruption, the 50 periods $InAs_{0.96}Sb_{0.04}/GaSb$ superlattices were then grown on the inner bulk layer in sequence. There was an interruption of 5 seconds after the deposition of every layer in the superlattice. It is worthy of being noted, that only the arsine was allowed to flow into the reactor to prevent thermal decomposition of group V elements during the interruption. At the end of growth procedure, a 60 second interruption occured. After that, a outer bulk layer was then deposited on the top of the superlattice.

In the growth procedure, the growth temperature and growth pressure were fixed at 500°C and 150 torr. TMSb, TMIn, TEGa, and arsine were used as the starting materials, DEZn and silane were used as the p-type and n-type dopants, respectively. The bubbler temperature of TMIn, TEGa,TMSb, DEZn were fixed at 20°C, 10°C, -14°C and -18°C, respectively.

RESULTS AND DISCUSSIONS

The effects of well width on C1-hh1, C1-lh1 and hh1-lh1

The samples, as shown in Fig.1, were prepared for comparing the effects of well widths on the transition energy. Figure 2 shows the FTIR spectra of the Fig.1 samples. The GaSb thickness was fixed at 30 Å, the InAsSb thickness varied from 15 to 60 Å. The heavy hole and light hole subband energy levels increased, and the conduction band energy decreased with increasing InAsSb thickness. It is hard to decide whether the transition energies went down or up when the InAsSb layer thickness was increased. The envelope function approximation was used to predicted the minibands in the superlattices. The plots of transition energies versus InAsSb thickness are shown in Fig.3, where curve (a) shows the C1-lh1 transition, curve (b) shows the C1-hh1 transition and curve (c) shows the hh1-lh1 transition. Those marks are the experimental results. There is excellent agreement between calculated data and experimental results, as shown in Fig.3 curves (a) and (b). However, the calculated data are discrepant with experimental results about the hh1-lh1 transition energies for 10 and 30Å thickness of InAsSb, as shown in Fig.3 curve (c). The discrepancy of curve (c) is mainly due to the strong band mixture between hh1 and lh1. The Kronig Penney model theoretically predicted that the hh1-lh1 transition only occured at $K_{//}=0$ (i.e. Γ point). But the FTIR spectroscopy measured the minimum transition that occured at the position of $K_{//}=0.025(2\ /a)$, where a is lattice constant. So the predicted transition energies were slightly larger than the FTIR spectroscopy. And the discrepancy of curve (c) became more serious when the InAsSb (well) thickness was decreased to less than 60Å, due to the increasing wavefunction coupling effect between the GaSb and InAsSb layers.

The effects of the inner bulk layer

The inner and outer bulk layer can affect the transition strongly. The thickness of inner bulk layer plays an important role to fix the fermi level. If the inner bulk n-InAs:Si is too thin, the fermi-level will be decided by GaSb substrates. The fermi-level thus appears at inappropriate level. The hh1-lh1 transition that is the most favorable intersubband transition will not happen, because the fermi-level did not appear between hh1 and lh1 subband energy levels. Figure 4 curves (a), (b) and (c) show the absorption spectra when the inner bulk layer thickness was 1μm, 0.6μm and 0.2μm, respectively. It was observed that the optical transition were so much different between them. The inner bulk layer InAs(Si) must be thick enough, otherwise the fermi-level will be affected by GaSb substrate. Figure 4 curve (a) shows that if n-InAs:Si inner bulk layer is thick enough then the effect of GaSb substrate can be ignored. If the thickness of inner bulk layer decreased, the effect of GaSb substrate upon the fermi-level will increase. In Fig.4 curves (b) and (c), the transitions are rather different from Fig.4 curve (a). This is because the fermi level appears at an inappropriate level. The Fig.4 curve (b) shows only C1-lh1 and hh1-lh1 transitions. It is because the inner bulk layer thickness is so thin that the effect of the GaSb substrate on fermi-level can not be neglected. In Fig.4 curve (c), the fermi-level was decided by GaSb substrate almost completely. The fermi-level was thus located between C1 and hh1 bands. Because of the inappropriate fermi-level, the intersubband transition disappeared.

The effects of dopant concentration in inner bulk layer

As previous mentioned, the fermi-level location is a very important parameter and the transition energy can be modulated by varying the fermi-level. The fermi-level can be modulated by adjusting the flow rate of silane when the inner bulk layer was grown. The dopant concentration increased as the flow rate of silane increased. The fermi-level thus moved up toward the C1 band. Figure 5 shows the effects of different doping concentrations. Two interesting phenomena can be found in Fig.5, where the flow rate of silane were 0, 2 and 4 sccm, respectively. First, the C1-hh1 and C1-lh1 transition energy levels increased as the doping concentration increased. This is because the transition occured at different in-plane wave vector ($K_{//}$). Secondly, there is a relationship between the intensties of C1-hh1 and hh1-lh1 transitions. The intensity of hh1-lh1 decreased and C1-hh1 increased when doping concentration was increased. It is due to the changing carrier distribution when the dopant concentration was increased. The density of states was changed when the dopant concentration increased.

The effect of the outer bulk layer

The effect of outer bulk layer thickness seems to be similar to that of the inner bulk layer. The fermi-level can't be pinned to an appropriate level by only the inner bulk layer, even if the inner bulk layer is thick. This fact is shown in Fig.6. The thickness of outer bulk layers were 90Å, 1500Å and 3000Å in curve (a), (b) and (c), respectively. In Fig.6 curves (a) and (b), the absorption spectra are similar to each other. This shows that the outer bulk layer is thick enough when the thickness is over 1500Å. When it is thick enough, there is no large difference in the absorption spectra. In Fig.6 curve (c), the absorption spectra is different from the others, this is because the outer bulk layer is too thin to fix the fermi-level at the appropriate state.

The p-type InAsSb/GaSb superlattice

The p-type InAsSb/GaSb superlattices will be discussed. The schematic of p-type superlattice is shown in Fig.7. The fermi-level appears between first conduction band and first heavy hole band. This structure was formed for the study of interband optical transition. Figure 8 curve (a) shows the absorption spectra of superlattice sandwiched by p^+-GaSb layers, in which InAsSb and GaSb thickness were all 30Å. The amount of periods was 50 and the inner bulk layer and outer bulk layer we're fixed at 1 and 3 μm, respectively. It shows that the strong interband transition C1-hh1 occured. There is no absorption peak in Fig.8 curve (b). The sample is a superlattice sandwiched by intrinsic GaSb (p-type) bulk layers. The reason why the absorption peak disappeared is that the fermi-level is so high in intrinsic GaSb bulk layers that conduction and heavy hole subbands in superlattice are all filled with electrons causing the absorption peak to disappear.

CONCLUSIONS

The n-type InAsSb/GaSb superlattice has ben proposed to be the promising structure for fabricating long wavelength devices due to the strong hhl-lh1 intervalence subband optical transition elements. The envelope function scheme has been used to calculate the subband energies. The transition energies have been measured by means of FTIR spectroscopy. The samples were grown with different GaSb (barrier) and InAsSb (well) widths to characterize their effects on the transition energies. The measured results are in excellent agreement with the theoretical calculations of the C1-hh1 and C1-lh1 transitions. There is a discrepancy between experimental results and calculated data in predicting the hh1-lh1 transition. That is due to the band mixing. The C1-hh1 and C1-lh1 transition energies increased as the dopant concentration of inner bulk layer increased. The thickness of the layers which sandwiched the superlattice also affects the transition strongly. If the bulk layers which sandwiched the superlattices are too thin, the fermi level will be decided not only by the bulk layer but also by the substrate. The p-type InAsSb/GaSb superlattice structure has been grown to study the interband transition and had a strong response in the range of 3-5 μm.

REFERENCES

1. H. D. Law, R. Chin, K. Nakano and R. A. Milano, IEEE J. Quantum Electron. vol. QE-17, 275(1981).
2. T. H. Chiu, J. L. Zyskind and W. T. Tsang, J. Electron. Materials, vol.16, 57(1987).
3. C. Cancau, J. Lyskind, J. W. Sulhoff, T. E. Glover, J. Centanni, C. A. Burrus, A. G. Dendai and M. A. Pollack, Appl. Phys. Lett. vol.51, 764(1987).
4. A. E. Drakin, P. G. Jelliseev, B. N. Sverdlov, A. E. Bichkarev, L. M. Dolgino and L. V. Druzhin, Druzhinina, vol. QE-23, 1089(1987).
5. G. B. Stringfellow, J. Cryst. Growth, vol.98, 108(1989).
6. P. K. Chiang and S. M. Bedair, J. Electrochem. Soc. vol.131, 2422(1984).
7. T. Kaneko, H. Asahi, Y. Itani, Y. Okuno and S. I. Gonda, J. Cryst. Growth, vol.111, 638(1991).
8. H. Asahi, T. Kaneko, Y. Okuno, Y. Itani, K. Asami and S. Gonda, J. Cryst. Growth, vol.120, 252(1992).
9. C. P. Tigges, J. E. Schirber, H. P. Hjalmarson, I. J. Fritz and L. R. Dawson, Solid-State Electron. vol.32, 1509(1989).
10. L. R. Dawson, J. Cryst. Growth, vol.98, 220(1989).
11. R. C. Hughes, Optical Engineering, vol.26, 249(1987).
12. S. R. Kurtz, L. R. Dawson and T. E. Zipperian, IEEE Electron Device Lett. vol.11, 54(1990).
13. S. R. Kurtz, L. R. Dawson, R. M. Biefeld, I. J. Fritz and T. E. Zipperian, IEEE Electron Device Lett. vol.10, 150(1989).
14. S. R. Kurtz, L. R. Dawson, T. E. Zipperian and S. R. Lee, Appl. Phus. Lett, vol.52, 1581(1988).
15. G. C. Osbourn, J. of Vac. Sci. & Technol. B. vol.2, 176(1983).
16. S. Eliest, A. Kriert, I. R. Cleverley, and K. Singer, J. Phys. D:Appl. Phys. vol.26, 159(1993).

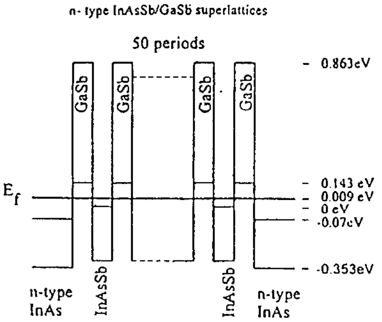

Figure 1. The scheme of n-type superlattice.

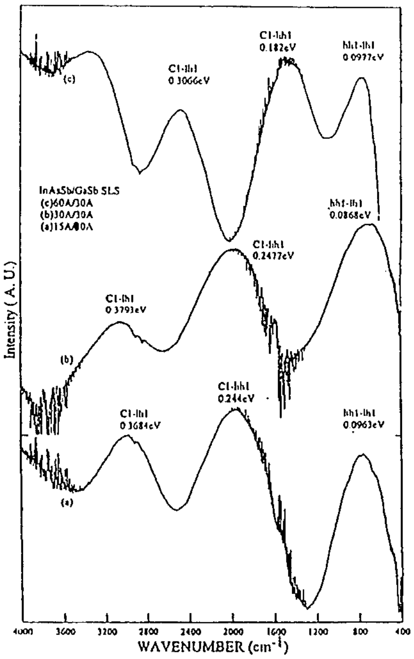

Figure 2. The FTIR spectra for InAsSb/GaSb SLS with different well (InAsSb) width of (a)15Å, (b)30Å and (c)60Å at fixed barrier (GaSb) width of 30Å.

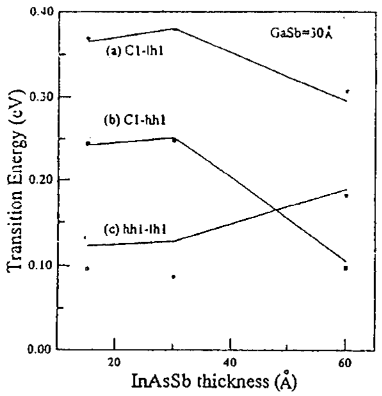

Figure 3. The plot of the C1-hh1, C1-lh1 and hh1-lh1 transition energies versus the InAsSb well thickness at fixed GaSb barrier width of 30Å

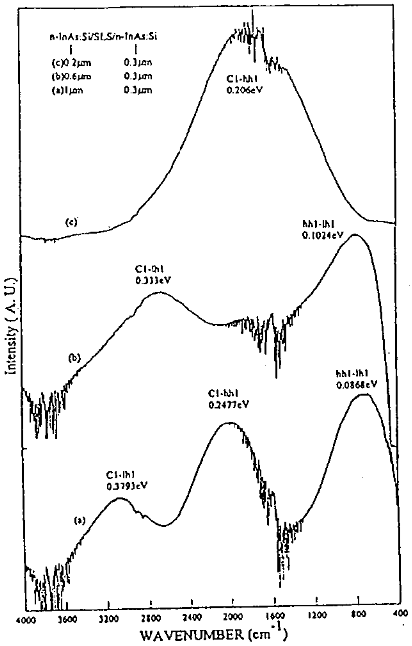

Figure 4. The FTIR spectra for n-InAs:Si/SLS/n-InAs:Si structures with different inner bulk layer (n-InAs:Si) width of (a)1μm, (b)0.6μm and (c)0.2 μm at fixed outer bulk layer (n-InAs:Si) width of 0.3μm.

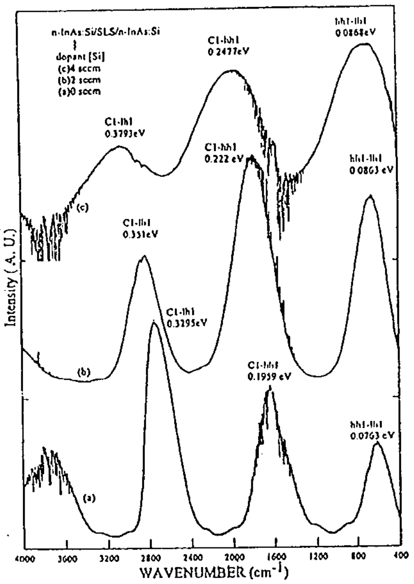

Figure 5. The FTIR spectra for n-InAs:Si/SLS/n-InAs:Si structures with different dopant concentrations for bulk n-InAs:Si layer of (a)0, (b)2 and (c)4sccm.

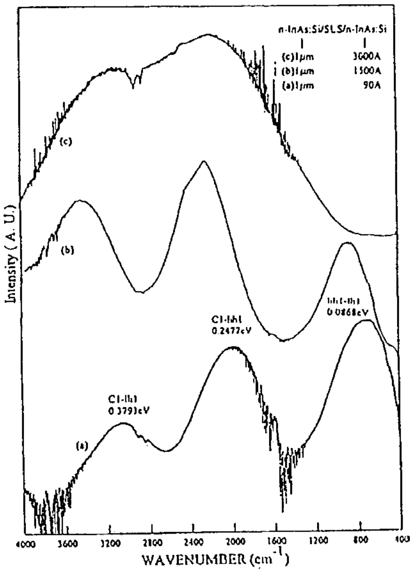

Figure 6. The FTIR spectra for n-InAs:Si/SLS/n-InAs:Si structures with different outer bulk layer (n-InAs:Si) width of (a)90Å, (b)1500Å and (c)30000Å at fixed inner bulk layer (n-InAs:Si) width of 1μm.

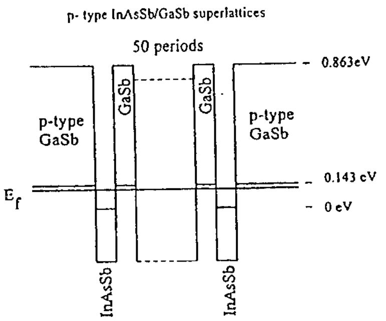

Figure 7. The scheme of p-type superlattice.

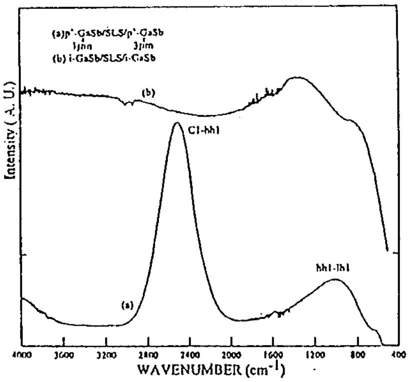

Figure 8. The FTIR spectra for p-type InAsSb/GaSb SLS with different bulk dopant concentrations of (a)p$^+$-GaSb(1μm)/SLS/P$^+$-GaSb(3μm) and (b)undoped GaSb/SLS/undoped GaSb

MULTICOLOR QUANTUM WELL INFRARED PHOTODETECTORS AND GRATING COUPLING EFFECT

M. Z. Tidrow, K. K. Choi, A. J. DeAnni and W. H. Chang
Army Research Laboratory, Fort Monmouth, NJ 07703-5601

ABSTRACT: A two-stack, two-color multi-quantum well infrared photodetectors (QWIP) with 2-D gratings of different period spacings are presented in this paper. The peak wavelength of each stack is 4.8 μm and 9.4 μm respectively, covering the two atmospheric windows. 2-D gratings of box-shaped cavities with grating period either in 3 μm or in 4.6 μm spacing are used to couple normal incident light into the detector. Comparing detectors with and without gratings, detectors with 3 μm gratings show more efficient light coupling for both wavelengths even though it is optimized for 10 μm wavelength detection. The fact is that the longer wavelength in the present case is an integral multiple of the shorter wavelength. The optimized long wavelength grating couples the shorter wavelength through additional higher orders of diffraction. A band pass energy filter grown on top of the two-stack QWIP is used to study the hot electron energy distribution and the transport properties. The temperature dependence of the voltage distribution in the two stacks is also studied.

I. INTRODUCTION

Quantum well infrared photodetectors (QWIP) have been developing rapidly during the past several years.[1,2] Detectors at 10 μm with low dark current and high detectivity at 77 K have been demonstrated recently and the performance meets the requirements of focal plane array applications.[3] Using bandgap engineering, one can extend the functionality of a QWIP and perform multi-color detection using different quantum well structures.[4,5,6] Theoretically, only the normal component of the electric field is absorbed in a n-type QWIP. However, roughly 30% of photocurrent is consistently measured in our experiments under normal incidence without a grating, when it is compared to the result of the standard 45° incidence. This normal incidence photocurrent could be caused by the light reflection specularly from the mesa edge[7] or diffusively from the alloyed top metal contact. Some possible theoretical explanations of intrinsic light absorption at normal incidence have been given[8]. In any case, although photoconductivity in normal incidence is observed in QWIPs, its magnitude needs to be improved for applications. Grating coupling is one of the efficient ways in increasing the absorption. Under this light coupling scheme, however, the quantum efficiency was found to be strongly dependent on the wavelength, leading to a narrowing of the spectral linewidth even for a single color detector.[9,10] Therefore, whether grating coupling is a viable scheme for multi-color detection in covering both the 3 to 5 μm and 8 to 12 μm atmospheric windows has yet to be determined. In this paper, 2-D gratings of period either in 3 μm or in 4.6 μm were fabricated on top of a two-color QWIP which has detection peaks λ_p at 4.8 μm and 9.4 μm. The results show that a single grating optimized for the longer wavelength is also capable of increasing the responsivity of the shorter wavelength even though the improvement is to a different extent.

II. ENERGY BAND STRUCTURE AND SPECTRA

The sample was grown on semi-insulating GaAs (100) by molecular beam epitaxy. It has two stacks of multiple quantum wells (MQW) as the active region. The first stack has 20 periods of 300-Å $Al_{0.38}Ga_{0.62}As$ barrier and 25-Å $In_{0.2}Ga_{0.8}As$ well sandwiched between two 5-Å GaAs. The second stack consists of 20 periods of 500-Å $Al_{0.25}Ga_{0.75}As$ barrier and 50-Å GaAs well. The Si doping density in the wells is 2.0×10^{18} cm^{-3} for the first MQW and 0.5×10^{18} cm^{-3} for the second MQW. The quantum well structures are clad between two Si-doped GaAs contact layers with doping density 1×10^{18} cm^{-3}. Transfer matrix method is used in theoretical design. There is one bound state in each quantum well. The first MQW is designed to have the peak wavelength λ_p at 4.5 μm and the second λ_p at 9.8 μm. The energy band structure of the sample is given in Fig. 1.

Fourier Transform Infrared Spectroscopy is obtained by a Nicolet Magna FTIR spectrometer at room temperature and zero bias. Brewster angle incidence is used to increase coupling of the electric field in the normal direction and to reduce the Fabry-Perot oscillation. The result is shown in figure 2 (b). The absorption peaks at 5 μm and 10 μm are closely consistent with the theoretical calculations. The apparent absorption peak at 7 μm does not generate photocurrent, its origin has not been identified. Figure 2 also gives the photocurrent of the sample at 45° incidence. A monochromator with a globar source and a chopper is used and the photocurrent is collected using a lock-in amplifier. Positive bias is applied on the devices with the substrate contact grounded. At a relatively low bias of 5 V, a single detection peak is observed at 4.7 μm as shown in Fig. 3(a). At this voltage, most of the potential is dropped across the $In_{0.2}Ga_{0.8}As/Al_{0.38}Ga_{0.62}As$ MQW due to its larger impedance. Therefore, the QWIP is only sensitive at the shorter wavelengths. When the bias increases to 6 V, the potential drop across the $GaAs/Al_{0.25}Ga_{0.75}As$ MQW becomes appreciable and the photocurrent peak at 9.4 μm is observed, which is shown in Fig. 2(b). When the bias increases further to 7 V, the 9.4 μm peak shown in Fig. 2(a) becomes dominant. These results demonstrate the multi-color detection capability of this device and its voltage tunability. The photocurrent peaks are slightly blue-shifted from their absorption peaks, which is due to the increasing tunneling probability at higher electron energies.

III. GRATING COUPLING EFFICIENCY

In order to compare the grating coupling efficiency, a metal mask is designed to fabricate different devices with grating periods of 3 μm, 4.6 μm and no grating at the same time when doing processing. All the samples reported here, including the grating structures, were processed by wet chemical etching. Gratings with dry plasma etching on other QWIP structures show similar coupling effect as those with wet etching. The mesa area is 2.25×10^{-4} cm^2 for all devices. Devices with four different light coupling schemes are characterized. Device D has no grating, it is a standard 45° coupling device. Devices A, B and C are the neighboring devices and were measured at the same time using normal incidence through the substrate. Device A has neither a grating nor a 45° polished edge. Devices B and C have 2-D gratings of square symmetry and box-shaped cavities. The gratings are fabricated on the top GaAs contact layer with a depth of 0.7 μm. This grating depth is chosen to allow destructive interference between the normally reflected beams from the top and the bottom of the grating grooves, which effectively eliminates the zeroth order of the diffraction pattern. Since the zeroth order of diffraction does not initiate optical transition in QWIPs, it will not be further considered. The grating period and the cavity width are 4.6 μm and 2.3 μm respectively for device B (referred as grating B), and 3 μm and 1.5 μm respectively for device C (referred as grating C). AuGe/Au are evaporated on top of the grating for ohmic contact. The substrate is 625 μm thick, and there is no substrate thinning performed on any of the devices.

In grating design, it is highly desirable to have the normal incident light diffracted off the grating at large angles close to 90°. Under this light coupling condition, the grating equation is

$$n \sin \theta_m = \frac{m\lambda}{d} ,$$

where n (= 3.135 around 10 μm) is the refractive index of the GaAs substrate, λ is the incident wavelength in air, d is the grating period, and θ_m is the mth order diffracted angle with respect to normal. The ideal condition for maximum absorption is to have the first order diffracted at 90°. Using d = 3 μm and m = 1, the grating C couples most efficiently at $\lambda = 9.4$ μm, which is also approximately at the peak absorption wavelength of the present GaAs/AlGaAs MQW. Grating B has a grating period of 4.6 μm, which couples most efficiently at 14 μm.

Dark current of the four samples were measured in liquid helium dewar. Window photocurrent under 300 K background radiation is also measured at 10 K with a field of view 36°. Fig. 3 shows the 77 K dark current and the window photocurrent of the four devices. The dark current of all devices are nearly identical at 77 K, which indicates the high uniformity of the intrinsic detector characteristics. The window photocurrent of the devices, on the other hand, are different, with device A (no grating) the smallest and device D (45° incidence) the largest. This result indicates that 45° coupling in the present device configuration is the most efficient way to couple the full spectrum of photocurrent due to its wavelength independence.

Photocurrent spectra of devices A, B, C and D are measured and the detector responsivity are shown in Fig. 4. and Fig. 5. The responsivity was calibrated by a commercial HgCdTe detector. There is no power correction for the reflection from the substrate for all devices. In addition, there is no optical area correction for device D. The special light polarization characteristics from the monochromator, which only affects device D, were also ignored.

From Fig. 5, grating C is seen to enhance the light coupling at 9.2 μm, consistent with the prediction from the grating equation. For d = 3 μm and λ_p of 9.2 μm, only the first order diffraction is possible, which corresponds to $\theta_1 = 78°$. For d = 4.6 μm as for grating B, the corresponding θ_1 for the 9.4 μm light is 41°. Since the absorption is proportional to $\sin^2\theta$, the ratio of the peak coupling efficiency of grating B to grating C in this wavelength regime should be $\sin^2 41°/\sin^2 78° = 0.45$, which is quite consistent with the measured ratio of 0.52. The relative experimental peak responsivity are summarized in table 1, in which the peak responsivity of device D in each wavelength band is normalized to unity. From this table, device C has the highest peak response in the 8 μm to 12 μm region, which is 4 times that of A (no grating, normal incidence) and 1.3 times that of D (no grating, 45° incidence).

In the 8 to 12 μm region, the responsivity of device C is 1.32 that of device D, while in the 3 to 6 μm, the responsivity ratio is 0.83. Therefore, the grating coupling efficiency of the 3 μm grating at the shorter wavelength is 0.63 of that at the longer wavelength. With d = 3 μm and $\lambda_p = 4.8$ μm, the nonvanishing orders are at $\theta_1 = 31°$ and $\theta_2 = 90°$. If only the strongest first order is considered, the coupling efficiency of sample C at $\lambda = 4.8$ μm is expected to be about ($\sin^2 31°/\sin^2 78°$) or 0.28 of that at $\lambda =$ 9.4 μm, which is smaller than 0.63. The larger observed value is then attributed to the additional nonvanishing second order diffraction in the shorter wavelength band.

Similarly, for d = 4.6 μm, three orders of diffraction exist with diffraction angles of 19°, 42° and 87° in the shorter wavelength region, in contrast to only one at 41° in the longer wavelength region. The larger number of nonvanishing orders compensates for the smaller first order diffraction angle, leading to the same coupling efficiency of grating B in both wavelength bands. On the other hand, in the shorter wavelength region, the existence of two nonvanishing orders at larger angles as for grating C was found to be more efficient than having three nonvanishing orders at smaller angles as for grating B.

The experimental data in Fig. 5 are presented without the most common correction factors. For example, for device D, when considering the 45° projection area is the actual area to receive light, its responsivity should be 30 % larger. Also, since the p-polarized light from the grating monochromator, which is the polarization absorbed by the QWIP, is smaller than the s-polarized light, it turns out that there is another 30 % increase in device D responsivity when it is used to detect randomly polarized light. On the other hand, the responsivity of grating coupled detectors is expected to increase when the substrate is thinned or An AlAs waveguide layer is included to allow multiple reflections. However, the extent of increase will depend on the detector size and the diffraction angle of a particular order. When θ is large, the increase will be smaller. Typically, the responsivity can be increased by a factor of two.[9,10] Other than these corrections, another 30 % increase in responsivity is anticipated for device D if an antireflection coating on the substrate is adopted. The same advantage can also be applied to grating coupled devices if θ is larger than the critical angle (= 34°) for internal total reflection in the presence of a coating.

IV. THE ELECTRON TRANSPORT AND ENERGY DISTRIBUTION

A major advantage of the two-stack, two-color QWIP is shown in Fig. 2. It can either have detection wavelengths in the two atmospheric windows separately, or simultaneously depending on the bias voltage. It can also have an extra contact in between the two stacks for simultaneous read-out. When the device is operated under voltage tunable condition, it is interesting to know the electron energy distribution when they are transported to the base from each stack of MQW and have a better understanding of the hot electron transport mechanism in the two-stack QWIP. An electron energy band pass filter is used to analyze the hot electron distribution at the base as shown in figure 6. The band pass filter is grown *in situ* on top of the QWIP with 40 Å $Al_{0.3}Ga_{0.7}As$ as barriers and 55 Å GaAs as the well. The band pass energy is 224 meV with a bandwidth of 20 meV. The transmission coefficient of the band pass filter is given in Fig. 7. Only a fraction of hot electrons with energy coincide with the band pass filter can pass through the filter and arrive at the collector. The band pass energy can be varied by biasing between the base and the collector. Transfer Matrix method is used and a calculated relationship between the collector bias and the band pass energy is given in Fig. 8.

In order to study the electron energy distribution from the two stacks as a function of temperature, the bias voltage between the emitter and the base is fixed at 8 V at which voltage the two stacks have photoresponse simultaneously. Fig. 9 gives the collector photoresponse of the device at 4.8 μm and 9 μm as a function of collector bias, with a temperature change from 10 K to 80 K. The derivative of the response to the collector bias, which is directly proportional to the electron energy distribution, is given in Fig. 10. It is easy to see that the peaks of the hot electron energy distribution shift to lower collector bias, (which means higher electron energy, see Fig. 10), when the temperature increases. It is very noticeable that the peaks of the electron energy distribution from the two different stacks are at exactly the same location under the same temperature, even though the excited states of the 5 μm stack is much higher. When the exact transport mechanism of the electrons from then two stacks is not quite clear at present time, this interesting phenomenon indicates that when electrons from the 5 μm stack is been transported through the 10 μm stack, a localized thermal equilibrium state is maintained in each well. It also indicates that no ballistic transport has occurred in the two-stack QWIP.

V. THE VOLTAGE DISTRIBUTION BETWEEN THE TWO STACKS

From Fig. 9 we can see that even though the emitter bias is maintained at 8 V, the photoresponse of the device at two different wavelengths changes in a different fashion with temperature. Fig. 11 gives the peak response of the device at the peak wavelengths as a function of temperature. Even though the dark current is not involved in AC photocurrent measurement, a qualitative explanation can be given here considering the contribution of the dark current. The distribution of the bias voltage drop on the two stacks depends on the impedance of each stack which is strongly influenced by the dark current of each stack. The relative response of the two peaks does not change at temperature from 10 K to 30 K, indicating that the bias voltage does not change during this temperature range. At this temperature range, the direct tunneling dark current dominants and does not depend on the temperature change. When temperature changes from 30 K to 60 K, dark current of thermally assisted and impurity assisted tunneling increases as temperature increases. From Fig. 11 we can see that the photoresponse of the 5 μm stack decreases in this temperature range, which indicates that the dark current of this stack has a larger increase comparing with the 9 μm stack. Since the total bias voltage does not change during the experiment, the 9 μm stack has a relatively larger impedance and therefore larger voltage drop. When temperature goes beyond 60 K, the photoresponse of the 9 μm stack starts to decrease, indicating that the voltage drop on this stack starts to decrease as a function of temperature. It is easy to understand that when thermionic emission dominants, the 9 μm stack has a much higher dark current due to it lower potential barrier.

VI. SUMMARY

In summary, a two-stack, two-color QWIP with 2-D gratings of square symmetry and box-shaped cavity is demonstrated. The grating with a 3 μm period has a better coupling efficiency than that of 4.6 μm in both atmospheric windows. Comparing these two windows, the photoresponse of the 3 μm grating in the shorter wavelength window is only slightly less than that in the longer wavelength window due to presence of higher order diffraction. Since the photoresponse of the 5 μm stack is only one order of magnitude smaller than that in the 10 μm region, while the dark current could be 4 orders of magnitude lower when the detector is sensitive in the shorter wavelength region, the detection in the two atmospheric window is feasible. A band pass filter is used to study the hot electron transport properties and the electric potential distribution between the two stacks. The results provide interesting information for a better understanding of the device physics and optimization.

REFERENCES

1. B. F. Levine, J. Appl. Phys. , **74**, R1 (1993).
2. M. A. Kinch and A. Yariv, Appl. Phys. Lett. **55**, 2093 (1989).
3. K. K. Choi, M. Z. Tidrow, M. Taysing-Lara, W. H. Chang, C. H. Kuan, C W. Farley, and F. Chang, Appl. Phys. Lett. **63**, 908 (1993).
4. I. Grave, A. Shakouri, N. Kuze, and A. Yariv, Appl. Phys. Lett., **60**, 2362 (1992).
5. K. L. Tsai, K. H. Chang, C. P. Lee, K. F. Huang, J. S. Tsang, and H. R. Chen, Appl. Phys. Lett. **62**, 3504 (1993).
6. M. Z. Tidrow, K. K. Choi, C. Y. Lee, W. H. Chang, F. J. Towner, and J. S. Ahearn, Appl. Phys. Lett., **64**, 1268 (1994), M.Z. Tidrow, K.K. Choi, C.W. Farley, and F. Chang, Appl. Phys. Lett., **65**, 2997 (1994), M. Z. Tidrow, K. K. Choi, A. J. DeAnni, W. H. Chang, and S. P. Svensson, Appl. Phys. Lett., **67**, 1800 (1995).
7. L. J. Kozlowski, G. M. Williams, G. J. Sullivan, C. W. Farley, R. J. Anderson, J. Chen, D. T. Cheung, W. E. Tennant, and R. E. DeWames, IEEE Trans. of Elect. Dev., **38**, 1124 (1991).
8. L. H. Peng, H. Ehrenreich, R. V. Jones, and C. G. Fonstad, J. Appl. Phys., **77**, 747 (1995), R. Q. Yang, Appl. Phys. Lett., **66**, 959 (1995).
9. L. Lundqvist, J. Y. Andersson, Z. F. Paska, J. Borglind, and D. Haga, Appl. Phys. Lett., **63**, 3361 (1993).
10. B. F. Levine, G. Sarusi, S. J. Pearton, K. M. S. Bandara, and R. E. Leibenguth, "Quantum Well Intersubband Transition Physics and Devices" edited by H. C. Liu, B. F. Levine, and J. Y. Andersson, NATO ASI Series E: Applied Sciences- Vol. 270 (1994).

Table I. Relative experimental peak responsivity of devices A (with no grating), B (grating period = 4.6 μm), C (grating period = 3 μm), and D (no grating, 45° incidence) in the two atmospheric windows.

DEVICES	A	B	C	D
GRATING	NONE	d_B= 4.6 μm	d_C = 3 μm	45° facet
8-12 μm (diffraction angle)	0.34 -----	0.68 (41°)	1.32 (78°)	1 ----
3-6 μm (diffraction angle)	0.52 ----	0.68 (19°, 42°, 87°)	0.83 (31°, 90°)	1 ----

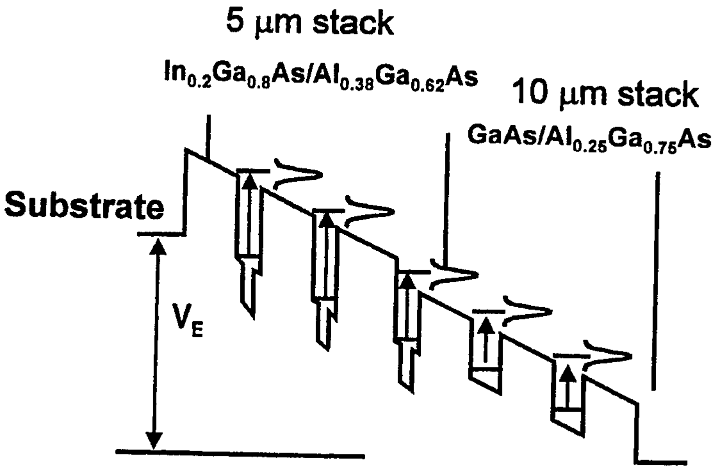

Fig 1. The energy band structure of the two-stack, two-color QWIP. There are 20 periods in each MQW stack.

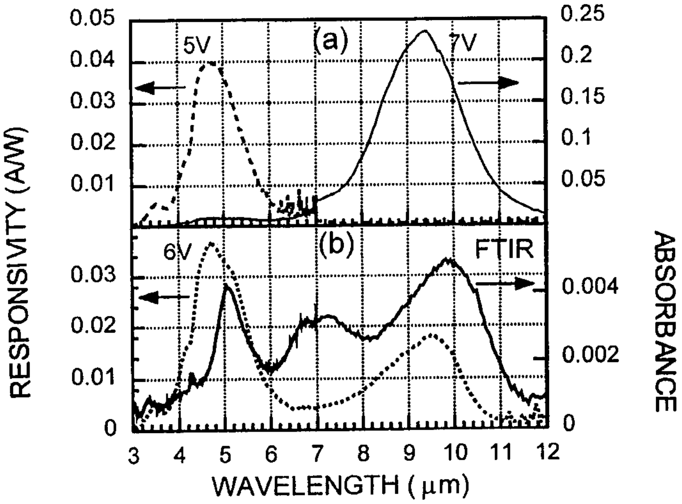

Fig 2. Responsivity of device (45° incidence) at (a) V = 5 V (dash curve) and 7 V (solid line), and (b) V = 6 V (dotted line) and FTIR absorption spectrum.

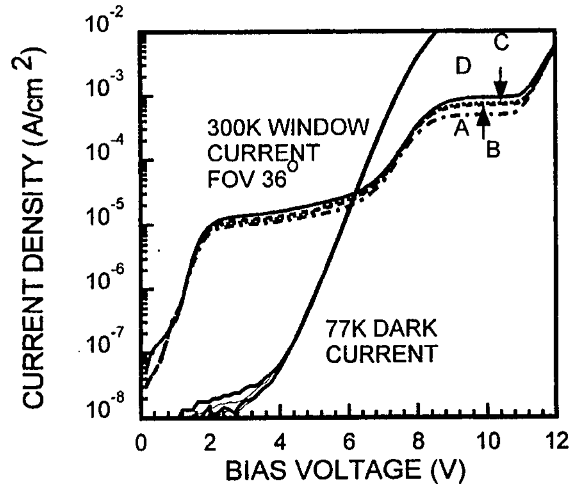

Fig 3. 77 K dark current of the four devices, and the 300 K background window current of the four devices measured at 10 K with a field of view 36°. A (with no grating), B (grating period = 4.6 μm), C (grating period = 3 μm), and D (no grating, 45° incidence).

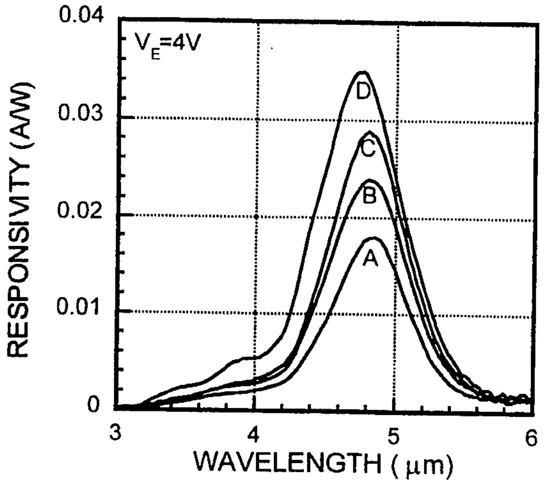

Fig 4. Responsivity of device A (with no grating), B (grating period = 4.6 μm), C (grating period = 3 μm), and D (no grating, 45° incidence) in the 3 μm to 6 μm region at V = 4 V.

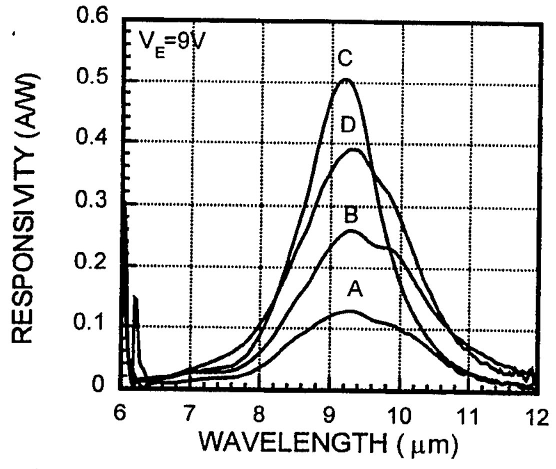

Fig 5. Responsivity of device A (with no grating), B (grating period = 4.6 μm), C (grating period = 3 μm), and D (no grating, 45° incidence) in the 8 μm to 12 μm region at V = 9 V.

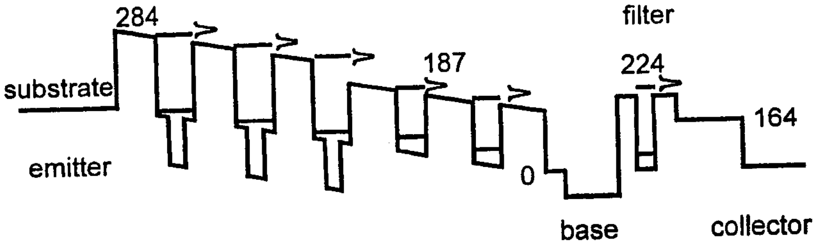

Fig 6. The two-stack, two-color QWIP with an electron band pass filter made of 40 Å $Al_{0.3}Ga_{0.7}As$ as barriers and 55 Å GaAs as the well. The band pass energy is 224 meV with a bandwidth of 20 meV.

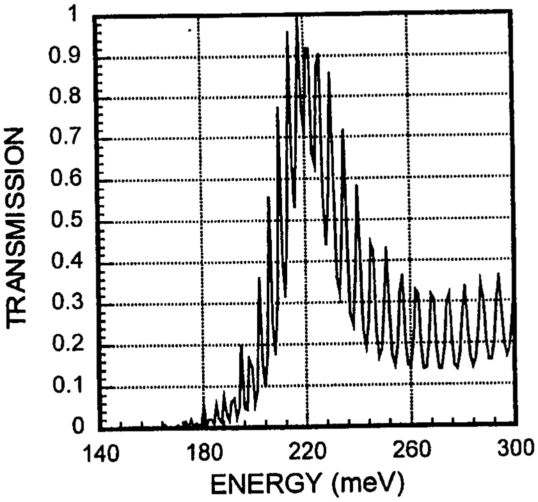

Fig 7. The transmission of the band pass filter as the function of the electron energy.

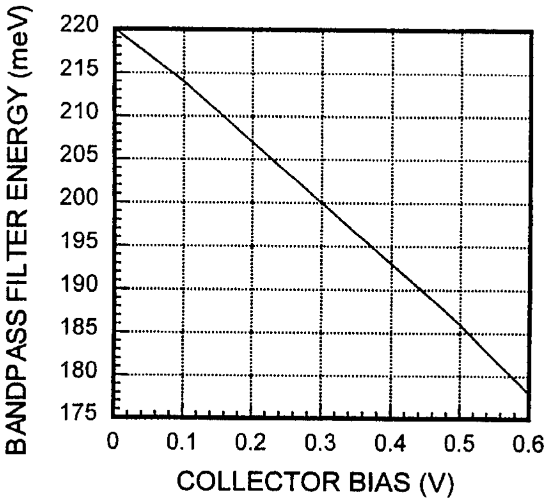

Fig 8. Calculated relationship between the band pass filter energy and the collector bias.

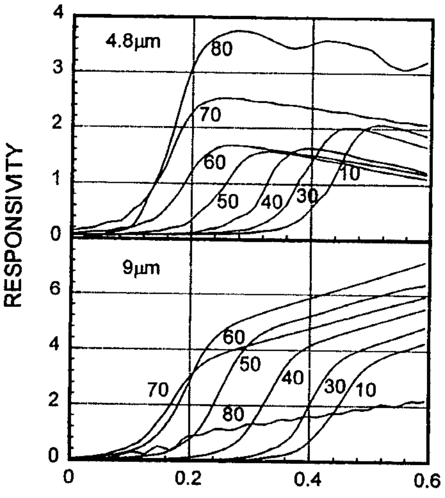

Fig. 9. The collector responsivity of the two stacks at different temperature as a function of collector bias (V_E=8 V).

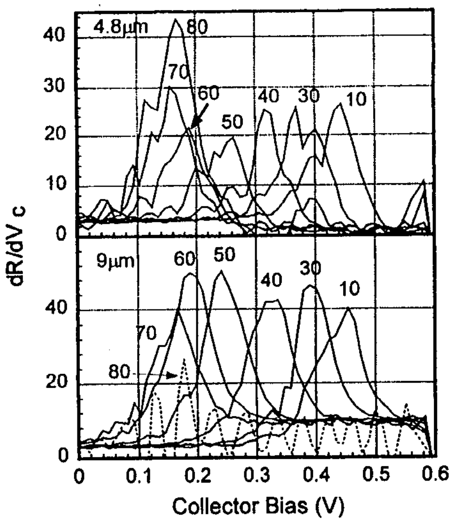

Fig 10. The hot electron distribution of the two stacks at different temperature as a function of collector bias (V_E=8 V).

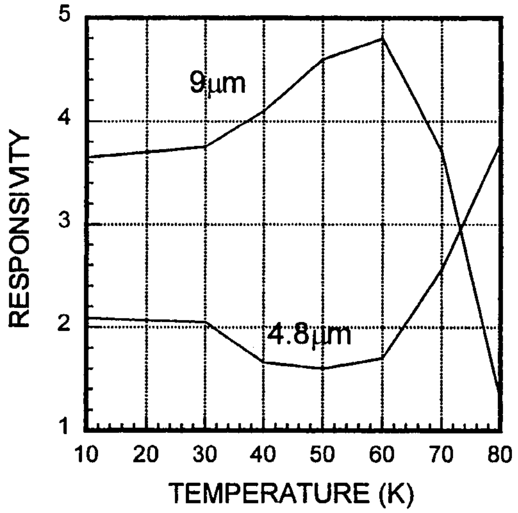

Fig 11. The collector responsivity change of the two stacks as a function of temperature.

LONG-WAVELENGTH (8-14 µm) InAsSb-BASED HETEROSTRUCTURE INFRARED PHOTODETECTORS

J. D. Kim, D. Wu, J. Wojkowski, S. J. Park, Y. H. Choi,
J. Xu, J. Piotrowski, and M. Razeghi

Center for Quantum Devices, Department of Electrical Engineering and
Computer Science, Northwestern University, Evanston, Illinois 60208

High performance $InAs_{1-x}Sb_x$ photodetectors operated without cryogenic cooling in the 3-14 µm region are reported. The photodetctors are based on $InAs_{1-x}Sb_x/InSb$ heterostructures grown on (100) semi-insulating GaAs substrates by low pressure metalorganic chemical vapor deposition (LP-MOCVD). Photoresponse up to 14 µm has been obtained in an $InAs_{0.23}Sb_{0.77}$ photoconductor at 300 K, which is in good agreement with the measured infrared absorption spectra. The effective carrier lifetime was calculated to be 0.14ns at 300 K. A photovoltaic detector with the p^+-InSb/p-$InAs_{0.15}Sb_{0.85}$/n^+-InSb double heterojunction showed photoresponse up to 13 µm at 300 K with a peak responsivity of 9.13×10^{-2} V/W at 8 µm.

INTRODUCTION

Photodetectors operating in the 8-12µm wavelength range are of great importance for applications in infrared (IR) thermal imaging. HgCdTe has been the dominant material system at this wavelength range. However, it suffers from instability and non-uniformity problems over large area due to high Hg vapor pressure during material growth. As an alternative, there has been a lot of interest in the use of InAsSb alloys and strained layer superlattices (1-7) because of the advanced material growth and processing technology available for InSb-based materials.

Earlier data suggested that InAsSb can exhibit a cut-off wavelength up to 10 µm at 77 K and 12.5 µm at 300 K (1). Some recent experimental results demonstrated that the cutoff wavelength of InAsSb epitaxial materials can be longer than 12.5 µm at near room temperature(3). This may be due to structural ordering (8,9). However, the exact mechanism has not been explained yet. In comparison to $Hg_{1-x}Cd_xTe$, $InAs_{1-x}Sb_x$ exhibits inherent advantages of high stability, well behaved donor and acceptor impurities, high mobility, and availability of low cost and high quality substrates such as GaAs. These results show promise for long-wavelength (8-14 μm) InAsSb photodetectors operated at near room temperature. However, InAsSb photodetectors have poor performance at high temperatures due to strong thermal generation and recombination of charge carriers. Several solutions have been proposed to suppress the noise due to thermal generation (10,11). These include the optimization of the detector structure by controlling the composition, doping level, and thickness.

In this paper, we report $InAs_{1-x}Sb_x$ photodetectors operated without cryogenic cooling in the 8-14 μm range. A cut-off wavelength around 14 μm was observed at 300 K.

MATERIAL GROWTH AND CHARACTERIZATION

The photodetectors are InAsSb-based heterostructures grown on (100) semi-insulating GaAs by LP-MOCVD. Trimethylindium, trimethylantimony, and 5% arsine diluted in hydrogen were used as precursors. N- and p-type doping were achieved by Sn and Zn using tetraethyltin and diethylzinc as respective precursors.

Structural characterization on the epitaxial layer was performed using high-resolution x-ray diffraction spectra at (400) orientation. The composition has been determined from x-ray diffraction data using Vegard's law.

Hall measurements were performed using a Bio–Rad HL 5560 system and Van der Pauw method at both 300 K and 77 K. A p-doped InAsSb epitaxial layer exhibited n–type conductivity at 300 K with a concentration of $3 \cdot 10^{16}\,cm^{-3}$ and mobility of 36,000 $cm^2/V \cdot s$. At 77 K, p-type conductivity was observed with a concentration of $3.6 \cdot 10^{16}\,cm^{-3}$ and mobility of 923 $cm^2/V \cdot s$. The change in sign of Hall coefficient shows that the layer is p-type and has bulk-like carrier transport property (7).

Infrared optical transmission measurements were carried out using a Fourier Transform Infrared (FTIR) spectrometer. Significant absorption at wavelengths exceeding 10 μm was clearly observed. The optical bandgap was determined as the photon energy at which the absorption coefficient is equal to 500 cm^{-1} (Fig. 1). A bandgap of ≈103 meV and ≈83 meV was derived for an $InAs_{1-x}Sb_x$ layer with $x=0.77$ and $x=0.65$, respectively.

DEVICE FABRICATION AND CHARACTERIZATION

Detector structures

The photoconductors consist of 2.8μm p-InAsSb/1.2μm p-InSb heterostructures grown on GaAs substrate. To reduce Auger generation-recombination rate at near room temperature, p-type doping with $3\times10^{16}cm^{-3}$ is used in the active InAsSb layer. The p-type InSb layer, which is doped at the same level as InAsSb, acts both as a buffer layer for the growth and a carrier confinement layer.

For the realization of InAsSb photovoltaic detectors, p^+-InSb/p- $InAs_{1-x}Sb_x$/n^+-InSb double heterojunction structures were grown on semi-insulating GaAs substrates. The bottom n^+-InSb layer with 2 μm thickness was doped at $2\times10^{18}cm^{-3}$ both for increased quantum efficiency due to the pronounced Moss-Burstein effect and for a low series resistance due to high electron mobility. The doping level of the active $InAs_{1-x}Sb_x$ layer was $3\times10^{16}cm^{-3}$ to suppress the Auger generation-recombination rate at near room temperature. The thickness of the active layer was around 5 μm which ensures both high quantum efficiency and high optical gain. The top contact layer p^+-InSb was 0.5 μm thick and doped at the level of $10^{18}cm^{-3}$.

Device processing

The geometry of the photoconductor is rectangular 4×3 mm^2. Au/Ti contacts were deposited by an e-beam evaporator. The sample had resistance of 23 Ω at room temperature and 220 Ω at 200 K.

Photovoltaic detectors were fabricated with simple 400×400 μm^2 mesa structures prepared by standard photolithography techniques and wet chemical etching. Ohmic contacts for both n- and p- type layers were made by depositing Au/Ti by e-beam evaporator. The contact pattern was defined again by standard photolithography techniques and selective etching ($KI:I_2:H_2O$ for Au and HF for Ti etching). The chips were assembled using standard integrated circuit technologies including die separation, mounting, and Au-wire bonding.

Measurements

The photodetectors were mounted in a liquid nitrogen cooled cryostat system and measurements were taken at temperatures between 77 K and 300 K. The relative photoconductivity spectra were measured with a FTIR spectrometer. Then the responsivity was calibrated using a blackbody test set, which is composed of a blackbody source (Mikron 305), preamplifier (EG&G PA-6), lock-in amplifier (EG&G 5209), and chopper system (Stanford Research System SR540). Responsivity measurements as a function of frequency showed that the thermal effect could be neglected at frequency higher than 200 Hz. The measurements were carried out with a blackbody source at a temperature of 800 K and modulating frequency of 450 Hz.

Photoconductors

Fig. 2 shows the spectral responsivities of the photoconductor sample at 200 K and 300 K. The peak responsivity at 300 K is about 4.0×10^{-3} V/W at 8 μm under bias voltage of 1 volt. A cut-off wavelength around 14 μm was observed at 300 K. The relatively noisy spectral response may be caused by the noise of the FTIR preamplifier since the contribution of thermal response is found negligible at measuring frequency of 1.2 KHz.

Fig. 3 displays the bias voltage dependent responsivity at 10.6 μm. It increases with applied voltage and reaches saturation at around 3 volts, which corresponds to a value of 5.8×10^{-3} V/W at 300 K and 1.08×10^{-2} V/W at 200 K

Based on the voltage responsivity, the electron mobility-effective carrier lifetime product $\mu_e\tau$ and effective carrier lifetime τ can be derived. According to the simple theory of photoconductivity, the voltage responsivity is

$$R_v = \frac{q\lambda}{hc}\frac{\eta\mu_e\tau V_b R_D}{L^2}\left(1+\frac{1}{b}\right) \qquad [1]$$

where q is the electron charge, λ is the wavelength, g is the photoconductive gain, η is the quantum efficiency, b is the electron-to-hole mobility ratio, L is the detector length, V_b is the bias voltage, and R_D is the detector resistance. Assuming an internal quantum efficiency of ≈ 1, quantum efficiency η has been calculated using

$$\eta = (1-r)\frac{\left(1-e^{-\alpha t}\right)}{\left(1-re^{-\alpha t}\right)} \qquad [2]$$

where r is the reflectance, α is the absorption coefficient, and t is the thickness of the layer. The $\mu_e\tau$ has been determined using Eq. [1]. If μ_e is known, τ can be estimated. Using the electron mobility at 300 K, where intrinsic electrons dominate Hall effect, the effective lifetime was estimated to be ≈ 0.14 ns.

Photodiodes

Fig.4 shows a cross section of the photodiode structure and the voltage response at various temperatures. The temperature-dependent cut-off wavelength is clearly observed. Photoresponse up to 13 μm has been obtained at 300 K in an $InAs_{0.15}Sb_{0.85}$ detector. The peak voltage-responsivity is 9.13×10^{-2} V/W at 300 K. At 77 K, it is only

2.85×10^1 V/W, which is much lower than the expected value. Possible reasons are the poor interface properties due to lattice mismatch between the absorber and contact layers and high dark current due to the high doping level in the active layer.

CONCLUSIONS

We have successfully grown InAsSb/InSb epitaxial layers with proper doping level, thickness, and composition on GaAs substrate by LP-MOCVD. Long wavelength photodetectors operating at room temperature using Sb-based materials have been demonstrated. Photoresponse of InAsSb photodetectors operating in photoconductive and photovoltaic modes was observed at near room temperatures. Cut-off wavelength up to 14 µm was observed in $InAs_{0.23}Sb_{0.77}$ photoconductors at 300 K. The voltage-responsivity at 10.6 µm is 5.8×10^{-3} V/W at 300 K. The cut-off wavelength of an $InAs_{0.15}Sb_{0.85}$ photovoltaic detector is about 13 µm. The peak voltage-responsivity is 9.13×10^{-2} V/W at 300 K. This is the first observation of photoresponse in Sb-based materials at wavelengths up to 14 µm at room temperature.

ACKNOWLEDGMENTS

The authors would like to acknowledge the support of Dr. Y. S. Park of the Office of Naval Research and Dr. R. Balcerak of the Advanced Research Project Agency. This work was supported by the Office of Naval Research under contract No. N00014-92-J1951 and No. N00014-94-1-0902 and the Strategic Defense Initiative Organization under contract No. N0001493-1-0409.

REFERENCES

1. J. C. Wooley and J. Warner, Can. J. Phys. **42**, 1879 (1964).
2. R. M. Biefeld, J. Crystal Growth, **75**, 255-263 (1986).
3. C.G. Bethea, B. F. Levine, M. Y. Yen, and A. Y. Cho, Appl. Phys. Lett. **53**, 291 (1988).
4. M. Y. Yen, J. Appl. Phys. **64**, 3306 (1988).
5. W. Dobbelaere, J. De Boeck, W. De Raedt, J. Vanhellemont, G. Zou, M. Van Hove, B. Brijs, R. Martens and G. Borghs, *Mat. Res. Soc. Proc.* **216**, 181 (1991).
6. A. Rogalski, SPIE Optical Engineering Press, Bellingham, Washington, (1994).
7. C. Besikci, Y. H. Choi, G. Labeyrie, E. Bigan, and M. Razeghi, J. Appl. Phys. **76**, 5820 (1994)

8. H. R. Jen, K.Y. Ma and G. B. Stringfellow, Appl. Phys. Lett. **54**, 1154–1156 (1989).
9. S. R. Kurtz, L. D. Dawson, R. M. Biefeld, D. M. Follstaedt and B. L. Doyle, Phys Rev. B46, 1909 (1992).
10. J. Piotrowski., in Infrared Photon Detectors, Chapter 11, ed. by A. Rogalski, SPIE, Bellingham (1995).
11. J. Piotrowski and M. Razeghi, Proc. SPIE **2397**, 180 (1995).

FIGURES

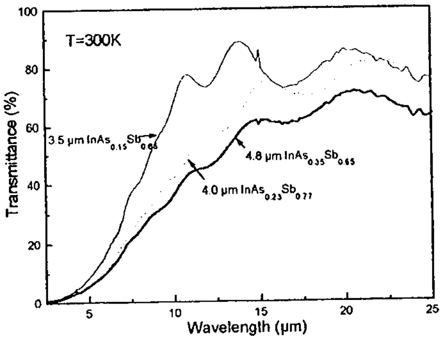

Fig. 1. Transmission spectra of InAsSb with different compositions.

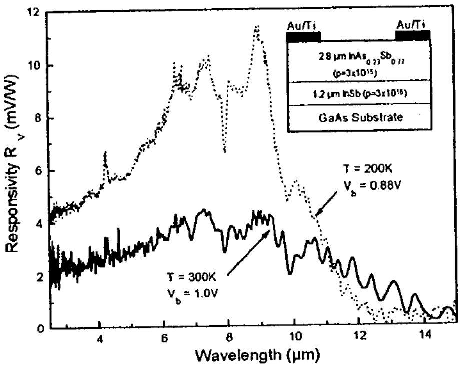

Fig.2. Spectral response of the $InAs_{0.23}Sb_{0.77}$ photoconductor at 200 K and 300 K.

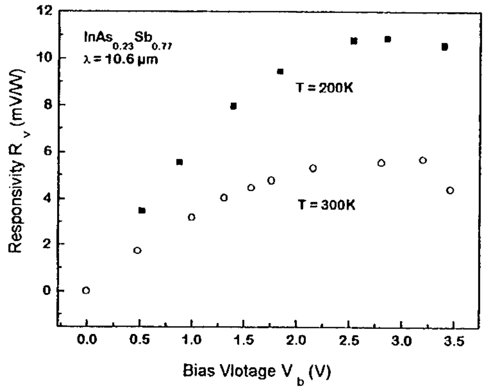

Fig. 3. Voltage-dependent responsivity of the $InAs_{0.23}Sb_{0.77}$ photoconductor at 10.6 μm.

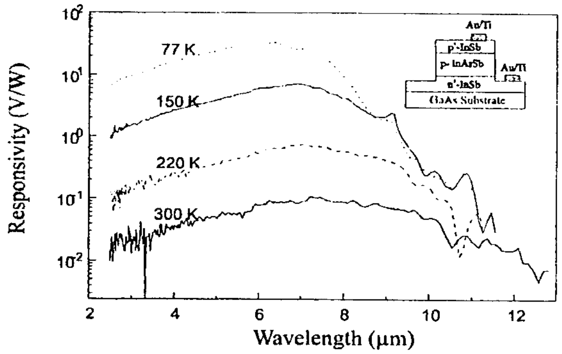

Fig. 4. Spectral responsivities of $InAs_{0.15}Sb_{0.85}$ photovoltaic detector.

GaInSb/InAs Type-II Superlattices for 10µm IR Detector Applications

R. H. Miles and J. A. Wilson*
Hughes Research Laboratories, Malibu CA 90265
**Santa Barbara Research Center, Goleta CA 93117*

ABSTRACT

Interest in infrared detectors based on GaInSb/InAs superlattices is predicated largely on calculated performances superior to those of HgCdTe and multi-quantum well devices, and on advantages in multicolor applications. Significant improvements in the optical quality of these superlattices have recently led to the realization of long wavelength detectors comparable in performance to those based on HgCdTe, although still below those projected for this technology. Single element superlattice detectors with $R_0A \approx 10\ \Omega$-cm^2 ($D^* \approx 1.5\times10^{11}$ cm$\sqrt{\text{Hz}}$/W) have been demonstrated at a temperature of 85K for energy gaps beyond 12µm. Work in two color, triple layer, heterojunction devices is now focusing on improved device designs making use of compatibility with the InAs/GaSb/AlSb family of semiconductors.

THEORETICAL

While III-V detectors are employed in a wide range of high performance mid-wave infrared (MWIR) focal plane systems, their application at longer wavelengths has been slowed by the immaturity of the heterostructures required or of the materials proposed. However, the desirability of III-V alternatives to devices based on HgCdTe has stimulated research in numerous directions, including quantum well intersubband photodetectors (QWIPs),[1,2] InAsSb epilayers and superlattices,[3,4] GaInSb/InAs superlattices,[5,6] and Tl-containing III-V alloys.[7] Our efforts have focused upon GaInSb/InAs superlattices as they are composed of fairly conventional materials, offer higher ultimate performance than the QWIPs or InAsSb, and are compatible with a family of "6.1Å" semiconductors, allowing flexibility in device design. Little experimental work has yet been devoted to the Tl-containing compounds.

Grein *et al.* have compared calculated detectivities for GaInSb/InAs and HgCdTe devices and find typical operating temperature enhancements of 20-50% for thick, long wavelength (8-12µm) detectors.[8] Predicted benefits derive mainly from Auger recombination and tunneling rates which are reduced relative to conventional technologies.[6] Both are consequences of the electronic band structure of GaInSb/InAs superlattices, which differs qualitatively from that of bulk zinc blende materials. Of greatest importance to detectors is typically the splitting between the light- and heavy-hole band edges, which can appreciably exceed the energy gap of this superlattice for long and very long wavelength infrared cutoffs. This splitting results in large imaginary wavevectors for states in the superlattice gap, reducing the probability of tunneling and hence the noise associated with this leakage mechanism. Further, designing a structure to have a minigap between superlattice subbands one energy gap below the valence band edge suppresses Auger processes for which the in-plane wavevector is small ($k_{\parallel} \approx 0$). Energy and momentum conservation require that an electron recombine with a hole having a sizable in-plane wavevector, but dispersion in $k_{\parallel}$ makes such a state unlikely to be occupied by a hole at low temperatures. Auger processes often dominate radiative processes in HgCdTe, whereas the opposite is often true in the GaInSb/InAs superlattice.

EXPERIMENTAL

While GaInSb/InAs superlattices of nearly ideal structural quality have previously been demonstrated,[9] their application as infrared detectors competitive with HgCdTe in both detectivity and operating temperature has been hindered by significant extrinsic problems, perhaps greatest of which is a high density of efficient Shockley-Read non-radiative recombination centers. However, we have recently demonstrated significant improvements in the optical quality of these superlattices by using a monomeric Sb source during growth by molecular beam epitaxy (MBE), in combination with a post-growth annealing procedure.[10] Coincident with increased optical efficiencies are reductions in background doping densities, leading us to speculate that use of monomeric Sb and an anneal alters the density or nature of point defects native to the GaInSb layers and/or superlattice interfaces.[11]

A typical single-color GaInSb/InAs detector structure is illustrated schematically in Fig. 1. Unlike the case of HgCdTe, p-type absorbing layers are desirable in the superlattice, for reasons of both transport and carrier lifetime. Although Auger processes can be suppressed in n-type superlattices, the effect is usually greater in p-type structures, and has already been demonstrated in non-optimized structures.[12] Further, growth-direction hole mobilities are predicted to be very small in these superlattices, while perpendicular electron mobilities should be similar to those of holes in HgCdTe ($\approx$500-1000 cm^2/V-s). Consequently good carrier collection efficiency is more practical for minority electrons than holes. We also note that the low hole mobility and ability to tailor an n-type superlattice for *shorter* lifetime are benefits in reducing noise currents associated with diffusion of minority carriers from the thin, $n+$ cap side of the photojunction.

Devices reported here incorporate active layers intentionally doped to densities of 10^{17} cm^{-3}, p-type. This is a near-optimal choice of doping for thick layer superlattice detectors.[13] Intrinsic detectivity is fairly insensitive to doping density for active layers with thicknesses less than the diffusion length, such as those considered here, in a radiatively dominated regime. (The diffusion-limited zero-bias resistance is given by

$R_0A = (kT/q^2t)(\tau_p/p_n)$, which is independent of doping density in the nondegenerate limit as both p_n and τ_n are proportional to $1/N_A$ for radiative processes.) However, the higher doping level is desirable in practice as it reduces excess carrier lifetimes below those of Shockley-Read centers, with intrinsic detectivity maintained fairly constant through a reduction in minority carrier concentration.

Any degradation of device performance associated with highly doping the active layers is expected to be primarily extrinsic in nature, rather than fundamental, and hence can in principle be avoided. An undoped layer was inserted at each *p-n* interface, with a thickness roughly equal to the depletion length of the material. This was employed to lower tunnel currents by reducing band bending at the heterojunction. Last, although the effects of higher doping densities on Shockley-Read lifetimes is not yet quantified, the observation of identical photoluminescent efficiencies in undoped and heavily doped mid-wave IR superlattices indicates negligible degradation of lifetime after intentional doping.[15]

GaInSb/InAs superlattice structures such as those depicted in Fig. 1 have yielded LWIR detectors comparable in performance to those based on HgCdTe, but still below those projected for this technology. Specifically, single element superlattice detectors with energy gaps beyond 12μm have been fabricated with $R_0A \approx 10$ Ω-cm^2 ($D^* \approx 1.5\times10^{11}$ cm√Hz/W) at a temperature of 85K. Temperature-dependent data are illustrated in Fig. 2 and values of R_0A summarized in Fig. 3. By comparison, HgCdTe arrays with 12μm cutoffs demonstrate comparable zero-bias impedances at 78K.

Although this LWIR performance is a record for high quantum efficiency III-V detectors operated at temperatures competitive with HgCdTe, the industry standard, impedances do not rise appreciably at shorter cutoff wavelengths, for reasons likely related to surface passivation. While the highest values of R_0A observed to date in GaInSb/InAs MWIR detectors are insensitive to temperature up to and beyond 200K, they rarely exceed 500 Ω-cm^2 for 3.5-4.0μm cutoffs. We suspect that this limit is associated with surface leakage, and are presently exploring surface passivation.

MULTICOLOR DEVICE DESIGN

In addition to work on single color detectors, we are developing sequential and simultaneous mode *p-n-p* two-color detectors. Both binaries and alloys are being explored for the n-type contact layer, as are AlSb/InAs superlattices. These particular superlattices benefit from ease of lattice match to a GaSb substrate, and can be tuned to provide conduction and valence band offsets well suited to isolating MWIR and LWIR junctions in forward and reverse bias.

A schematic of a two color device is illustrated in Fig. 4, with a band edge profile in Fig. 5. Although it is not essential to embed the electrical junctions within the GaInSb/InAs superlattices (instead placing them at the interface to a wider gap material such as an AlSb/InAs superlattice), we have chosen in initial devices to employ this design in view of uncertainties in superlattice band offsets. Use of a middle contact layer with a conduction edge not aligned to that of the active GaInSb/InAs superlattice layers would add a series resistance to the diode or increase leakage currents, depending upon whether the band edge of the wide gap layer lay above or below that of the detecting layers, respectively. As the conduction band edge of a structure such as an AlSb/InAs superlattice is readily tailored by adjusting constituent layer thicknesses, this issue is readily addressed experimentally; we have chosen to avoid it at the outset only to simplify the device for clarity. In its present form, the wide gap layer serves only to isolate LWIR and MWIR regions when the device is biased. Ultimately, this layer could in principle be employed at the heterojunction to suppress generation-recombination and tunneling processes in the depletion region, as well as diffusion of minority carriers from the wide gap layer.

CONCLUSIONS

GaInSb/InAs superlattices offer considerable potential for matching or surpassing the performance of HgCdTe -based detectors. Niches most immediately appropriate to the technology include very long wavelength detection, for which the uniformity and operating temperature advantages of the III-V superlattice are considerable, and multi-spectral detection, for which compatibility with other wide-gap III-V's holds significant advantages. Considerable progress has recently been made in growth of these superlattices by MBE. These successes are best illustrated by world record MWIR lasers,[16] but also underlie the demonstration of LWIR detectivities comparable to those of HgCdTe. The material can in all respects but maturity be regarded as a viable substitute for HgCdTe, suffering none of the diminished performance or adverse selection rules fundamental to the QWIP approach.[14]

ACKNOWLEDGMENTS

We are grateful to H. Dunlap, C. Haeussler, and L. Warren of HRL for their assistance in all aspects of the experimental work. We also wish to acknowledge G. Chapman and K. Kosai of SBRC for their ongoing roles in testing and modeling devices, respectively. RHM is indebted to C.H. Grein of the University of Illinois at Chicago, H. Ehrenreich of Harvard University, and D.H. Chow of HRL for numerous helpful insights and discussions. This work is supported in part by the Air Force Wright Patterson Laboratory under contract No. F33615-93-C-1354, and by ARPA/ONR under contract No. N00014-95-C-0107.

REFERENCES

1. J.S. Smith, L.C. Chiu, S. Margalit, A. Yariv, and A.Y. Cho, *J. Vac. Sci. Technol. B* **1**, 376 (1983).
2. L.J. Kozlowski, G.M. Williams, R.E. DeWames, K. Vural, V. Swaminathan, J.W. Stayt, Jr., K.G. Glogovsky, R.E. Leibenguth, L.E. Smith, and W.A. Gault, *Proc. 1st Intl. Symp. on Long Wavelength Infrared Detectors and Arrays: Physics and Applications; Electrochemical Society Proceedings* **94-5**, 5 (1995).
3. G. C. Osbourn, *J. Vac. Sci. Technol. A* **2**, 176 (1984).
4. S.R. Kurtz, *Proc. 1st Intl. Symp. on Long Wavelength Infrared Detectors and Arrays: Physics and Applications; Electrochemical Society Proceedings* **94-5**, 160 (1995).
5. D.L. Smith and C. Mailhiot, *J. Appl. Phys.* **62**, 2545 (1987).
6. R.H. Miles, J. N. Schulman, D. H. Chow, and T. C. McGill, *Semicond. Sci. Technol.* **8**, S102 (1993).
7. A. Sher, M. van Schilfgaarde, S. Krishnamurthy, M.A. Berding, and A.-B. Chen, *J. Electr. Materials* **24**, 1119 (1995).
8. C.H. Grein, H. Cruz, M.E. Flatté, H. Ehrenreich, *Appl. Phys. Lett.* **65**, 2530 (1994).
9. R. H. Miles, D.H. Chow, and W.J. Hamilton, *J. Appl. Phys.* **71**, 211(1992).
10. R.H. Miles, D.H. Chow, Y.-H. Zhang, P.D. Brewer, and R.G. Wilson, *Appl. Phys. Lett.* **66**, 1921 (1995).
11. P.D. Brewer, D.H. Chow, and R.H. Miles, *J. Vac. Sci. Technol.*, to be published.
12. E.R. Youngdale, J.R. Meyer, C.A. Hoffman, F.J. Bartoli, C.H. Grein, P.M. Young, H. Ehrenreich, R.H. Miles, and D.H. Chow, *Appl. Phys. Lett.* **64**, 3160 (1994).
13. P.M. Young, C.H. Grein, H. Ehrenreich, and R. H. Miles, *J. Appl. Phys.* **74**, 4774 (1993).
14. M. A. Kinch and A. Yariv, *Appl. Phys. Lett.* **55**, 2093 (1989) and **56**, 2354 (1990).
15. R.H. Miles, unpublished.
16. T.C. Hasenberg, R.H. Miles, A.R. Kost, and L. West, unpublished.

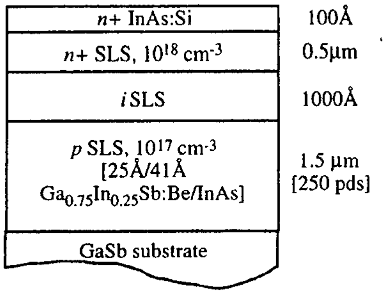

Fig. 1. Schematic of a baseline LWIR superlattice photovoltaic detector.

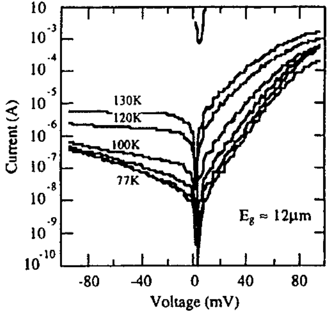

Fig. 2. Temperature dependent I-V characteristics of the device in Fig. 1.

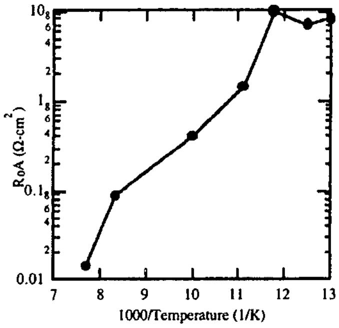

Fig. 3. R_0A for the device of Fig. 1, which has an energy gap beyond 12µm.

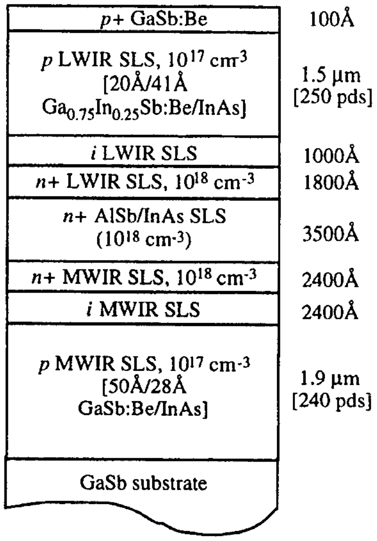

Fig. 4. Schematic of a 2-color detector based on GaInSb/InAs absorbing layers and an AlSb/InAs SWIR layer.

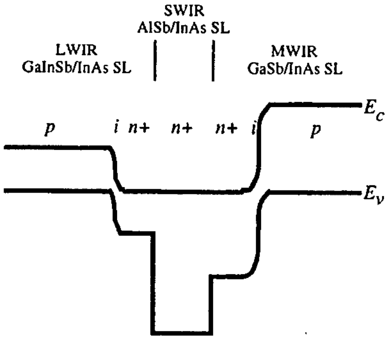

Fig. 5. Band edge profile for the 2-color detector of Fig. 4.

InAs/GaSb SUPERLATTICES FOR INFRARED DETECTION: STRUCTURAL CHARACTERIZATION AND OPTICAL PROPERTIES

J. Wagner, F. Fuchs, N. Herres, J. Schmitz, and P. Koidl
Fraunhofer-Institut für Angewandte Festkörperphysik,
Tullastrasse 72, D-79108 Freiburg, Federal Republic of Germany

$InAs/Ga_{1-x}In_xSb$ superlattices (SLs) are of current interest because of their potential application in infrared optoelectronic devices. We present a detailed study of the structural and optical properties of InAs/GaSb SLs with either InSb-like or GaAs-like interfaces (IFs). The SL structures were grown by molecular-beam epitaxy on top of a strain-relaxed GaSb buffer layer on (100) GaAs substrates. Special emphasis is laid on the dependence of the SL properties on the type of IF bonds formed. SLs with InSb-like IFs were found to have superior structural and luminescence properties, which allowed us to fabricate InAs/GaSb SL p-i-n diodes with InSb-like IFs showing photovoltaic response and electrically pumped emission up to room-temperature.

INTRODUCTION

Current work on $InAs/Ga_{1-x}In_xSb$ ($x \leq 0.4$) superlattices (SLs) is motivated by potential applications of these SLs in infrared detectors and lasers covering the 3 to 20 μm wavelength range (1-3). Because of the broken gap type-II band alignment between InAs and GaSb a spatially indirect SL band gap occurs for sufficiently thin InAs and/or GaSb layer thicknesses (4). The gap energy of InAs/GaSb short-period SLs can be adjusted by varying the individual layer widths (5). Since both the cation and the anion change across the InAs/GaSb interface (IF), there are two possible types of IF bonds, either InSb-like or GaAs-like, the formation of which can be controlled by the shutter sequence during the molecular-beam epitaxial growth. Here we report on the structural and optical properties of InAs/GaSb SLs grown with both types of IFs, thereby putting the emphasis on the dependence of these properties on the type of IF bonds.

EXPERIMENTAL

SL samples were grown by solid-source molecular-beam epitaxy (MBE) on undoped (100) GaAs substrates. Molecular beams of Sb_2 and As_2 were used with V_2/III beam equivalent pressure ratios between 1 and 2 for the growth of GaSb and 10 to 15 for the growth of InAs. Sample growth started with a GaAs buffer layer and a GaAs/AlAs SL, followed by a 100 nm thick AlSb nucleation layer and a GaSb/AlSb smoothing SL. Then a 1.1 μm thick GaSb buffer layer was deposited on top of which the 100 period InAs/GaSb SL was grown at a substrate temperature of 420°C. The InAs layer width was varied from 4 to 14 monolayers (ML), while the GaSb layer thickness was kept constant at 10 ML. Two series of SLs were grown with the shutter sequence for the growth of the interfaces chosen for the deposition of either 1 ML InSb or 1 ML GaAs, resulting in the formation of either InSb-like or GaAs-like interface bonds. For further details on sample growth see Ref. 6.

The structural properties of the SL samples were analyzed by high-resolution X-ray diffraction (HRXRD) measurements, including two-dimensional diffraction space maps, and Raman spectroscopy. Interband optical transitions across the effective SL band gap and across higher-lying band gaps were studied using Fourier-transform photocurrent (PC) and photoluminescence (PL) spectroscopy as well as spectroscopic ellipsometry.

RESULTS AND DISCUSSION

As an example of the HRXRD measurements the reflection profile of a 10 ML InAs/10 ML GaSb SL with InSb-like interfaces is displayed in Fig. 1. The measured profile covering the 004 reflection range shows besides diffraction peaks originating from the GaAs substrate, the AlSb nucleation layer, and the GaSb buffer layer, well resolved SL reflection peaks up to the 4th order indicated by "0", "±1", etc. The narrow widths of the SL peaks and the considerable intensities of the higher-order peaks indicate a good structural quality of the SL. For comparison also a simulated reflection profile is shown which reproduces well the peak positions and relative peak widths (7). For all samples studied, the SLs with InSb-like IFs showed significantly narrower SL reflection peaks than the SLs with GaAs-like IFs.

In Fig. 2 the average lattice parameters of the SL stack parallel ($a_{\parallel}$, Fig. 2 (a)) and perpendicular to the growth surface ($a_{\perp}$, Fig. 2 (b)), deduced from the X-ray diffraction profiles, are plotted versus the nominal width of the InAs layers. For the SLs with InSb-like IFs the lattice parameter $a_{\parallel}$ is close to the value of the strain relaxed GaSb buffer layer, which indicates lattice matched growth of the SL stack on the GaSb buffer. This holds also, at least for InAs layer thicknesses exceeding 6 ML, for the lattice parameter $a_{\perp}$, which reflects a nearly cubic metric. For SLs with GaAs-like IFs and InAs layer thicknesses ≥6 MLs the lattice parameter $a_{\perp}$ is significantly smaller than that of the GaSb buffer, whereas the lattice parameter $a_{\parallel}$ is still close to that of the buffer layer. These findings show that the SLs with GaAs-like IFs are under biaxial tension. From a profile fit to the broadened X-ray reflection peaks, an increasing relaxation of the strain within the SL stack with increasing distance from the buffer/SL interface has been deduced (7). For the 4 ML InAs/10 ML GaSb SL with GaAs-like IFs $a_{\perp}$ and $a_{\parallel}$ are equal, both lattice parameters being smaller than that of the GaSb buffer layer, which indicates a complete relaxation of the SL stack.

The results of the present HRXRD analysis are consistent with the view that InAs/GaSb SLs grown on a GaSb buffer with InSb-like IFs, are close to strain compensation because the larger lattice parameter of the InSb IF layers at least partially offsets the smaller lattice parameter of the InAs layers, depending on the SL period. For SLs with GaAs-like IFs, in contrast, the smaller lattice parameter of both the GaAs IF layers and of the InAs layers add up to an average SL parameter significantly smaller than that of the GaSb buffer layer. Thus, SLs with GaAs-like IFs are subjected to a significant tensile strain with a critical thickness for the onset of strain relaxation much smaller than for SLs with InSb-like IFs.

Fig. 3 shows low-temperature Raman spectra of two 4 ML InAs/10 ML GaSb SLs grown with shutter sequences appropriate for the formation of either In-Sb IF bonds (top spectrum) or Ga-As IF bonds (bottom spectrum). The spectra were recorded with optical excitation close to resonance with the 2.2 eV interband transition of the SL (8). Both SLs show scattering by longitudinal optical SL phonons (LO(InAs/GaSb)) in the frequency range 220 to 250 cm^{-1} (9,10). For the intended growth of GaAs-like interfaces the GaAs-like IF mode (IF(GaAs)) at 256 cm^{-1} is the dominant feature in the Raman spectrum (9,10). The intended growth of In-Sb IF bonds results in a complete disappearance of the GaAs-like IF mode. Instead, an InSb-like IF mode (IF(InSb)) appears at 190 cm^{-1} (9,10). The InSb-like IF mode, on the other hand, is not detected for the SL grown with nominally GaAs-like IF bonds. Thus, the present Raman spectra clearly demonstrate that MBE growth of InAs/GaSb SLs with essentially pure GaAs-like or InSb-like IFs has been achieved.

In addition to Raman scattering by longitudinal optical SL phonons and mechanical IF modes the InAs/GaSb SLs under study show well resolved scattering by zonefolded longitudinal acoustic (LA) phonons (11). Under resonant excitation, for SLs with InSb-like IFs zonefolded LA phonon doublets up to the 7th order were observed, whereas SLs with GaAs-like IFs showed such doublets up to the 5th order (11). The finding that for SLs with GaAs-like IFs zonefolded LA phonons were observed only up to lower orders than for corresponding SLs with InSb-like IF bonds, reflects the lower structural quality of the SLs with GaAs-like IFs observed already in the HRXRD analysis. In Fig. 4 the frequencies of the zonefolded LA phonon lines are plotted versus the average SL period, determined by HRXRD, for N ML InAs/10 ML GaSb SLs with InSb-like IFs. Also shown are calculated frequencies of zonefolded LA phonons as a function of the SL period P_{SL}. The calculations are based on the elastic continuum model with the frequency Ω of the $\pm m^{th}$ mode given by (12):

$$\Omega_{\pm m} = (m\,\pi/P_{SL} \pm \Delta k)\, v_{aver}. \qquad [1]$$

Here Δk is the momentum transferred in the backscattering experiment, which equals twice the momentum of the incident photon, and v_{aver} is the averaged sound velocity of the SL (11,12). There is excellent agreement between the experimental data and the calculated frequencies in particular for the lower order doublets. This agreement demonstrates the consistency of the present Raman spectroscopic data and the HRXRD results regarding the period of the SLs. For SLs with GaAs-like IFs (not shown here), however, the zonefolded LA phonon doublets occurred at consistently higher frequencies than for corresponding SLs with InSb-like IFs (11). According to Eq. 1 this frequency shift can be caused by either a reduction of the SL period or by an increase of the average sound velocitiy. As the SL periods determined by HRXRD were found to be very similar for both types of IF bonds (7), it has been concluded that the formation of GaAs-like IF bonds results in an increase of the average sound velocity (11).

The energetic position of the effective SL band gap was determined by low-temperature PL spectroscopy and in-plane PC measurements. The resulting band gap energies are plotted in Fig. 5 versus the nominal width of the InAs layers. For SLs with InSb-like IFs gap energies could be extracted from both the PL and the PC measurements, whereas for SLs with GaAs-like IFs the PL efficiency was too low for an accurate determination of the SL band gap. This difference in PL efficiency indicates a significant reduction in the minority carrier lifetime for SLs with GaAs-like IFs compared to SLs with InSb-like IFs (13). For the SLs with InSb-like IFs the band gap energies extracted from the PL and PC measurements agree well with each other and for InAs layer widths ≥6 ML a linear reduction of the gap energy with increasing InAs layer width is observed. The same holds for SLs with GaAs-like IFs and InAs layer widths ≥8 ML. The slope, however, is different and both curves intersect for an InAs layer width of 10 ML. One reason for the dependence of the SL band gap on the type of IF bonds is the difference in the strain situation within the SL stack because of the strain dependence of the fundamental gaps and of the band alignment (14). Another reason is the effect of the different IF dipoles, depending on the type of IF bond formed, on the band overlap and thus on the effective SL band gap (15). At InAs layer widths below 6 ML for InSb-like IFs and below 8 ML for GaAs-like IFs the experimental band gap energies deviate from the expected linear dependences towards lower energies. This lowering of the gap energy correlates with the strain relaxation observed in these SLs by HRXRD (see Fig. 2).

To probe interband transitions across higher lying band gaps, such as the E_1 and $E_1+\Delta_1$ gap, spectroscopic ellipsometry has been used (8). The imaginary part of the pseudodielectric function (ϵ_2), derived from room-temperature ellipsometric measurements in the 1.5 to 3.1 eV range, is plotted in Fig. 6 for two pairs of InAs/GaSb SLs with either InSb-like or GaAs-like IFs and InAs layer widths of 4 and 14 ML. Two interband transitions are resolved which occur for the 14 ML InAs/10 ML GaSb SLs at energies of 2.0 and 2.4 eV, irrespective of the type of IF bond (8).

The intensities and widths of these transitions, however, depend on the type of interface bonds with the two transitions being less well resolved for the SL with GaAs-like IFs. This observation is consistent with the lower structural quality of SLs with GaAs-like IF bonds. For the 4 ML InAs/10 ML GaSb SLs, however, also the transition energies were found to depend on the type of IF bonds. They are by 30 to 50 meV lower in energy for the SL with InSb-like IFs than for the SL with GaAs-like IFs (8). This shift of the interband transition energies can be related to the fact that both SLs are strain relaxed with lattice parameters significantly smaller (GaAs-like IFs) or slightly larger (InSb-like IFs) than that of the GaSb buffer (see Fig. 2). The present results are consistent in that the SL with the larger volume of the reduced unit cell shows, as expected, the lower transition energies.

The energetic position of the 2 eV interband transition averaged over the two different types of IF bonds is essentially independent of the InAs layer width (8), which indicates that for this transition, which can be assigned to the E_1 band gap of GaSb, quantisation effects are small. The averaged position of the 2.4 eV transition, however, increases by about 40 meV when the InAs layer width is reduced from 14 to 4 ML (8). Based on band gap energies and band overlaps taken from the literature (16-18) a band offset between the L conduction band minima of about 0.1 eV can be estimated with the band minima of InAs being lower in energy. Therefore the InAs E_1 gap transition can be expected to show quantisation effects resulting in an increasing transition energy with decreasing InAs layer width. Thus, the above estimate is consistent with the experimental observation of a high-energy shift of the 2.4 eV interband transition which can be assigned to a superposition of the E_1 band gap of InAs and the $E_1+\Delta_1$ gap of GaSb. However, this apparent consistency has to be taken with caution as the observed energy shifts lie within the accurracy limits of the available band structure data as well as of the ellipsometric data.

For the realisation of p-i-n diodes InAs/GaSb SLs with InSb-like IFs were grown with a 0.5 μm thick Be-doped GaSb p-contact layer on top of the GaSb buffer layer, followed by 100 periods of an undoped SL and a 50 period SL with Si-doped InAs layers acting as the n-contact. Unpassivated mesa structures were fabricated using standard photolithography and a combination of wet chemical etching and chemically assisted reactive ion beam etching (CAIBE). Fig. 7 shows the photovoltaic response and the PL and electroluminescence (EL) spectra recorded at low temperatures of a 10 ML InAs/10 ML GaSb p-i-n diode. The photovoltaic response shows a well defined onset at 0.3 eV (4.1 μm). At the same energy both the PL and the EL spectrum shows a narrow peak which originates from radiative recombination in the undoped SL region. In addition to this luminescence from the undoped region the PL spectrum shows a high-energy shoulder, not present in the EL spectrum, which arises from radiative recombination in the n-contact region. Because of band filling due to the n-type doping of the InAs layers, luminescence from the n-type SL extends to higher energies than that from the undoped SL. A 8 ML InAs/10 ML GaSb

SL p-i-n diode emitting at 0.35 eV (3.5 μm) showed electrically pumped emission up to room-temperature (19).

CONCLUSIONS

The structural and optical properties of InAs/GaSb SLs grown on top of a strain-relaxed GaSb buffer on (100) GaAs substrates by MBE have been studied by HRXRD, Raman spectroscopy, PC and PL spectroscopy, and spectroscopic ellipsometry. SLs with InSb-like IFs were found to be coherently strained and showed superior structural and luminescence properties. By contrast, SLs with GaAs-like IFs were found to be under biaxial tension showing significant strain relaxation. They showed a luminescence intensity by two orders of magnitude lower than SLs with InSb-like IFs. The variation of the energetic position of the SL band gap as a function of the InAs layer width was found to depend on the type of IF bond, reflecting the effect of both strain and different IF dipoles on the SL gap energy. Also, the spectrum of higher-lying interband transitions in the range of the E_1 and $E_1+\Delta_1$ band gaps of InAs and GaSb showed a dependence on the interfacial bonding in particular for the narrowest InAs layer widths. We note that the observed effect of the IF bonds on the interband optical properties arises from a combination of differences in the structural properties and of different IF dipoles. It is difficult to distinguish between these two different contributions from the present experiments. The superior properties of structures with InSb-like IFs allowed us to fabricate SL p-i-n diodes which showed photovoltaic response and electroluminescence up to room-temperature.

ACKNOWLEDGMENTS

The expert technical assistance of G. Bihlmann, J. Fleißner, F. Pohl, and K. Schwarz is greatfully acknowledged. K.M. Pavlov is thanked for help in the simulation of the X-ray reflection profiles. M. Ramsteiner, L. Schrottke, and G. Jungk (Paul-Drude-Institut für Festkörperelektronik, Berlin) are thanked for contributing the ellipsometric measurements.

REFERENCES

1. D.L. Smith and C. Mailhiot, J. Appl. Phys. **62**, 2545 (1987).

2. R.H. Miles, D.H. Chow, M.H. Young, B.A. Baumgratz, C.R. Chapman, and M.D. Jack, in Proc. IRIS Materials Speciality Group (1993).

3. R.H. Miles, D.H. Chow, Y.-H. Zhang, P.D. Brewer, and R.G. Wilson, Appl. Phys. Lett. **66**, 1921 (1995).

4. L.L. Chang, N. Kawai, G.A. Sai-Halasz, R. Ludeke, and L. Esaki, Appl. Phys. Lett. **35**, 939 (1979).

5. J. Shen, S.Y. Ren, and J.D. Dow, Phys. Rev. B **46**, 6938 (1992).

6. J. Schmitz, J. Wagner, F. Fuchs, N. Herres, P. Koidl, and J.D. Ralston, J. Cryst. Growth **150**, 858 (1995).

7. N. Herres, F. Fuchs, J. Schmitz, K.M. Pavlov, J. Wagner, J.D. Ralston, P. Koidl, C. Gadaletta, and G. Scamarcio, submitted to Phys. Rev. B.

8. D. Behr, J. Wagner, J. Schmitz, N. Herres, J.D. Ralston, P. Koidl, M. Ramsteiner, L. Schrottke, and G. Jungk, Appl. Phys. Lett. **65**, 2972 (1994).

9. J.R. Waterman, B.V. Shanabrook, R.J. Wagner, M.J. Yang, J.L. Davis, and J.P. Omaggio, Semicond. Sci. Technol. **8**, S106 (1993).

10. M. Yano, H. Furuse, Y. Iwai, K. Yoh, and M. Inoue, J. Cryst. Growth **127**, 807 (1993).

11. J. Wagner, J. Schmitz, N. Herres, J.D. Ralston, and P. Koidl, Appl. Phys. Lett. **66**, 3498 (1995).

12. See, e.g., B. Jusserand and M. Cardona, in "Light Scattering in Solids V", eds. M. Cardona and G. Güntherodt (Springer, Berlin, 1989), p. 49.

13. F. Fuchs, J. Schmitz, N. Herres, J. Wagner, J.D. Ralston, and P. Koidl, in "Proc. 7th Int. Conf. on Narrow Gap Semiconductors", Santa Fe, 1995 (to appear in Inst. Phys. Conf. Ser., IOP Publishing).

14. See, e.g., C.G. Van de Walle, Phys. Rev. B **39**, 1871 (1989).

15. L.A. Hemstreet, C.Y. Fong, and J.S. Nelson, J. Vac. Sci. Technol. B **11**, 1693 (1993).

16. Landolt-Börnstein, Numerical Data and Functional Relationships in Science and Technology, edited by O. Madelung (Springer, Berlin, 1982), Vol. II/17a.

17. J.R. Chelikowski and M.L. Cohen, Phys. Rev. B **14**, 556 (1976).

18. D.M. Symons, M. Lakrimi, R.J. Warburton, R.J. Nicholas, N.J. Mason, P.J. Walker, M.I. Eremets, and G. Hill, Phys. Rev. B **49**, 16614 (1994).

19. F. Fuchs, N. Herres, J. Schmitz, K.M. Pavlov, J. Wagner, P. Koidl, and J.H. Roslund, in "Proc. of the SPIE Conf. on Growth and Characterization of Materials for Infrared Detectors II", San Diego, 1995 , Proc. SPIE 2554 (1995).

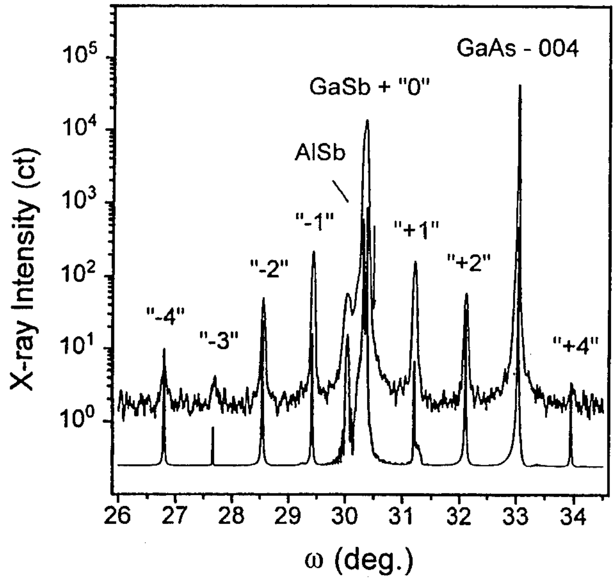

Figure 1: Measured (top) and simulated (bottom) X-ray reflection profiles of a 10 ML InAs/10 ML GaSb SL with InSb-like IFs.

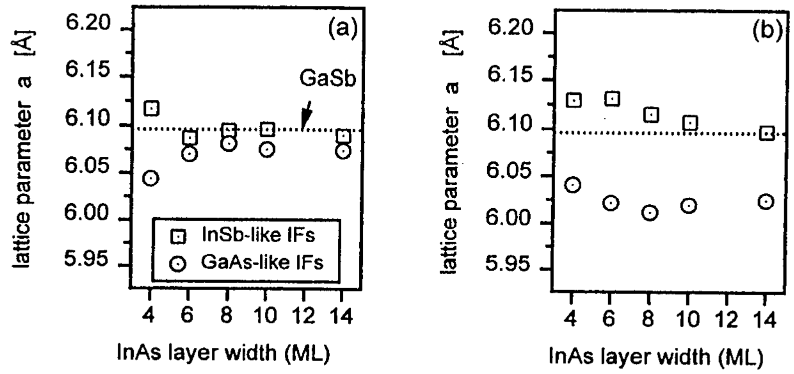

Figure 2: Average lattice parameter (a) parallel to the growth surface $a_{\parallel}$ and (b) perpendicular to the growth surface $a_{\perp}$ of N ML InAs/10 ML GaSb SLs with either InSb-like (squares) or GaAs-like IFs (circles) versus the nominal InAs layer width.

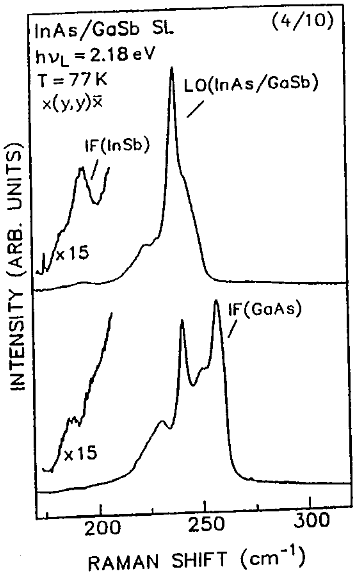

Figure 3: Low-temperature (77 K) Raman spectra of a pair of 4 ML InAs/10 ML GaSb SLs with In-Sb (top) and Ga-As IF bonds (bottom).

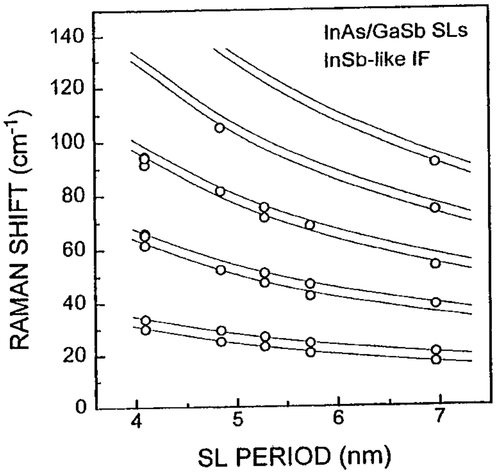

Figure 4: Frequencies of zonefolded LA phonons in InAs/GaSb SLs with InSb-like IFs versus the average SL period determined by HRXRD. Full lines show calculated frequencies.

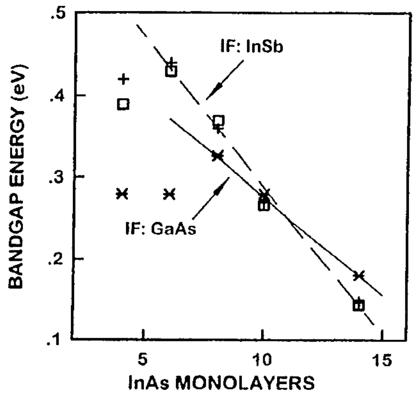

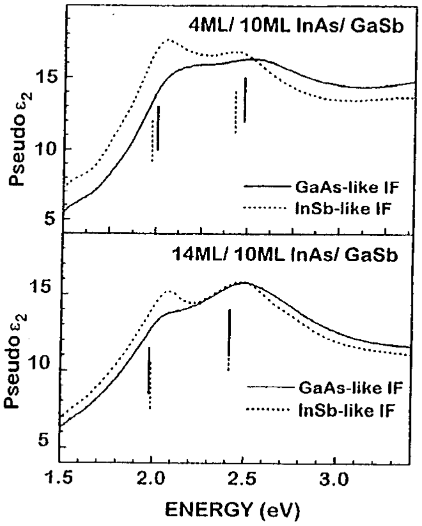

Figure 5: Energetic position of the effective SL band gap of N ML InAs /10 ML GaSb SLs with either GaAs-like IFs (PC data shown by asterisks) or InSb-like IFs (PC and PL data shown by crosses and squares, respectively). The straight lines are drawn to guide the eye.

Figure 6: Imaginary part of the pseudodielectric function (ϵ_2) of 4 ML InAs/10 ML GaSb SLs (top) and 14 ML InAs/10 ML GaSb SLs (bottom) with either InSb-like or GaAs-like IFs. Critical point energies are indicated by vertical lines.

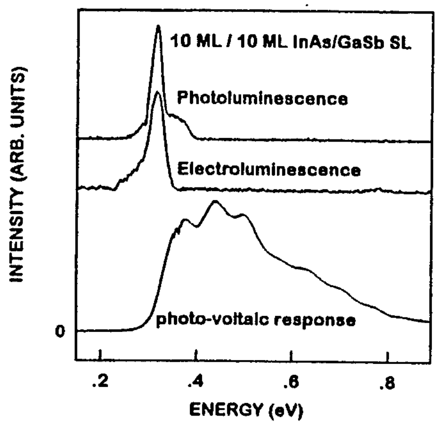

Figure 7: Photovoltaic response at 77 K (bottom) as well as EL (middle) and PL spectra (top) at 10 K of a 10 ML InAs/10 ML GaSb SL p-i-n diode with InSb-like IFs.

COMPARISON OF IDEAL InAs/InAs$_{1-x}$Sb$_x$ and InAs/In$_x$Ga$_{1-x}$Sb SUPERLATTICE IR DETECTORS

C.H. Grein
Physics Department, University of Illinois at Chicago, Chicago, IL 60607-7059

M.E. Flatté
Department of Physics and Astronomy, University of Iowa, Iowa, IA 52242

H. Ehrenreich
Division of Applied Sciences, Harvard University, Cambridge, MA 02138

The theoretical performance limits of 10μm 70.7ÅInAs/21ÅInAs$_{0.61}$Sb$_{0.39}$ and 11μm 39.8ÅInAs/15ÅIn$_{0.4}$Ga$_{0.6}$Sb superlattice-based IR detectors are compared. Detailed calculations of electronic band structures, radiative and Auger recombination rates, and detectivities are reported. Both systems promise superior performance to conventional technology based on HgCdTe, primarily due to suppressed band-to-band Auger recombination rates. The predicted optical absorption and detectivities of the InAs/InAs$_{1-x}$Sb$_x$ system are within a factor of two of those of the InAs/In$_x$Ga$_{1-x}$Sb superlattice over the 77K-200K range, while both have detectivities more than a factor of three greater than HgCdTe.

Introduction

The development of superlattice-based IR detectors is motivated by the promise of performance advantages over conventional technology based on bulk HgCdTe. Recent interest in InAs/InAs$_{1-x}$Sb$_x$ superlattices (SLs) for multi-spectral IR detection and emission prompts our evaluation of theoretical performance limits for ideal (defect-free) structures. Indications that defect levels in InAs-rich alloys lie in the conduction band rather than in the fundamental gap motivate the study of this superlattice[1, 2]. Although such superlattices are frequently grown on highly mismatched substrates such as GaAs[3], in this work we consider InAs/InAs$_{0.61}$Sb$_{0.39}$ superlattices grown on GaSb substrates, with layer widths chosen to balance the strain within a superlattice layer.

A similar system, InAs/In$_x$Ga$_{1-x}$Sb, has received extensive experimental[4] and theoretical[5, 6] attention. Ideal InAs/In$_x$Ga$_{1-x}$Sb detectors have greater detectivities than ideal HgCdTe detectors due to the suppression of Auger recombination[7, 8] and the reduction of tunneling currents. Carrier lifetimes up to two orders of magnitude longer than those of HgCdTe have been observed[9], and detectivities comparable to those of HgCdTe have been achieved in the long-wavelength infrared (LWIR) spectral range[10]. A comparison between InAs/InAs$_{1-x}$Sb$_x$ and InAs/In$_x$Ga$_{1-x}$Sb will help elucidate the potential of the former system.

Several similarities are apparent between these two systems. Since InAs and GaSb have almost the same lattice constant, the alloys $In_xGa_{1-x}Sb$ and $InAs_{1-x}Sb_x$ have roughly the same lattice constant for a given x. Similar deformation potentials and elastic constants imply these alloys will have similar heavy-light hole splittings. The band offset for intermediate alloy compositions is type II for both systems. For $InAs/InAs_{1-x}Sb_x$, experimental measurements[3, 11, 12] and theoretical calculations[13, 14] indicate the offset is type II for all but small values of x[15]. For intermediate values of x the band offsets are also comparable: for $InAs_{0.61}Sb_{0.39}$ the offset $\Lambda = 0.351$eV[12], while for $In_{0.4}Ga_{0.6}Sb$ the band offset is 560meV[16]. A qualitative difference in the band structures comes from the alloy band gap. Unstrained $InAs_{0.61}Sb_{0.31}$ has a smaller band gap than InAs (0.218eV versus 0.418eV) whereas unstrained $In_{0.4}Ga_{0.6}Sb$'s band gap is larger (0.483eV).

Methods and Results

The calculations were performed utilizing non-parabolic electronic band structures and momentum-dependent matrix elements calculated with a SL crystal $\mathbf{K} \cdot \mathbf{p}$ formalism[17, 18] using the parameters in Table I for InAs/InAsSb and those in Ref.[8] for InAs/InGaSb. The bands are found to be highly non-parabolic, and the momentum matrix elements show strong dispersion. The effective mass approximation, therefore, is not applicable. The bands of 10μm 70.7ÅInAs/21Å$InAs_{0.61}Sb_{0.39}$ are calculated for pseudomorphic growth on GaSb substrates and a type-II band alignment with a valence band offset of 0.351eV[12]. The alloy band gap is chosen as 0.218eV[19], close to other values of 0.183eV[20] and 0.192eV[21]. The alloy composition corresponds to the minimum gap for two of these parametrizations.

Figure 1 shows the calculated band structure of 10μm 70.7ÅInAs/21Å$InAs_{0.61}Sb_{0.39}$ grown on GaSb. Biaxial compression breaks the degeneracy of the heavy hole and light hole edges, shifting the heavy hole up and the light hole down. The corresponding SL heavy and light hole bands are therefore split. When this splitting exceeds the energy gap, the Auger recombination of the carriers is suppressed in p-type materials[22]. Strain in $InAs/In_xGa_{1-x}Sb$ SLs produces similar effects. The heavy-light hole splitting in the 70.7Å InAs/ 21Å $InAs_{0.61}Sb_{0.39}$ SL (0.20eV) is not as great as that of 39.8ÅInAs/15Å$In_{0.4}Ga_{0.6}Sb$ (0.24eV) due to slightly lesser strain. Since these splittings both substantially exceed the fundamental gap, the difference in Auger recombination rates is minor. The band structure of the InAs/InGaSb superlattice is shown in Ref.[8]. The heavy-hole mass in the InAs/InAsSb superlattice is heavier than in the InAs/InGaSb superlattice, enhancing Auger rates in the former.

Plotted in figure 2 is the calculated optical absorption spectrum of 70.7ÅInAs/21Å$InAs_{0.61}Sb_{0.39}$ compared with that of 39.8ÅInAs/15Å$In_{0.4}Ga_{0.6}Sb$ and bulk HgCdTe. Since the electrons are spread out over both SL layers, while the heavy holes are confined to the alloy regions, the wider InAs layers in the $InAs/InAs_{1-x}Sb_x$ superlattice produce smaller optical matrix elements between these bands than in the $InAs/In_xGa_{1-x}Sb$ superlattice. Weaker dipole matrix elements result in lower absorption in the former system. Nevertheless, an absorption coefficient of 1500 cm^{-1} is substantial enough to warrant further examination of the InAs/ $InAs_{1-x}Sb_x$ system for IR detection applications. The absorption coefficients of 1500 cm^{-1} and 2000 cm^{-1} were employed in the evaluation of the detectivities of the InAs/InAsSb and InAs/InGaSb systems, respectively.

Nonparabolic bands and momentum-dependent matrix elements were employed for the calculation of Auger and radiative recombination lifetimes[22]. We find that AM-7 transitions are the dominant band-to-band recombination transitions involving hole-hole collisions in these superlattices. These AM-7 transitions involve two holes in the heavy hole band, an electron in the lowest conduction band, and an electron in the light hole band[23].

Figure 3 shows calculated values of the detectivity D* for the two LWIR SLs. These theoretical maximum values of D* were obtained from the expressions $D^* = (\eta/2h\nu)(\tau_n/n_pL_n)^{1/2}$ for n-on-p photodiodes[24]. Here η is the quantum efficiency given by $L_{\{n\}}\alpha/(L_{\{n\}}\alpha + 1)$[25]. The minority carrier lifetime in the p-type layers is τ_n. The minority carrier diffusion length, L_n, is proportional to $\tau_n^{1/2}$ so that D^* is proportional to $\tau_n^{1/4}$. Calculated detectivities are theoretical upper bounds due to the neglect of other recombination mechanisims such as Shockley-Read-Hall. In both systems, we consider an acceptor density of 10^{17} cm^{-3} in the p-type layers (which is optimum for the InAs/InGaSb superlattice) and a vertical electron mobility of 1000 cm^2/V-s. In this doping range the SL D^* is over an order of magnitude greater than bulk HgCdTe. All other parameters are defined and given in refs. [7] and [24]. Further details concerning the evaluation of the detectivity may be found in Ref. [8].

Due to suppression of Auger recombination pathways in both SLs, τ_n is dominated by radiative recombination below about 100K in both systems. The larger gap of 70.7ÅInAs/21ÅInAs$_{0.61}$Sb$_{0.39}$ results in lower minority carrier concentrations, hence somewhat higher detectivities than 39.8ÅInAs/15ÅIn$_{0.4}$Ga$_{0.6}$Sb below 100K. The greater suppression of hole-hole Auger recombination in 39.8ÅInAs/15ÅIn$_{0.4}$Ga$_{0.6}$Sb due to its greater heavy-light hole band splitting results in greater detectivities for this system at higher temperatures. In comparison, the minority carrier lifetimes of bulk $Hg_xCd_{1-x}Te$ are dominated by Auger recombination over the plotted temperature range[22]. Hence, both LWIR SLs are predicted to have greater detectivities than bulk $Hg_xCd_{1-x}Te$.

11 μm HgCdTe detectivities are predicted to be lower than the upper bounds predicted for the optimum 11 μm InAs/InGaSb SL due to the heavy doping of the SL reducing the minority carrier density and hence the noise current. The minority carrier lifetimes are not as short as they would be in HgCdTe with the same doping due to the suppression of band-to-band Auger recombination in the SL. The greater detectivities of the SL lead to substantial improvements in background limited operating temperatures. The SL's are further benefited by their compatibility with III-V electronics, good material strength, and insensitivity to alloy potential fluctuations.

We conclude that the IR detector performance of $InAs/In_xGa_{1-x}Sb$ SLs slightly exceed that of $InAs/InAs_{1-x}Sb_x$ SLs. Both offer potential improvements in D^* of over a factor of three relative to optimally-doped bulk $Hg_xCd_{1-x}Te$ at 11 μm. The high predicted detectivities for $InAs/InAs_{1-x}Sb_x$ SLs with gaps in the LWIR suggest that they are promising for IR detector applications. The performance difference between $InAs/InAs_{1-x}Sb_x$ and $InAs/In_xGa_{1-x}Sb$ systems is small enough that the practical distinction will likely always originate from growth-related differences — such as possible ineffectiveness of the Shockley-Read-Hall mechanism in the $InAs/InAs_{1-x}Sb_x$ superlattices.

Acknowledgements

We are grateful to Y. Zhang for many helpful discussions and providing data before publication. This work was partially supported by the U.S. Advanced Research Projects Agency through the U.S. Office of Naval Research under contract no. N00014-93-1-0549.

References

[1] W.L. Walukiewicz, Mat. Res. Soc. Symp. Proc. **148**, 137 (1989).

[2] P.J.P. Tang, C.C. Phillips and R.A. Stradling, Semicond. Sci. Technol. **8**, 2135 (1993).

[3] P.J.P. Tang, M.J. Pullin, S.J. Chung, C.C. Phillips, R.A. Stradling, A.G. Norman, Y.B. Li, and L. Hart, Semicon. Sci. Technol. **10**, 1177 (1995).

[4] D.H. Chow, R.H. Miles, J.N. Schulman, D.A. Collins, and T.C. McGill, Semi. Sci. Technol. **6**, C47 (1991).

[5] D.L. Smith and C. Mailhiot, J. Appl. Phys. **62**, 2545 (1987). C. Mailhiot and D.L. Smith, J. Vac. Sci. Technol. A **7**, 445 (1989).

[6] C.H. Grein, P.M. Young, and H. Ehrenreich, Appl. Phys. Lett. **61**, 2905 (1992).

[7] P.M. Young, C.H. Grein, H. Ehrenreich, and R.H. Miles, J. Appl. Phys. **74**, 4774 (1993).

[8] C.H. Grein, P.M. Young, M.E. Flatté, and H. Ehrenreich, J. Appl. Phys. in press.

[9] E.R. Youngdale, J.R. Meyer, C.A. Hoffman, F.J. Bartoli, C.H. Grein, P.M. Young, H. Ehrenreich, R.H. Miles, and D.H. Chow, Appl. Phys. Lett. **64**, 3160 (1994).

[10] R.H. Miles, private communication

[11] P.J.P. Tang, M.J. Pullin, S.J. Chung, C.C. Phillips, R.A. Stradling, A.G. Norman, Y.B. Li, and L. Hart, unpublished.

[12] Y. Zhang, private communication.

[13] S. Picozzi, A. Continenza, and A.J. Freeman, Phys. Rev. B **52**, 5247 (1995).

[14] A. Zunger, unpublished.

[15] S.R. Kurtz and R.M. Biefeld, Appl. Phys. Lett. **66**, 364 (1995).

[16] Provides best agreement with band gaps published in R.H. Miles, D.H. Chow, J.N. Schulman, and T.C. McGill, Appl. Phys. Lett. **57**, 801 (1990).

[17] N.F. Johnson, H. Ehrenreich, P.M. Hui, and P.M. Young, Phys. Rev. B **41**, 3655 (1990).

[18] M.E. Flatté, P.M. Young, L.-H. Peng, and H. Ehrenreich, Phys. Rev. B in press.

[19] Binary gaps from Semiconductors: Group IV Elements and III-V Compounds, edited by O. Madelung, (Springer, New York, 1991). Band bowing parameter from A. Sasaki, M. Nishiuma, and Y. Takeda, Jap. J. Appl. Phys. **19**, 1695 (1980).

[20] S.R. Kurtz and R.M. Biefeld, Phys. Rev. B **44**, 1143 (1991).

[21] M.Y. Yen, R. People, K.W. Wecht, and A.Y. Cho, Appl. Phys. Lett. **52**, 489 (1988).

[22] C.H. Grein, P.M. Young, and H. Ehrenreich, Appl. Phys. Lett. **61**, 2905 (1992); C.H. Grein, H. Cruz, M. Flatté, and H. Ehrenreich, Appl. Phys. Lett. **65**, 2530 (1994).

[23] A.R. Beattie, J. Phys. Chem. Solids **24**, 1049 (1962).

[24] M.A. Kinch and S.R. Borrello, Infrared Physics **15**, 111 (1974).

[25] M.B. Reine, A.K. Sood, and T.J. Tredwell, in *Semiconductors and Semimetals*, edited by R.K. Willardson and A.C. Beer (Academic, New York, 1981), Vol. 18, p. 201.

Table I-Input Parameters for Band Structure and Detectivity Calculations

	InSb	InAs	$InAs_{0.61}Sb_{0.39}$	InAs/InAsSb
lattice constant[1] (Å)	6.479	6.058		
a deformation potential[1] (eV)	-7.7	-5.8		
b deformation potential[1] (eV)	-2.0	-1.8		
c_{11}[1] (10^{11} dyn cm^{-2})	6.918	8.329		
c_{12}[1] (10^{11} dyn cm^{-2})	3.788	4.526		
energy gap[1] (eV)		0.4180	0.2175	
spin orbit splitting Δ[1] (eV)	0.803	0.38		
m^*_{hh} in (100) direction[2]		0.4	0.34	
$\frac{2}{m}\|P^{\perp}_{hh,c}\|^2$ [3](eV)				21.0
valence band offset[4] (eV)				0.351
index of refraction n[1]				3.5
$\perp$ electron mobility[5](cm^2/V-s)				1000

Notes: All values are at T=0K. Hydrostatic deformation potentials of the valence bands are neglected. All parameters for $InAs_{0.61}Sb_{0.39}$ are linearly interpolated from InAs and InSb unless otherwise noted in the $InAs_{0.61}Sb_{0.39}$ column. The superlattice is assumed to be grown on a GaSb substrate.

[1] *Semiconductors-Group IV Elements and III-V Compounds*, edited by O. Madelung (Springer, New York, 1991).

[2] G. Bastard, Acta Electronica **25**, 147 (1983).

[3] Momentum matrix element deduced from m^*_c of InAs and InSb.

[4] Y. Zhang, private communication.

[5] Same value as $InAs/In_xGa_{1-x}Sb$.

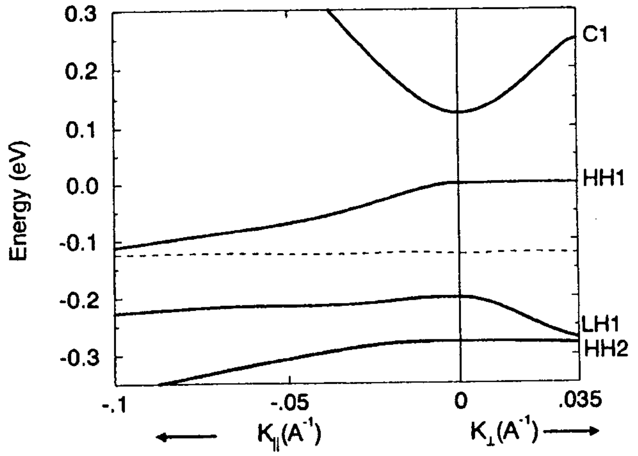

Figure 1 Calculated band structure of 10μm 70.7ÅInAs/ 21ÅInAs$_{0.61}$Sb$_{0.39}$. Bands are plotted in the in-plane (‖) and growth-axis (⊥) directions.

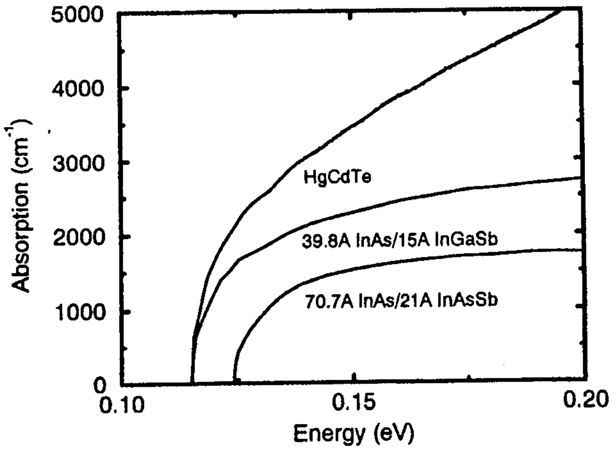

Figure 2 The optical absorption coefficients calculated employing $k \cdot p$ theory for 10μm 70.7ÅInAs/21ÅInAs$_{0.61}$Sb$_{0.39}$, 11μm 39.8ÅInAs/ 15ÅIn$_{0.4}$Ga$_{0.6}$Sb and 11μm bulk HgCdTe.

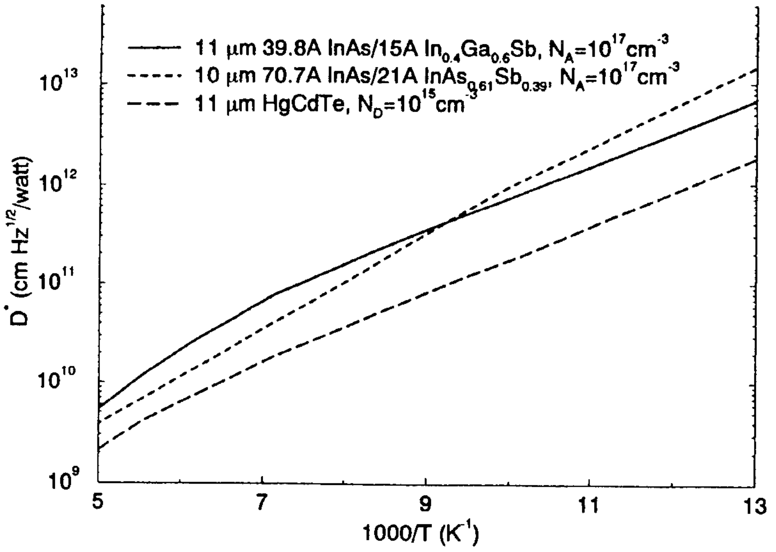

Figure 3 Predicted specific detectivities for IR detectors with ideal 10μm 70.7ÅInAs/ 21ÅInAs$_{0.61}$Sb$_{0.39}$, 11μm 39.8ÅInAs/ 15ÅIn$_{0.4}$Ga$_{0.6}$Sb, and 11μm bulk HgCdTe active layers. The n-on-p SL p-type layers have an acceptor concentration of 10^{17} cm^{-3}. The p-on-n HgCdTe n-type layer has a donor concentration of 10^{15} cm^{-3}.

EXCITON AND PHONON CONFINEMENT IN GaP QUANTUM DOTS

D. O. Henderson, R. Mu, Y. S. Tung, A. Ueda, and W. E. Collins
Chemical Physics Laboratory, Physics Department, Fisk University
Nashville, TN 37208

C. W. White, R. A. Zuhr, and Jane G. Zhu
Oak Ridge National Laboratory, P. O. Box 2008
Oak Ridge, TN 37831-6057

Gallium and phosphorous were sequentially implanted into optical grade fused silica at doses of 1, 3, 6, and 10 x10^{16} ions/cm^2. TRIM calculations were performed to determine the implantation energies of the two ions to provide a maximum overlap of the two implanted layers. The degree of overlap was established by Rutherford backscattering measurements whenever possible. Electronic and vibrational spectra were obtained for the as-implanted silica substrates. A broad featureless tail extending into the ultraviolet was observed in the spectra of the as-implanted samples is attributed defect formation associated with heavy ion implantation. No structure was observed in the far-infrared spectra of the as-implanted samplesexcept for the highest dose sample. The implanted substrates were then annealed in a controlled atmosphere at temperatures ranging from 473-1273 K. The electronic spectra of the implanted materials revealed a band in 300-400 nm region which was most intense for the highest dose sample. This band is expected to arise for confinement of the exciton. The band center also depended on the ion dose. Far-infrared reflectance spectra indicated a band at 380 cm^{-1} after the annealing the highest dose sample and is attributed to the surface phonon polariton of GaP.

INTRODUCTION

The onset of absorption of light in a semiconductor is accompanied by the creation of a bound electron hole pair known as an exciton. When the size of a semiconductor is reduced in dimension, for example to a two dimensional film, a one dimensional wire, or a zero dimensional dot, the exciton can experience a confinement potential if the particle size is on the order on the exciton radius. Under such conditions, quantum effects become important and are expressed as a blueshift in the absorption onset, and the oscillator strength is concentrated into a few optical transitions. It is the onset of size induced quantum confinement that that attracted the attention of scientists from a standpoint of fundamental and applied research. Clearly, one of the aims from the basic science perspective is to develop an understanding of how the electronic and optical properties of a material evolves from a single molecule to a cluster and then onto the bulk phase. Numerous applications have been suggested for size quantized semiconductors that encompass devices based on their large third order nonlinear susceptibility. These have included, to mention a few, all-optical switches, optical phase conjugation, self focusing of light, and devices that are based on optical bistability.

Several investigations on quantum size effects have been devoted to CdS (1), CdSe (2), CdSeS (3), but fewer studies have focused on the III-V semiconductors in the form of quantum dots. However, because of the growth of molecular beam epitaxy, the literature is extensive on III-V semiconductors confined in one dimension. The lack of these studies on III-V quantum dots seems to emanate from the inherent difficulties associated with fabricating these materials.

Gallium phosphide is a III-V semiconductor with a zinc-blende lattice structure and has an indirect band gap, meaning the vertical Franck-Condon transition is not the lowest energy transition in the spectrum. A nonvertical, phonon assisted transition is the lowest energy transition in the absorption spectrum. The Franck-Condon transition is allowed is because it conserves electron momentum. Because it is allowed, it carries most of the transition strength and therefore corresponds to a false origin of the spectrum. The true origin requires the simultaneous absorption of a photon and the creation or annihilation of a phonon, making it a higher order process which carries less transition strength.

Experimental studies on gallium phosphide quantum dots are limited. Macdougall et al. (4) reported the electronic spectra for gallium phosphide quantum dots confined in zeolite y. They observed a blueshift in the band gap (shift from the direct gap of 546 nm) to ~300 nm depending on the loading of the zeolite. Theoretical studies on band gap shifts for gallium phosphide based on pseudopotential calculations have predicted a continuous blueshift with decreasing particle size for the indirect gap. However, for the direct gap transition, there is initially a redshift observed when the particle size is decreased, followed by a blue shift for very small particles (5).

The infrared and Raman spectra of gallium phosphide microcrystals have also investigated (6,7). The primary interest in these studies originates from the effect of finite particle size on the lattice modes. The theory for phonon confinement has been reviewed by Ruppin (8), Fuchs (9), and Hayashi (10). The effect of confining phonons is manifest in the appearance of mode that lies between the transverse and longitudinal optical phonons of the bulk material. Thus, when a particle becomes so small, it can no longer sustain the wavevector of the phonon and the mode becomes localized at the surface. This is referred to as surface phonon polariton. The theory also predicts that the oscillator strength increases as the particle size is reduced and that the frequency of surface phonon polariton decreases as the dielectric constant of the surround medium increases. We have observed phonon polariton at 380 cm^{-1} for gallium phosphide and it can be used as an indication of nanocrystal gallium phosphide formation.

We have investigated the electronic and infrared spectrum of gallium phosphide formed by sequential ion implantation into optical grade fused silica. We observe effects in the far-infrared spectra which support the presence of a surface phonon polariton and size quantization is evident in the electronic spectra.

EXPERIMENTAL

Optical grade fused silica substrates were implanted with Ga only at doses of 1, 3, 6, and 10 $x10^{16}$ $ions/cm^2$ at and energy of 160 keV. Phosphorous only was implanted into fused silica substrates at doses of 1, 3, 6 and 10^{16} $ions/cm^2$ at an energy of 70 keV. A third set of fused silica substrates were then implanted sequentially with P followed by Ga at the same energies used in the solo implants. These implantation energies assured a maximum overlap of the depth profiles of the two ions. Rutherford backscattering (RBS) measurements were made on all samples to obtain the depth profiles of the implanted layer. A 2 MeV He^{2+} beam was used for all of the backscattering measurements.

The samples were annealed isochronally for 30 minutes at temperatures ranging from 473-1273 K in a 5% H_2 + 95% Ar atmosphere. Spectra were recorded before and after the annealing treatments.

The electronic spectra were recorded with a Hitachi model 3501 UV-Vis-NIR dual beam spectrometer. The spectra were normalized against the through-put of a virgin window placed in the reference beam. All transmission spectra were normalized to the virgin window. The resolution was typically ~0.2 nm. Repeated measurements showed the photometric accuracy to be ±0.3% and ±0.2 nm in wavelength accuracy in the 200-800 nm range.

The infrared reflectance spectra were measured with a Bomem DA3.02 Fourier transform interferometer. A silicon carbide source, a series of 3, 6 and 12 μm mylar beamsplitters, and a deuterated triglycine sulfate detector equipped with a polyethylene window were used to cover the 800-50 cm^{-1} region. The samples were mounted on a laboratory-built reflectance accessory with a fixed angle of incidence of 15° and spectra were recorded by coadding 400 interferograms. The spectra were normalized against the spectra of a virgin fused silica window to enhance the differences between the virgin and implanted substrates. All measurements were made under a vacuum of ~0.1 torr to minimize the absorption from the rotational-vibrational transitions of water vapor.

Results

The RBS spectra were measured for Ga only, P only, for Ga implanted in a Ga+P sequentially implanted substrate, and for P in a Ga+P sequentially implanted substrate, respectively. The Ga implantation profile can be reasonably approximated by a Gaussian function for the lowest ion dose of 1 x 10^{16} ions/cm^2 and has maximum at 0.11 μm below the surface. At higher doses, however, two maxima appear in the RBS spectra at 0.05 and 0.15 μm below the surface indicating a bimodal distribution. The RBS for the P implanted substrates for the two highest doses of 6 and 10 x 10^{16} ions/cm^2 show a maximum is at ~0.1μm below the surface. The RBS signal for the lower doses of P were not observed due to the strong interference from Si scattering. The RBS for Ga in the sequentially implanted substrate shows a maximum near 0.1 μm and evidence of asymmetric broadening toward the bulk and has a FWHM of ~0.1 μm. The P in the sequentially implanted substrate has a maximum centered near 0.05 μm below the surface and a FWHM of 0.1μm. The ion doses delivered to the substrates are summarized in Table I.

Table I. Ion Doses for Implanted Fused Silica Substrates in 10^{16} ions/cm^2

P only	P in Ga+P	Ga Only	Ga in Ga+P
5.4	1.5	6.3	7.2
5.0	2.5	4.2	5.7
		2.3	2.9
		0.81	0.80

The electronic spectra are shown in figs. 1a, 1b 1c and 1d for the P only and Ga only implanted with 1x10^{17} ions/cm^2 and annealed at various temperatures together with their corresponding second derivative spectra. The spectra for Ga (fig. 1a) shows a decrease in transmission at ~300 nm which becomes larger as the annealing temperature increases to 1173 K. At 1273 K the spectra appear to be flat in this region showing no decrease in transmission. The second derivative spectra allow for a better identification of the minima in the transmission spectra (in the second derivative spectra the they appear as maxima). For the as-implanted sample shown in fig. 1b, a peak is observed at 261 nm which moves to 234 after annealing at 1073 K. Further annealing at 1173 K causes the 234 peak to shift to 221 and broad feature appears at 275 nm. The 300-800 nm spectral region appears to be void of structure. Additional annealing at 1273 K produces a flat featureless spectrum.

Spectra for the phosphorous samples are illustrated in figs. 1c and 1d for substrate implanted with 1 X 10^{17} P ions/cm^2 annealed at various temperatures. The transmission spectra show a tail of decreasing transmission which begins near 400 nm for the as-implanted substrate and extends to 200 nm. Annealing the samples tends to shift the absorption onset to longer wavelengths as is indicated for the P implanted sample annealed at 1273 K. The corresponding second derivative spectra shown in fig. 1d show two peaks at 250 and 298 nm for the as-implanted sample. Annealing the sample causes the intensity of the 298 nm peak to vanish and the 250 nm to shift to 218 nm.

Electronic spectra are shown for the sequentially as-implanted substrates in fig. 2a for the transmission spectra and 2b for their derivative spectra for Ga and P implanted with nominal ion doses between 1 and 10 x10^{16} ions/cm^2. For the doses of 1 and 3 x10^{16} ions/cm^2 (dose in this case refers to the dose of each ion, not the sum of the two) two peaks are observed at 256 and 220 in the derivative spectra shown in fig 2b. For the sample dosed with 6 x10^{16} ions/cm^2 the is increasing absorption starting near 300 nm and for the sample dosed with 10 x10^{16} ions/cm^2 the absorption starts near 400 and two poorly resolved peaks are noted at 381 and 280.

The effect of annealing the substrates sequentially implanted with 10 x10^{16} ions/cm^2 is shown in figs 3a and 3b. For the sequentially as-implanted substrates (fig. 3a), a broad featureless absorption is observed that has an onset near 400 nm and increases to 200 nm. At an annealing temperature of 1173 K, a knee begins to appear in the transmission spectrum and becomes more pronounced at 1273 K. The second derivative spectra show peaks at 272 and 367 for the sequentially as-implanted substrates. Annealing the samples results in peak at 220 nm and another feature near that has absorption between 300 and 375.

The far-infrared spectra are shown in fig 4a for a substrate sequentially implanted with 10 x 10^{16} ions/cm^2 and in 4b for the same sample annealed at 1273 K for 1 hour. In the as implanted sample there is some evidence of a peak at 380cm^{-1}. However, after annealing the sample, the intensity of this peak grows significantly.

DISCUSSION

The implantation of ions into an insulator host often leads to damage of the host material. The damage to can be attributed to three processes : 1) electronic, 2) nuclear or elastic collision processes, and 3) radiolysis or photochemical processes. For silica implanted with Ga and P at the energies used in the current study, both nuclear displacement and electronic defect centers are expected to be present. Much of the absorption that is observed at wavelengths shorter than 250 nm can be attributed to B_2, $E_2^{'}$ and $E_1^{'}$. These defect center can account for the decreased transmission observed for the solo ion and dual ion implanted silica substrates. This assignment is also consistent with the observation that there is increased transmission this range when the samples are annealed. Such increase in transmission indicates that the defects are annealed away at 1273 K.

The trend in the decreased absorption in the 200-400 nm region observed for the P only and Ga only samples differ. At an annealing temperature of 1273 K, the spectra for the Ga implanted sample is essentially flat, while that for the P only implant shows absorption in this region. The difference we expect is derived from the rates of diffusion of P and Ga in fused silica. This hypothesis is supported by the fact that the RBS measurements (not shown) indicate that no Ga remained in the sample after annealing at 1273 K. Some of the absorption that remains in the P only implanted sample could conceivably be attributed to the formation P colloids. However, it appears that at the ion doses used, there is little chance for colloid formation (11). Thus we expect much of the damage that remains is related to defects arising from the P impurity.

The second derivative electronic spectra of dual implanted silica substrates before annealing differ from the spectra of the both of the solo implants and they can not be reproduced by numerically adding the spectra of the solo implants. This would seem to indicate either new defects or new species have been formed in the dual implanted silica substrates. This appears to be most evident from the appearance of a absorption between 300 and 400 nm observed for the samples dosed with 6 and 10 x 10^{16} ions/cm^2, fig. 2b. The spectra for the dual implants that were annealed show the development of a knee near 315 nm (fig. 3a) which is not present in the spectra of the annealed solo implants. Again, we suggest that the appearance this feature is related to a new species or a defect. The evidence for the peak is more pronounced in the derivative spectra, fig 3b.

The infrared spectra for the sequentially as-implanted sample dosed with 10 x10^{16} ions/cm^2 shows evidence of a band at 380 cm^{-1} that grows upon annealing. This frequency is between the transverse optical (366 cm^{-1}) and longitudinal optical (402 cm^{-1}) modes of bulk GaP (12). While it may be argued this absorption could be assigned to a molecular species of gallium phosphide, it can ruled out as an assignment since the absorption for molecular gallium phosphide at 283 cm^{-1} (13). The possibility of assigning this feature to a more complex molecular species such as Ga_2P is also eliminated since this absorption is observed at 281 cm^{-1}. Thus we suggest that the 380 cm^{-1} should be assigned to the surface phonon polariton of gallium phosphide quantum dots. This is consistent with the theoretical predictions of Ruppin (8), Fuchs(9), and Hayashi (10).

It is noteworthy that the 380 cm^{-1} feature which increases in intensity after annealing the sample at 1273 K correlates with the increased absorption at 315 nm observed in the electronic spectra of the substrates sequentially implanted and annealed at 1273 K. The simultaneous changes observed in the infrared and electronic spectra strongly suggest that gallium phosphide quantum dots have formed after annealing the sample at 1273 K. Thus, we conclude that the assignment of the 315 nm feature to an electronic transition of quantum confined gallium phosphide supported by the appearance of the surface phonon polariton observed in the far infrared spectra.

CONCLUSION

The vibrational and electronic spectra of Ga and P sequentially implanted into optical grade fused silica were measured in the as-implanted and annealed states. The annealed samples revealed a band at 315 nm in the electronic spectra that is assigned to an electronic transition of gallium phosphide quantum dots. The vibrational spectra show band at 380 cm^{-1} that is attributed to the surface phonon polariton of gallium phosphide. These results indicate that the combined application of vibrational and electronic spectroscopy is a powerful method for probing the presence of quantum dots. Further studies are underway to explore the potential of these materials for nonlinear optical applications. Specifically, time resolved degenerate four wave mixing studies are planned to determine their third order nonlinear susceptibility and their dephasing time. Also, other ion implantation experiments have been performed for fabricating InAs, InSb, InP, GaSb, and GaAs quantum dots. The electronic and vibrational linear optical spectra of these materials will be reported in the near future together with their nonlinear optical properties.

ACKNOWLEDGMENTS

D. O. H. acknowledges DOE for supporting this work under grant # DE-F605-94ER45521 and NASA under under NAG-1066. W. E. C. acknowledges NASA for supporing this work under grant #NAG3-1430. The work at ORNL was is sponsored by the the Division of Materials Science, U. S. Department of Energy under contract DE-AC05-84OR21400 with Lockheed Martin Energy Systems.

REFERENCES

1. Y. Wang and N. Herron, J. Phys. Chem, **92**, (1988).
2. H. Ma, A. S. L. Gomes, C. B. De Araujo, J. Opt. Soc. Am., **B9**, 2230 (1992).
3. N. Chestnoy, R. Hull, and L. E. Brus, J. Chem. Phys., **85**, 2237 (1986).
4. J. E. MacDougall, H. Eckert, G. D. Stucky, N. Herron, Y. Wang, K. Moller, T. Bein and D. Cox, J. Am. Chem. Soc., **111**, 8006 (1989).
5. M. V. Rama Krishna and R. Friesner, J. Chem. Phys., **95**, 8309 (1991).
6. S. Hayashi, Solid State Commun., **56**, 375 (1985).
7. S. Hayashi and H. Kanamori, Phys. Rev., **B26**, 7097 (1982).
8. R. Ruppin, J. Phys. C: Solid State Phys., **8**, 1969 (1975).
9. R. Fuchs, Phys. Rev. **B11**, 1732, (1975).
10. S. Hayashi, Jpn. J. Appl. Phys., **22**, 665 (1984).
11. H. Hosono, Y. Suzuki, Y. Abe, K. Oyoshi, S. Tanaka, J. Non-Cryst. Solids, **142**, 287, (1992).
12. K. Maslin, C. Patel, and T. J. Parker, Infrared Phys., **32**, 303 (1991).
13. S. Li, R. J. Van Zee and W. Weltner, Jr., J. Phys. Chem., **97** (1993).

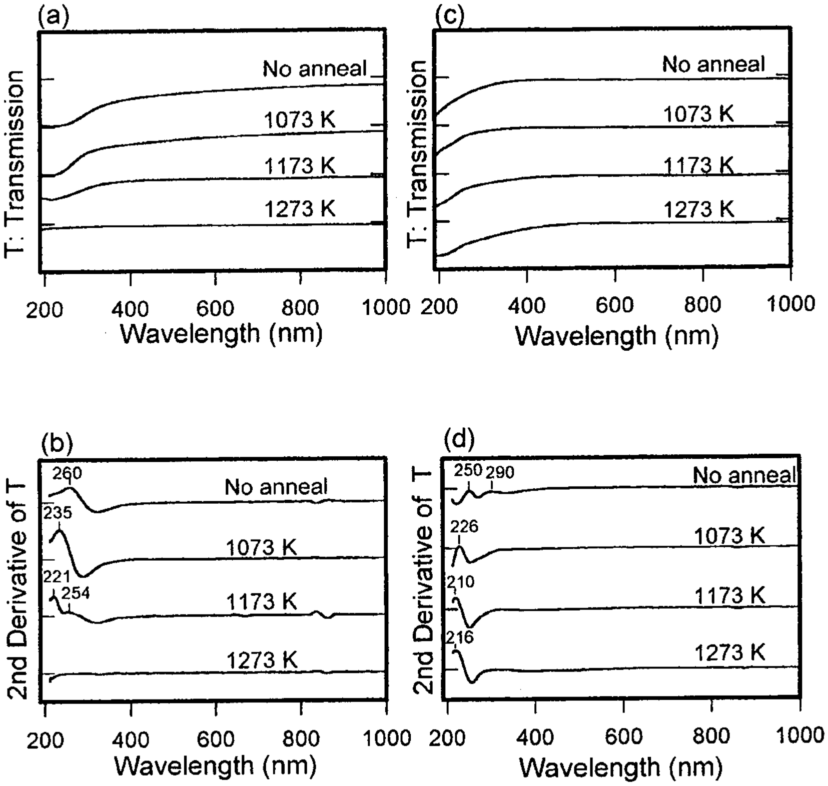

Fig.1 Transmission spectra; (a)Ga implanted in silica and annealed at temperatures indicated (1×10^{17}ions/cm^2), (b)the second derivative spectra of (a), (c) P implanted in silica and annealed at temperatures indicated (1×10^{17}ions/cm^2), and (d)the second derivative spectra of (c).

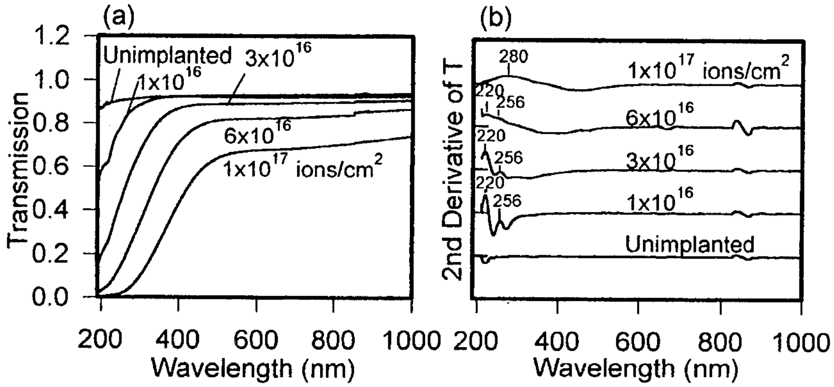

Fig.2 (a) Silica sequentially implanted with ion doses indicated in the figure. Dose refers to the concentration of each ion; (b)The second derivative spectra of (a).

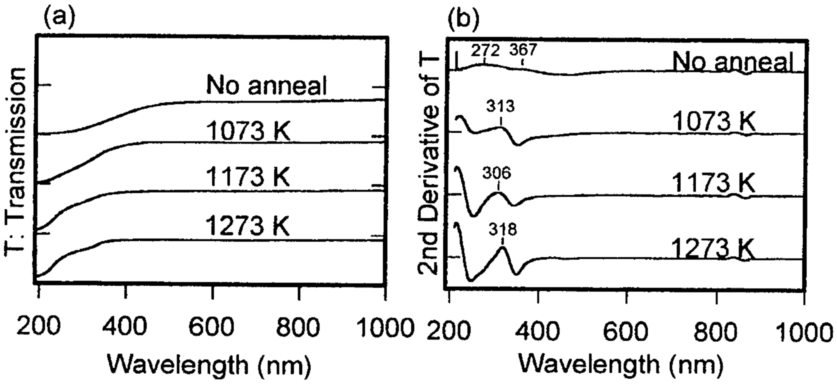

Fig.3 (a)Ga+P sequentially implanted into silica and annealed at the temperatures indicated. (b)The second derivative spectra of (a).

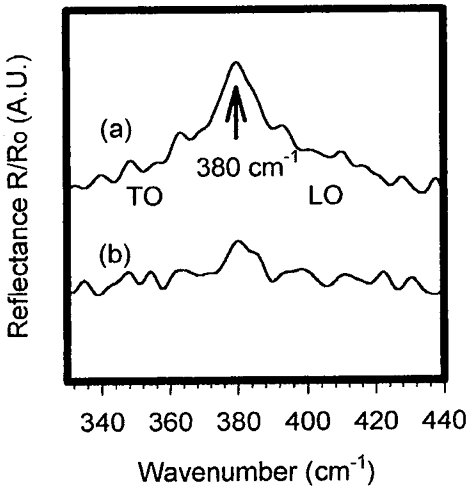

Fig.4 Surface phonon of GaP. (a) Infrared spectrum of Ga+P in silica (1×10^{17}ions/cm^2)annealed at 1000°C and (b) for as-implanted sample.

Spectroscopic Study of Plasmon Anisotropyin Heavily Doped GaAs/AlAs Superlattices

Yu.A.Pusep, M.T.O.Silva and J.C.Galzerani, A.G.Milekhin*, N.T.Moshegov*, A.I.Toropov*,
Departamento de Fisica, Universidade Federal de São Carlos, C.P.676, 13565-905
São Carlos, SP, Brasil
*Institute of Semiconductor Physics, 630090 Novosibirsk, Russia

ABSTRACT

We present infrared and Raman studies of the plasmon-LO phonon vibrational modes in heavily dopedGaAs/AlAs superlattices. The experimental results reveal the dispersions of electrons normal and parallel to the layers which was found in good agreement with the miniband dispersions calculated in the envelope function approximation when both Γ and X conduction electron states were taken into account. We did not find any evidence of the contribution of the 2D electron states to the vertical transport.

1. Introduction

During the last years artificially synthesized solid structures attracted much attention due to their great importance in the development of new electronic devices. The earliest proposed man-made materials were the superlattices (SL's) which are multilayer periodic structures consisting of alternating layers of two compounds [1]. Due to the different periods in the directions parallel and normal to the layers, the SL's reveal the properties of an anisotropic crystal with the axis normal to the plane of layers. A great number of papers were devoted to the study of phonons in SL's (see for instance the references in [2]) where a strong anisotropy of the vibrational properties was found. The behavior of electrons in isolated quantum wells presents the properties similar to those of the optical phonons - free propagation parallel to the layers and confinement in normal direction [3]. With the decrease of the barrier thickness the electron wavefunctions in neighboring quantum wells become overlapping and the subband structure caused by the periodicity of a SL is formed. Now electrons can move through an entire SL like free particles with a new effective mass determined by the dispersion of a miniband.

The first demonstration of the miniband transport (normal to the layers) in SL's with thin enough barriers, leading to the negative resistance, has been presented by L.Esaki et.al. [4]. However, only recently the modern technology made it possible to grow quite perfect SL's where the vertical transport through a Bloch-type miniband states could be studied in details [5-7]. The first evidence of the electron movement through a miniband without application of an external electric field has been obtained by Fourier-transform infrared (FTIR) spectroscopy of the superlattice plasmon [8,9].

In the present paper we apply both FTIR and Raman spectroscopies to the investigation of plasma electron excitations polarized normal and parallel to the layers in the doped GaAs/AlAs SL's. It was obtained that the vertical (superlattice) plasmon contributes to the infrared spectra while the in-plane plasmon was found in Raman scattering. Our results testify to the miniband dispersion which was found in good agreement with the calculated one obtained by the envelope-function approximation. The role of the different conduction band electron states has been investigated as well.

2. Experimental details

The $(GaAs)_{17}(AlAs)_2$ SL's studied here were grown by moleqular beam epitaxy on (100) GaAs substrates. To eliminate an interference due to the total thickness of the sample either we used heavily Si doped substrates or the SL's were grown on the 1 μcm thick doped buffer layer.The doping of the SL's was achieved with Si donors.

The p-polarized reflection spectra were recorded with a Bruker IFS-113V Fourier-transform infrared spectrometer. The Raman spectra were taken with a Jobin-Yvon double grating spectrometer supplied with usual photon counting system; the 5145 Å line of an Ar^+ ion laser was used for excitation. All the spectra were measured at the temperature T=80 K.

The values of relevant plasmon frequencies were obtained by the comparison of the measured optical vibrational spectra of the samples under investigation with those calculated according to the dielectric continuum theory. The optical mode frequencies were determined through the fitting of the calculated reflection spectra to the experimental ones as it has been reported in [10]; the Raman spectra were fitted by the spectra calculated as a sum of Lorenzian peaks.

In order to study the role of different electron states in the formation of the miniband structure we compared the frequencies of the miniband plasmon measured in samples with different electron densities with those computed using the envelope-function approximation when the direct Γ-Γ and X-X and pseudodirect Γ- X electron transfers were taken into account (here the first character is associated with the GaAs and the second one - with the AlAs). The details of these calculations can be found in [9].

In accordance with the miniband calculations the lowest miniband in the $(GaAs)_{17}(AlAs)_2$ SL is formed by the Γ conduction electron states of GaAs and AlAs. This miniband can be completely filled for a doping electron density of about $2.5 \cdot 10^{18}$ cm^{-3} which is quite available with Si donors. Thus the anisotropy of the conducting properties of this SL can be probed at different electron densities, from the case of partially filled miniband up to a completely filled one.

3. Results and discussion

The p-polarized reflection spectra of the samples studied here are presented in Fig.1 while the corresponding Raman spectra are shown in Fig.2. As it has been already mentioned above, the p-polarized infrared spectra reveal the lines originated from both transverse and longitudinal optical vibrational modes. Moreover, according to the Berreman effect, in this case only the longitudinal modes with an electric polarization parallel to the SL axis (z direction normal to the layers) are active. Thus we labeled the corresponding phonon lines observed in the reflection spectra as TO_x and LO_z modes. The deep minimum of reflectivity around 270 cm^{-1} relates rather to the TO phonon of the GaAs substrate. The fitting of the reflection spectra gave us the possibility to find the oscillator strengths R_T and R_L (introduced in formulas (2) and (3)) of the observed optical modes and through them to obtain the values of the frequencies of the interface modes TO_z and LO_x. The calculated reflection spectra are shown in Fig.1 by broken lines. The discrepancy between the measured and calculated reflectivities around GaAs optical phonons observed in some of the samples occurs because of the transparency of the doped GaAs buffer between the SL and the substrate which was not taken into account in the calculations and caused a significant reflectivity from the nondoped GaAs substrate in the reststrahlen band frequency range.

In order to avoid any influence of the substrate we analyzed the AlAs-like vibrational modes. All the characteristic frequencies of the AlAs-like optical vibrational modes found by the reflection spectra are depicted by arrows in the Raman spectra of the corresponding samples.

The different filling of the lowest Γ miniband causes a different shift of the longitudinal AlAs-like mode, labeled as L_z^+ coupled plasmon-LO phonon mode, which was clearly observed in the reflection spectra (Fig.1). At the beginning the frequency of this L_z^+ mode increases with the electron density and than starts to decrease; the maximum value of the plasmon-LO phonon mode frequency relates to the inflection point of the Γ miniband dispersion. In the sample with the highest electron concentration ($n=5.6 \cdot 10^{18}$ cm^{-3}) the position of the L_z^+ mode actually corresponds to the frequency of the first LO_{z1} confined AlAs-like mode in a nondoped sample. This is because at such an electron density the lowest Γ miniband is completely filled and electrons cannot move parallel to the SL-axis and , consequently, they cannot couple with the LO_z phonons. In such a case the SL reveals a dielectric character even at so high doping level.

The Raman spectra of the doped $(GaAs)_{17}(AlAs)_2$ SL's (Fig.2) reveal a larger shift of the AlAs-like longitudinal mode due to the plasmon-LO phonon coupling than it was observed in the infrared spectra. Only in the sample with the lowest concentration of electrons ($n=1 \cdot 10^{17}$ cm^{-3}) we detected a line corresponding to the optical longitudinal vibration, which was in good agreement with the frequency of the L_z^+ mode measured by FTIR. In the other SL 's we did not observe neither a tendency of the decrease of the plasma frequency with increasing electron density, nor the dielectric behavior as it was found in the infrared spectra. Due to these reasons we conclude that in the samples with high electron concentrations the plasmon with an in-plane electric polarization contributes to the Raman spectra. In this case, the larger shift of the plasmon-LO phonon mode relates to the higher frequency of the ω_{px} plasmon, comparatively to the ω_{pz} plasmon in the same sample; this is due to the smaller value of the m_x electron effective mass with respect to the m_z one. Weak lines, with frequencies close to the frequencies of the L_z^+ mode measured by FTIR, were observed in $(GaAs)_{17}(AlAs)_2$ SL's with $n=7 \cdot 10^{17}$ cm^{-3} and $n=1.4 \cdot 10^{18}$ cm^{-3}. No contribution due to the L_z^+ mode was found in the samples with higher electron concentrations. Thus, we conclude that in slightly doped SL's the back-scattered Raman spectra probe optical longitudinal modes with an electric polarization parallel to the SL axis, which is in agrement with the wavevector conservation law; in heavily doped SL's even the modes propagating parallel to the layers can be active due to the electron scattering by crystal imperfections and therefore, the Raman scattering of SL's with different doping levels presents the effect of different fillings of the 2D Γ subbands.

The frequency dependencies of the ω_{px} and ω_{pz} plasmons on the electron density obtained from the Raman and reflection spectra respectively of the doped $(GaAs)_{17}(AlAs)_2$ SL's are shown in Fig.3. The dependence of the superlattice plasmon ω_{pz} on the electron density directly relates to the miniband dispersion. The $\omega_{pz}(n)$ curves calculated in the envelope-function approximation are depicted by full and broken lines. The full line corresponds to the nominal compositional profile of the $(GaAs)_{17}(AlAs)_2$ SL with a rectangular potential while the broken line was calculated for the broad $Al_{0.5}Ga_{0.5}As$ barrier with the thickness of 4 monolayers. Such an alteration of the compositional profile is expected due to the smoothing of the interfaces which has been already studied in the two-monolayer wide AlAs barriers in [11]. As it turned out, this broadening of the AlAs barrier is almost completely compensated by the decrease of its height and an electron effective mass, giving the same miniband dispersion as in the nominal barrier, which explains our experimental results quite well. The values of the electron damping constant γ_{pz} obtained from the fitting of the reflection spectra are also plotted in Fig.3a.

As it has been established theoretically in [12], when the Fermi level is located in the minigap between two minibands, 2D electron states should contribute to the vertical transport (along the superlattice axis) giving rise of conductivity. Hence, the nonzero vertical conductivity, and as a consequence the nonzero plasma frequency ω_{pz}, are expected even in the SL's with completely filled minibands. As it follows from Fig.3a, our experiments do not present any evidence of such contributions due to the 2D electrons.

The frequency of the in-plane plasmon ω_{px} versus the electron density is shown in Fig.3b. The full line was calculated with an effective mass at the bottom of the 2D Γ subband equal to $m_x = 0.067m_o$. The data obtained from the Raman spectra measured with the different orientation of an electric polarization of the light are presented in Fig.3b. We clearly observed the in-plane anisotropy of the ω_{px} plasmon in the sample with $n = 7 \cdot 10^{17}$ cm^{-3} which can be seen in the Raman spectra of this sample presented in Fig.2 as well. This anisotropy can be caused by the miniband anisotropy revealed at the high enough position of the Fermi level in the relevant miniband.

Acknowledgment. We appreciate the financial support from CNPq, FAPESP and CAPES.

References:

1. L.Esaki, R.Tsu, IBM J.Res.Dev.**14**, 61 (1970)
2. B.Jusserand and M.Cardona, in Light Scattering in Solids V, ed by M.Cardona and G.Güntherodt, Springer-Verlag, 1989, p.49.
3. A.Pinczuk, G.Abstreiter, ibid, p.153.
4. L.Esaki, L.L.Chang, W.E.Howard, V.L.Rideout, Proc. of the 11th Int. Conf. on the Physics of Semiconductors, Poland, 1972, PWN-Polish Scientific Publishers, p.431.
5. E.E.Mendez, F.Agulló-Rueda, J.M.Hong, Phys.Rev.Lett., **60**, 2426 (1988)
6. A.Sibille, J.F.Palmer, H.Wang, F.Mollot, Phys.Rev.Lett. **64**, 52 (1990)
7. H.T.Grahn, K. von Klitzing, K.Ploog, G.H.Döhler, Phys.Rev. **B43**, 12094 (1991)
8. Yu.A.Pusep, A.G.Milekhin, A.I.Toropov, Sol.St.Electronics, **37**, 613 (1994)
9. Yu.A.Pusep, A.G.Milekhin, A.I.Toropov, J.Phys.: Cond.Matter **6**, 93 (1994)
10. Yu.A.Pusep, A.G.Milekhin, A.I.Toropov, Superlattices and Microstructures, **13**, 115 (1993)
11. Yu.A.Pusep, S.W.da Silva, J.C.Galzerani, A.Milekhin, V.Preobrazhenskii, B.Semyagin, I.Marahovka , Phys.Rev. **B52**, 2610 (1995)
12. S.-R.E.Yang, S.Das Sarma, Phys. Rev. **B37**, 10090 (1988)

4. Figure captions

Fig.1. The p-polarized reflection spectra of the doped $(GaAs)_{17}(AlAs)_2$ superlattice measured at the temperature T=80 K. Dotted lines are the calculated spectra.

Fig.2. The Raman spectra of the doped $(GaAs)_{17}(AlAs)_2$ superlattice measured at the temperature T=80 K in the frequency range of the AlAs-like phonons; the spectra obtained with x || [100] and x′ ||[110] are presented. The nonlabeled arrows indicate the frequencies of the optical modes obtained by reflection spectra.

Fig.3. Dependence of the superlattice plasmon (ω_{pz}) (a) and the in-plane plasmon (ω_{px}) (b) on an electron concentration in the $(GaAs)_{17}(AlAs)_2$ superlattice. Crosses show the values of the electron damping constant (γ_{pz}); the squares and triangles in (b) relate to the in-plane electric polarization of the incoming light parallel to the [100] and [110] respectively.

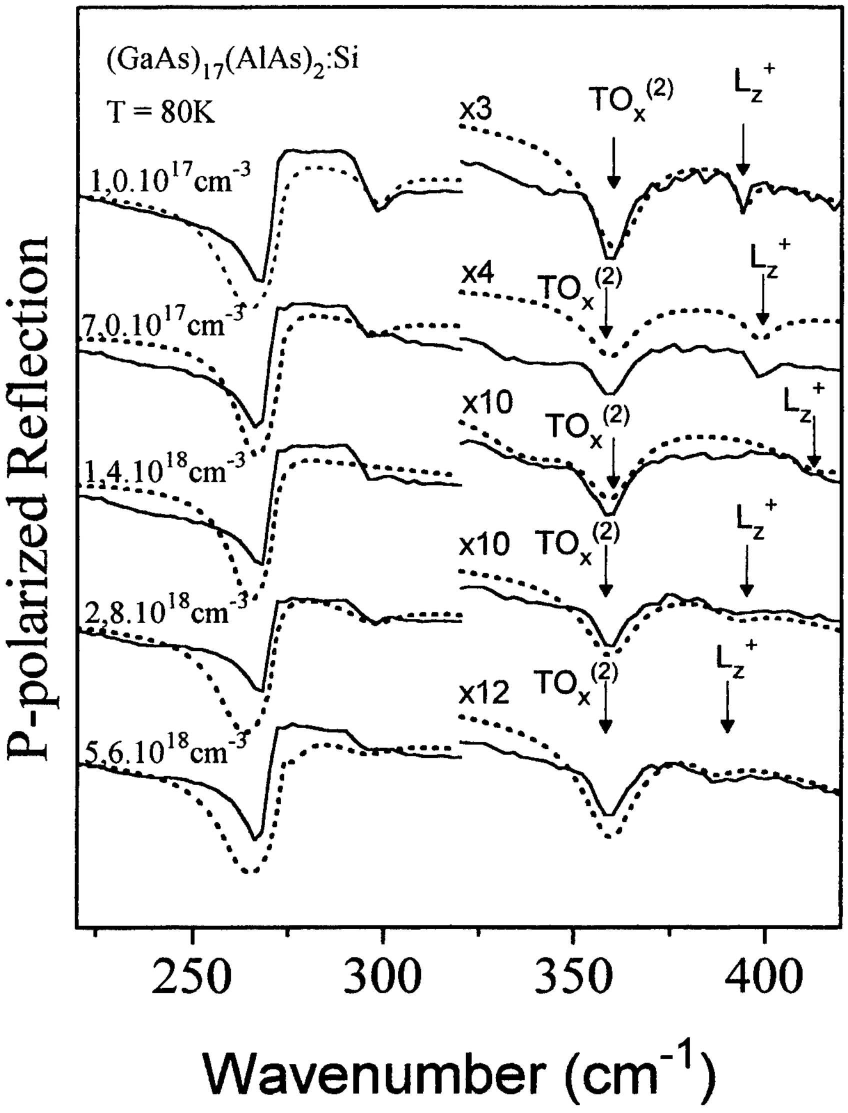

$(GaAs)_{17}(AlAs)_2$:Si
T = 80K
1,0.10^{17}cm^{-3}
7,0.10^{17}cm^{-3}
1,4.10^{18}cm^{-3}
2,8.10^{18}cm^{-3}
5,6.10^{18}cm^{-3}
x3
x4
x10
x10
x12
$TO_x^{(2)}$
L_z^+
P-polarized Reflection
250
300
350
400
Wavenumber (cm^{-1})

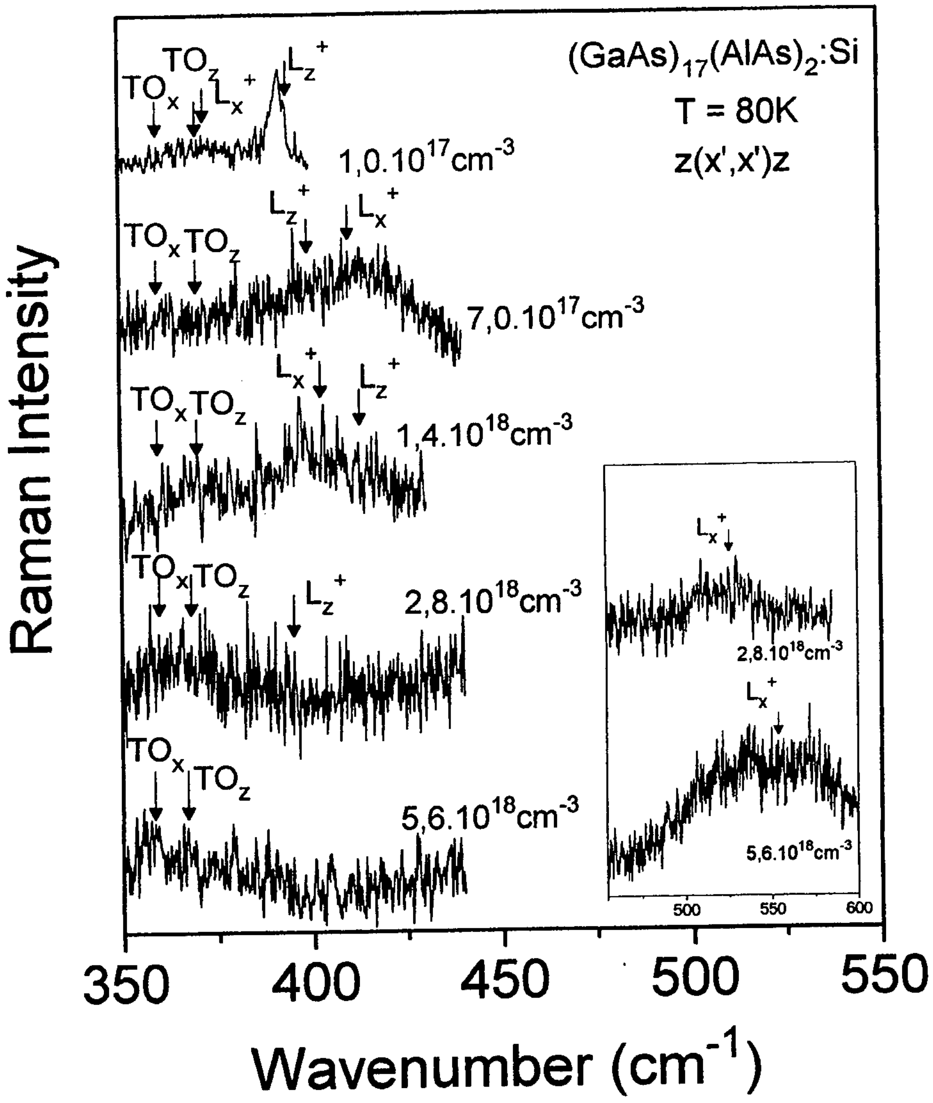
(GaAs)$_{17}$(AlAs)$_2$:Si
T = 80K
z(x',x')z
TO$_x$ TO$_z$ L$_x^+$ L$_z^+$
1,0.10^{17}cm^{-3}
TO$_x$ TO$_z$ L$_z^+$ L$_x^+$
7,0.10^{17}cm^{-3}
TO$_x$ TO$_z$ L$_x^+$ L$_z^+$
1,4.10^{18}cm^{-3}
TO$_x$ TO$_z$ L$_z^+$
2,8.10^{18}cm^{-3}
TO$_x$ TO$_z$
5,6.10^{18}cm^{-3}
L$_x^+$
2,8.10^{18}cm^{-3}
L$_x^+$
5,6.10^{18}cm^{-3}
500
550
600
350
400
450
500
550
Raman Intensity
Wavenumber (cm^{-1})

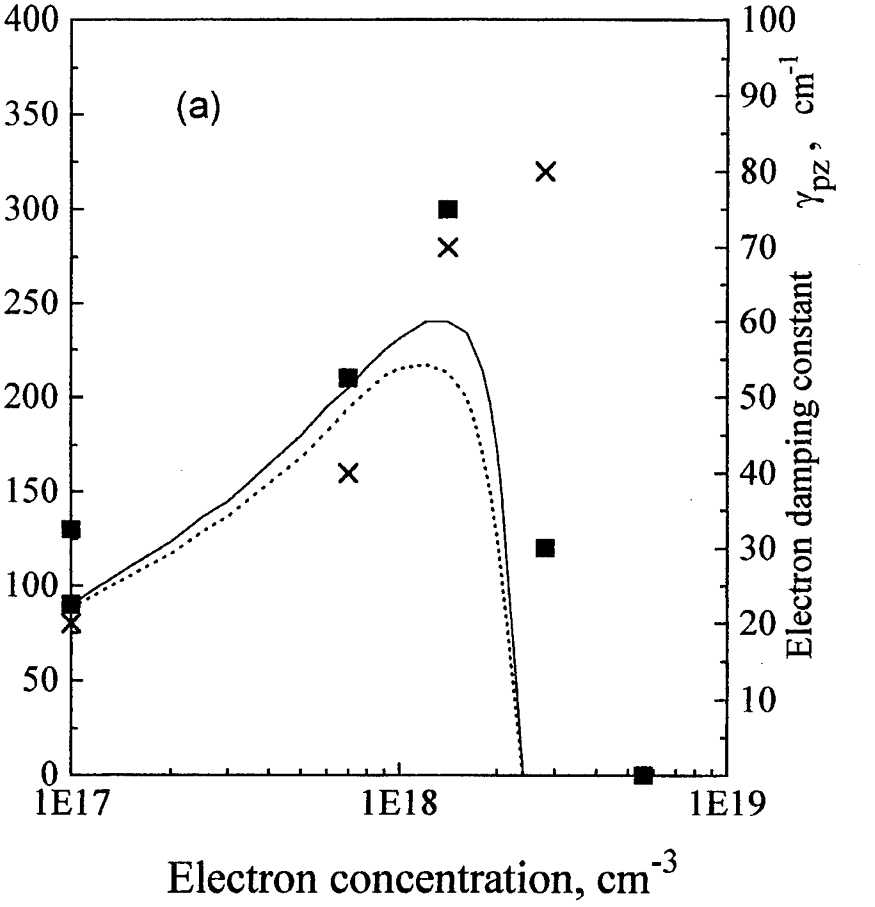
(a)
400
350
300
250
200
150
100
50
0
1E17
1E18
1E19
Electron concentration, cm^{-3}
100
90
80
70
60
50
40
30
20
10
Electron damping constant γ_{pz}, cm^{-1}

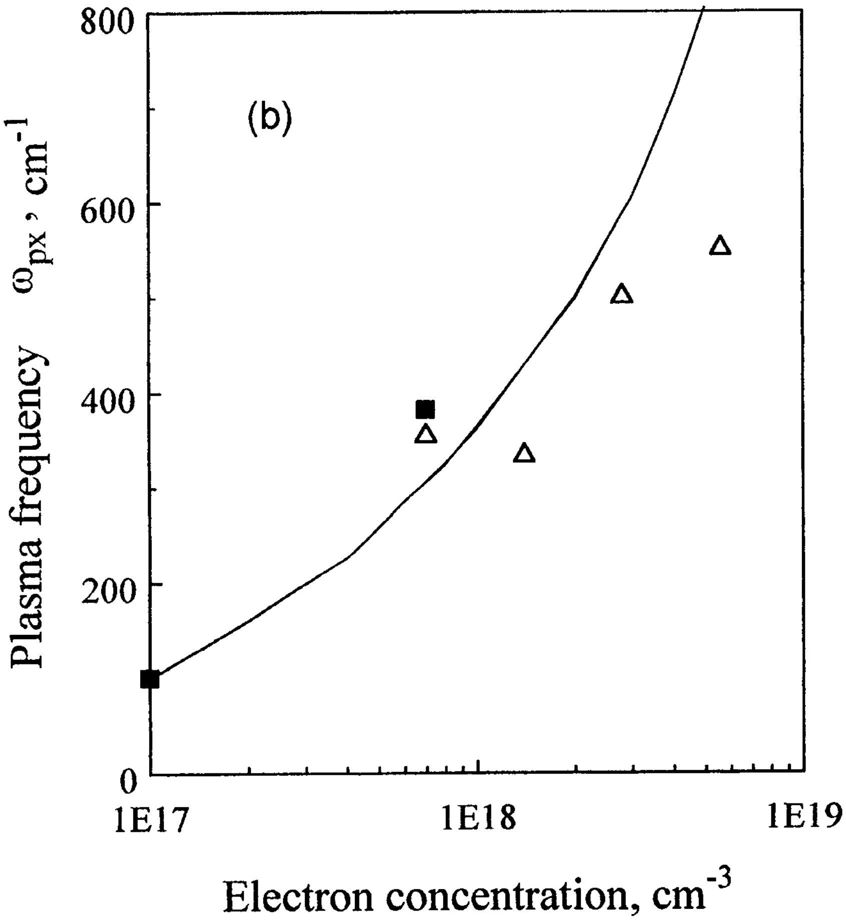
(b)
Plasma frequency ω_{px}, cm^{-1}
800
600
400
200
0
1E17
1E18
1E19
Electron concentration, cm^{-3}

Theoretical Modeling of the Intersubband Transitions in $Al_{0.3}Ga_{0.7}As/GaAs$ Semiconductor Quantum Wells

M. O. Manasreh[†], Danhong Huang[‡] and Godfrey Gumbs[*]

[†]Phillips Laboratory (PL/VTRP), Kirtland AFB, NM 87117
[‡]Dept. of Elec. & Computer Engg., Wayne State Univ., Detroit, MI 48202
[*]Dept. of Phys., Hunter College of CUNY, 695 Park Ave., New York, NY 10021

Abstract

Infrared absorption spectroscopy is used to study the conduction electron intersubband transition between the ground and first excited states in Si-doped $Al_{0.3}Ga_{0.7}As/GaAs$ quantum wells. A line shape calculation is presented for the optical absorption for different values of temperature T and electron density n_{2D}. The good agreement between the numerical results and experimental data is achieved. The measured blue-shift or red-shift of the peak position is reproduced as T or n_{2D} is reduced, respectively. In our theory, a self-consistent screened Hartree-Fock calculation is done with the use of the $z-$dependent effective mass of electrons and material dielectric constant, and the non-parabolic energy dispersion. The screened exchange interaction is evaluated by a generalized Thomas-Fermi model. The optical absorption is calculated by the many-body theory including the depolarization-shift and excitonic-shift.

I. INTRODUCTION

An infrared (IR) detector can be regarded as a transducer converting the IR radiation into the electrical signal. The electromagnetic wave with wavelength ranging from 1 to 1000 μm is said as *infrared radiation* which can penetrate many crystalline, plastic and gaseous materials and the earth's atmosphere but not metals[1]. Infrared radiation can further be divided into the long-wavelength infrared ($1-30$ μm) and far-infrared (> 30 μm). Infrared detectors are classified as thermal and photon devices[2]. The former operates by raising the device temperature when absorbing the incident light. The latter, quantum detector, responses to the incident light through the photo-emission of electrons from the surface, electron interband and intersubband transitions, whose output is determined by the rate of photon absorption.

Recently, there have been much effort toward designing semiconductor structures with tailored electronic and optical properties for the long-wavelength infrared quantum detector[3,4]. To implement bandgap engineering of infrared detectors, we have to precisely control the composition, doping, and thickness of the semiconductor layers. The molecular-beam-epitaxy (MBE) techniques make it possible for us to deposit ultrathin (10 – 100 Å) epitaxial layers of precisely controlled alloy compositions on semiconductor substrates on an atomic layer-by-layer basis[5]. The MBE techniques is also applied to deposit multi-layers of two different kinds of semiconductor materials with atomically abrupt interfaces[6].

When there exists a conduction band (or a valence band) offset in energy at the heterostructure interface due to difference in the bandgap of alternating layers with different compositions, quantum well is formed in the band structure. In a single-particle picture, the electron wave functions and energy subbands are completely decided by the depth and the thickness of the quantum well. When the quantum well is doped with electrons, the many-body effect brings into the dependence of the wave functions and energy subbands on the electron density n_{2D} and temperature T.

One way of monitoring changes in the material optical response is applying a probe light that perturbs the materials studied. Optical absorption has been proven to be one of the simplest and most applicable methods[7–10] to characterize materials. A full understanding of their optical properties is important because of the potential use of them as opto-electronic devices, such as, detectors, modulators and lasers. The band-structure design of these devices requires a simple but accurate theory for the device modeling. Early work[11] on the intersubband transitions in Si-doped quantum wells showed that the exchange energy plays a nontrivial role on the subband structure. Bandara, *et al.*[11] explicitly calculated the exchange-correction to the Hartree interaction for electrons in a quantum well with only lowest subband occupied. But their study was restricted to zero T and the infinite barrier model. Szmulowicz, *et al.*[12] has generalized it to finite T. But there is an overestimation of the blue-shift of the peak position as T is reduced at low n_{2D}. Simple and intuitive attempts to model the T-dependence of the absorption peak positions have shown an increase in the intersubband transition energy as T is increased, contrary to the experimental data[7,8]. As pointed out by Gumbs, *et al.*[13] the reason for this failure may be an inadequate treatment of the many-body effects. However, there is still a 10 % difference[13] in the T dependence of the peak energies compared with the measurement[7,8].

In this paper, we improve the agreement between the theory and experiment for the peak positions and line shapes. For this, we include the non-parabolic dispersion, screened exchange energy, the depolarization and excitonic shifts. In Refs. 12, 14 and 15, both the depolarization shift and unscreened exchange energy were included but the vertex correction[16] was neglected. Another effect not included by these authors concerns the interference of the refractive index function with the energy loss function, which enter the absorption coefficient. This has a significant effect on the peak position and asymmetry of the line shape. The exchange energy calculated in Refs. 12, 14 and 15 is overestimated because the screening of the exchange interaction was neglected and the electrons were confined by two infinite potential walls. The many-body and interference effects are T and n_{2D} dependent since the Coulomb interaction between electrons depends on the subband population which varies with T and n_{2D}.

In this paper, we calculate the absorption spectrum for different values of T and n_{2D} so that both the peak positions and line shapes can be compared with the experimental data. The rest of paper is organized as follows. In Sec. II, we introduce our model for *AlGaAs/GaAs* quantum wells. The formula of the self-consistent screened Hartree-Fock calculation is given. In Sec. III, we generalize the Thomas-Fermi static screening model by including the finite-size quantization effect. Section IV is devoted to the renormalization of electron kinetic energy by the screened exchange interaction. In Sec. V, we derive the general formula for the quasi-particle linear optical absorption coefficient and refractive index function. In Sec. VI, we analyze the many-body effect on the linear optical response by the collective dipole moment and vertex corrections. Section VII displays our numerical results and experimental data and their comparison. The last section contains the conclusions of the paper and some remarks.

II. MODEL AND SELF-CONSISTENT SCREENED HARTREE-FOCK CALCULATION

We model a $Al_xGa_{1-x}As/GaAs$ quantum well by a square-well potential profile with finite barriers at both sides

$$V_{QW}(z) = \begin{cases} \Delta E_c(x), & -L/2 \leq z \leq L/2 \\ 0, & \text{others} \end{cases} , \tag{1}$$

where x is the alloy-composition index, L is the quantum well width and the barrier height is $\Delta E_c(x) = 0.57 \times 1.247x\ (eV)$ with $x = 0.3$. The Schrödinger equation, determining the wave function $\phi_j(z)$ and subband edge E_j, in the self-consistent Hartree approximation[8,13] is

$$\left[-\frac{\hbar^2}{2} \frac{d}{dz} \left(\frac{1}{m^*(z)} \frac{d}{dz} \right) + V_{QW}(z) + V_H(z) \right] \phi_j(z) = E_j\ \phi_j(z)\ , \tag{2}$$

where $j = 1,\ 2,\ 3,\ \ldots$ is the subband index, and

$$m^*(z) = \begin{cases} m_{GaAs}, & -L/2 \leq z \leq L/2 \\ m_B, & \text{others} \end{cases} . \tag{3}$$

The non-parabolic electron energy dispersion in the bulk $GaAs$ well material is included through[17]

$$\frac{m_e}{m_W(k)} = 1 + \frac{E_p}{3} \left[\frac{2}{E_g + \hbar^2 k^2 / 2m_{GaAs}} + \frac{1}{E_g + \Delta_0 + \hbar^2 k^2 / 2m_{GaAs}} \right] , \tag{4}$$

which depends on the wave number k. Here, m_e is the free electron mass, m_{GaAs} is the effective mass in the bulk $GaAs$ well material, the energy gap, the spin-orbit splitting and the interband Kane matrix elements for the bulk $GaAs$ well material[17] are $\Delta_0 = 0.341\ (eV)$, $E_p = 22.71\ (eV)$ and

$$E_g = 1.5192 - 5.405 \times 10^{-4} \left(\frac{T^2}{204 + T} \right) (eV) . \tag{5}$$

Because the effective masses of electrons in the well and barrier materials are different, we obtain the "average" effective mass of electrons in the jth subband of the quantum well using the first-order perturbation theory[13,17]

$$\frac{1}{m_j^*(k)} = \frac{P_j}{m_W(k)} + \frac{1 - P_j}{m_B} , \tag{6}$$

which depends on the subband index j and k. Here, m_B is the effective mass of electrons in the bulk $Al_xGa_{1-x}As$ barrier material, and the electron quantum-well dwelling probability is

$$P_j = \int_{-L/2}^{L/2} dz\ |\phi_j(z)|^2 . \tag{7}$$

Using the virtual-crystal approximation[8] for the bulk $Al_xGa_{1-x}As$ barrier material, we get

$$\frac{1}{m_B} = \frac{x}{m_{AlAs}} + \frac{1 - x}{m_{GaAs}} \tag{8}$$

with $x = 0.3$, where m_{AlAs} is the effective mass in bulk $AlAs$ material.

Classically, every electron in the quantum well will be acted on by a total Coulomb force from all the other electrons and ionized donors. The quantum-mechanical counterpart of this force is the Hartree potential in Eq. (2). It can be determined from the Poisson's equation[8,13]

$$\frac{d}{dz} \left[\epsilon_s(z) \frac{d}{dz} V_H(z) \right] = 4\pi e^2\ [\ N_{im}(z) - \rho(z)\ ] , \tag{9}$$

where $\epsilon_s(z) = 4\pi\epsilon_0\epsilon_b(z)$ depends on z, $\epsilon_b(z)$ represents the dielectric constant in the well and barrier materials. The impurity doping profile in Eq. (9) is

$$N_{im}(z) = N_{im}^{3D}(z) + \sum_i N_{im}^{2D}(i)\ \delta(z - z_i) , \tag{10}$$

where $N_{im}^{2D}(i)$ is the sheet density of the δ-doping in the ith layer at $z = z_i$. The electron density function in Eq. (9) is

$$\rho(z) = 2 \sum_j |\phi_j(z)|^2 \left[\frac{1}{2\pi} \int_0^{+\infty} dk\ k\ n_j(k) \right] , \tag{11}$$

where the jth subband occupation factor in the k-space is

$$n_j(k) = \frac{1}{1 + \exp\{\ [\ E_j(k) - \mu\ ]/k_B T\ \}}\ , \tag{12}$$

where $E_j(k)$ is the Coulomb interaction renormalized electron kinetic energy, which will be give in section IV, and μ denoting the chemical potential. The charge neutrality condition in the system yields

$$\int_{-\infty}^{+\infty} dz\ \rho(z) = n_{2D} = \int_{-\infty}^{+\infty} dz\ N_{im}^{3D}(z) + \sum_n\ N_{im}^{2D}(n)\ , \tag{13}$$

where n_{2D} is the electron density. For fixed n_{2D}, Eq. (13) can be used to determine the chemical potential μ in a self-consistent way. The electron-electron interaction can shift the chemical potential in the mean-field theory. This gives rise to the induced-charge density in the system, which, in turn, constrains the electron-electron interaction through the Poisson's equation as discussed in the next section.

III. GENERALIZED THOMAS-FERMI SCREENING MODEL

From Eq. (11), we can rewrite the electron density function as

$$\rho(z) = \sum_j\ |\phi_j(z)|^2\ \mathcal{N}_j(\mu)\ , \tag{14}$$

where

$$\mathcal{N}_j(\mu) = \frac{1}{\pi} \int_0^{+\infty} dk\ k\ n_j(k)\ . \tag{15}$$

In the mean-field theory, we can treat the electron-electron interaction as an induced potential which is determined through the Poisson's equation

$$-\ \nabla^2\ \psi^{ind}(\mathbf{r}_{\|}, z) = \frac{1}{\epsilon_0 \epsilon_b}\ \left[\ \rho^{ext}(\mathbf{r}_{\|}, z) + \rho^{ind}(\mathbf{r}_{\|}, z)\ \right]\ , \tag{16}$$

where $\mathbf{r}_{\|} = (x, y)$ is a 2D position vector in the quantum-well plane, ϵ_b is the average background dielectric constant, $\rho^{ext}(\mathbf{r}_{\|}, z)$ is the external test-charge density, and $\rho^{ind}(\mathbf{r}_{\|}, z)$ is the induced-charge density, calculated as the additional part of $\rho(z)$ to the first-order as the chemical potential μ is shifted by $-e\ \psi^{ind}(\mathbf{r}_{\|}, z)$[18]

$$\rho^{ind}(\mathbf{r}_{\|}, z) = -e^2\ \psi^{ind}(\mathbf{r}_{\|}, z)\ \sum_j\ |\phi_j(z)|^2\ \frac{d\mathcal{N}_j(\mu)}{d\mu}\ . \tag{17}$$

By inserting Eq. (17) into Eq. (16), we obtain

$$-\nabla^2 \; \psi^{ind}(\mathbf{r}_\parallel, z) + 2\sum_j \; |\phi_j(z)|^2 \; q_j^{TF} \; \bar{\psi}_j^{ind}(\mathbf{r}_\parallel) = \frac{1}{\epsilon_0\epsilon_b} \; \rho^{ext}(\mathbf{r}_\parallel, z) \; , \tag{18}$$

where we have defined the following notations

$$\bar{\psi}_j^{ind}(\mathbf{r}_\parallel) = \int_{-\infty}^{+\infty} dz \; |\phi_j(z)|^2 \; \psi^{ind}(\mathbf{r}_\parallel, z) \; , \tag{19}$$

$$q_j^{TF} = \frac{e^2}{8\pi\epsilon_0\epsilon_b \; k_B T} \int_0^{+\infty} dk \; k \; \cosh^{-2}\left[\frac{E_j(k) - \mu}{2k_B T} \right] \; . \tag{20}$$

After a series of Fourier transformations

$$\psi^{ind}(\mathbf{r}_\parallel, z) = \int \frac{d^2\mathbf{q}_\parallel}{(2\pi)^2} \int \frac{dq_z}{2\pi} \; \exp\left[i(\mathbf{q}_\parallel \cdot \mathbf{r}_\parallel + q_z z)\right] \; \psi^{ind}(q_\parallel, q_z) \; , \tag{21}$$

$$\bar{\psi}_j^{ind}(\mathbf{r}_\parallel) = \int \frac{d^2\mathbf{q}_\parallel}{(2\pi)^2} \; \exp\left(i\mathbf{q}_\parallel \cdot \mathbf{r}_\parallel\right) \; \bar{\psi}_j^{ind}(q_\parallel) \; , \tag{22}$$

$$\rho^{ext}(\mathbf{r}_\parallel, z) = \int \frac{d^2\mathbf{q}_\parallel}{(2\pi)^2} \int \frac{dq_z}{2\pi} \; \exp\left[i(\mathbf{q}_\parallel \cdot \mathbf{r}_\parallel + q_z z)\right] \; \rho^{ext}(q_\parallel, q_z) \; , \tag{23}$$

$$|\phi_j(z)|^2 = \int \frac{dq_z}{2\pi} \; \exp\left(iq_z z\right) \; f_j(q_z) \; , \tag{24}$$

Eq. (18) reduces to a matrix equation

$$\sum_j \left[\delta_{n,j} + \frac{q_j^{TF}}{q_\parallel} \; \mathcal{F}_{nj}(q_\parallel) \right] \; \bar{\psi}_j^{ind}(q_\parallel) = \psi_n^{ext}(q_\parallel) \; , \tag{25}$$

where $q_\parallel$ is the modulus of a 2D wave vector in the quantum-well plane,

$$\begin{aligned}\mathcal{F}_{nj}(q_\parallel) &= 2q_\parallel \int \frac{dq_z}{2\pi} \; \frac{f_n(-q_z) \; f_j(q_z)}{q_\parallel^2 + q_z^2} \\ &= \int_{-\infty}^{+\infty} dz \int_{-\infty}^{+\infty} dz' \; |\phi_n(z)|^2 \; \exp(-q_\parallel \; |z - z'|) \; |\phi_j(z')|^2 \; ,\end{aligned} \tag{26}$$

is the form factor due to the finite-size effect, and

$$\begin{aligned}\psi_n^{ext}(q_\parallel) &= \frac{1}{\epsilon_0\epsilon_b} \int \frac{dq_z}{2\pi} \; \frac{f_n(-q_z) \; \rho^{ext}(q_\parallel, q_z)}{q_\parallel^2 + q_z^2} \\ &= \frac{1}{2\epsilon_0\epsilon_b \; q_\parallel} \int_{-\infty}^{+\infty} dz \int_{-\infty}^{+\infty} dz' \; |\phi_n(z)|^2 \; \exp(-q_\parallel \; |z - z'|) \; \rho^{ext}(q_\parallel, z') \; ,\end{aligned} \tag{27}$$

$$\bar{\psi}_j^{ind}(q_\parallel) = \int \frac{dq_z}{2\pi} \; f_j(-q_z) \; \psi^{ind}(q_\parallel, q_z) \; . \tag{28}$$

From Eq. (25), we find the static dielectric-function matrix for the generalized Thomas-Fermi model

$$\varepsilon_{nj}(q_\parallel) = \delta_{n,j} + \frac{q_j^{TF}}{q_\parallel} \; \mathcal{F}_{nj}(q_\parallel) \; , \tag{29}$$

which will be applied to screen the exchange interaction in the next section.

IV. QUASI-PARTICLE KINETIC ENERGY

The *first effect* of the Coulomb interaction is the renormalization of the electron kinetic energy by including the screened exchange interaction effect. From the calculated self-consistent wave functions $\phi_j(z)$ and subband edges E_j, we can further calculate the screened exchange interaction which strongly depends on T and n_{2D} and bring it into the self-consistent calculation presented in section II. The renormalized electron kinetic energy in Eqs. (12) and (20) can be calculated through[19]

$$E_j(k) = E_j + \frac{\hbar^2 k^2}{2m_j^*(k)} + \sum_{i,\mathbf{k}'} n_i(k') \left[\sum_n \varepsilon_{in}^{-1}(|\mathbf{k}-\mathbf{k}'|)\, V_F^{nj}(|\mathbf{k}-\mathbf{k}'|) \right] , \qquad (30)$$

where $\varepsilon_{in}^{-1}(q_{\|})$ is the inverse of the generalized Thomas-Fermi static dielectric-function matrix given by Eq. (29), and the exchange-interaction matrix element is[13,19]

$$V_F^{nj}(|\mathbf{k}-\mathbf{k}'|) = -\frac{e^2}{2\epsilon_0\epsilon_b|\mathbf{k}-\mathbf{k}'|} \times \int_{-\infty}^{+\infty} dz \int_{-\infty}^{+\infty} dz'\, \phi_j^*(z)\phi_n(z)\, \exp(-|\mathbf{k}-\mathbf{k}'||z-z'|)\, \phi_n^*(z')\phi_j(z') , \qquad (31)$$

As an electron is excited from the nth subband to the jth subband at the z position, there will be another electron simultaneously making a intersubband transition from the jth subband to the nth subband at the z' position. Equivalently, there is an exchange between these two indistinguishable electrons at these two positions. Their fermion character produces a negative sign in the exchange interaction. This completes our way of including the effect of the Coulomb interaction in the quasi-particle kinetic energy. The Hartree interaction can only produce a shift of the subband edge. However, this shift in the subband-edge difference depends weakly on the subband index, T and n_{2D} compared with the part of subband-edge difference produced by the exchange interaction. The dominant exchange interaction also gives rise to an additional non-parabolic energy dispersion. The other effects of the Coulomb interaction on the optical response are described below.

V. QUASI-PARTICLE LINEAR OPTICAL RESPONSE

When an external z-polarized electromagnetic field is applied, the resulting perturbation in the electron density function will produce a quasi-particle optical response from a normal mode of density fluctuation. In the long wavelength limit, only vertical intersubband transitions need be considered.

A theory for optical response can be constructed using the time-dependent perturbation approach. For a probe field interacting weakly with electrons in quantum wells and the perturbation $\hat{V}$ induced by the probe field, the absorption coefficient is defined as the ratio of the energy absorbed per unit volume and per unit time to the incident flux[20]

$$\beta_{abs}(\omega) = \frac{\hbar\omega}{n(\omega)\ \sqrt{\epsilon_b}\ \epsilon_0\ c\ \mathcal{E}^2_{probe}}\ W(\omega)\ , \tag{32}$$

where $\mathcal{E}_{probe}$ is the amplitude of the probe field, ω is the frequency of the probe field, $n(\omega)$ is the scaled frequency-dependent refractive index function and $W(\omega)$ is the intersubband transition probability per unit time for the system to make a intersubband transition from an initial state $|i\rangle$ with energy E_i to a final state $|f\rangle$ with energy E_f. The intersubband transition probability is given by Fermi's golden rule in the first-order time-dependent perturbation theory

$$W(\omega) = \frac{\pi}{\hbar}\sum_f \left|\langle f\left|\hat{V}\right|i\rangle\right|^2\ \delta\,(E_f - E_i - \hbar\omega)\ . \tag{33}$$

Making use of

$$\hat{V} = \frac{-\,e}{\sqrt{LA}}\int d\mathbf{r}_{\|}\int dz\ \delta\rho(\mathbf{r}_{\|}, z, t)\ \varphi^{ext}(\mathbf{r}_{\|}, z)\ , \tag{34}$$

where $\delta\rho(\mathbf{r}_{\|}, z, t)$ is the induced density fluctuation and A is the cross-sectional area of the sample, we obtain by using the fluctuation-dissipation theorem

$$W(\omega) = \frac{1}{\hbar^2}\ \Re e\int_{-\infty}^{0} dt\ \langle\hat{V}_{int}(0)\hat{V}_{int}(t)\rangle\ \exp(-i\omega t) = \frac{-\,e^2}{LA\hbar^2}\ [1 + \rho_{ph}(\omega)]$$

$$\times\ \Re e\left\{i\hbar\int_{-\infty}^{+\infty} dt\int d\mathbf{r}_{\|}\int dz\ \exp(-i\omega t)\ \delta\rho(\mathbf{r}_{\|}, z, t)\ \varphi^{ext}(\mathbf{r}_{\|}, z)\right\}\ , \tag{35}$$

where $\rho_{ph}(\omega) = [\exp(\hbar\omega/k_BT) - 1]^{-1}$ is the photon distribution factor, $\hat{V}_{int}(t)$ is perturbation operator $\hat{V}$ in the interaction picture. Noticing that $\varphi^{ext}(\mathbf{r}_{\|}, z) = -\mathcal{E}_{probe}\ z$, and using the notation

$$\alpha_L(\omega) \equiv \frac{-e}{\mathcal{E}_{probe}LA}\int d\mathbf{r}_{\|}\int dz\ \delta\rho(\mathbf{r}_{\|}, z, \omega)\ z\ , \tag{36}$$

we obtain the absorption coefficient in terms of the Lorentz ratio $\alpha_L(\omega)$[21]

$$\beta_{abs}(\omega) = \frac{\omega\sqrt{\epsilon_b}}{cn(\omega)}\ [\ \rho_{ph}(\omega) + 1\ ]\ \Im m\ \alpha_L(\omega)\ . \tag{37}$$

From the Maxwell's equation for any transverse electromagnetic field[22]

$$\frac{1}{\epsilon_b}\ \nabla^2\ \mathcal{E}(\mathbf{r}, \omega) + \frac{\omega^2}{c^2}\ [1 + \Re e\ \alpha_L(\omega)]\ \mathcal{E}(\mathbf{r}, \omega) + i\ \frac{\omega^2}{c^2}\ \Im m\ \alpha_L(\omega)\ \mathcal{E}(\mathbf{r}, \omega) = 0\ , \tag{38}$$

we get the dispersion relation for the plane wave form of $\mathcal{E}(\mathbf{r},\omega)$

$$\left[\frac{\omega}{c}\, n(\omega) + \frac{i}{2\sqrt{\epsilon_b}}\, \beta_{abs}(\omega) \right]^2 = \frac{\omega^2}{c^2} \left[1 + \Re e\ \alpha_L(\omega) + i\Im m\ \alpha_L(\omega) \right] . \tag{39}$$

From Eq. (39), we obtain the refractive index function as

$$n(\omega) = \frac{1}{\sqrt{2}} \left\{ 1 + \Re e\ \alpha_L(\omega) + \sqrt{[1 + \Re e\ \alpha_L(\omega)]^2 + [\Im m\ \alpha_L(\omega)]^2} \right\}^{\frac{1}{2}} . \tag{40}$$

VI. MANY-BODY EFFECTS

The density fluctuation due to the probe field can be written in terms of the perturbation part of the density-matrix

$$\int d\mathbf{r}_{\|}\ \delta\rho(\mathbf{r}_{\|}, z;\ \omega) = 2 \sum_{j,j'} \phi^*_{j'}(z)\phi_j(z) \left[\frac{1}{2\pi} \int_0^{+\infty} dk\ k\ \rho_{jj'}(k,\omega) \right] . \tag{41}$$

The Lorentz ratio in Eq. (36) can be calculated as[21]

$$\alpha_L(\omega) = - \frac{e}{\pi\epsilon_0\epsilon_b\mathcal{E}_{probe}L} \sum_{j,j'} \int_0^{+\infty} dk\ k\ \rho_{jj'}(k,\omega)\ F_{j'j}\ . \tag{42}$$

For non-interacting electrons, the first-order perturbation part of the density-matrix element in the linear response theory can be obtained from the Liouville's equation[13,21]

$$\left(i\hbar\frac{d}{dt} - i\gamma_{jj'} \right) \rho_{jj'}(k,\omega) = e\mathcal{E}_{probe}\ F_{jj'}\left[n_{j'}(k) - n_j(k)\right] + \left[E_j(k) - E_{j'}(k)\right] \rho_{jj'}(k,\omega)\ , \tag{43}$$

where the bare dipole moment for non-interacting electrons is

$$F_{jj'} = F^*_{j'j} = \int_{-\infty}^{+\infty} dz\ \phi^*_j(z)\ z\ \phi_{j'}(z)\ . \tag{44}$$

The steady-state solution of the Liouville's equation in Eq. (43) is

$$\rho_{jj'}(k,\omega) = e\mathcal{E}_{probe}F_{jj'} \left[\frac{n_j(k) - n_{j'}(k)}{\hbar\omega - E_{j'}(k) + E_j(k) + i\gamma_{jj'}} \right] , \tag{45}$$

where $\gamma_{jj'} = (\gamma_j + \gamma_{j'})/2$ is the dephasing rate. In our numerical calculations, we have used the phenomenological formula[8,17] for the homogeneous broadening of jth subband due to impurity-scattering

$$\gamma_j\ (meV) = 3.144 + 0.101 \times 10^{-11}\ n_{2D}(10^{11}\ cm^{-2}) + 2.55 \left[\frac{1}{\exp\left(\hbar\omega_{ph}/k_BT\right) - 1} \right] . \tag{46}$$

Here, γ_j is independent of the subband index j, the optical phonon frequency is $\hbar\omega_{ph} = 36.7\ meV$. The quadratic n_{2D} term[8] in γ_j is neglected since the impurity scattering is proportional to n_{2D} in the Born approximation[18].

Collective Dipole Moment

The *second effect* of the Coulomb interaction is the screening of the bare Coulomb interaction. When an electron is excited to a high subband, it induces a density fluctuation in neighboring electrons through the long-range Coulomb force. This will introduce a screening on the Coulomb interaction.

In the quantum statistical theory, by including the Hartree interaction part in the perturbation we obtain the density fluctuation from Eqs. (41) and (45)

$$\delta\rho(z;\ \omega) \equiv \int d\mathbf{r}_{\parallel}\ \delta\rho(\mathbf{r}_{\parallel}, z;\ \omega) = \sum_{j<j'} \phi^*_{j'}(z)\phi_j(z)\ e\mathcal{E}_{probe}\ [\ F_{jj'} + D_{jj'}(\omega)\ ]\ \chi^{(1)}_{jj'}(\omega)\ , \tag{47}$$

where $D_{jj'}(\omega)$ is the collective dipole moment as a correction to the bare dipole moment $F_{j'j}$, and $\chi^{(1)}_{jj'}(\omega)$ is the susceptibility for the interacting electrons, given below. By solving the Poisson's equation for the Hartree interaction, we can get from the self-consistent-field theory[13,21]

$$D_{nn'}(\omega) = \frac{1}{e\mathcal{E}_{probe}} \int_{-\infty}^{+\infty} dz \int_{-\infty}^{+\infty} dz'\ \phi^*_n(z)\phi_{n'}(z) \left(-\frac{e^2}{2\epsilon_0\epsilon_b}\,|z-z'|\right) \delta\rho(z';\ \omega)\ . \tag{48}$$

This leads us to the following linear-matrix equation for $n < n'$

$$\sum_{j<j'} D_{jj'}(\omega) \left[\delta_{n,j}\delta_{n',j'} - \chi^{(1)}_{jj'}(\omega) \int_{-\infty}^{+\infty} dz \int_{-\infty}^{+\infty} dz' \phi^*_n(z)\phi_{n'}(z) \left(-\frac{e^2}{2\epsilon_0\epsilon_b}\,|z-z'|\right) \phi^*_{j'}(z')\right.$$

$$\left. \times\ \phi_j(z')\right] = \sum_{j<j'} \chi^{(1)}_{jj'}(\omega) \int_{-\infty}^{+\infty} dz \int_{-\infty}^{+\infty} dz' \phi^*_n(z)\phi_{n'}(z) \left(-\frac{e^2}{2\epsilon_0\epsilon_b}\,|z-z'|\right) \phi^*_{j'}(z')\phi_j(z')\ . \tag{49}$$

We can see that the screening has been included through the dielectric-function shown as a coefficient matrix in Eq. (49).

Vertex Correction

The *third effect* of the Coulomb interaction is the vertex correction to the non-interacting electron polarizability. At the same time when an electron is excited to a higher subband, it creates a "hole" state in the initial occupied subband. This will lead to an "excitonic" interaction between the excited electron and the "hole" state.

In Eq. (47), the susceptibility for interacting electrons is

$$\chi^{(1)}_{jj'}(\omega) = \frac{1}{\pi}\int_0^{+\infty} dk\; k\; \chi^{(0)}_{jj'}(k,\omega)\;\Gamma_{jj'}(k,\omega)\;, \tag{50}$$

where $j < j'$, and the polarizability for non-interacting electrons is

$$\chi^{(0)}_{jj'}(k,\omega) = \frac{n_j(k) - n_{j'}(k)}{\hbar\omega - E_{j'}(k) + E_j(k) + i\gamma_{jj'}} + \frac{n_{j'}(k) - n_j(k)}{\hbar\omega + E_{j'}(k) - E_j(k) + i\gamma_{jj'}}\;. \tag{51}$$

The vertex part $\Gamma_{jj'}(k,\omega)$ in Eq. (50) is due to the excitonic interaction[16], and can be calculated by summing over all the ladder diagrams which yields the following Bethe-Salpeter's equation[21] for $j < j'$

$$\Gamma_{jj'}(k',\omega) = 1 + \frac{1}{(2\pi)^2}\int d^2\mathbf{k}$$

$$\times\chi^{(0)}_{jj'}(k,\omega)\;\Gamma_{jj'}(k,\omega)\left[\sum_{m\leq m'}\varepsilon^{-1}_{jj',mm'}(|\mathbf{k}'-\mathbf{k}|,0)\;V_F^{mm'}(|\mathbf{k}'-\mathbf{k}|)\right]\;. \tag{52}$$

In Eq. (52), the small exciton-coupling effect is neglected for the low n_{2D}, and we have also used the inverse of the static dielectric-function matrix of the system to screen the vertex correction. In the random-phase approximation, the intersubband-type Lindhard's dielectric-function matrix beyond the long-wavelength limit for $j < j'$ and $m \leq m'$ can be written as

$$\varepsilon_{jj',mm'}(q_{\|},\omega) = \delta_{j,m}\;\delta_{j',m'} - U_{jj',m'm}(q_{\|})$$

$$\times\left\{\frac{2}{(2\pi)^2}\int d^2\mathbf{k}\;\frac{2[n_m(k) - n_{m'}(|\mathbf{k}+\mathbf{q}_{\|}|)][E_{m'}(|\mathbf{k}+\mathbf{q}_{\|}|) - E_m(k)]}{(\hbar\omega + i\gamma_{jj'})^2 - [E_{m'}(|\mathbf{k}+\mathbf{q}_{\|}|) - E_m(k)]^2}\right\}\;, \tag{53}$$

where the intersubband excitation coupling is

$$U_{jj',m'm}(q_{\|}) = \frac{e^2}{2\epsilon_0\epsilon_b q_{\|}}\int_{-\infty}^{+\infty} dz\int_{-\infty}^{+\infty} dz'\;\phi_j^*(z)\phi_{j'}(z)$$

$$\times\exp\Big(-\,q_{\|}\,|z-z'|\Big)\;\phi^*_{m'}(z')\phi_m(z')\;. \tag{54}$$

Finally, by combining the effects of collective dipole moment and the vertex correction, Eq. (42) can be generalized into

$$\alpha_L(\omega) = -\frac{e^2}{\pi\epsilon_0\epsilon_b L}\sum_{j<j'} F_{j'j}\left[F_{jj'} + D_{jj'}(\omega)\right]\int_0^{+\infty} dk\; k\;\chi^{(0)}_{jj'}(k,\omega)\;\Gamma_{jj'}(k,\omega)\;. \tag{55}$$

The effect due to screening and the vertex correction tends to shift the peak position up and down, respectively. In addition, the screening will shrink the peak width but the vertex correction expand it.

VII. NUMERICAL RESULTS AND DISCUSSIONS

In Fig. 1, we present the absorption coefficient $\beta_{abs}(\omega)$ from both our calculated results using Eqs. (37), (40) and (55) and experimental data which are recorded at the Brewster angle using a FTIR spectrometer for two samples at $T = 5\ K$. The peak energy increases with n_{2D}. The positive Hartree energy, depending on n_{2D}, shifts both subbands upward, while leaving their separation almost unchanged. The negative exchange energy shifts the first subband down more than the second subband, thereby increasing their separation. For an increased n_{2D}, the exchange energy gradually becomes dominant. Therefore, the peak position moves to the right. In addition, we find that the calculated peak positions coincide well with those from the experiment for both the low-density and high-density samples. The peak strength of the low-density sample is slightly lower than that observed in the experiment. The line shapes show slight deviations at energies away from the peak energy and a small peak width is obtained in comparison with the measurement. The absorption coefficient $\beta_{abs}(\omega)$ in Eq. (37) contains the ω-dependent refractive index function $n(\omega)$ in the denominator. This produces an interference which changes both the line shape and the peak position. For high n_{2D}, the second subband begins to be populated. The collective dipole moment $D_{jj'}(\omega)$ due to the Hartree interaction is found to shrink the peak width, while the exchange interaction expands the peak width. We attribute the asymmetrical line shape to the interference effect, strong non-parabolic energy dispersion and the exchange interaction at large k.

In Fig. 2 we present a quantitative comparison between $\beta_{abs}(\omega)$ from our numerical simulations and experimental data for the low-density sample at two values of T. The peak energy increases with reducing T, shown as a blue-shift. The crucial negative exchange energy brings down the first subband more than the second subband, and increases the separation between them. With increase T, the exchange interaction becomes weaker, and then, the peak energy decreases. Moreover, we find that the calculated peak positions also coincide with those measured at both low and high T. The peak strength of the high-T peak seems a little bit smaller than that observed. The asymmetrical line shape of both curves displays very small deviations on the lower energy side.

Figure 3 shows the numerical comparison between $\beta_{abs}(\omega)$ with the experimental data for the high-density sample at two different values of T. The peak energy again increases when T is reduced, with a large blue-shift compared with Fig. 2 due to the high n_{2D}. Similarly, the negative exchange energy lowers the first subband more than the second subband. Therefore, their separation increases with exchange interaction. By reducing T, the exchange interaction is strengthened, so that the peak energy shifts upward. Furthermore, we know that both calculated peak positions and peak strengths for the high-density sample coincide very well with those measured at both low and high T. The line shape of both energy peaks, however, slightly differs at energies away from the peak energy. The peak width calculated is smaller than that measured.

VIII. CONCLUSIONS AND REMARKS

In conclusion, by demonstrating for the first time reasonably good agreement between our theory and experimental data for optical absorption from electron intersubband transitions between the ground and first excited states in $Al_{0.3}Ga_{0.7}As/GaAs$ QW as a function of n_{2D} and T, we have established a simple but accurate formula for the band-structure design of infrared photo-detectors. Our model does not contain any adjustable parameters for comparing the peak positions except for the subband broadening γ_1, γ_2 which are used to fit the full width at half-maximum in the experimental data. The blue-shift and red-shift of the absorption peak position found in the experimental data are quantitatively reproduced theoretically as T and n_{2D} are reduced, respectively.

In our calculation, we have found that the exchange interaction plays a crucial role in T- and n_{2D}-dependence of the peak position and lineshape. However, the Hartree interaction only produces a rigid shift in the peak position and shrink very little of the peak width. Both of them show very weak dependence on T and n_{2D}. The correct estimation of the screening of exchange interaction greatly affect the agreement between the numerical results and experimental data. The unscreened model is found to overestimate the T and n_{2D} dependence, while the plasmon-pole screening model is found to underestimate the dependence. The generalized Thomas-Fermi model derived here is found simple but quantitatively applicable in the renormalization of electron kinetic energy. The static random-phase screening to the vertex correction beyond the long-wavelength limit is found quantitatively adequate.

REFERENCES

[1] J. D. Vincent, *Fundamentals of Infrared Detectors Operation and Testing*, (John Wiley and Sons, New York, 1990).

[2] J. Wilson and J. F. B. Hawkes, *Optoelectronics an Introduction*, (Prentice-Hall, Englewood Cliffs, New Jersy, 1983).

[3] F. Capasso, J. Vac. Sci. Technol. B **1**, 457 (1983).

[4] F. Capasso, Science, **235**, 172 (1987).

[5] R. Dingle, "Lightwave Communication Technology", in *Semiconductors and Semimetals*, ed. R. K. Willardson and A. C. Beer, **22** (Academic Press, Orlando, Fla., 1985).

[6] R. Dingle, W. Wiemann, and C. H. Henry, Phys. Rev. Lett. **33**, 827 (1974).

[7] M. O. Manasreh, F. Szmulowicz, D. W. Fischer, K. R. Evans, and C. E. Stutz, Appl. Phys. Lett. **57**, 1790 (1990).

[8] M. O. Manasreh and J. P. Loehr in *Semiconductor Quantum Wells and Superlattices for Long Wavelength Infrared Detection*, (Artech, Boston, 1993), Chap. 2.

[9] M. O. Manasreh, F. Szmulowicz, T. Vaughan, K. R. Evans, C. E. Stutz, and D. W. Fischer, Phys. Rev. B**43**, 9996 (1991).

[10] P. von Allmen, et al., Semi. Sci. and Technol. **3**, 1211 (1988); Superlattices and Microstructures **5**, 259 (1989).

[11] K. Bandara, D. D. Coon, O. Byungsung, Y. F. Lin, and M. H. Francombe, Appl. Phys. Lett. **53**, 1931 (1988).

[12] F. Szmulowicz, M. O. Manasreh, C. E. Stutz, and T. Vaughan, Phys. Rev. B**50**, 11618 (1994).

[13] G. Gumbs, D. Huang, and J. P. Loehr, Phys. Rev. B**51**, 4321 (1995).

[14] M. Załużny, Solid State Commun. **82**, 565 (1992).

[15] M. Załużny, Phys. Rev. B**43**, 4511 (1991).

[16] G. D. Mahan, *Many-Particle Physics* (Plenum, New York, 1981), Chap. 5.

[17] G. Bastard and J. A. Brum, IEEE J. Quantum Electron. QE-**22**, 1625 (1986).

[18] K. Esfarjani, H. R. Glyde, and V. Sa-yakanit, Phys. Rev. B**41**, 1042 (1990).

[19] A. H. MacDonald, J. Phys. C: Solid State Phys. **18**, 1003 (1985).

[20] J. Callaway, *Energy Band Theory*, (Academic, New York, 1964), p. 287.

[21] G. Gumbs, D. Huang, Y. Yin, H. Qiang, D. Yan, F. H. Pollak, and T. F. Noble, Phys. Rev. B**48**, 18328 (1993).

[22] H. Haug and S. W. Koch, "*Quantum Theory of the Optical and Electronic Properties of Semiconductors*," (World Scientific Publishing Co. Pte. Ltd. Singapore), (1990) p.12.

FIGURES

FIG. 1. Comparison between the calculated $\beta_{abs}(\omega)$ (dashed lines) with the measurements (solid lines) at $T = 5\ K$ for samples with $n_{2D} = 7.5$ and $37.5 \times 10^{11}\ cm^{-2}$. The high-energy peak is for the high-density sample. In the calculations, the parameters are chosen as: $\epsilon_b = 13.0$, $L = 75\ \mathring{A}$, $m_W = 0.0665\ m_e$, $m_{AlAs} = 0.124\ m_e$.

FIG. 2. Comparison between the calculated $\beta_{abs}(\omega)$ (dashed lines) of the sample with $n_{2D} = 7.5 \times 10^{11}\ cm^{-2}$ at $T = 5\ K$ and $300\ K$ with the experimental measurements (solid lines). The high-energy peak is for $T = 5\ K$. The chosen parameters for ϵ_b, L, m_W, and m_{AlAs} are the same as in Fig. 1.

FIG. 3. Comparison between the calculated $\beta_{abs}(\omega)$ (dashed lines) of the sample with $n_{2D} = 37.5 \times 10^{11}\ cm^{-2}$ at $T = 5\ K$ and $300\ K$ with the experimental measurements (solid lines). The high-energy peak is for $T = 5\ K$. The chosen parameters for ϵ_b, L, m_W, and m_{AlAs} are the same as in Fig. 1.

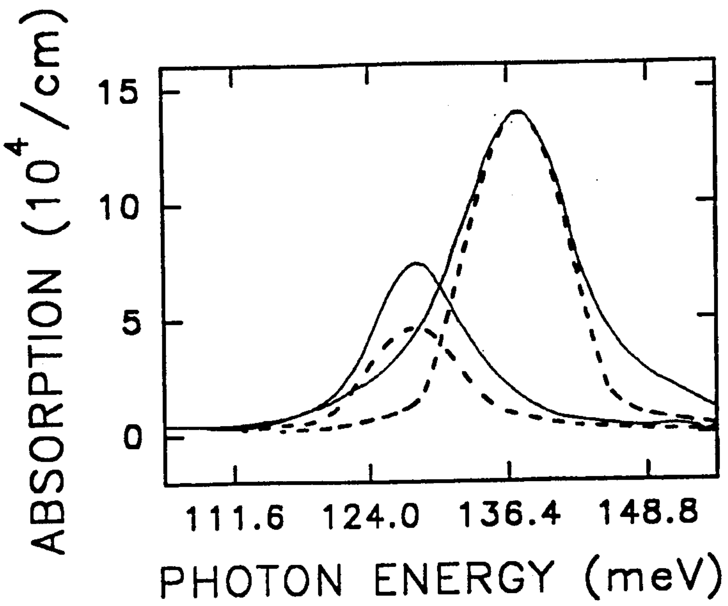

FIG. 1. Comparison between the calculated $\beta_{abs}(\omega)$ (dashed lines) with the measurements (solid lines) at $T = 5$ K for samples with $n_{2D} = 7.5$ and 37.5×10^{11} cm^{-2}. The high-energy peak is for the high-density sample. In the calculations, the parameters are chosen as: $\epsilon_b = 13.0$, $L = 75$ $\mathring{A}$, $m_W = 0.0665$ m_e, $m_{AlAs} = 0.124$ m_e.

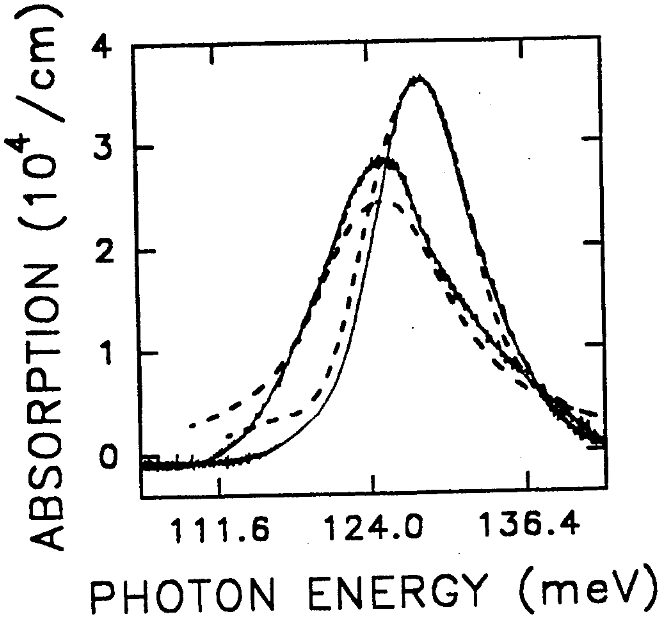

FIG. 2. Comparison between the calculated $\beta_{abs}(\omega)$ (dashed lines) of the sample with $n_{2D} = 7.5 \times 10^{11}\ cm^{-2}$ at $T = 5\ K$ and 300 K with the experimental measurements (solid lines). The high-energy peak is for $T = 5\ K$. The chosen parameters for ϵ_b, L, m_W, and m_{AlAs} are the same as in Fig. 1.

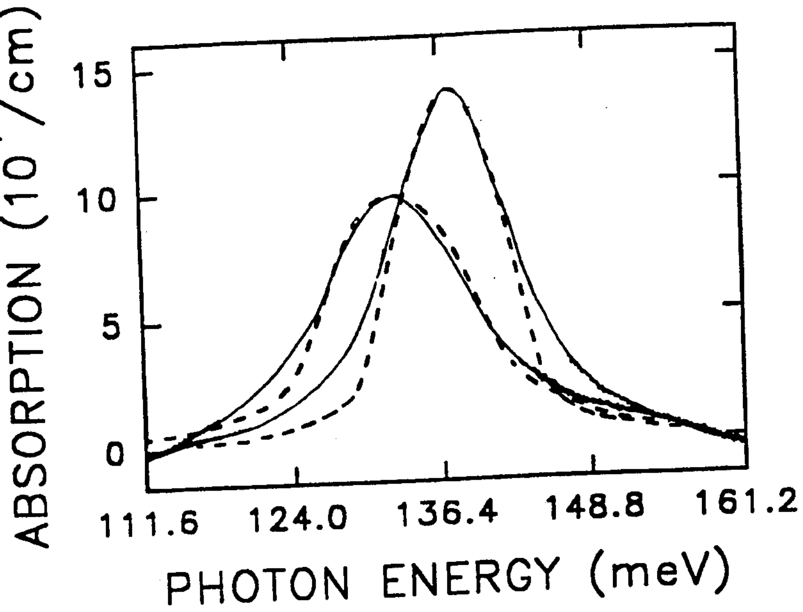

FIG. 3. Comparison between the calculated $\beta_{abs}(\omega)$ (dashed lines) of the sample with $n_{2D} = 37.5 \times 10^{11}$ cm^{-2} at $T = 5$ K and 300 K with the experimental measurements (solid lines). The high-energy peak is for $T = 5$ K. The chosen parameters for ϵ_b, L, m_W, and m_{AlAs} are the same as in Fig. 1.

LINEAR ABSORPTION IN $Hg_{1-x}Cd_xTe$

Vaidya Nathan

Phillips Laboratory/VTRP, Kirtland AFB, NM 87117-5776

INTRODUCTION

$Hg_{1-x}Cd_xTe$ is a material widely used for modern infrared detectors. The detector's photo responsivity is directly dependent on it's optical absorption coefficient. Besides if the incident radiation is of very short duration and the absorbed energy cannot be efficiently conducted away, it can give rise to temperature increase in the material and degrade it's properties. Hence it is important to thoroughly study the linear absorption in this material. However, to date there have been very few studies of this subject[1-4]. Most of the above studies restrict themselves to the absorption edge and the tail below the edge, and do not deal with energies greater than the bandgap. There is only one published work[4] that predicts absorption coefficients for energies greater than the bandgap, and this was based on the band structure model of Kane[5]. However, the formulae obtained in ref.4 are cumbersome and not in readily useable form. In this paper we present theoretical calculation of the intrinsic absorption spectrum of $Hg_{1-x}Cd_xTe$ for x=0.192 at 77K using a nonparabolic band structure due to Keldysh[6], taking into account the Burstein-Moss shift.

ABSORPTION COEFFICIENT CALCULATIONS

Following Anderson[4] we start with the following equation for the linear absorption coefficient of electromagnetic radiation of angular frequency ω in a solid with direct energy gap E_g

$$\alpha(\omega) = \frac{\varepsilon_\infty^{0.5}}{c} \int\int\int W(k) \left[\frac{1}{1+\exp[(E_V(k)-F)/k_B T]} - \frac{1}{1+\exp[(E_c(k)-F)/k_B T]} \right] \frac{2d^3k}{(2\pi)^3}, \qquad [1]$$

where

$$W(\mathbf{k}) = \frac{2\pi}{\hbar} |H_{vc}|^2 \, \delta[E_c(\mathbf{k}) - E_v(\mathbf{k}) - \hbar\omega] . \qquad [2]$$

In (1) and (2) c is the velocity of light in vacuum, $\hbar$ is Planck's constant divided by 2π, ε_∞ is the high frequency dielectric constant, H_{vc} is the interaction Hamiltonian, k_B is Boltzmann's constant, F is the Fermi energy, **k** is the wave vector and T is the temperature. In order to evaluate (1) one needs detailed knowledge of $E_v(\mathbf{k})$ and $E_c(\mathbf{k})$. For this we use the model described by the following equations due to Keldysh[6]

$$E_v(\mathbf{k}) = -\frac{E_g}{2}\left(1+\frac{\hbar^2 k^2}{\mu^* E_g}\right)^{0.5}, \qquad [3a]$$

$$E_c(\mathbf{k}) = \frac{E_g}{2}\left(1+\frac{\hbar^2 k^2}{\mu^* E_g}\right)^{0.5}, \qquad [3b]$$

in a system where the zero of energy is taken to be at the center of the fundamental energy gap and μ^* is the reduced effective mass of the valence and conduction bands. After some mathematical simplifications we obtain

$$\alpha(\omega) = \frac{2q^2}{c\hbar^2}\left(\frac{\mu^* E_g}{\varepsilon_\infty}\right)^{1/2}\left[\left\{\frac{\hbar\omega}{E_g}\right\}^2 - 1\right]^{1/2} \mathrm{BM}, \qquad [4]$$

where

$$\mathrm{BM} = \left\{1+\exp\left[\frac{-\hbar\omega-2F}{2k_B T}\right]\right\}^{-1} - \left\{1+\exp\left[\frac{\hbar\omega-2F}{2k_B T}\right]\right\}^{-1}. \qquad [5]$$

Eq. (4) and (5) represent closed form, compact formulae to calculate the absorption coefficient of narrow direct gap semiconductors, in contrast to the cumbersome formulae obtained by Anderson[4]. These equations were used to calculate the absorption coefficient of $Hg_{0.808}Cd_{0.192}T$ at 77K as a function of wavelength for different electron concentrations in the conduction band. This was done separately for the light hole and heavy hole bands and the results were added to obtain the effective absorption coefficient. The composition and temperature dependence of the energy gap was obtained from the equation [7]

$$E_g = \left[-304 + \frac{0.63T^2(1-2x)}{11+T} + 1858x + 54x^2\right]\mathrm{meV}. \qquad [6]$$

The effective masses of the electron and hole were obtained from **k.p** theory[8]. According to this method the electron effective mass m_e^* is given by

$$\frac{m}{m_e^*} = 1 + \frac{8mP^2\pi^2}{3h^2}\left[\frac{2}{E_g} + \frac{1}{E_g+\Delta}\right], \qquad [7]$$

where m is the free electron mass, P is the interband momentum matrix element, and Δ is the spin-orbit splitting. For $Hg_{1-X}Cd_XTe$, P is given by [9]

$$8mP^2\pi^2 / h^2 \approx 19 \text{ eV}, \qquad [8]$$

and Δ is equal to 1 eV. The light hole effective mass is equal to the electron effective mass. The heavy hole effective mass is insensitive to composition and temperature. Most of the magneto-optical experiments are consistent with a heavy hole effective mass between 0.38m and 0.53m and a value of 0.443m appears to be the best value to date[10], and is used in this calculation. A value of 13 was used for the optical dielectric constant of $Hg_{0.808}Cd_{0.192}T$[11]. The Fermi levels were calculated according to the method outlined in Anderson[4].

RESULTS

In Figure1 the calculated absorption coefficient of $Hg_{0.808}Cd_{0.192}T$ at 77K is presented as a function of wavelength for free electron concentrations of 0, $2x10^{16}$ and $10^{17}cm^{-3}$ in the conduction band. Qualitatively our results are similar to those of Anderson[4]. Quantitatively our results are somewhat larger than Anderson's. Perhaps this difference arises from the different band structures used in the two works. Also we do not have information on the values of effective masses and dielectric constant used by Anderson which may be different from those employed in this work. Needless to say that accurate experimental measurement of the intrinsic absorption spectrum of $Hg_{1-X}Cd_XTe$ will be enlightening.

REFERENCES

1. M. W. Scott, J. Appl. Phys. **40**, 4077 (1969).

2. J. A. Mroczkowski, D. A. Nelson, R. Murosako, and P. H. Zimmerman, J. Vacuum. Sci. Technol. **A1**, 1756 (1983).

3. K. H. Hermann, M. Happ, H. Kissel, K. P. Mollman, J. W. Tomm, C. R. Becker, M. M. Kraus, S. Yuan, and G. Landwehr, J. Appl. Phys. **73**, 3486 (1993).

4. W. W. Anderson, Infrared Phys. **20**, 363 (1980).

5. E. O. Kane, J. Phys. Chem. Solids **1**, 249 (1957).

6. L.V. Keldysh, Soviet Phys.-J. Exper. Theor. Phys. **6**, 763 (1958).

7. M. H. Weiler, in Semiconductors and Semimetals, Vol. 16, Ed. R. K. Willardson and A. C. Beer, Academic Press, New York 1981 (p.180).

8. E. O. Kane, J. Phys. Chem. Solids **2**, 181 (1960).

9. Y. Guldner, C. Rigaux, A. Mycielski and Y. Couder, Phys. Stat. Sol. **b82,** 149 (1977).

10. R. W. Miles, in Properties of Mercury Cadmium Telluride, Ed. J. Brice and P. Capper, INSPEC, Inst. Electrical Engineers, New York 1987 (p.116); M. H. Weiler, R. L. Agarwal and B. Lax, Phys. Rev.**B16**, 3603 (1977).

11. J. Baars and F. Sorger, Solid State Commun. **10**, 875 (1972).

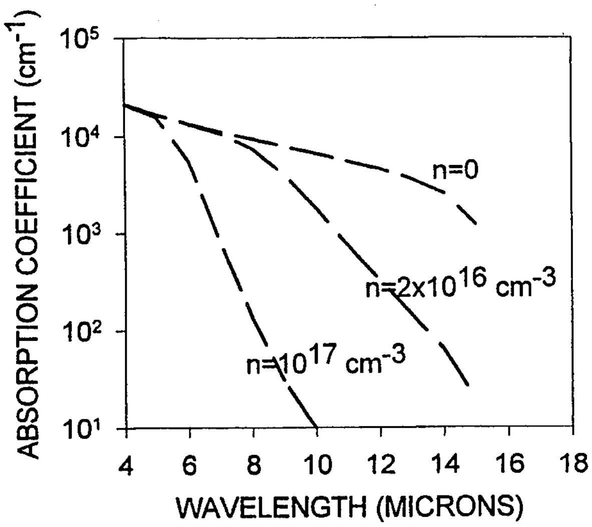

Figure 1. Calculated absorption coefficient of $Hg_{0.808}Cd_{0.192}Te$ at 77K as a function of wavelength. The n values refer to the density of free electrons in the conduction band.

SUBJECT INDEX